THE FORMATION AND REACTIVITY OF POSITIVE MUON MOLECULAR IONS

By

DONALD JOSEPH ARSENEAU

B. Sc. (Chemistry) St. Francis Xavier University

M. Sc. (Chemistry) University of British Columbia

A THESIS SUBMITTED IN PARTIAL FULFILLMENT OF

THE REQUIREMENTS FOR THE DEGREE OF

DOCTOR OF PHILOSOPHY

in

THE FACULTY OF GRADUATE STUDIES

CHEMISTRY

We accept this thesis as conforming

to the required standard

Canada

Department of Chemistry

The University of British Columbia

6224 Agricultural Road

Vancouver, Canada

V6T 1W5

Date: _October 10, 1992_

Abstract

Thermal (117–445 K) ion–molecule reaction rates are measured, using the μSR technique, for the muonated molecular ions $HeMu^+$, $NeMu^+$, $ArMu^+$, and N_2Mu^+ reacting with a wide variety of polar and non-polar neutral species. Mu is a light (0.11 amu) isotope of H with a positive muon replacing the proton. In almost all cases, both charge- and muon-transfer reactions are observed. Since charge transfer is endothermic in many cases, the reaction is believed to occur from rovibrationally excited states, $(HeMu^+)^*$ and $(NeMu^+)^*$, in accordance with the low efficiencies of He and Ne moderators for collisional deactivation. The total experimental rate constants are generally in good agreement with capture theories (Langevin, ADO, AADO) and in excellent agreement with the few corresponding protonated ion measurements, regardless of the degree of internal excitation.

The reacting muonated ions are found to form by association of a μ^+ with the bath gas at muon kinetic energies $\lesssim 1$ eV, and much of the binding energy is retained as rovibrational excitation. Collisional deactivation was investigated by varying the bath gas pressure (500~3000 torr) and by adding 0~2 torr Ar. A mechanism of de-excitation of $(NeMuX^+)^*$ (for reactive gas X) is suggested, while direct quenching of $(NeMu^+)^*$ and $(HeMu^+)^*$ is less important, though it does occur.

Table of Contents

List of Tables

List of Figures

5 KINETICS DISCUSSION

Acknowledgement

I wish to express my appreciation and gratitude to the numerous people I have worked with during my tenure as a graduate student. Drs. David Garner, Masa Senba, and Ivan Reid have made major contributions both to the research for this thesis and to my education. Thanks are also due to my colleagues James Kempton, Alicia Gonzalez, Randy Mikula, Susan Baer, James Pan, Alexandra Tempelmann, and Rodney Snooks; our research and discussions have been helpful, stimulating, and fun.

It is my pleasure to acknowledge the help and support rendered by Dr. Donald Fleming, who has shown not only enduring patience in his role as supervisor, but enthusiasm as a research colleague. Thank you.

Finally, I wish to thank my parents, Donald and Grace, whose teaching, love, and support have brought me this far.

Chapter 1

INTRODUCTION

The study of gas phase ion chemistry has a long history dating from the beginning of the 20th century when it was spurred by the development of mass spectrometry and the attendant need to interpret extraneous peaks. The first molecular ion identified was H_3^+ [1] whose formation was correctly attributed [2] to the ion–molecule reaction

$$H_2^+ + H_2 \longrightarrow H_3^+ + H \,, \tag{1.1}$$

and HeH^+ was discovered not much later [3]. Protonated ions have been well studied ever since. Interest waned somewhat in the 1930's due to the improved vacuum techniques of the time, but enjoyed a resurgence in the 1950's after the Manhattan project had pushed ion beam development and CH_5^+ had been unexpectedly discovered [4]. Since the 1970's there has been a continuing explosion in the study of ion–molecule reactions, and although recent interest has expanded towards negative ions and ion clusters [5], protonated ions are still central to the field of molecular ion chemistry. Though their importance to the understanding of mass spectrometry has long since passed, ionic reactions still have important applications in the fields of plasma physics, especially for relatively cool plasmas, radiolysis, astro-chemistry [6–9], and atmospheric chemistry [10], both for the earth's upper atmosphere and for other planets.

Ionic reactions are very important for building molecules in interstellar clouds [6–9], especially in dust-free gas clouds (since neutral reactions proceed mainly on the surface of dust grains [6,7,11]), and many extraterrestrial ions have been identified spectroscopically [6,7]. Ions are produced by photoionization by stellar UV radiation or, in dark regions, by cosmic rays. The H_3^+ ion has been sought spectroscopically in interstellar space, and while H_2D^+ has been detected [12], H_3^+ has only been seen in auroral emissions on Jupiter [13,14]. Nevertheless, H_3^+ is regarded as an important interstellar reactant [15], as are a number of other protonated species, especially HCO^+ [9,16].

Another significant astrochemical ion is protonated helium, though its role is not pivotal. Despite helium's natural abundance, and notwithstanding a premature report [17], HeH^+ has yet to be discovered outside the laboratory [18], though its presence has been implicated in the tenuous interstellar medium [19], in planetary nebulae, and in other irradiated dense clouds, including the ejecta from supernova 1987A [15,20]. Helium is ionized by UV or cosmic rays, and, in dense clouds, usually reacts by charge transfer with heavier atoms/molecules to form N^+, O^+, and particularly C^+, which react further to form still larger ions and molecules. In low density clouds or in the vacuous interstellar medium He^+ will radiatively associate with H to form HeH^+ [21]. Alternatively, HeH^+ may be formed by

$$He^+ + H_2 \longrightarrow HeH^+ + H \tag{1.2}$$

or by excited[1] dihydrogen ions

$$(H_2^+)^* + He \longrightarrow HeH^+ + H \tag{1.3}$$

although neither of these reactions is favored. In each case, the HeH^+ formed is a precursor to the formation of heavier, more stable ions.

---

[1] Throughout this thesis, an asterisk is used to indicate excited species, whether that excitation is electronic or vibrational.

The protonated rare gases are interesting for other reasons too. They are the *simplest closed-shell* molecular ions (with HeH$^+$ second only to the open-shelled H$_2^+$ for fewest particles) and so are probably the best examples of point-charge molecular ions. They are extremely strong acids, even in the Brønsted–Lowry sense of a proton donor; for instance, based on the proton affinities of 371 and 1400 kJ/mol for Ar and Cl$^-$, respectively, ArH$^+$ is a much stronger gas phase acid than the isoelectronic HCl, with NeH$^+$ and HeH$^+$ stronger still. Measurements of proton transfer are important for setting such acidity scales [22–24], and comparisons of gas phase acidities with liquid values can provide valuable information on solvation, and how it relates to molecular/ionic structure. HeH$^+$, NeH$^+$, and ArH$^+$ are isoelectronic with H$_2$, HF, and HCl respectively, and they are the 'nuclei' of the Rydberg atoms HeH*, NeH*, and ArH*. It is a bit strange, then, that reactions of the protonated rare gases have received only limited study. There are extensive measurements of proton transfer from other protonated gases [24–26], but with relatively little data on the protonated *rare gases*, and in particular, there are practically no measurements of NeH$^+$ reactivity [26].

This thesis is concerned with the formation and reactions of the muonated inert gases: HeMu$^+$, NeMu$^+$, and to some extent ArMu$^+$ and N$_2$Mu$^+$, which are isotopomers of the protonated gases with the proton (H$^+$) replaced by a positive muon ($\mu^+ =$ Mu$^+$). These ions react with a wide range of neutral atoms and molecules by a combination of muon transfer (in analogy with proton transfer) and charge transfer (forming Mu $= \mu^+e^-$, analogous to H). Only a few of the corresponding H-ion reactions have been studied before. The results to be presented herein, along with the portions already published [27,28], extend the data base considerably, particularly in the area of charge-transfer reactions, which are rarely observed for protonated gases. Furthermore, the pressure range investigated ($\gtrsim 1$ atm) is far above what is accessible to other experimental methods, and a comparison could reveal whether some H-ion rate constants, especially for slow reactions, are truly bimolecular or are instead due to termolecular processes.

The very low μ^+ mass, only 1/9 the proton mass, raises the possibility of entirely new behaviour. Quantum tunnelling could greatly increase the reaction rate, especially for muon transfer, in the same way that it enhances neutral Mu reactivity [29–31]. Tunnelling of hydrogen (H and H_2) through the rotational barrier has been seen in the break-up of ion–molecule complexes [32–35] but tunnelling is not generally as important for ionic reactivity as for neutral chemistry. The light μ^+ also gives muon molecular ions much higher vibrational zero-point energies and more widely spaced rotational/vibrational levels than their protonic analogs. These should affect the energetics of reactions, especially in regards to vibrational excitation and quenching. Some studies [36,37] of deuterated and protonated ions have attributed isotope effects to the differences in the densities of rovibrational states; such effects should be much larger for muonated ions.

In addition to comparisons with protonated ions, measurements of muonated gases should prove useful for interpreting μSR results in liquids and even in some insulating solids. Much of the diamagnetic μSR signal in liquids and even very-high-density gases can be attributed to molecular ion formation [38,39]; N_2Mu^+, $COMu^+$, and O_2Mu^+ have been clearly implicated in μSR studies of condensed N_2, CO, and O_2 [40–42], as has H_2Mu^+ in similar studies of solid H_2 [43]. Studies of muonated molecular ions in the gas phase should increase our understanding of those environments. The present study had its origins in an earlier investigation of gas-phase Mu formation [44], which identified the diamagnetic species in noble gases as μ^+ molecular ions, and which even detected some relaxation in Xe/Ne mixtures, though the form of the relaxation was not then resolved.

1.1 Positive Muons as Protons

Muons are elementary particles which were first discovered in cosmic rays [45] but are now produced artificially with particle accelerators. They come in two charge states, μ^- and μ^+. To a particle physicist, a muon resembles an electron as they both belong to the class of particles known as leptons, but a muon is heavier, weighing 207 times as

much, and unlike the electron (or positron) a muon is unstable, decaying weakly with a mean life of $2.2\,\mu$s. To a chemist though, a positive muon is more like a light proton with a mass of 0.11 amu.

Although muons do not feel the strong force and do not form nuclear matter as protons and neutrons do, a positive muon does form an atomic bound state with an electron just as a proton does in hydrogen. This is the muonium atom ($\text{Mu} = \mu^+\text{e}^-$). Since a muon is much heavier than an electron, it remains an almost stationary nucleus, giving muonium a reduced mass 0.996 as great as hydrogen's. Consequently, their Bohr radii, ionization potentials, and other properties are nearly identical, as shown in table 1.1. Unlike the positronium atom, muonium can truly be regarded as an isotope of hydrogen. But what an isotope! Muonium is only 1/9 as massive as hydrogen or 1/27 as heavy as tritium! This great difference is commonly exploited by μSR to investigate the mass dependence of H atom reactions and other physical processes involving hydrogen. Of particular import for this thesis is the ability of a positive muon to attach to a neutral atom or molecule to form a muonated molecular ion analogous to a protonated ion, and the subsequent reactions such ions undergo.

1.2 The Study of Ion–Molecule Reactions

Ion–molecule reactions are studied by a wide range of techniques which fall into two broad categories: ion beams/traps and flow/drift tubes. These have been thoroughly reviewed elsewhere [46–51] but brief synopses of the methods are given below to highlight the differences with the techniques used for this thesis.

The original means of examining ion–molecule reactions was to use a mass spectrometer with a less-than-perfect vacuum. The straightforward extension of this is the high-pressure mass spectrometer, where the ionization region may be at relatively high pressure (~ 5 microtorr to 1 torr), but with the mass selector and detector at low pressure. The reactants are mixed together in the ionization cell, allowed to ionize and react, and

Table 1.1 Some Properties of the Positive Muon and Muonium, Compared With Protons and Hydrogen

	value (μ^+)	$\div$ value (p^+)	$\div$ value (e^-)
Charge	$+1$		
Spin	$1/2$		
Mass	$105.6595\,\mathrm{MeV}\,c^{-2}$	0.112610	206.7687
Magnetic moment	$4.4905 \times 10^{-23}\,\mathrm{erg}\,\mathrm{G}^{-1}$	3.18333	0.004836
Mean lifetime	$2.19713\,\mu\mathrm{s}$		
Gyromagnetic ratio	$13.5544\,\mathrm{kHz}\,\mathrm{G}^{-1}$	3.18333	0.004836

	value (Mu)	$\div$ value (H)
Mass	$0.113978\,\mathrm{amu}$	0.113093
Reduced mass	$0.995187\,m_e$	0.995729
Ionization potential	$13.533\,\mathrm{eV}$	0.9952
Bohr radius	$0.5315\,\text{Å}$	1.0044
Hyperfine frequency	$4.4633\,\mathrm{GHz}$	3.1423

products diffuse to the mass spectrometer orifice where they are sampled continuously. Although it is easy to monitor a particular reactant or product, it is difficult to characterize the reacting mixture. Ionization is typically achieved by electron impact (from a filament) on the appropriate gas or on an inert gas (helium) which may transfer charge to another molecular gas mixed with it. By using low energy electrons, excited helium (metastables) can be produced which create the desired ions through Penning ionization. Most of the instruments mentioned below have similar ionization regions and mass spectrometric ion detectors, but different ways of selecting the reactants.

Given a suitable ion source, the ions may be selected, accelerated by an electric field to a particular energy, and the resulting beam collided with another ion beam or a molecular beam. Ion beams [51,52] allow the most detailed study of reaction dynamics, in principle selecting reactants according to mass, energy, and internal state, while identifying all products, their energies, internal states, and trajectories. Measured differential cross sections may be integrated to give total cross sections, which give rate constants upon further integration over an appropriate thermal energy distribution (the beam energy is non-thermal). In practice, not all these goals are attainable, with limitations on signal intensity (seeing any reaction at all!), on minimum feasible beam energy (which prevents measurements at energies appropriate to low temperatures), and on characterization of reactant and product states.

A more generally practical technique is to trap the ions while they react, and the preeminent trap is the ion cyclotron resonance (ICR) cell [47,48,53]. In this device, ions produced by electron impact are constrained to circle or spiral in an applied magnetic field, and they are detected by applying RF at the cyclotron frequency and either measuring the small RF power loss or detecting the faint RF emission at the same frequency; the latter is Fourier transform ICR [54]. When neutral reactants are introduced to the cell at low pressures (10^{-7} torr) the ion signal will decay in proportion to any chemical reaction. In order to have better selection of the reacting ions, the tandem-ICR was developed [53]

in which there is a source ICR cell for production and selection of the desired ions, and a reaction cell where those ions react with some other species. Between the two cells, the ions are accelerated through a mass selector, decelerated, and velocity-selected by a Wein filter[2] so the reacting ion and reaction energy are well characterized; the energies are not generally in a thermal distribution, but can be controlled from below 0.1 eV to several keV. Reaction times are from just a few to hundreds of milliseconds, and pressures must be very low, 10^{-7} torr. Detection of products is possible by ejecting ions from the cell with a pulsed electric field.

In order to measure truly thermal reaction rates, higher pressures are needed, which leads to the flow-tube methods. In a flowing-afterglow (FA [50]) a flowing gas mixture or pure carrier gas is ionized to a weak plasma or "afterglow" by electric discharge. (Some other gas may be injected downstream to create the desired ions if the carrier gas alone is ionized.) After the ions have some time to be collisionally thermalized in the ~ 1 torr flowing carrier gas, a reactive gas is introduced. At the end of the flow tube (which takes milliseconds to traverse) is an orifice leading to a high-vacuum mass spectrometer which monitors the reactant and product ions. Reaction rates are measured by varying the flow rate of the carrier or the injection point of the reactant. The main disadvantage of the FA is that the afterglow may contain many reactive species, including free electrons and many different ions, whose presence makes product detection difficult, and with side-reactions that obscure the reaction of interest.

The SIFT (selected ion flow tube) method [46,50,55] works like a FA, but the afterglow plasma must pass through a quadrupole mass filter and the selected ions are injected into a fresh stream of carrier gas to then react with an injected reagent. This not only prevents unwanted reactions, but facilitates much better product analysis. Like a FA, the reactants are well thermalized (80–600 K) in the 0.1–1 torr bath gas, typically flowing at

---

[2] See the discussion of the beam "separators" in section 1.4.

~ 30 m/s for a reaction time of ~ 50 ms.

Both SIFT and FA devices may be converted to drift tubes by fitting them with electrodes to continuously accelerate the ions as they are swept down the tube by the carrier gas. These devices are used to investigate non-thermal (fraction of an eV) reactions.

To measure reactions at very low temperatures, there is the CRESU apparatus [56,57], in which a gas mixture is expanded through a nozzle to form a low-pressure (5×10^{-3} to 0.1 torr) supersonic (mach 2–5) jet with a temperature of ~ 8–80 K. Ionization happens by electron impact in or shortly after the nozzle. Since no ion selection is performed, this method may suffer from the same deficiencies as the FA.

This thesis introduces a new technique to the field: μSR. The Muon Spin Rotation method is outlined below, but some important differences with the usual ion chemistry techniques must be mentioned. Since μSR observes only species containing a muon, it cannot be used for most ions, but it is ideal for studying the muon analogs of protonated ions. These muonated ions are not produced by ionization of a neutral molecule, but by stopping a beam of positive muons in an appropriate gas mixture so the μ^+ associates with the moderator gas to form for example $HeMu^+$, $NeMu^+$, $ArMu^+$, or N_2Mu^+, which may then react with other gases present. There is no debris of electron bombardment to cause problems, although at very high densities the radiolysis track left by the μ^+ might come into play [38,39,58]. Reactions are monitored by the disappearance of the reactant, or, more correctly, by the loss of the muon spin polarization. The time-scale of reaction is short, on the order of microseconds, limited by the 2.2 μs radioactive lifetime of the muon, but that is still plenty of time for full thermalization as the pressures employed are 1 atm or greater—much higher than in other ion–molecule reaction studies. In comparing SIFT with μSR, the factor of 1000 shorter reaction time is matched by the factor of 1000 increase in pressure.

1.3 Protonated and Muonated Gases

As mentioned above, protonated ions are an important class of molecular ions, of interest astrochemically and for setting bacicity scales. The measure of a molecule's gas phase basicity is its proton affinity (PA), which is high for all neutral atoms and molecules. Triethylamine, for example, has a PA of 975 kJ/mol (10.1 eV), and water's is 697 kJ/mol (7.2 eV), and even helium has a PA of 178 kJ/mol (1.84 eV). To put these in perspective, the Boltzmann factor for deprotonation of H_3O^+ (at 20° C) is 10^{-88}, which implies there is *not one* free H^+ in the world's oceans, and, moreover, *there never has been!* Even in helium and neon (PA = 2.08 eV) there is essentially no chance that a proton will remain unbound, and the same is true for a positive muon.

The protonated rare gases have been the subjects of several theoretical and spectroscopic studies, although the first spectrum (of HeH^+ [59]) was not measured until 1979. Calculations of potential energy curves and vibrational states for HeH^+ [60–62], NeH^+ [63–65], ArH^+ [64–66], KrH^+ [65], and N_2H^+ [67] agree well with potentials determined from elastic scattering [68,69] and with the measured spectra [59,70–74], as should be expected for these relatively simple ions.

The potentials for the muonated ions are essentially the same as for their protonated counterparts, with little break-down of the Born–Oppenheimer (BO) approximation — while Mu is much lighter than H, it is still *very* much heavier than an electron. Figure 1.1 shows the potential for $NeMu^+$ (NeH^+, from [65]) and for the unbound $NeMu$ (NeH, from [76]); the energy difference at large separations is 13.6 eV, the ionization potential of H (Mu). Also shown is the attractive Langevin charge–induced-dipole potential for $NeMu^+$ (see chap. 3). For both HeH^+ and NeH^+, the Langevin potential matches the ab initio potential neither at short range (which is not surprising) nor at long range (see inset of figure 1.1) where better agreement could be expected; but calculations for $Ar^+ + H_2$ show Langevin behavior beyond 4 Å [77]. Perhaps the low polarizabilities of
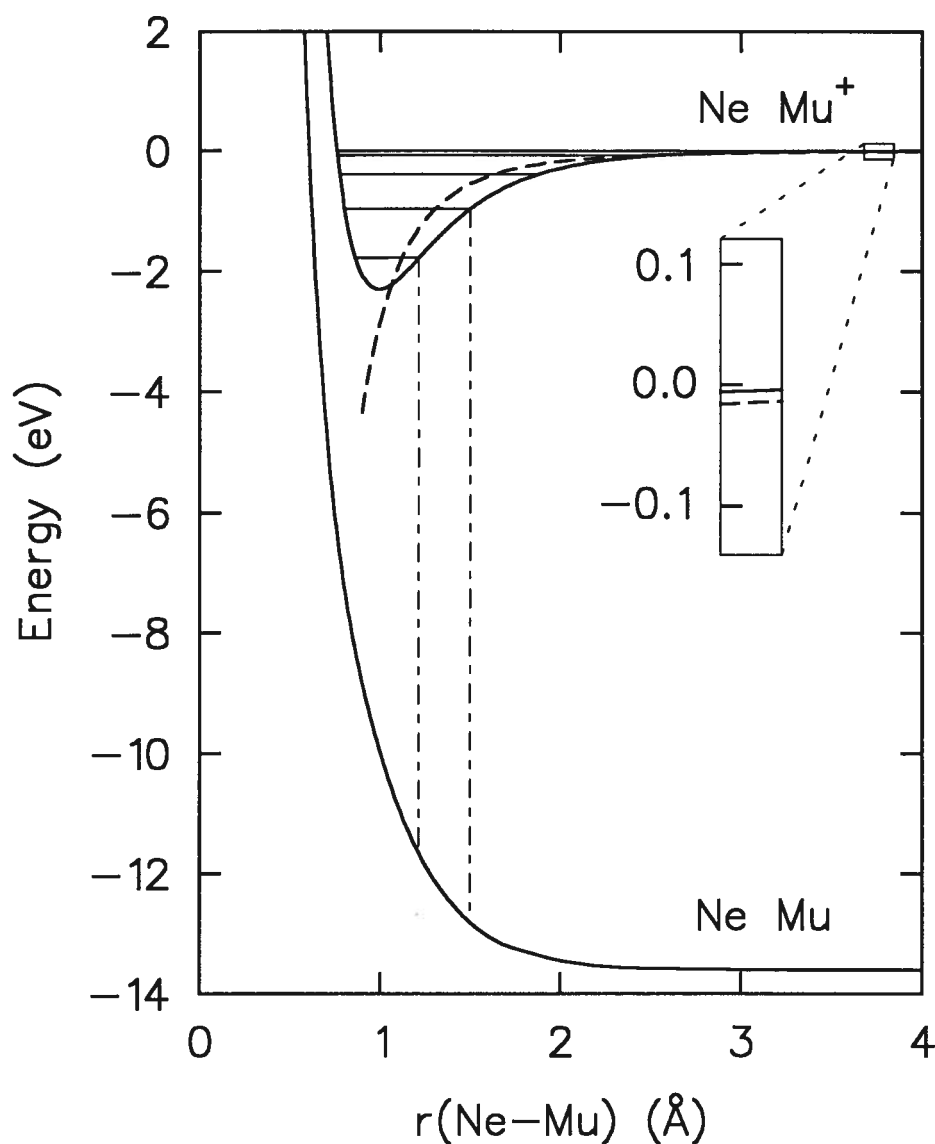
Figure 1.1 Potential energy curves for NeMu$^+$ and NeMu with the vibrational energy levels for NeMu$^+$ [75] (which are clearly anharmonic). The zero of energy is for separated Ne + Mu$^+$. The dashed line is the charge–induced-dipole potential for Ne–Mu$^+$, which does not accurately match the calculated potential at either short or long range (inset). Vertical transitions are shown for the neutralization of NeMu$^+$ from $v = 0$ and 1; these show how excitation increases the exothermicity at both ends of the transition, as long as it is vertical (see discussion in section 5.2).

He and Ne make the Langevin potential a poor approximation at any distance, or more likely, the detailed calculations are not very accurate at large separations, although the ab initio potential of Kołos and Peek for HeH$^+$ [61] is claimed to be good out to 4.5 Å [61]. Fournier, LeRoy, and Lassier-Govers [75] applied a slight BO correction to the Kołos potential (which is BO-approximate) to give the HeMu$^+$ potential, but the energy differences were very small.

In contrast to the potentials, the rovibrational energy levels are very different from those of the protonated ions: due to the low mass of muonium, the rotational and vibrational energy spacings, including the zero-point energies, are approximately three times greater than for the protonated ions. Fournier and co-workers [75] have determined the energy levels and lifetimes of the rovibrational states of HeMu$^+$ and NeMu$^+$, using the potential of Rosmus and Reinsh [65] in the latter case, and these are reproduced in table 1.2. Approximate values for the (D_0) binding energies have also been calculated by Wedlich et al. [78]. There are only 5 bound vibrational levels in NeMu$^+$ (shown in figure 1.1), 4 in HeMu$^+$, and 8 in ArMu$^+$, compared with 10 for both NeH$^+$ and HeH$^+$, and 24 for ArH$^+$ [61,78]. The sparseness of these states may be an important factor in any rovibrational excitation and quenching of these ions [79].

Besides giving widely spaced vibrational levels, the low μ^+ mass gives a much higher vibrational zero-point energy for any Mu-bearing molecule or molecular ion. The difference in zero-point energy at the transition state makes some reactions much slower for Mu than for H [82], but such effects are expected to be unimportant for ion–molecule reactions. Zero-point shifts for muonated molecular ions reduce their binding energies below their protonated counterparts, which can seriously alter the energetics of a reaction involving a muonated reactant or product. Table 1.3 gives the binding energies and zero-point shifts for the muonated gas ions studied in this thesis. There have been no calculations of the energy levels in N$_2$Mu$^+$, so the binding energy was calculated from the N$_2$H$^+$ value of 5.13 eV [67] by subtracting an estimate of the difference in zero-point

Table 1.2

Rovibrational Energy Levels and Predissociation Lifetimes[a] of $HeMu^+$ and $NeMu^+$ [75]

$HeMu^+$	J	$v = 0$	$v = 1$	$v = 2$	$v = 3$	
	0	−1.5195	−0.7252	−0.2191	−0.0166	
	1	−1.4634	−0.6830	−0.1923	−0.0086	
	2	−1.3544	−0.6010	−0.1420	$0.0021 \ (2.56 \times 10^{-13})$	
	3	−1.1964	−0.4841	−0.0743		
	4	−0.9967	−0.3395	−0.0015		
	5	−0.7634	−0.1770			
	6	−0.5066	−0.0108			
	7	−0.2377	$0.1303 \ (3.32 \times 10^{-14})$			
	8	$0.0291 \ (3.51 \times 10^{-7})$				
	9	$0.2689 \ (5.31 \times 10^{-14})$				

$NeMu^+$	J	$v = 0$	$v = 1$	$v = 2$	$v = 3$	$v = 4$
	0	−1.7863	−0.9750	−0.4026	−0.0836	−0.0023
	1	−1.7524	−0.9476	−0.3824	−0.0723	−0.0003
	2	−1.6850	−0.8934	−0.3428	−0.0508	
	3	−1.5853	−0.8137	−0.2852	−0.0219	
	4	−1.4550	−0.7100	−0.2119	$0.0080 \ (7.92 \times 10^{-13})$	
	5	−1.2963	−0.5849	−0.1262		
	6	−1.1118	−0.4414	−0.0334		
	7	−0.9050	−0.2835	$0.0561 \ (2.78 \times 10^{-13})$		
	8	−0.6795	−0.1164			
	9	−0.4398	$0.0523 \ (9.16 \times 10^{-10})$			
	10	−0.1912	$0.2071 \ (6.46 \times 10^{-14})$			
	11	$0.0595 \ (4.22 \times 10^{-6})$				
	12	$0.3013 \ (7.62 \times 10^{-13})$				

[a] Energies are given in eV with zero being separated He (Ne) + Mu^+, predissociation (tunnelling) lifetimes are given, in seconds, for quasibound states.

Table 1.3

Binding Energies and Zero-Point Energy Shifts for Muonated Ions.

Ion	$D_0{}^a$	ΔZPE^a	states[b]		ref
HeMu^+	1.53	0.31	4	10	61,75
NeMu^+	1.79	0.29	5	10	65,75,78
ArMu^+	3.57	0.27	8	24	78
N_2Mu^+	~4.73	0.40^c		—	67,80
$\text{H}_2\text{Mu}^{+\ d}$	3.99	0.39		—	81

[a] ground-state binding energies and the difference in Mu and H zero-point energies; given in eV.

[b] number of bound vibrational states for MMu^+ and MH^+ (respectively).

[c] there are no calculations for N_2Mu^+, so the zero-point correction (ΔZPE) was taken from the vibrational frequency of N_2H^+ [80], and this was used to calculate D_0 for N_2Mu^+ from the N_2H^+ binding energy [67].

[d] H_2Mu^+ was not observed. Since the trihydrogen ion cannot exist in $J = 0$, ΔZPE includes the $J = 0 \rightarrow 1$ excitation energy of H_3^+.

energy, as given by the vibrational spacing of N_2H^+ [80].

Besides the bound states, there are several quasibound states of HeMu^+ and NeMu^+ (and probably the other ions as well, but these have not been calculated). However, there are only two with substantial predissociation (tunnelling through the rotational barrier) lifetimes: the HeMu^+ $v = 0$, $J = 8$ state at $+0.029\,\text{eV}$ with a lifetime of $3.5 \times 10^{-7}\,\text{s}$ and the NeMu^+ $v = 0$, $J = 11$ state at $+0.060\,\text{eV}$ which lasts $4.2 \times 10^{-6}\,\text{s}$ [75]. (The HeMu^+ lifetime estimate was reduced from the value of $3.4 \times 10^{-6}\,\text{s}$ calculated initially [75], and since the NeMu^+ lifetime was not recalculated, it may be lower as well.) Radiative lifetimes for *all* rovibrational states of HeMu^+ were calculated, and the shortest lifetime was $36\,\mu\text{s}$ ($v = 1$, $J = 0$); much longer than the muon's radioactive lifetime, but marginally

accessible to a μSR experiment. Except for $v = 0$, higher J states have longer lifetimes.

1.4 Muon Beams

The properties of muonated rare gases have now been described, and related to their protonated counterparts. Also, the μSR technique has been mentioned, without saying what it measures, or how. The remainder of this chapter seeks to answer these questions while providing an introduction to the μSR method.

Muon production begins with the acceleration of particles such as protons to energies above 145 MeV by a particle accelerator (man-made or cosmic). For instance, the TRIUMF cyclotron, where these experiments were performed, produces a beam of 500 MeV protons. When such a beam collides with a target, many types of particles are created, but the ones of interest here are positive pions. Pions are the lowest-mass mesons and, like all mesons, are short-lived, decaying with a mean life of 26 ns through the process

$$\pi^+ \rightarrow \mu^+ + \nu_\mu \tag{1.4}$$

which is exoergic by 34 MeV and produces a 4.1 MeV μ^+ in the pion rest frame. More importantly, it is a parity violating process producing muons with 100% negative helicity (their momentum and spin vectors are opposed). This happens because the neutrino produced, like all neutrinos, must have negative helicity, and since the pion has zero spin, angular momentum conservation forces the muon to have negative helicity as well. (Negative muons formed by $\pi^- \rightarrow \mu^- + \bar{\nu}_\mu$ have positive helicity.) All μSR (for "muon spin rotation" or "relaxation") experiments depend on this well-defined muon spin.

For the experiments presented in this thesis, a surface μ^+ beam was used [83], for which muons are produced by the decay of pions at rest on the surface of the production target. Surface muons form an essentially monoenergetic 4.1 MeV beam with 100% longitudinal spin polarization. This beam is collected, focused, and momentum-selected by a series of magnets and other devices which form the secondary beamline; in the case of

these experiments, the M20B or M15 channels at TRIUMF. Figure 1.2 shows the layout of the M15 channel which was specially designed for surface muon beams, and commissioned during the early stages of this thesis work by myself and others, similar to our earlier work on the refurbished M20 [84].

As the experiments of this thesis usually involved gases, such as helium, with very low muon stopping power, the momentum selection of the beam was critical. Muons that scatter from the entrance window or pass through the gas without stopping give a diamagnetic signal when they are stopped in the sides or end of the aluminum target vessel. This is an insidious background because the signal of interest is also diamagnetic. Selecting a narrow range of momenta minimizes the variations in stopping distance in the gas and so minimizes the unwanted diamagnetic "wall signals." Both the M20 and M15 channels possess movable slits placed at a dispersed-momentum focus, as well as spin rotators which act as velocity selectors, allowing these experiments to be run with $\Delta p/p \leq 5\%$. Nevertheless, the wall signals were often a problem; but one that could have been much greater were it not for the spin rotators on the secondary beamlines.

It was found in some early studies for this thesis, given the typical experiment geometry at that time with a magnetic field perpendicular to the beam direction, that wall signals exhibited a short lifetime and hence were indistinguishable from the relaxing molecular ion signals under study. With such a configuration, no wall signal at all could be accepted. While some measurements of Xe in Ne [27] were successful, measurements in He were difficult to impossible. However, with the magnetic field applied along the beam direction, wall signals became long-lived, presumably because of the greater field homogeneity around the circumference of the target vessel in this orientation. In this situation, the wall signal contributes to any other long-lived signal, and the measured non-relaxing amplitude is easily corrected by subtracting the wall signal amplitude. In principle, such a longitudinal field could focus the muon beam slightly as it slows in the gas. Most of the experiments in this thesis involved transverse field μSR, in which the
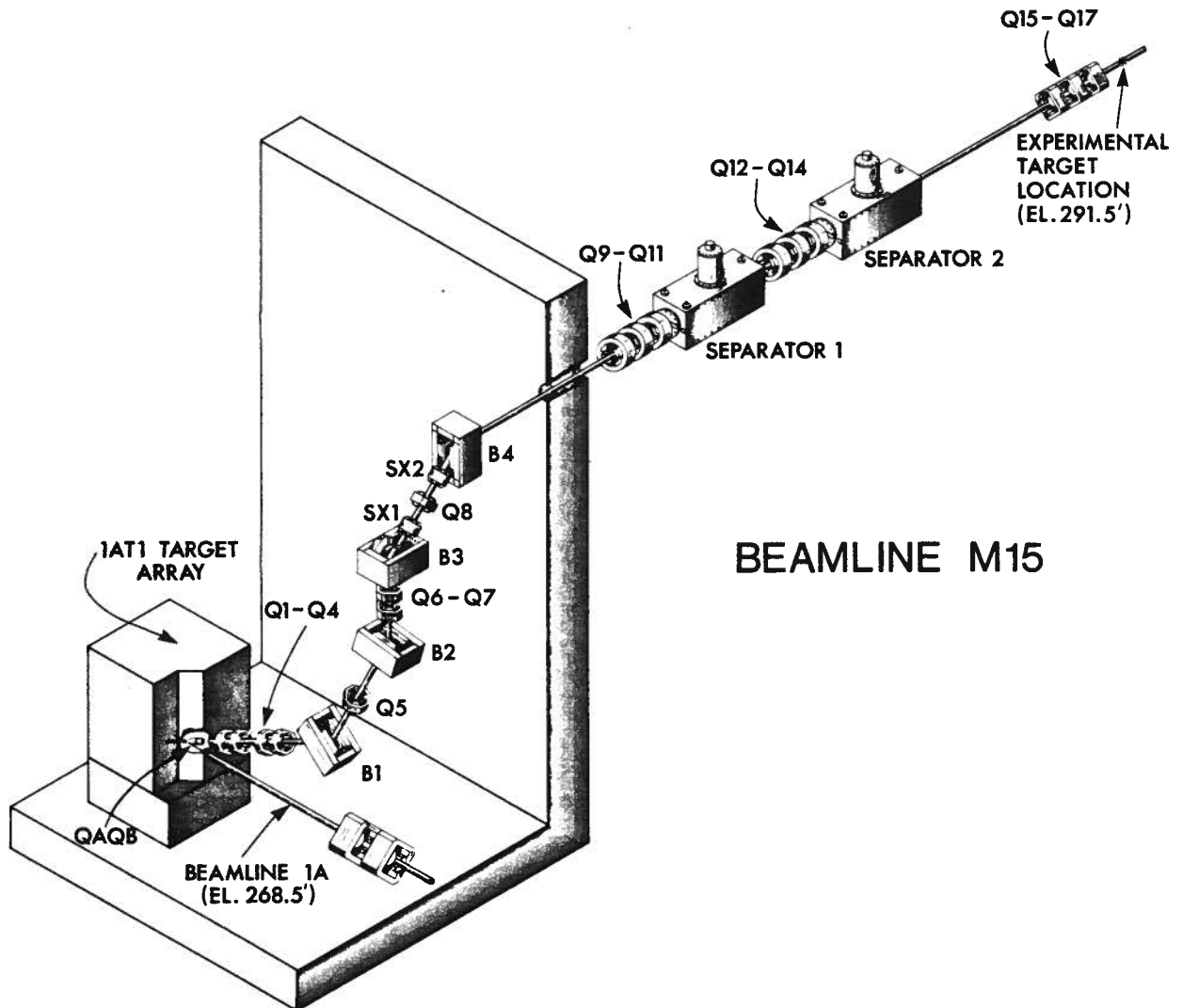
Figure 1.2 The M15 beamline at TRIUMF. This beamline is specially designed for (low-energy) surface muons, and uses a train of magnetic quadrupoles (Q) and dipoles (B) to deliver muons to the experiment. It rises above the muon production target 1AT1, and climbs to ground level, as it needs no heavy shielding. Its length eliminates pion contamination, and the dual separators/spin-rotators eliminate positron contamination. The spin rotator is split, with a triplet of quadrupole magnets in the middle, to reduce beam dispersion at full spin rotation.

muon spin was perpendicular to the magnetic field direction, but wall signals demanded that the magnetic field be parallel to the beam direction; thus it was necessary to rotate the muon's spin from its natural orientation, through 90°, to make it perpendicular to the beam direction. This was accomplished by passing the beam through a spin rotator [84]: a box containing crossed magnetic and electric fields. If it were not for the electric field, the magnetic field would bend both the muon beam and the spin vector through 90°, but the electric field cancels the beam deflection, leaving only the spin rotation. The spin rotator provides two additional benefits: it reduces the momentum spread of the beam because the electric field exactly opposes the magnetic field only for particles of a particular velocity (it is a Wein filter), and it removes positron contamination from the beam as positrons have much higher velocities than muons of the same momentum.

1.5 Muons in Gases

When a muon exits the beamline and enters the μSR apparatus, it is not ready to participate in chemical processes as it still has 3–4 MeV (not meV!) of energy. The process of a muon slowing down in gases can be roughly divided into three stages or energy regions [85,86]: Bethe–Bloch ionization, cyclic charge exchange, and thermalization. The Bethe–Bloch regime occurs above roughly 100 keV and is characterized by the loss of the muon's kinetic energy through the ionization and inelastic excitation of moderator atoms [87].

At energies between 100 keV and 20 eV, the μ^+ undergoes a series of charge changing collisions with the moderating gas

$$\mu^+ + M \xrightarrow{\sigma_{10}} Mu + M^+$$

$$Mu + M \xrightarrow{\sigma_{01}} \mu^+ + M + e^-$$

(1.5)
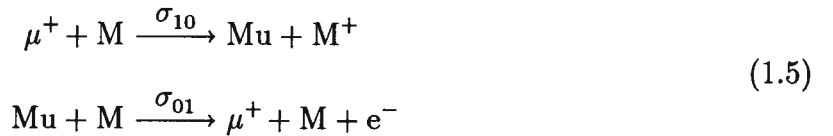
determined by the electron loss (σ_{01}) and capture (σ_{10}) cross sections as well as by the energy moderation cross section for the specific gas. In a high-IP gas like He, there are

approximately 80 of these cycles before cyclic charge exchange ceases due to a marked decrease in the μ^+ neutralization cross section below about 100 eV [85,86], although the threshold for Mu formation is only about 14 eV. If the medium has a lower ionization potential than Mu (13.53 eV), the threshold for electron loss is reached at ≈ 10 eV, whereas muonium formation is exothermic and can continue even after *cyclic* charge exchange has ceased. In the absence of chemical reactions, one would expect 100% muonium formation for such gases. It takes about 15 ns [88] for a muon to be slowed from 3 MeV to the 10 eV typical of final Mu formation in 1 atm of Ar [85]. After the charge exchange regime, other thermalization processes dominate: moderator excitation, elastic scattering, and hot atom/ion reactive collisions. These processes then dictate the ultimate thermalization of the muon.

While the effect of pressure, or the time between collisions, upon the muon polarization is negligible for Bethe–Bloch ionization, it is of considerable importance in the charge exchange regime. Since electrons in the moderator are unpolarized, whereas the μ^+ is polarized, muonium forms equally in two spin states, $|\alpha_\mu\alpha_e\rangle$ and $|\alpha_\mu\beta_e\rangle$. The $|\alpha_\mu\alpha_e\rangle$ state is an eigen-state of the μ^+e^- hyperfine interaction, but the $|\alpha_\mu\beta_e\rangle$ state is a superposition of the singlet and $M = 0$ triplet eigen-states and hence is not a stationary state. In this case then, the muon polarization oscillates between $|\alpha_\mu\beta_e\rangle$ and $|\beta_\mu\alpha_e\rangle$ at the hyperfine frequency, $\nu_0 = 4.5$ MHz. Consequently, the lost polarization (P_L, or 'missing fraction') will be significant if the period of cyclic charge exchange cycles is comparable to $1/\nu_0 = 0.22$ ns, or longer. Since the thermalization time is inversely proportional to pressure, P_L will increase as pressure decreases. This effect sets a minimum workable gas pressure of ~ 300 torr [85,89,90]. In most gases, there is no loss of polarization (signal loss) for pressures of one or a few atmospheres [85,89], although there are notable exceptions [89,91]. At much higher pressures, the ionization in the muon's radiolysis track may be near enough to interfere, causing additional depolarization [38,39,58], although there is no intrinsic upper limit on the density of targets that can be investigated by

μSR [31,38,92].

Emerging from cyclic charge exchange, a (small) portion of the muon ensemble polarization has been lost (P_L), and the rest is distributed between bare muons (P_D) and muonium atoms (P_{Mu}; $P_D + P_{Mu} + P_L = 1$). Most molecular gases have lower IP's than Mu, so 100% Mu formation would be expected, but in *all* molecular gases studied to date, there is a significant diamagnetic component of polarization [38,89,90], indicative of hot atom reactivity. Chemical reactions of translationally 'hot' Mu (e.g., $Mu^* + C_2H_6 \rightarrow MuH + C_2H_5$) convert muonium to diamagnetic species, thereby depleting P_{Mu} and correspondingly increasing P_D. The study of such hot-Mu reactions is a rich and ongoing field of research [89,90,93].

In a pure inert gas, and even in an inert gas doped with a small quantity of molecular gas, hot atom reactions are not expected to be important because any Mu that emerges from the charge-exchange regime will collide mainly with the inert bath gas. In a high-IP moderator like He or Ne no Mu is formed from charge exchange, but the bare μ^+ can undergo its own reactions. Even helium and neon have muon (proton) affinities > 1.5 eV [see §1.3 and ref. 75] so they will be muonated (protonated) in the three-body process

$$Mu^+ + He \xrightarrow{He} (MuHe^+)^* \qquad (1.6)$$

where Mu^+ is just a bare muon, and the product is shown as vibrationally excited because the entire binding energy is unlikely to be carried off by just the one moderator collision. The problem of energy disposal implies that the association occurs at low μ^+ kinetic energies, < 1 eV.

While the final thermalization of Mu is quite inefficient [91] due to its low mass and resulting small energy loss per collision, kinetic studies [29,30,82] show thermal behavior for Mu at times $\gtrsim 0.1 \ \mu$s. The charged μ^+ is expected to thermalize more quickly than Mu due to higher collision cross sections [94]. However, a muonated molecular ion has

a mass almost equal to the moderator gas and so loses, on average, half its energy per collision. Once formed, molecular ions thermalize very rapidly.

1.6 Muon Spin Rotation

After the muon beam has stopped in the gas of interest, the muons decay with a mean lifetime of 2.2 μs according to

$$\mu^+ \rightarrow e^+ + \nu_e + \overline{\nu}_\mu \,, \tag{1.7}$$

emitting a positron preferentially along the muon spin axis [95]. For a perfectly polarized ensemble of muons, the spatial anisotropy of positron emission is given by

$$N(\theta)/N = 1 + A \cos\theta \tag{1.8}$$

after averaging over positron energy (0.0–52.8 MeV) and where θ is the angle between the muon spin and the path of the decay electron. The technique of μSR relies on detecting the decay positrons and tabulating these decays in a histogram of positron counts vs. time. In this time-differential method, the muon that created each decay positron must be unambiguously determined, necessitating that only one muon be in the target at a time. This requirement is ensured by the electronic logic used in the experiment's data acquisition system. If all positrons were detected with equal efficiency, and the muon beam was 100% polarized, then $A = 1/3$ [96]. In practice, higher energy positrons are detected more easily while low energy ones may not even get out of the target, the beam is somewhat less than 100% polarized, and the polarization may decrease with time (relaxation) so A is always treated as an empirical factor A_0 multiplied by a relaxation function $G(t)$ which describes the loss of polarization over time. Moreover, θ may also be time-dependent (precession).

In the simple case where there is no coherent muon precession, such as when the magnetic field is zero or it is aligned with the muon spin, θ is constant, and the longitudinal field relaxation function is denoted $G_z(t)$. Thus, the histogram of positron decays

is described by

$$N(t) = N_0\, e^{-t/\tau}\, [1 + A_0\, G_z(t)\cos\theta] + b \qquad (1.9)$$

where N_0 is a normalization, b is a time-independent background due to random events, τ is the mean muon lifetime (2.2 μs), and t is the time the muon spent in the target before decaying. The subscript z identifies the relaxation as longitudinal or T_1 relaxation in NMR parlance.

However, the experiments for this thesis were performed with a magnetic field applied perpendicular to the muon initial spin direction. In this case, the muon precesses with a characteristic Larmor frequency until it decays. The resulting variation of θ with time is seen as oscillations in the muon decay histogram, of which a typical example is shown in figure 1.3 for μ^+ stopped in neon. Such a simple spectrum is described by the equation

$$N(t) = N_0 e^{-t/\tau}\big[1 + A_{\mathrm{D}}G_x(t)\cos(\omega_{\mathrm{D}}t + \phi_{\mathrm{D}})\big] + b \qquad (1.10)$$

$$\equiv N_0 e^{-t/\tau}\big[1 + A(t)\big] + b$$

where ω_{D} is the Larmor angular frequency for muons in diamagnetic environments ($\omega_{\mathrm{D}}/B = 85165\ \mathrm{s}^{-1}\mathrm{G}^{-1}$), and ϕ_{D} is the initial phase angle between the muon spin and the direction of the detector; $\omega_{\mathrm{D}}t + \phi_{\mathrm{D}}$ is θ in equation (1.8). A_{D} is the initial amplitude for the diamagnetic precession, equivalent to A_0 above. The relaxation function, describing transverse field dephasing in analogy with T_2 relaxations in NMR, is here denoted $G_x(t)$. In the gas phase, relaxations are generally simple 'Lorentzian' exponential decays $\big(G_x(t) = e^{-\lambda t}\big)$ due to chemical reactions or spin exchange. The relaxing oscillations constitute the signal of interest: the precessing decay asymmetry $A(t)$, often denoted $S(t)$. A representative "asymmetry plot" is shown in figure 1.4, and such plots will be used for illustration through the remainder of this thesis.
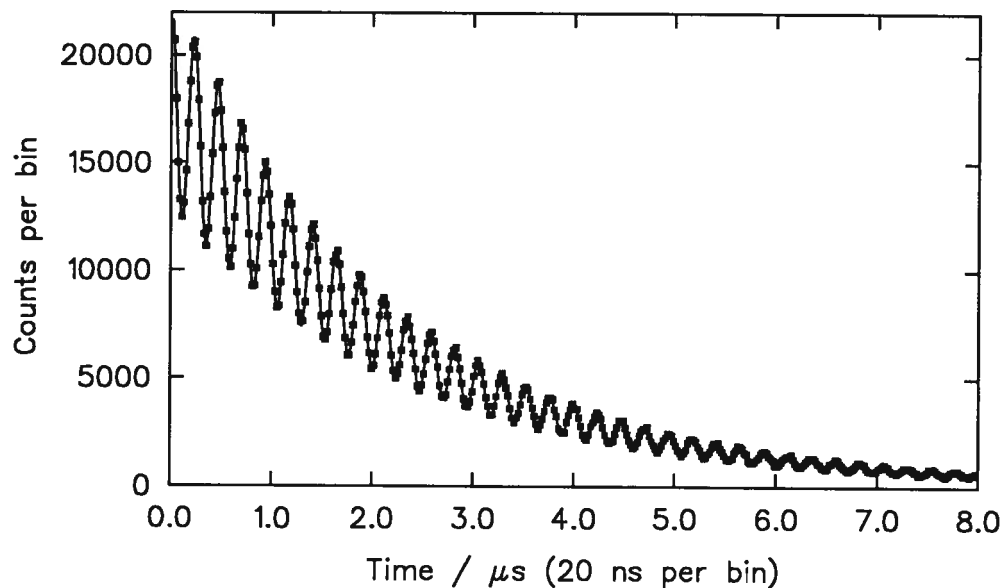
Figure 1.3 μSR histogram for 800 torr neon. The points represent the number of positrons counted within each time bin, (20 ns wide for the plot, but only 2.5 ns in the raw data) and the curve is the fit to equation (1.10). The error bars are due to Poisson counting statistics alone: $\sigma = \sqrt{N}$, but they are smaller than the squares so are not visible.
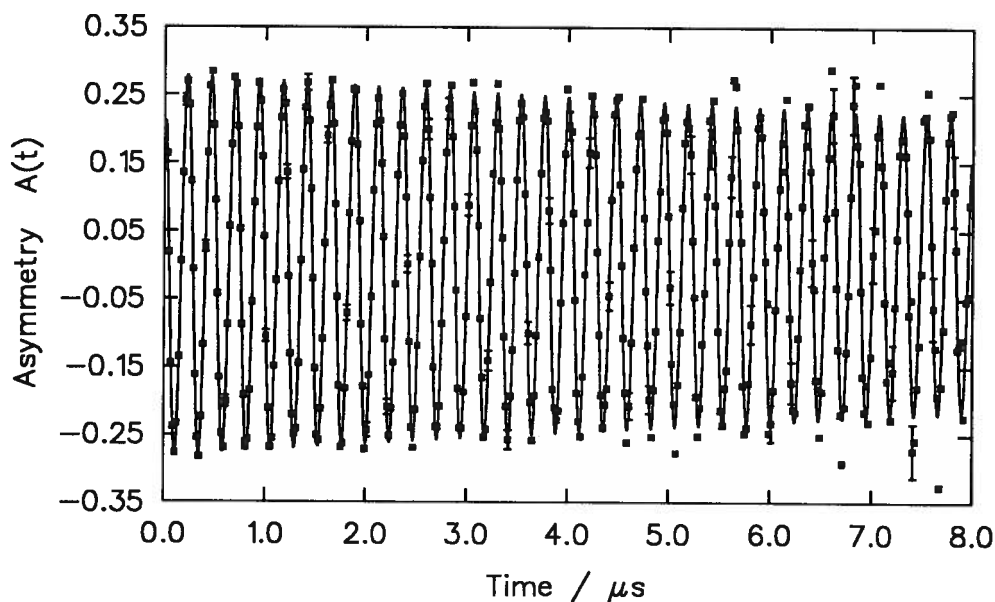
Figure 1.4 The corresponding asymmetry plot, giving $A(t)$ vs. t. The error bars include the uncertainty in the values for N_0 and b and are shown on every tenth point. They increase at later times due to the low statistics after many muon lifetimes. The very slow signal relaxation of $\lambda = 0.03 \ \mu\text{s}^{-1}$ is due to magnetic field inhomogeneity.

The above is an over-simplification, however. As discussed earlier, the muon may wind up in any one of many different magnetic environments: diamagnetic, paramagnetic, or a host of others relevant only to the solid state [97], so equation (1.10) could be extended to include many precession terms, but only two terms are of interest for this thesis. Since the molecular ions studied are diamagnetic, the most important term is given by equation (1.10) above, for it applies to all muons in diamagnetic environments (D); the few-parts-per-million frequency differences for various diamagnetic species cannot generally be resolved by μSR, which is limited to a frequency resolution of ~ 0.5 MHz by the short muon lifetime. More accurate frequency measurements have required special techniques [98]. The other environment of interest is the paramagnetic muonium atom. In most substances other than metals, the muon will take an electron from the moderator to form muonium, as outlined earlier. While muons in diamagnetic environments are coupled only to the field (ignoring small chemical shifts), the muon spin in muonium is coupled to both the external field and the electron spin. The details of the time dependence of muon precession in muonium are tedious but straightforward, and are treated well elsewhere [97,99]; and a simplified view of Mu precession is all that is needed for this thesis.

For the case of polarized muons meeting unpolarized electrons at low magnetic fields, muonium atoms are formed equally in each of two ensembles: those with parallel spins and those with opposed spins. Muonium with opposed spins (sometimes loosely referred to as "singlet" Mu, but here termed "antiparallel") is a mixture of singlet and triplet states for which the muon spin direction oscillates at the magnetic hyperfine frequency of 4463 MHz—too fast to be resolved by most μSR apparatuses, although it has been directly measured in a high resolution experiment [100]. Parallel (or "triplet") Mu is a mixture of triplet states in a weak (≤ 10 G) magnetic field, and the muon spins precess coherently with essentially half the electron's magnetic moment in the opposite sense to

diamagnetic precession and with a frequency ω_{Mu} 103 times higher than ω_{D}. The μSR spectrum at low fields is thus described by

$$N(t) = N_0 e^{-t/\tau} \left[1 + A_{\mathrm{D}} G_{x,\mathrm{D}}(t) \cos(\omega_{\mathrm{D}} t + \phi_{\mathrm{D}}) + A_{\mathrm{Mu}} G_{x,\mathrm{Mu}}(t) \cos(-\omega_{\mathrm{Mu}} t + \phi_{\mathrm{Mu}}) \right] + b \quad (1.11)$$

where the new parameters are analogous to those in equation (1.10). The asymmetry signal for such a histogram is shown in figure 1.5.

Mu is not the principal focus of this thesis, so very few runs were taken at low fields. The main interest is in reactions of diamagnetic ions as revealed by diamagnetic signal relaxations, $G_{x,\mathrm{D}}(t)$, which are more clearly visible at higher magnetic fields with proportionately higher ω_{D}. Most runs were performed at the highest field attainable with the gas chemistry apparatus described later, ≈ 300 G. At such fields, ω_{Mu} is split into two frequencies [97], but both are too high to be seen with most μSR apparatuses. Thus, equation (1.10) describes the bulk of the μSR data for this thesis.
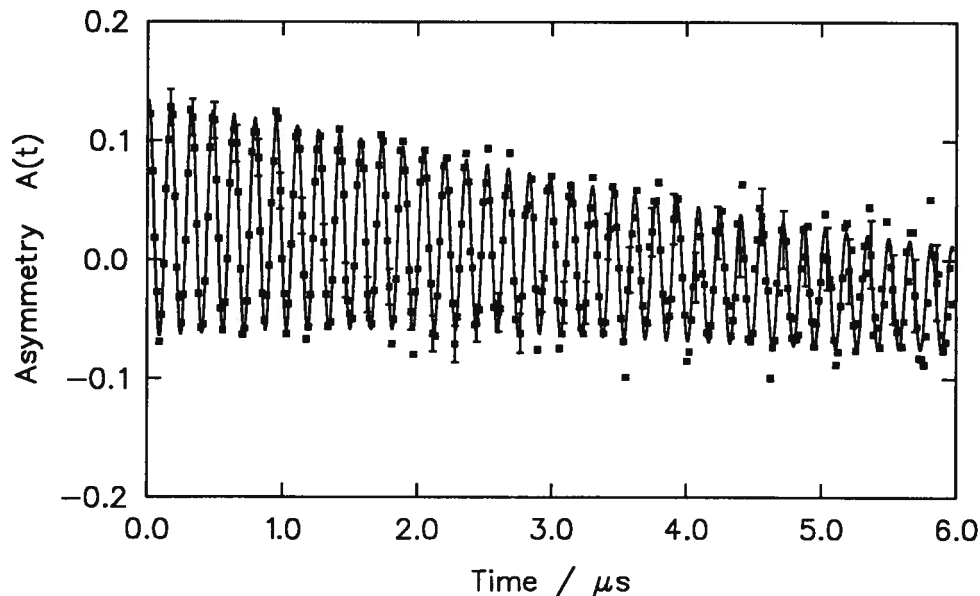
Figure 1.5 The asymmetry signal, $A(t)$ vs. t, for 1 atm nitrogen. The small diamagnetic precession ($A_{\mathrm{D}} = 0.036$ vs. $A_{\mathrm{Mu}} = 0.10$) is visible as a slow shift in the Mu precession. The Mu relaxation rate of $\lambda = 0.15\,\mu\mathrm{s}^{-1}$ is slightly faster than the diamagnetic relaxation in figure 1.4 because the faster (even at the applied field of 5 G) Mu precession exacerbates the problem of magnetic field inhomogeneity.

1.7 Relaxation Functions

The most important quantity measured for this thesis is the relaxation of the μSR signal. This is not apparent from figure 1.4, which displays a signal undergoing almost no relaxation, but is much clearer in figure 1.6 and in the corresponding figures in chapter 4 where the results are reported. In general, the relaxation functions $G_z(t)$ and $G_x(t)$ take many forms, depending on the physical mechanisms of relaxation. In the solid state, for example, relaxation functions are often Gaussian but may take many other forms [97,101]. In the realm of gas phase chemistry, however, there is only one[3] relaxation function of interest: the exponential relaxation, $G(t) = e^{-\lambda t}$, whether in a longitudinal (G_z) or transverse (G_x) magnetic field. That is not to say that muons exhibit a Lorentzian distribution of precession frequencies, just that the oscillations are damped by a simple exponential decay.

In transverse magnetic fields, chemical reactions relax μSR signals by changing the magnetic environment, and so the precession frequencies, of muons at random times. The most common case, exploited in studies of Mu kinetics [29,30,82,99,102,103], involves reactions of the Mu atom to form diamagnetic products. The reverse also works: reactions of diamagnetic species (molecular ions) to form Mu or some other paramagnetic species are manifest as relaxing diamagnetic signals, as illustrated, for example, in figure 1.6 showing the reaction of NeMu$^+$ with NO. Regardless, the necessary condition is that the muon precession frequency be changed incoherently on a time scale greater than the reciprocal of the difference in frequency. For reactions Mu$\rightarrow$D and D$\rightarrow$Mu, this condition is met when the reaction is slower than one period of Mu precession. With this simple transverse field relaxation mechanism, and concentrating on the case of principal interest

---

[3] This is not strictly true, depending on what is "of interest." An obvious example is relaxation due to inhomogeneity of the applied magnetic field; the distribution of fields over the stopping distribution of the muon beam is almost certainly never Lorentzian.

to this thesis, a diamagnetic reactant (D) forming Mu, the relaxation function is given by the fraction of reactant remaining at any time,

$$G(t) = [D]_t/[D]_0, \tag{1.12}$$

where square brackets denote concentration or density.[4] Thus, the relaxation function is given directly by some kinetic mechanism.

The preceding is not exactly true because the muon spins may be dephased by processes other than chemical reaction. It was noted above that magnetic field inhomogeneity may cause non-Lorentzian relaxation; however, if the inhomogeneity is low, making the relaxation rate low, the deviation from a simple exponential is very small. This is the situation for this thesis, as illustrated by the almost-non-relaxing signal in figure 1.4. The muonium relaxation in figure 1.5 is slightly faster due to the higher precession frequency, but it is still apparently exponential. As long as such systematic relaxations can be treated as exponential, they may easily be accounted for.

Since only a few million muons are used per experiment, and only one muon is allowed in the target at a time, the muons are near infinite dilution and the kinetics for muon chemistry are invariably pseudo-first-order:

$$[D]_t/[D]_0 = e^{-\lambda t} = G_x(t). \tag{1.13}$$

In the absence of background relaxation, the relaxation rate λ is identified with the pseudo-first-order rate constant. For the second-order reaction $D + X \rightarrow Mu + Y$, with a rate coefficient k,

$$\lambda([X]) = k\,[X] + \lambda(0). \tag{1.14}$$

where the terms $k\,[X]$ and $\lambda(0)$ give the pseudo-first-order rate constant and a background relaxation respectively. More complex kinetic schemes may give more elaborate relaxation functions, but they will always be built of exponential relaxations.

---

[4] Units of number density are used for concentrations in this thesis.
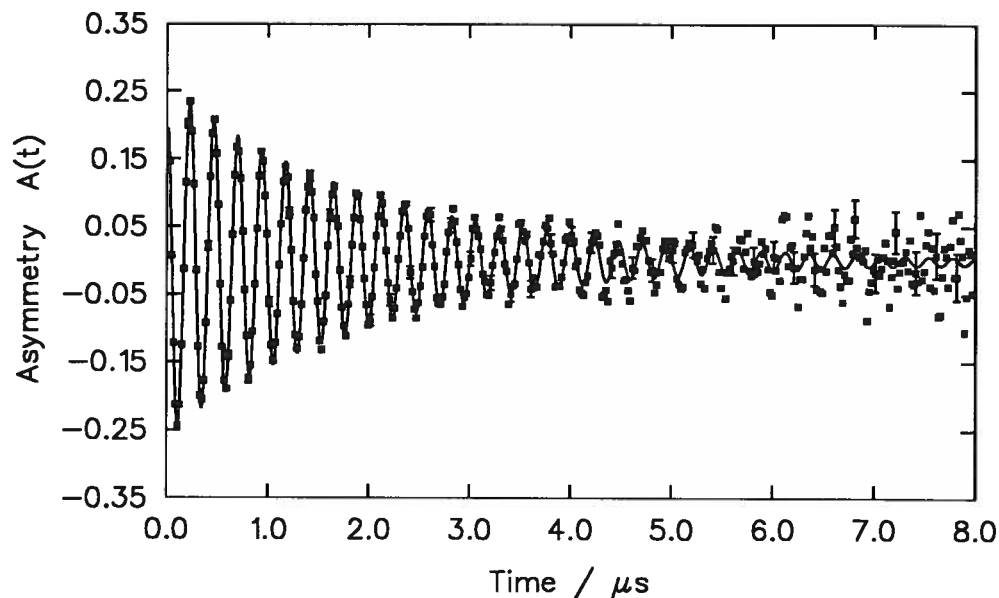
Figure 1.6   The relaxing asymmetry signal seen in neon with 6.74×10^{14} molec cm^{-3} of added nitric oxide. This is actually an unusual relaxation shape for this thesis — two-component relaxations were usually observed. The relaxation is due to the formation of paramagnetic Mu and maybe to formation of paramagnetic NOMu$^+$, as discussed in chapter 5.
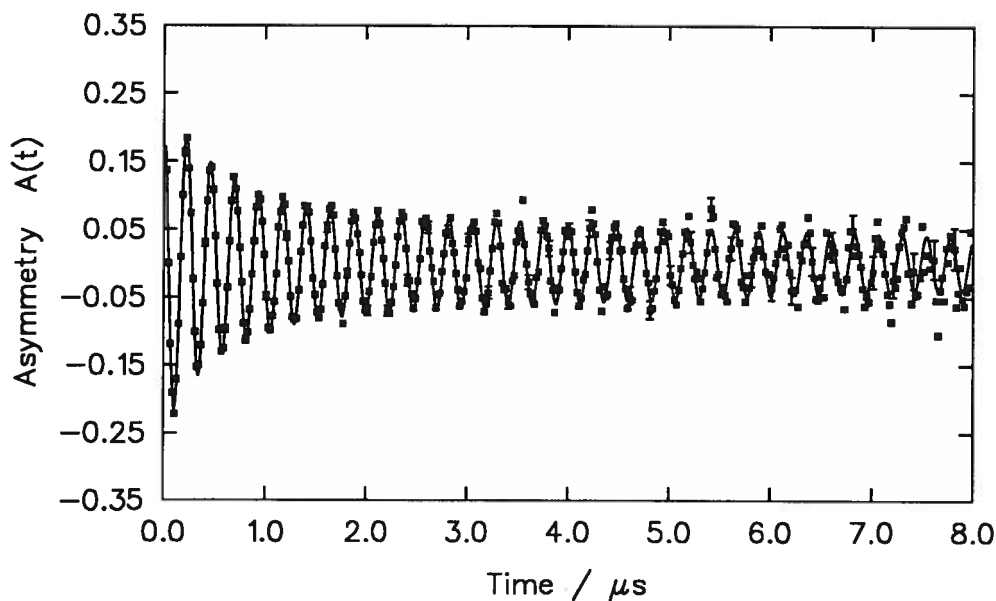
Figure 1.7   Two-component relaxation seen in 800 torr neon with 22.5×10^{14} molec cm^{-3} of added CF$_4$. The interpretation of the fast and slow relaxation rates, and their amplitudes, is left for later chapters.

Anticipating the results to be given later, the μSR histograms for molecular ion reactions typically give relaxing asymmetries that look like figure 1.7 showing the signal for Ne doped with CF_4. These were analyzed using a relaxation function of the form

$$A_D\,G(t) = A_1\,e^{-\lambda_1 t} + A_2\,e^{-\lambda_2 t}\,. \qquad (1.15)$$

The interpretation of this, to be discussed later, is based on a model of competing reactions, only one of which causes depolarization.

Chapter 2

EXPERIMENTAL TECHNIQUES

The rare gas molecular ions studied for this thesis were prepared simply by directing positive muons into a target vessel filled with the appropriate inert gas moderator: helium, neon, argon, or nitrogen. Ion–neutral reactions were induced by doping the rare gas with a few parts-per-million of a reactive gas, the neutral species. These formation and reaction processes were investigated by monitoring the muons' magnetic environment through the technique of μSR.

2.1 Apparatus

The layout of the μSR apparatus is shown in figure 2.1. It consisted of a large target vessel mounted on a cart between Helmholtz coils and arrays of scintillation counters. The upper scintillators were moveable vertically so as to accommodate the varying sizes of target vessels; for the large molecular ion gas target, the scintillators were raised fully. The target vessel and collimator could be rolled independently along rails and the whole apparatus could be rolled in tracks on the floor. This allowed the target and collimator to remain fixed in space while the coils and counters were repositioned along the line of the beam to match the muon stopping distribution. Generally, though, the beam momentum was varied to adjust the muon stopping distribution so the center of the coils could be placed near the center of the target.
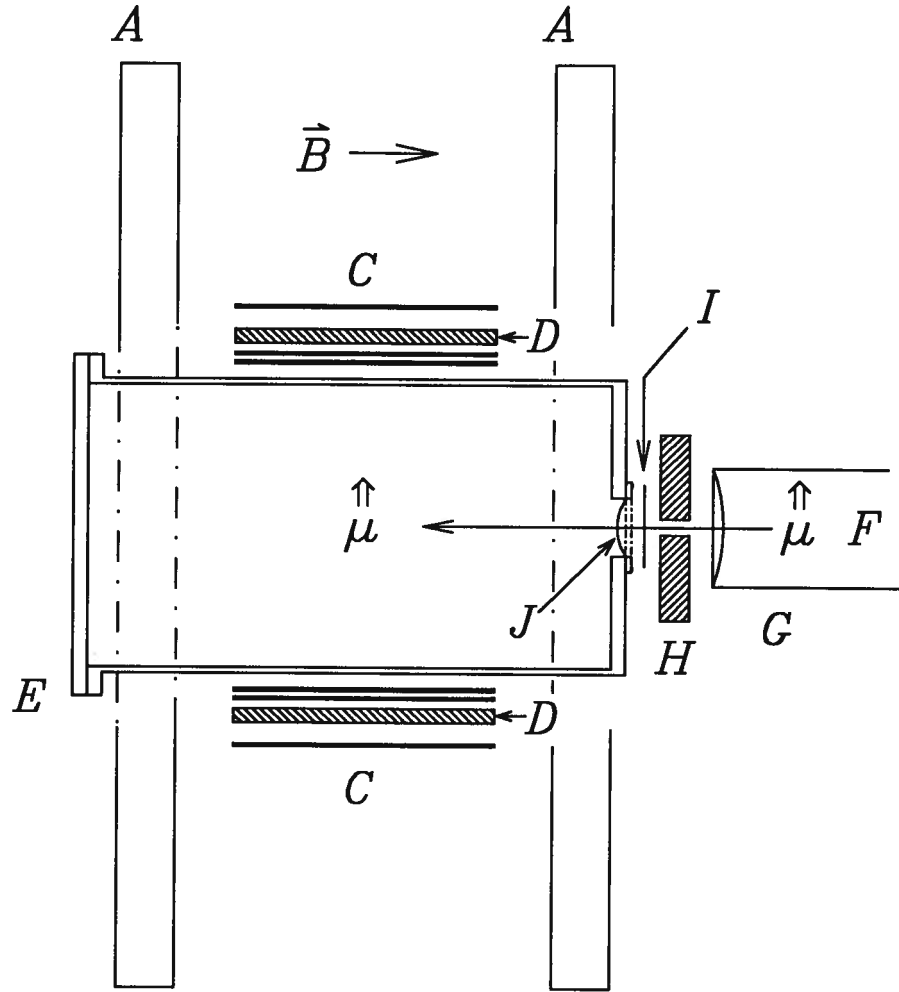
Figure 2.1 The μSR gas chemistry apparatus. The Helmholtz coils (A) are oriented for spin-rotated muons, giving a 300 G magnetic field in direction $\vec{B}$. There are both upper and lower positron counter arrays (C), each with three scintillators and graphite degrader (D). The target vessel (E) is shown without its variable-temperature insert. The spin polarized ($\Uparrow$) muon beam (F) traverses the evacuated beam-pipe (G), passes through a brass collimator (H), triggering the thin muon counter (I), before entering the target through a thin Kapton window (J). The muons stop near the center of the target, retaining most of their initial polarization. Each muon precesses (out of the plane of the page) until it decays, emitting a positron which may be detected by one of the counter arrays (C).

The main 1.5 m diameter Helmholtz coils provided magnetic fields from 0 gauss to in excess of 300 gauss oriented horizontally, and homogeneous to $\sim 1\%$ over a 5 litre volume. There were also two other pairs of coils, capable of generating a few gauss, which were used to accurately zero the field and to provide a weak vertical field when necessary.

A single thin (0.025 cm) scintillator placed between a beam collimator and the target served as the incident muon counter. Two arrays of three 0.6 cm thick scintillation counters placed above (Top) and below (Bottom) the target—at right angles to both the field and the beam directions—were used for detecting decay positrons. Each array consisted of two 25 cm × 45 cm scintillators, followed by 2.5 cm of graphite degrader and one 41 cm × 45 cm scintillator. Sometimes, such as when using the variable temperature insert (see below) which slowed the emitted positrons, or when one counter was weak, only two counters of three were used. A positron decay was detected by simultaneous counts in all three (or two) counters of an array.

The reaction/target vessel used for room-temperature measurements was a 174 litre hollow aluminum cylinder: 90.4 cm long by 49.5 cm in diameter. The large volume was necessary because the low stopping power of helium would allow muons to reach the walls of a smaller vessel, giving rise to unwanted diamagnetic signals. The muon beam entered through a thin (0.25 mm) Kapton window at one end of the "can." At the other end were inlet and pumping ports for the gas samples.

For experiments not conducted at room temperature, the big can was fitted with an insert as shown in figure 2.2. The space between the insert and the outside shell served as an insulating vacuum jacket; it contained aluminized mylar heat shields, and was continuously pumped on. The insert had a central sample volume of 75.4 litres (73.7 cm long × 36.1 cm in diameter) with a 0.025 mm stainless steel window. A plastic inner window was used at first but was abandoned because in those runs carried out with helium as moderator, too much He diffused through it, ruining the insulating vacuum. The muon beam entered the gas by first passing through a 0.125 mm Kapton window
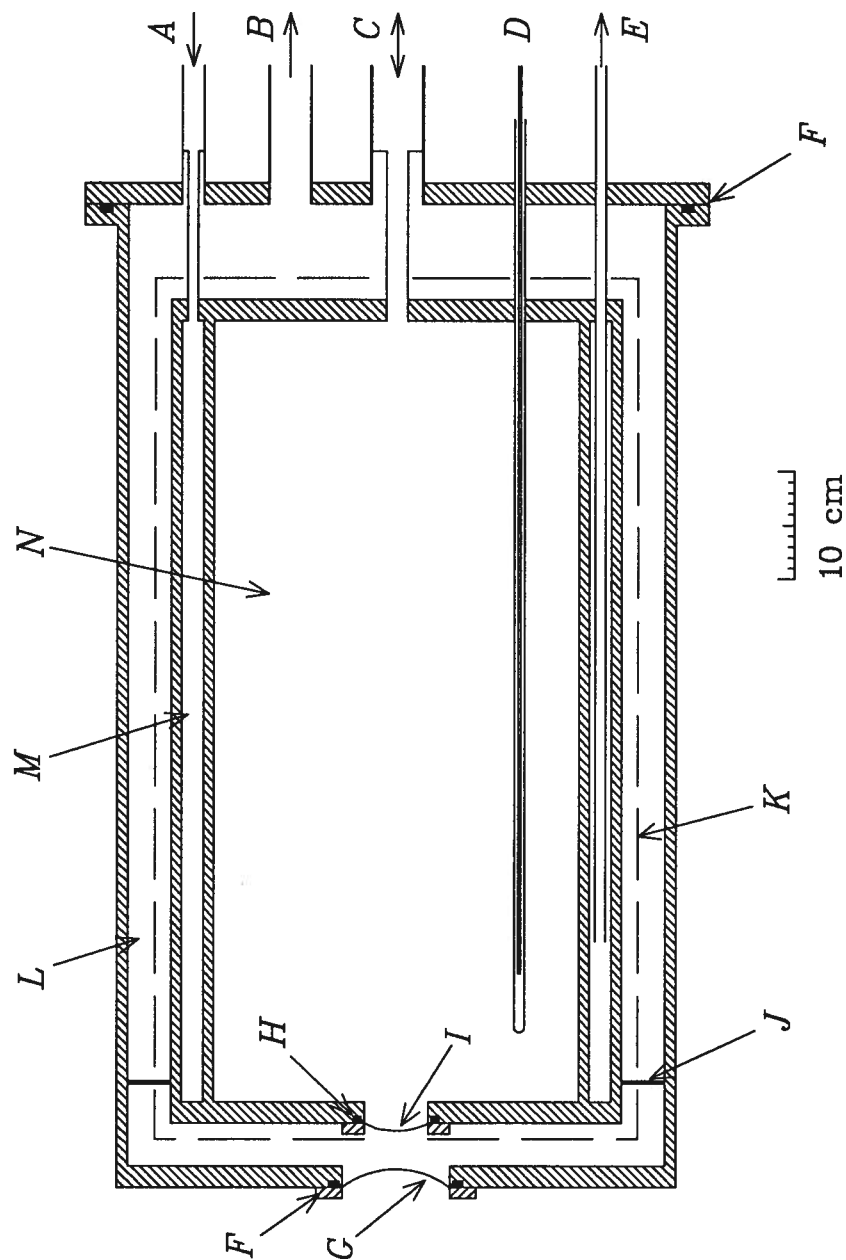
Figure 2.2   Diagram of the variable-temperature target vessel. Legend: *A)* thermal exchange gas inlet, *B)* vacuum jacket pumping port, *C)* sample gas inlet/outlet, *D)* thermocouple in pressure-tight tube, *E)* exchange gas outlet, *F)* Viton O–rings, *G)* 0.125 mm Kapton window, *H)* Teflon O–ring, *I)* 0.025 mm stainless steel window, *J)* stainless steel wire support, *K)* aluminized mylar heat shield (perforated for easy pumping), *L)* insulating vacuum jacket, *M)* thermal exchange gas space, *N)* sample gas space.

in the outer shell, traversing the vacuum space, then passing through the inner steel window. In order to prevent leaks at low temperatures, the inner window was sealed against a Teflon O-ring, which remained pliable in the cold; and aluminum screws were used to hold the aluminum flange against the window. In fact, the window *did* leak when cooled down, but that was easily fixed by removing the outer window and tightening the screws while cold.

The insert was double-walled on the sides, allowing the sample gas temperature to be varied by flowing pre-heated or chilled air in the space between the walls. Compressed air was first dried by flowing through a room-temperature zeolite moisture trap, and then either heated by an electric (Chromalox) heater, or cooled by flowing through a coil immersed in liquid nitrogen. The sample temperature, as monitored by a thermocouple in a sealed tube projecting into the central volume, was controlled by adjusting the flow rate of the exchange gas. In first use, the lowest temperature attained was $-100°C$, but after the installation of the heat shields (and a steel inner window) the vessel was easily cooled to $-170°C$. Temperature homogeneity along the insert was excellent, less than $1°C$, so temperature errors were dominated by variations over the time needed for a series of runs. High temperature runs were kept within a range of $±3°C$, while the more difficult low temperature regulation gave a range of $±5°C$, with the fluctuations recorded on a strip-chart recorder. There was no temperature control for the "room temperature" runs, and some of these may have temperature errors in excess of $±5°C$, although detailed records were not kept.

2.2 Data Acquisition

The data acquisition system was logically equivalent to what had been used in earlier gas phase μSR studies at TRIUMF [102] and the details are given therein, but some simplifications and improvements have taken place, so it is worth giving a precis here of how the current data acquisition system operates.

Figure 2.3 Logic diagram for μSR data acquisition. The signals proceed generally from the top to the bottom of the picture, starting at the scintillation counters. Constant-fraction discriminators (CFD) are used for the thin counter (μ) and the first counter in each of the positron counter arrays (T or B) to give better timing. Scalers are not strictly necessary but provide a quick indication of problems. The circles at the bottom are various inputs for the Le Croy TDC. A good event is recorded when all three counters of an array fire after there has been a muon counted (data gate, G), but only one muon (no pileup, $\bar{P}$); and no subsequent muon (bit 0) or positron (bits 1, 2) is detected within the gate.

Figure 2.3 gives the logic diagram for the signal processing used to collect the μSR data for this thesis; it is best understood with reference to the diagram of the apparatus, figure 2.1. A muon, upon leaving the beamline, passes through a collimator in a 2.5 cm thick brass shield and then through the thin counter. If there is no other muon in the target (i.e., the "pileup" gate is not already active), the discriminated counter pulse starts a high precision (125 ps time-resolution) Le Croy 4204 time-to-digital converter (TDC) or "clock". (If there is pileup, both muons are rejected.) Within about ten nanoseconds, the muon has thermalized and precesses in the applied magnetic field until it decays, perhaps a few microseconds later, emitting a positron as discussed before. This positron may pass through a triplet of counters and stop the clock. Then the clock writes the time to a CAMAC-resident histogramming memory module, which increments the bin corresponding to the time of the decay in the histogram appropriate for the counter array (Top or Bottom). The clock resets if no positron is detected within a gate period of a few muon lifetimes, or if two (or more) positron "stop" signals are received before the data gate expires.

In the original TRIUMF implementation for μSR data acquisition [102] almost all the good-event filtering had to be done with NIM logic modules and an MBD microcomputer. This was not only more cumbersome, but missed some events while the computer was busy. Then, also, the histograms resided in PDP11 memory, a scarce resource needed for networking software. In the present scheme, the histograms are periodically copied from the CAMAC histogramming memory module to a file on the PDP11 computer, which is subsequently copied to a VAX computer for analysis and backup. After the data acquisition for this thesis was completed, the PDP11 computer was retired, and now VAX computers are interfaced directly with the CAMAC modules.

2.3 Data Analysis

The data histograms were analyzed individually with a version of the non-linear, multi-parameter optimization program MINUIT [104]. Diamagnetic spectra were fitted by equation (1.10) with G given by equation (1.15) or (1.13); and the few low transverse field runs were analyzed according to equation (1.11). The best fit is determined by minimizing the chi-square

$$\chi^2 = \sum_i \left(\frac{N_i - f(t)}{\sigma_i} \right)^2 \tag{2.1}$$

where $f(t)$ is the appropriate expression for $N(t)$, N_i is the number of counts in bin i, and σ_i is its uncertainty. Given the Poisson counting statistics of these experiments, $\sigma_i = \sqrt{N_i}$. In situations where the data was over-determined, one parameter was often fixed at its expected value. In particular, when the "fast" relaxation was quite slow at low reagent concentration, the slow relaxation rate was usually fixed to a value determined at a higher concentration.

These were not the only fits necessary; the parameters determined by fitting a series of runs were subsequently analyzed in terms of various models, say $y = f(x)$. These fits took account of both "x" and "y" uncertainties by minimizing the modified chi-square

$$\chi^2 = \sum_i \frac{(y_i - f(x_i))^2}{\sigma_{yi}^2 + \left(f'(x_i)\sigma_{xi} \right)^2} \tag{2.2}$$

where f' represents the derivative of f and so converts σ_x into an uncertainty in y uncorrelated with σ_y. When necessary, these fits were performed with a version of MINUIT [104], but the many linear fits were done with the modified linear regression outlined next.

In the case of a straight line fit, $y = f(x) = ax + b$, the modified chi-square (2.2) may be written

$$\chi^2 = \sum_i \frac{(y_i - ax_i - b)^2}{\sigma_{yi}^2 + (a\sigma_{xi})^2} . \tag{2.3}$$

The minimum of this χ^2 (and the best a and b) could be determined by a general-purpose non-linear fitting program like MINUIT, but the the approach used in this thesis was based on the analytical linear regression [105]. The minimum χ^2 occurs where

$$0 = \frac{\partial \chi^2}{\partial a} = \sum_i \left[\frac{-2x_i(y_i - ax_i - b)}{\sigma_{yi}^2 + (a\sigma_{xi})^2} - \frac{2a\sigma_{xi}^2(y_i - ax_i - b)^2}{[\sigma_{yi}^2 + (a\sigma_{xi})^2]^2} \right] \tag{2.4}$$

and

$$0 = \frac{\partial \chi^2}{\partial b} = \sum_i \frac{-2(y_i - ax_i - b)}{\sigma_{yi}^2 + (a\sigma_{xi})^2} \tag{2.5}$$

are simultaneously satisfied. For the case of $\sigma_x = 0$, these equations can be solved for both a and b to give the familiar expressions for a weighted linear regression [105], but in the present situation, the best that can be done is to solve equation (2.5) to give b as a function of a. This is useful because it reduces the problem to that of numerically solving the single equation (2.4). This was accomplished easily and efficiently using the Newton–Raphson method [105]. This technique requires the full second derivative $d\partial\chi^2/da\partial a$ and an initial guess for a. The derivative is easy to calculate analytically and the familiar analytical regression provides an excellent initial guess. The partial second derivatives must also be calculated to get the uncertainties in a and b.

2.4 Reagent Gases

The bulk of each sample mixture was the moderator gas, usually He or Ne, but some studies were also performed using Ar, H_2, and N_2. All of these were UHP grade, with quoted purities of 99.999%. Nevertheless, given the low concentrations of reagent added to these gases, the impurities were significant; thus, the moderator gases (He, Ne, and H_2) were further purified as they flowed into the target by passing them through a trap filled with type 4A molecular sieve and cooled in liquid nitrogen. Before this cold trapping procedure was adopted, values for $\lambda(0)$, the molecular ion relaxation rate extrapolated to zero concentration of reagent gas, were 1–3 μs^{-1}, but trapping caused a sharp decline

in these values to $\leq 0.3\,\mu s^{-1}$, but still varying between experiments. This effect will be discussed in later chapters.

Many of the reactant gases were of research grade ($>99\%$ pure), obtained in lecture bottles, and were used without further treatment. However, the low proportion of reactant gas used (~ 100 ppm) indicates that impurities in the moderator are of far more concern than reactant impurities.

Some reactants were liquids under standard conditions, so they were poured into stainless steel sample bottles to use as sources of vapor. It was important to remove the air admitted to the bottle as well as air dissolved in the liquid, especially since air is selectively concentrated in the vapor phase and O_2 rapidly depolarizes muonium through spin exchange [106]. To degas the liquid samples, the small steel bottle was immersed in liquid nitrogen to freeze its contents, it was evacuated and pumped on, and then the sample was melted and boiled by immersion in hot water or a flame. These freeze-pump-thaw cycles were repeated at least three times, which, from previous experience [89], reduces oxygen contamination sufficiently, even for much higher vapor concentrations. This procedure was followed even when only the diamagnetic signal was to be measured.

To put the sample into the target vessel, a small measured volume (usually ~ 110 cm^3) was filled with the desired reagent gas, from either a lecture bottle or liquid sample bottle, up to a desired pressure (such as 100 torr) as measured on an MKS Baratron capacitance manometer with 0.5% accuracy; then the sample was admitted to the evacuated target vessel. Finally, the vessel was filled to the desired pressure with moderator gas, typically 1 atm or more of He, Ne, or Ar. In a typical experimental determination of ion–molecule reactions, four or more reagent concentrations were run in order to obtain a good fit to the bimolecular rate constant.

Chapter 3

THEORIES OF ION–MOLECULE CAPTURE

REACTIONS

The dynamics of ion–neutral reactions are dominated by long range attractive potentials: charge–dipole, charge–induced-dipole, charge–quadrupole etc. These make it possible to ignore the structural details of the reactants and calculate reaction rates from the long-range potential alone. Such calculations have been thoroughly reviewed [107–109] and a limited review is the purpose of this chapter. The common feature of all such calculations is the concept of a capture collision by which the reactants that have less than some critical impact parameter are brought together and, in the absence of short range repulsion, pass through each other. The results of such calculations are often called "orbiting" cross sections, but that is misleading as the only orbiting trajectories are those with exactly the critical impact parameter. "Capture" is the most common term, and is the one used in this thesis, but it really is more applicable to the assumption that the reactants form a long-lived complex. The long-range potential in no way guarantees capture in that sense, and moreover, "capture theories" do not require complex formation, only that reaction must occur when the reactants are drawn together. When "capture" is used here, complex formation is not implied. Perhaps the least misleading term is just "collision," distinguishing between the calculated collision rate and the measured reaction rate.

Even (or especially) when the capture assumption of 100% reaction efficiency fails, calculations of the capture cross section are important because the difference between the calculated collision cross section and the measured reaction cross section gives an insight to the real dynamics of a particular reaction. Discussion of steric repulsion, additional attractions, or energy disposition must begin with the calculated capture rates.

3.1 Langevin Reaction Rates

Theoretical rate constants for the reaction of a point charge with a polarizable molecule having no permanent dipole moment were derived by Gioumousis and Stevenson in 1958 [110], and earlier by Eyring, Hirschfelder, and Taylor [111], and by Vogt and Wannier [112], drawing from work done by Langevin at the turn of the century [113]. The reaction is controlled by the long range charge–induced-dipole interaction, which has the potential

$$V(r) = -q^2\alpha/2r^4, \qquad (3.1)$$

where q is the charge of the ion and α is the isotropic polarizability of the molecule. Langevin calculated trajectories for collisions involving this potential, but the operation of ion–molecule capture is best seen by using the effective potential

$$V_{\text{eff}} = -\frac{q^2\alpha}{2r^4} + E_{\text{orb}}, \qquad (3.2)$$

where

$$E_{\text{orb}} = \frac{L^2}{2mr^2} = \frac{m^2v^2b^2}{2mr^2} = \frac{b^2E}{r^2} \qquad (3.3)$$

which gives the "centrifugal repulsion" due to the orbital (non-radial) motion of the colliding pair; and where v is the relative initial velocity of the pair, E is the relative initial kinetic energy, $\frac{1}{2}mv^2$, b is the impact parameter, and m is the reduced mass. (The notation of this thesis is already over-burdened with μ's.) The distance of closest approach r_0

(i.e., the turning-point of the trajectory, as shown in figure 3.1) is simply the value of r that gives $V_{\text{eff}} = E$ in equations (3.2) and (3.3); if V_{eff} is always less than E, $r_0 = 0$.

The maximum in V_{eff} occurs where $\partial V_{\text{eff}}/\partial r = 0$, at the collision, or capture, or critical radius

$$r_{\text{c}} = \sqrt{q^2\alpha/Eb^2}\,. \tag{3.4}$$

There is a critical impact parameter b_{c} for a given E, found by setting $V_{\text{eff}}(r_{\text{c}}) = E$ and eliminating r_{c} to give

$$b_{\text{c}} = (2q^2\alpha/E)^{1/4}. \tag{3.5}$$

Trajectories with $b \geq b_{\text{c}}$ bring the reactants no closer than $r_{\text{c}} = b_{\text{c}}/\sqrt{2}$, while those with $b < b_{\text{c}}$ have the reactants, ideally, passing through each other. This discontinuity at $b = b_{\text{c}}$ is clear in figure 3.1. If no reactions can occur at separations greater than r_{c}, and if trajectories bringing the reactants into close proximity always lead to reaction,
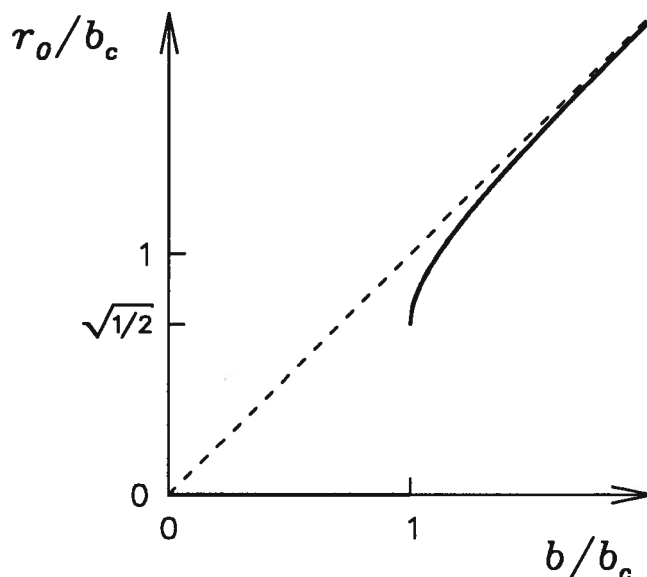
Figure 3.1 Dependence of the Langevin distance of closest approach r_0 upon the impact parameter b, given in terms of the critical impact parameter $b_{\text{c}} = (2q^2\alpha/E)^{1/4}$. Capture occurs for all impact parameters $b < b_{\text{c}}$. The dashed line at $r_0 = b$ shows the relationship in the absence of potential.

then the reaction cross section is

$$\sigma(E) = \pi b_c^2 = \pi\sqrt{2q^2\alpha/E}\,, \tag{3.6}$$

and the corresponding rate constant is

$$k_L = v\sigma = 2\pi q\sqrt{\alpha/m}\,. \tag{3.7}$$

This is the Langevin–Gioumousis–Stevenson rate constant and it is energy independent; there is no need to average over energy distributions, and k_L is both the microscopic and macroscopic rate constant, independent of temperature. (The same result had been derived in 1936 by Eyring et al. [111], but the derivation required a Maxwellian velocity distribution, an unnecessary restriction.)

The energy independence of k_L must break down at high energies, when the capture radius becomes smaller than the radius of the "hard core." However, the Langevin rate has been used to predict reaction rates at 100 eV energies [114]. It can also fail because of changes to the long-range potential due to anisotropy of the polarizability or to other long-range interactions, such as radical–radical or charge–dipole attractions.

3.2 The Locked Dipole

The case of an ion reacting with a molecule possessing a permanent electric dipole moment is more difficult. The potential depends on the angle θ that the dipole makes with the line connecting the colliding particles,

$$V(r) = -\frac{\alpha q^2}{2r^4} - \frac{\mu_D q}{r^2}\cos\theta \tag{3.8}$$

where μ_D is the electric dipole moment. It is the rotation of the dipole (variation of θ) that complicates the treatment of this system. If the dipole is assumed to have a fixed orientation, however, capture rates can be easily calculated.

For $\theta = 90°$, the potential is the same as for a non-polar molecule [equation (3.1) above] and the capture rate is identical to the Langevin rate. This angle is not favored

so this result is unrealistic; but if the dipole is rotating very rapidly, such that its period of rotation is much less than the collision time, its effect averages to zero—the case of the 90° locked dipole. So, anticipating more accurate treatments, it is clear that one requirement for a proper description of ion–dipole reactions is that the predicted rate approach the Langevin or 90° locked dipole rate at high temperatures.

For $\theta = 0°$ [115], the dipole interaction is at its maximum

$$V(r) = -\frac{\alpha q^2}{2r^4} - \frac{\mu_D q}{r^2}\,.$$

(3.9)

Repeating the treatment of equations (3.2) through (3.5) gives

$$b_c^2 = q\mu_D/E + \sqrt{2\alpha q^2/E}$$

(3.10)

which yields the microscopic rate constant

$$k_{LD}(E) = \pi\mu_D q\sqrt{2/mE} + 2\pi q\sqrt{\alpha/m}\,.$$

(3.11)

This time, though, the rate constant depends on energy, and the microscopic rate must be averaged over the velocity distribution of the reactants to get the bulk rate. Since ion–molecule reactions are often studied with mass spectrometers or ion flow tubes, the velocity distribution used when taking the average must be appropriate to the particular apparatus used. However, taking the Maxwell–Boltzmann average gives the thermal rate constant

$$k_{LD}(T) = \frac{2\pi q}{\sqrt{m}}\left(\sqrt{\alpha} + \mu_D\sqrt{2/\pi kT}\right)$$

(3.12)

where k is Boltzmann's constant (distinguished from rate constants by context) and T is the absolute temperature.

Unfortunately, the 0° locked dipole rate constant grossly overestimates experimental rate constants. This is not surprising because the electric field of the ion is not strong

enough to lock the dipole into a fixed orientation at more than a few degrees Kelvin. Nevertheless, the $0°$ locked dipole rate constant does provide an upper limit on ion–dipole capture rate constants.

An empirical correction can be made to equation (3.12) by introducing a "dipole locking constant" C which can have values from 0 to 1,

$$k_{\text{PLD}} = \frac{2\pi q}{\sqrt{m}} \left(\sqrt{\alpha} + C\mu_{\text{D}} \sqrt{2/\pi kT} \right) . \tag{3.13}$$

The value of C for a "Partially Locked Dipole" is determined by experimental data, and for real systems is quite small, $\lesssim 0.2$ [116].

Equation (3.13) is a semiempirical formula, not really a theory of reaction and is of little predictive use. However, there are descriptions which try to evaluate C through a proper average of $\cos\theta$ in equation (3.1). Some of these follow.

3.3 The Average Dipole Orientation Treatments

The average dipole orientation (ADO) theory of Su and Bowers [116] calculates averages[1] of $\cos\theta$ at a number of reactant separations which are then used in the modified potential

$$V_{\text{eff}}(r) = \frac{L^2}{2mr^2} - \frac{\alpha q^2}{2r^4} - \frac{q\mu_{\text{D}}}{r^2} \overline{\cos\theta}(r) . \tag{3.14}$$

Writing the potential this way assumes that there is no energy transfer between the rotation of the polar molecule and the orbital motion of the system as a whole. (Thus, angular momentum conservation is not obeyed, as the rotational angular momentum of the molecule *does* vary in this approximation.) As before, the conditions $\partial V_{\text{eff}}/\partial r = 0$

---

[1] In the original derivation of the ADO theory, $\bar{\theta}$ was calculated, but Su, Su, and Bowers [117] later corrected this to give the treatment outlined here. This change increased C slightly, increasing the predicted rate constants—an improvement. The corrected values of C are used in this thesis.

at b_c and $V_{\text{eff}}(r_c) = E$ are invoked to give

$$b_c^2 = r_c^2 + \frac{\alpha q^2}{2r_c^2 E} + \frac{q\mu_D}{E} \overline{\cos\theta}(r_c) \tag{3.15}$$

or

$$\sigma(E) = \pi r_c^2 + \frac{\pi\alpha q^2}{2r_c^2 E} + \frac{\pi q\mu_D}{E} \overline{\cos\theta}(r_c) \tag{3.16}$$

and

$$E = \frac{2\alpha q^2}{m^2 r_c^4} + \frac{2q\mu_D}{m^2 r_c} \left(\frac{\partial \overline{\cos\theta}}{\partial r} \right)\bigg|_{r=r_c} \tag{3.17}$$

which are still, alas, functions of r_c. While r_c cannot be eliminated from these equations explicitly, they can be solved implicitly; the real problem is to calculate $\overline{\cos\theta}$.

The starting point is, of course, to write the definition of average in terms of θ and its probability $P(\theta)$;

$$\overline{\cos\theta}(r) = \frac{\int \cos\theta P(\theta)\, d\theta}{\int P(\theta)\, d\theta} . \tag{3.18}$$

Solving this using equilibrium statistical mechanics is not what is needed because it was assumed that there was no net energy transfer from rotation, so no equilibrium is established. Since the molecule spends less time at an angle where $\dot\theta$ is high and more where $\dot\theta$ is low,

$$P(\theta) \propto \sin\theta/\dot\theta \tag{3.19}$$

where $\sin\theta$ is simply a geometric factor. Substituting the square root of the rotational kinetic energy for $\dot\theta$, but writing it as the total rotational energy E_{rot} minus the rotational potential gives

$$\overline{\cos\theta} = \int \frac{\cos\theta \sin\theta\, d\theta}{\sqrt{E_{\text{rot}} + q\mu_D \cos\theta/r^2}} \bigg/ \int \frac{\sin\theta\, d\theta}{\sqrt{E_{\text{rot}} + q\mu_D \cos\theta/r^2}} \tag{3.20}$$

which must be evaluated for two cases: (1) When $E_{\text{rot}} < q\mu_D/r^2$ the motion is oscillatory and the integrations are from $\theta = 0$ to κ, where κ is given by $E_{\text{rot}} = -(q\mu_D/r^2)\cos\kappa$.

(2) For $E_{\text{rot}} > q\mu_D/r^2$ the motion is rotational and $\dot{\theta}$ oscillates between a minimum and maximum value; the integration is from $\theta = 0$ to π. Both integrals are tractable. The average angle is an average of the two cases for $\overline{\cos\theta}$, weighted by the fraction of molecules with $E_{\text{rot}} > q\mu_D/r^2$ as determined from the initial reactant energy distribution, usually thermal; recall the assumption that no energy is transferred between rotational and orbital motion. Both $\overline{\cos\theta}(r)$ and $\partial\overline{\cos\theta}/\partial r$ are substituted into equations (3.16) and (3.17), and the function $\sigma(E)$ is determined implicitly. Thermal rate constants may then be calculated numerically.

So how is this any better than classical trajectory or Monte Carlo calculations of rate constants for every reaction system? There are simplifying assumptions in ADO to lessen its accuracy, notably its non-conservation of angular momentum, yet it still requires numerical calculations and gives no final "formula." The answer is that there *is* a formula: equation (3.13). The ADO theory has been used to calculate values for the
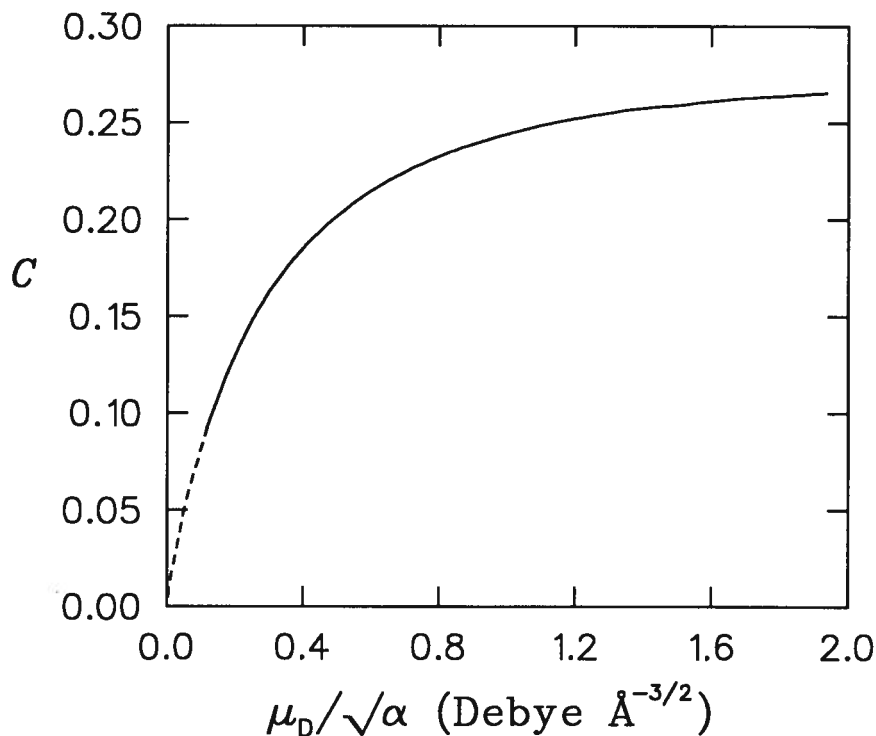
Figure 3.2 A plot of the ADO theory locking constant C vs. $\mu_D/\sqrt{\alpha}$ at 300 K; taken from reference 117.

locking constant C which depend only on T and $\mu_D/\sqrt{\alpha}$. Figure 3.2 shows values of C at 300 K. Experimenters can then read a value of C from such published curves [116,117] to calculate rate constants for their reactions. This simple parameterization is probably the salient reason for the ADO treatment's wide appeal.

In the years since its introduction, there have been refinements to the ADO treatment, notably the AADO theory [117] in which angular momentum transfer between rotation and translation is treated approximately. In the AADO treatment the orbital angular momentum is written

$$L(r) = mvb - C_L \, , \tag{3.21}$$

where

$$C_L = p_\theta - \sqrt{IkT} = \sqrt{2IE} - \sqrt{IkT} \tag{3.22}$$

for a system with moment of inertia I, making the effective potential

$$V_{\text{eff}}(r) = \frac{(mvb - C_L)^2}{2mr^2} - \frac{\alpha q^2}{2r^4} - \frac{q\mu_D}{r^2}\overline{\cos\theta}(r) \, . \tag{3.23}$$

The two equations expressing σ vs. E are more complex than before:

$$\sigma(E) = \pi b_c^2 = \pi \left[\left(r_c^2 + \frac{\alpha q^2}{2r_c^2 E} + \frac{q\mu_D}{E}\overline{\cos\theta}(r_c) \right)^{1/2} + \frac{C_L}{\sqrt{2mE}} \right]^2 , \tag{3.24}$$

$$E = \frac{m}{4}\left(B + \sqrt{B^2 - 4D} \right) \tag{3.25}$$

where

$$B = \frac{2q\mu_D}{mr_c}\left(\frac{\partial\overline{\cos\theta}}{\partial r} \right)\Big|_{r_c} - \frac{2\alpha q^2}{mr_c^4} - \frac{1}{m^2}\left(\frac{\partial C_L}{\partial r} \right)\Big|_{r=r_c}^2 ,$$

and

$$D = \frac{\alpha q^2}{m^2 r_c^4}\left\{ \frac{\alpha q^2}{r_c^4} - \frac{2\mu_D q}{r_c}\left(\frac{\partial\overline{\cos\theta}}{\partial r} \right)\Big|_{r_c} - \frac{1}{m}\left(\frac{\partial C_L}{\partial r} \right)\Big|_{r_c}^2 \right\}$$

$$+ \frac{q\mu_D}{m^2 r_c^2}\left\{ q\mu_D\left(\frac{\partial\overline{\cos\theta}}{\partial r} \right)\Big|_{r_c}^2 - \frac{2}{m}\overline{\cos\theta}(r_c)\left(\frac{\partial C_L}{\partial r} \right)\Big|_{r=r_c}^2 \right\} .$$

When $\overline{\cos\theta}$ is evaluated as for ADO, these equations can be parameterized to give the simple equation

$$k_{\text{AADO}} = \frac{2\pi q}{\sqrt{m}}\left(\sqrt{\alpha} + C\mu_{\text{D}}\sqrt{2/\pi kT} + \frac{Z\mu_{\text{D}}\sqrt{I}}{m^{1/4}}\right), \qquad (3.26)$$

which is valid for very small molecules ($I < 10^{-39}\,\text{g}\,\text{cm}^2$), and where Z is a parameter which depends (inversely) on temperature alone ($Z = 8.63 \times 10^{-18}\,\text{s}\,\text{cm}^{-5/4}\,\text{g}^{-1}$ at 300 K). A parameterization for larger molecules at 300 K is also given as

$$k_{\text{AADO}} = \frac{2\pi q}{\sqrt{m}}\left\{\sqrt{\alpha} + C\mu_{\text{D}}\sqrt{2/\pi kT} + \left(\frac{0.790I + 1.40 \times 10^{37}I^2}{0.106 \times 10^{-37} + FI}\right)^{1/2}\frac{\mu_{\text{D}}}{\alpha^{1/4}}\right\}, \qquad (3.27)$$

where

$$F = \frac{1.39}{\alpha \times 10^{24} + 2.74} + 0.375,$$

and α is in cm^3, μ_{D} is in Debye, and I is in $\text{g}\,\text{cm}^2$.

In the AADO theory, strict energy conservation is abandoned in favor of angular momentum conservation. Is it an improvement? According to data [117] presented by its developers it is, raising the predicted rate constants by 10–20% over ADO, to agree much better with experiment. Perhaps more importantly, AADO agrees better with classical trajectory calculations [118–120] than does ADO. This comparison is shown in figure 3.3 which shows the predictions of various classical theories over a wide range of reduced temperature, defined as $T_{\text{R}} = 2\alpha kT/\mu_{\text{D}}^2$, to be explained in the next section.

A further development in the ADO lineage is the AQO theory [108] which incorporates the charge–quadrupole attraction. It is developed much like the AADO theory but with the modified potential

$$V(r) = -\frac{\alpha q^2}{2r^4} - \frac{\mu_{\text{D}}q}{r^2}\cos\theta - \frac{q\mu_{\text{Q}}}{2r^3}\left(1 - 3(\cos\theta)^2\right) \qquad (3.28)$$

where μ_{Q} is the quadrupole moment of the molecule. According to the AQO theory, rate constants are not affected much by the quadrupole moment; and measurements on molecules with substantial quadrupole moments have shown no influence at all [57]. Bates has
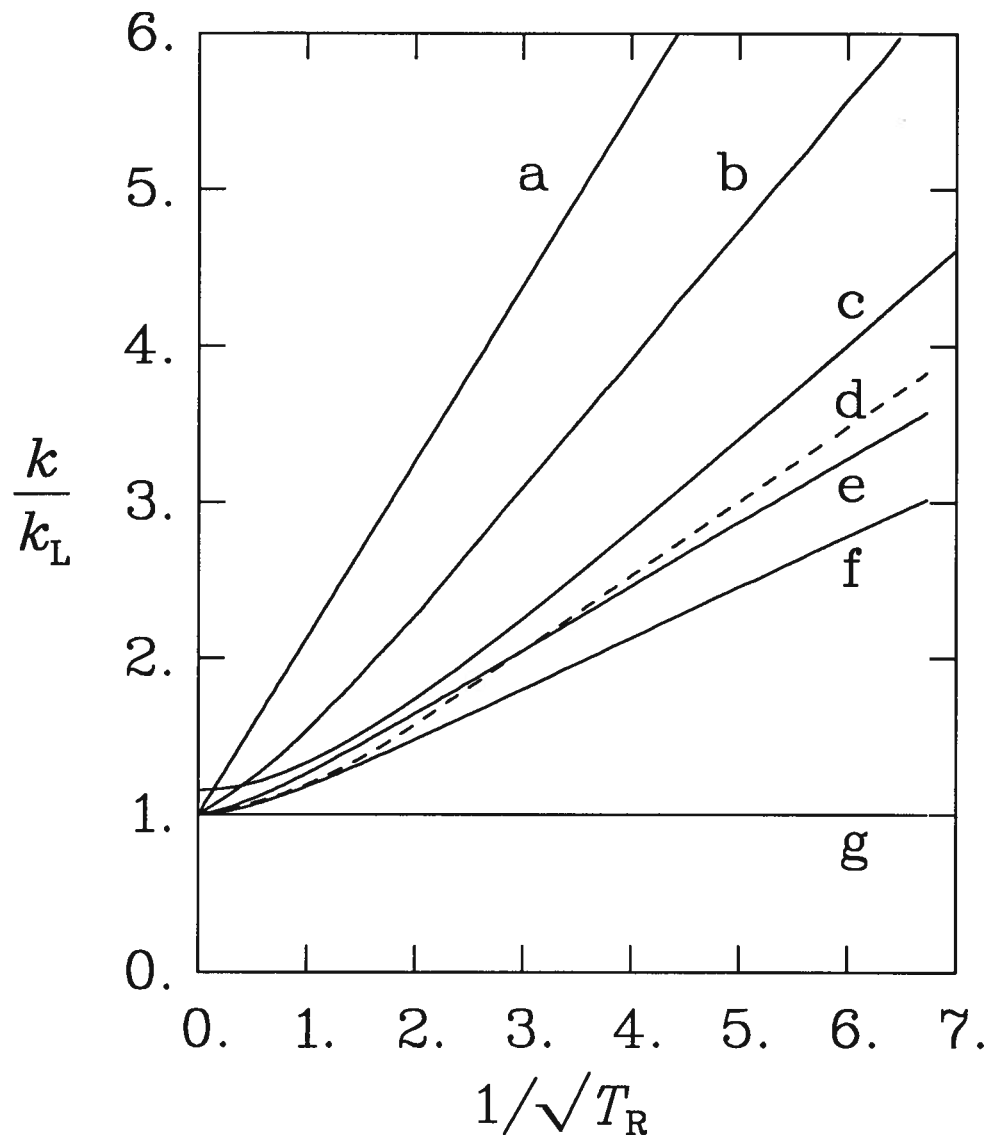
Figure 3.3 Plot of k/k_L vs. $1/\sqrt{T_R} = \mu_D/\sqrt{2\alpha kT}$ for various classical theories of ion–molecule capture: a) locked dipole [115]; b) Barker and Ridge average energy treatment [119]; c) variational transition state theory [120]; d) parameterized trajectory calculations [118], dashed for legibility; e) AADO theory [117]; f) ADO theory [116,117]; g) Langevin rate, ignoring the dipole [110]. The VTST and AADO lines come closest to the trajectory calculations, with AADO being best, but other theories have distinct shortcomings. Note that all except the VTST theory approach the Langevin result in the limit of high T_R.

also worked on versions of the ADO theory [121], proposing alternate averaging procedures that still conserve angular momentum. Furthermore, he prefers that the factor $\overline{\cos\theta}$ be applied to the force rather than the energy.

It was stated without justification above that a thermal average of $\cos\theta$ was inappropriate for examining ion–dipole collisions. The justification is the same as used for introducing the AADO theory: as a dipole approaches an ion, orbital angular momentum (thus, energy) is transferred to the dipole's rotation. The rotation of the dipole cannot be characterized by its original temperature; or, indeed, by any temperature, as the rotational energy loses its Boltzmann distribution.

Nevertheless, such an equilibrium treatment was used by Barker and Ridge [119] who calculated an average interaction energy based on the rotational temperature of the dipole. Their analysis overestimates most ion–dipole reaction rates, but not as badly as the locked dipole approximation, both shown in figure 3.3. Their method, however, does agree reasonably well with data for momentum transfer collisions [119,122–124], probably because such elastic collisions without capture take place at large separations where the rotational temperature of the dipole is relatively unperturbed. Ridge et al. [125,126] modified this treatment to calculate an average free energy for the interaction, and the results were much more acceptable for ion–dipole capture reactions. In fact, the averaging procedure was shown [126] to be the same as canonical variational transition state theory.

3.4 Transition State Theory

More in the mainstream of reaction rate theory are the transition state treatments of ion–molecule reactivity. These include both canonical and microcanonical analyses for polar and non-polar molecules. Transition state theory (TST) does assume an equilibrium between degrees of freedom of the system, although the use of microcanonical TST allows for non-thermal distributions.

An opportune starting point is the rederivation of the Langevin capture rate constant which can serve as a model for the more involved ion–dipole derivation. The canonical transition state derivation [111] was the original but it is limited to reactants with an equilibrium thermal energy distribution, so what follows is a microcanonical variational derivation. It is similar to that presented by Chesnavich and Bowers [107] which was formulated in terms of flux through the surface in phase space dividing reactants from products.

The microcanonical rate constant is

$$k(E) = \frac{W^{\ddagger}(E - V)}{h\rho_t(E)} \tag{3.29}$$

where $\rho_t(E)$ is the translational density of states at infinite separation; h is Planck's constant; and $W^{\ddagger}(E - V)$ is the number of internal states of the activated complex, not counting the one degree of freedom corresponding to the reaction coordinate, taken to be the radial direction. Thus $W^{\ddagger}$ is evaluated at some fixed $r = r^{\ddagger}$. Note that $W^{\ddagger}$ is a function of $E - V$ which is the translational energy of the colliding pair, in this case at the transition state. Classically,

$$\rho_t(E) = 2\pi (2m/h^2)^{3/2} E^{1/2} \tag{3.30}$$

and $W^{\ddagger}$ is given by the volume of the phase sub-space at the transition state:

$$W^{\ddagger}(E - V) = \frac{1}{h^2} \int_0^{2\pi} \int_0^{\pi} \iint_{E_{orb}=0}^{E-V} dp_\phi \, dp_\psi \, d\phi \, d\psi \,. \tag{3.31}$$

This is integrated in appendix A to give

$$W^{\ddagger}(E - V) = \frac{8\pi^2 m r^2}{h^2} \left(E + \alpha q^2/2r^4\right). \tag{3.32}$$

When equations (3.30) and (3.32) are substituted into eq. (3.29) and evaluated at $r = r^{\ddagger}$, the result is

$$k(E, r^{\ddagger}) = \frac{2\pi r^{\ddagger 2}(E + \alpha q^2/2r^{\ddagger 4})}{\sqrt{2mE}}\,. \tag{3.33}$$

At this point, $r^{\ddagger}$ could be assigned according to the Langevin criterion for r_c, but that would defeat the purpose of this exercise. Instead, the variational method is used to find $r^{\ddagger}$:

$$\frac{\partial k}{\partial r^{\ddagger}} = 0 = \frac{2\pi}{\sqrt{2mE}} \left(2r^{\ddagger}E - \alpha q^2/r^{\ddagger 3} \right) \tag{3.34}$$

$$\therefore \quad r^{\ddagger} = \left(\frac{\alpha q^2}{2E} \right)^{1/4} \tag{3.35}$$

which, when substituted into eq. (3.33) gives

$$k(E) = 2\pi q \sqrt{\alpha/m}$$

which is just k_{L} as given in equation (3.7).

The case of ion–dipole capture is complicated by the rotation of the dipole — with a non-central potential the reaction coordinate is no longer simply the radial direction. Recently there has been a suggestion [127] for an iterative version of TST to cope with the non-spherical dividing surfaces of ion–dipole capture, but there is as yet no complete solution; all other TST treatments assume a spherically symmetric dividing surface. Since, even assuming spherical symmetry, the dividing surface varies with energy, canonical TST can only provide an upper bound to a microcanonical treatment, which gives an upper bound to the reaction rate. The method of choice is then the microcanonical variational TST analysis of Chesnavich, Su, and Bowers [120].

If the dividing surface is spherical, the number of states of the activated complex can be written as a ten-fold integral analogous to equation (3.31), adding three angular degrees of freedom for rotation of the dipole. With some care for angular momentum and energy conservation, integration over most variables is relatively straightforward as in the Langevin case, but the final integration over θ must be divided into the same two ranges

as for the ADO calculation: oscillators and rotors. Finally, the variation of $r^{\ddagger}$ gives

$$
k(E) = \begin{cases} k_{\mathrm{L}} \dfrac{27}{1024 \mathcal{E}^{3/2}} \left[8\mathcal{E}^2 + 20\mathcal{E} - 1 + (8\mathcal{E}+1)^{3/2} \right], & \mathcal{E} \leq 5/9 \\[4mm] k_{\mathrm{L}} \dfrac{1}{9 \mathcal{E}^{3/2}} \left[2(99\mathcal{E}^2 + 3\mathcal{E} + 1)^{3/2} + (3\mathcal{E}+2)(6\mathcal{E}+1)(3\mathcal{E}-1) \right]^{1/2}, & \mathcal{E} \geq 5/9 \end{cases}
$$
$$(3.36)$$

where

$$
\mathcal{E} = 2\alpha E / \mu_{\mathrm{D}}^2 \,.
$$

Note that this variational rate constant bundles all the dipole dependence into the reduced energy $\mathcal{E}$. Thus, the thermal average rate constant depends only on the reduced temperature

$$
T_{\mathrm{R}} = 2\alpha kT / \mu_{\mathrm{D}}^2 \,. \tag{3.37}
$$

Figure 3.3 uses this reduced temperature to compare the various theories. At low reduced temperatures, the VTST treatment agrees well with both AADO and trajectory calculations, lending confidence to each, but at high temperatures the VTST result goes to $\sqrt{4/3}\, k_{\mathrm{L}}$ instead of the true Langevin limit! This failure is caused by the TST assumption that energy is continuously redistributed among all degrees of freedom: in the case of zero dipole moment or a rapidly spinning dipole there is no mechanism for the (dipole) rotational energy to be transferred to orbital motion.

3.5 Trajectory Calculations

The best way to evaluate the relative merits of these treatments is not really by comparison with experiment because they all make the capture assumption which may not be borne out for any particular reaction. The usual way to test the *approximations* of a theory is to perform simulations incorporating the same *assumptions*. When classical dynamics are assumed, it is straightforward to calculate trajectories of the reactants from any initial state and, assuming simple capture, to determine if they react from that state.

Dugan and Magee [128] were the first to perform numerical ion–dipole trajectory calculations, reporting capture cross sections for a number of systems, real and fictitious. They calculated random trajectories starting at $r = 50$ Å separation by numerically integrating the Lagrangian equations of motion, and assumed capture occurred if the reactants approached within 2 Å. They found "capture" rates between the Langevin and locked-dipole extremes, and relatively insensitive to the moment of inertia of the molecule.

Chesnavich et al. [120] also performed trajectory calculations, but integrated the Hamiltonian equations of motion with time reversal: the trajectories started at the Langevin capture radius for $b = b_{\mathrm{c}}$

$$r_{\mathrm{c}} = \left(\alpha q^2/2E\right)^{1/4} \tag{3.38}$$

and were terminated when the reactants re-crossed r_{c} (non-reactive) or reached $r_{\mathrm{c}} + 16$ Å (reactive). This method improves efficiency by eliminating from consideration many non-reactive trajectories. Their five sample systems spanned a wide range of T_{R} but all fell just below the VTST results, perhaps suggesting that their k_{TST} is high by $(\sqrt{4/3} - 1)k_{\mathrm{L}}$ at all T_{R}. In addition, they showed that k depends only on the reduced parameters for temperature $T_{\mathrm{R}} = 2\alpha kT/\mu_{\mathrm{D}}^2$ and for moment of inertia $I^* = \mu_{\mathrm{D}}I/\alpha qm$, although the I^* dependence is small. Continuing this line of research, Su and Chesnavich [118,129] performed a series of trajectory calculations and found k was insensitive to I^* in the region

$$I^* < \left(0.7 + T_{\mathrm{R}}^{-1}\right) \big/ \left(2 + 0.6T_{\mathrm{R}}^{-1/2}\right) \tag{3.39}$$

where the rate is given by

$$\frac{k}{k_{\mathrm{L}}} = \begin{cases} 0.4767T_{\mathrm{R}}^{-1/2} + 0.6200\,, & T_{\mathrm{R}} \leq 0.25 \\[2mm] \dfrac{\left(T_{\mathrm{R}}^{-1/2} + 0.5090\right)^2}{10.526} + 0.9754, & T_{\mathrm{R}} \geq 0.25\,, \end{cases} \tag{3.40}$$

shown in figure 3.3. Unfortunately, they did not parameterize k in the large region where it is sensitive to I^*, which includes low temperatures, but they did [129] tabulate some

values for some molecules at selected low temperatures, some of which are shown in figure 3.4.

3.6 Quantum Mechanical Theories

All the methods reviewed so far are classical. They are very accurate at moderate to high temperatures because the orbital motion of the colliding bodies as well as rotational motion of the dipolar molecule is still relatively unhindered at the capture radius, and so densely quantized—the case of the loose activated complex [130]. Nevertheless, the classical approximation must break down at some point as the energy or temperature is lowered; and much of the interest in ion–molecule reactivity is for very cold interstellar reactions [131].

The early treatment of Langevin capture by Vogt and Wannier [112] was, in fact, quantum mechanical. Their analysis gives Langevin capture except when the de Broglie wavelength of the particle approaches or exceeds the classical capture radius. This is not relevant for chemistry except for capture of bare electrons—the *raison d'être* for that paper.

A complete quantum description of ion–dipole capture is made much more difficult by the same circumstance that makes classical treatments so useful: there are so many rovibrational states to consider. Even at temperatures around 10 K, where a quantum treatment is necessary, there are too may states available for a complete solution; however, there have been approximate treatments proposed recently by Troe [132,133], Sakimoto and Takayanagi [124,134–136], and Clary [137–139]. It may not be apparent at first that a QM treatment is necessary at *any* temperature because the translational energy increases markedly as the reactants approach capture. The important quantization, however, is of the initial reactants; each initial state leads to a separate reaction "channel."

The approach used by Troe is called the statistical adiabatic channel model, SACM, which was originally applied to unimolecular processes by Quack and Troe [140]. The adiabatic approximation implies that each initial reactant state can be identified with an individual adiabatic potential energy curve describing the smooth evolution of that state from reactant to product. Furthermore, motions are separable, implying that the reaction coordinate is purely radial. The maximum of each channel potential curve gives a channel threshold energy E_0 which is used to calculate the activated complex partition function

$$Q^* = \sum_i \exp(E_{0i}/kT)\,, \tag{3.41}$$

where i enumerates each combination of the orbital quantum number l, the quantum number for molecular rotation j, and its projection m_j on the $\vec{r}$ direction. Then canonical transition state theory can be used to calculate the rate constant.

Unfortunately, the adiabatic potential curves are still too difficult to evaluate exactly. In the original treatment [132], the threshold energies were given by an interpolation between free and hindered rotor potentials; but they were later [133] approximated both by perturbation theory and by two terms of an expansion in r to give the thresholds

$$E_{0i} = \begin{cases} \dfrac{BG^2}{2\left[F(j,m_j) + \alpha B/\mu_{\mathrm{D}}^2\right]}\,, & F \geq 0 \\[3ex] \dfrac{Ba^2}{2(1-G)} + \dfrac{Bb}{4} - Bj(j+1)\,, & F < 0 \end{cases} \tag{3.42}$$

where

$$G = \hbar^2 l(l+1)/2mq\mu_{\mathrm{D}}\,,$$

$$F = \frac{3m_j^2 - j(j+1)}{j(j+1)(2j-1)(2j+3)}\,,$$

$$a = 2j - |m_j| + 1\,,$$

$$b = m_j^2 + 2|m_j|j - 2j^2 + |m_j| - 2j - 2\,,$$

and where B is the rotational constant of the molecule. The sum over l in eq. (3.41) is replaced by an integral over G (making this treatment semiclassical) which is parameterized to agree with the extreme cases of $T \to 0$ and $T \to \infty$ (where it can be integrated analytically) and with numerically integrated values between, giving the state-resolved rate constants

$$\frac{k(j, m_j, T)}{k_L} \approx \left\{ y\sqrt{\frac{2B}{\pi kT}} + \exp\left(-a^{4/3}y^{2/3}\frac{3B}{4kT}\right) \right\}$$
$$\times \left\{ 1 - \exp\left[-I_0\left(\frac{1 + 1.5I_0}{1 + I_0}\right)\right] \right\} \tag{3.43}$$

for $F(j, m_j) \geq 0$, and

$$\frac{k(j, m_j, T)}{k_L} \approx \left\{ y\sqrt{\frac{2B}{\pi kT}} + \exp\left(-a^{4/3}y^{2/3}\frac{3B}{4kT}\right) \right\}$$
$$\times \exp\left(-\left[\tfrac{1}{2}a^2 - j(j+1)\right]\frac{B}{kT}\right) \Big/ \left(1 + a^2B/2kT\right) \tag{3.44}$$

for $F(j, m_j) < 0$; where

$$I_0 = \sqrt{\pi kT\left[y^{-2} + F(j, m_j)\right]/2B}$$

and

$$y = \mu_D/\sqrt{\alpha B} \ .$$

These state-resolved rate constants can be averaged to get a thermal average rate.

The equations given above are for the case of a linear dipole with isotropic polarizability, although they are not very accurate unless the dipole dominates over the polarizability. Troe [133] also applied SACM to non-linear dipoles, quadrupoles, and anisotropic polarizabilities. He found that anisotropy of the polarizability should reduce rate constants below k_L.

The integration over G above suggests a different approach: treat the translational motion classically but use a full quantum treatment for the rotation/vibration. This is

the method chosen by Sakimoto and Takayanagi for their perturbed rotational state (PRS) analysis [124,134,135]. They constructed adiabatic potential curves u_{jm_j} and perturbed rotational states $\chi_{jm_j}(\theta, \phi, x)$ which are the solutions to

$$H\chi_{jm_j}(\theta, \phi, x) = u_{jm_j}(x)\chi_{jm_j}(\theta, \phi, x)\,, \tag{3.45}$$

$$H = \mathbf{j}^2 + \frac{\cos\theta}{x^2}\,, \tag{3.46}$$

where θ and ϕ give the orientation of the dipole relative to the $\vec{r}$ direction (a rotating reference frame), $\mathbf{j}$ is the angular momentum operator, and x is a reduced distance $x = r\sqrt{B/\mu_{\mathrm{D}}q}$. Since $V \to 0$ as $r \to \infty$, in the same limit $\chi_{jm_j}(\theta, \phi, x) \to Y_{jm_j}(\theta, \phi)$, the spherical harmonic free-rotor eigen-function, and $u_{jm_j} \to j(j + 1)$. These limits define j and m_j as the quantum numbers for, respectively, the magnitude and $\vec{r}$-projection of the molecule's rotational angular momentum.

The relative motion is treated classically, appealing to energy and angular momentum conservation, though the coordinates must be changed to a non-rotating frame to apply the latter. The angular velocity of the rotating frame is $\Omega = \hbar\omega/B$ in reduced units. The time-dependent rotational wave function $\psi(\tau)$ is determined by the time-dependent Schrödinger equation

$$i\frac{\partial}{\partial\tau}\psi(\tau) = H\psi(\tau)\,, \tag{3.47}$$

using the reduced time $\tau = Bt/\hbar$. ψ is expanded in the PRS basis functions:

$$\psi(\tau) = \sum_{j'm_j'} C_{j'm_j'}(\tau)\,\chi(\theta, \phi, x(\tau))\exp\left[-i\int_{\tau_0}^{\tau}\left\{u_{jm_j}(x(\tau)) - m_j'\,\Omega\cdot\hat{r}\right\}d\tau\right] \tag{3.48}$$

and solved. Far fewer states are needed for accuracy using this expansion than for an expansion in unperturbed rotational states.

One drawback of this solution is that total angular momentum is not conserved in non-adiabatic transitions between PRS's because the rotational and orbital motions are

treated by different mechanics. The effect of this is minimal, though, because the rotational angular momentum is much less than the orbital for the low j values considered. Results for initial rotational states $j = 0$ and 1 agree well with the SACM results [133].

Another difficulty is that the coupled solution becomes impractical at higher j values. One fix is to allow transitions only between states of the same j, which was used [124] for distant momentum transfer collisions. This may be less accurate for capture collisions, but the classical ADO treatment gives no coupling at all.

A different approach is to treat even the rotation semiclassically when j is high. Sakimoto [136] used the adiabatic invariant [121,142]

$$n + \tfrac{1}{2} \equiv \oint p_\theta \, d\theta / \pi \tag{3.49}$$

to characterize classical adiabatic channels, where p_θ is given in

$$\epsilon = B\big(p_\theta^2 + p_\phi^2/(\sin\theta)^2\big) + \mu_\mathrm{D} \cos\theta/r^2 \,. \tag{3.50}$$

The rotation is then quantized by applying the Bohr–Sommerfeld quantization rule to n, giving channel curves that are close to the quantum PRS curves. The channel selected cross sections are calculated from the potential curves just as for classical Langevin capture. Morgan and Bates [141] have provided a parameterization for this semiclassical "adiabatic invariant method" which reproduces the full PRS calculations very well. This parameterization is used for the PRS curve of figure 3.4.

Clary's treatment [137,138] is quite similar in that it is also an adiabatic channel model, but it uses the centrifugal sudden approximation for non-reactive scattering to evaluate the adiabatic channel potential curves. Thus the method is called ACCSA, for adiabatic capture–centrifugal sudden approximation. The CSA assumes there is no coupling between different M-states (where M is the projection of the system's total angular momentum J). As long as only M-averaged rate constants are reported, this approximation should be reasonable, even for the long range ion–molecule interaction. To reduce the
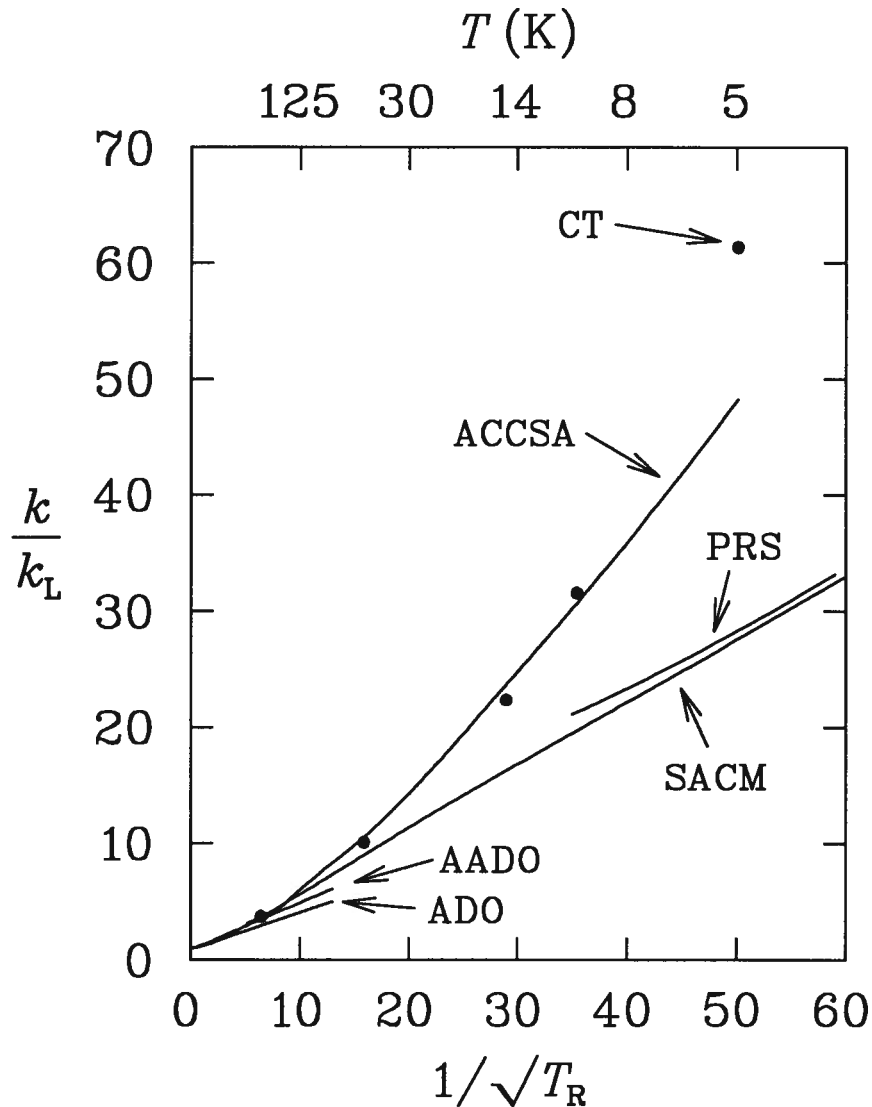
Figure 3.4 Comparison of the SACM, parameterized PRS, and ACCSA quantum mechanical treatments of $H_3^+ + HCN$ association at low temperatures, along with classical trajectory (CT, •), ADO, and AADO calculations. The CT and ACCSA results agree very well even below 10 K, perhaps fortuitously, while PRS and SACM agree on much lower values of k. The PRS parameterization of Morgan and Bates [141] is only for $j \leq 2$ so it is limited to low temperatures. Conversely, the ADO and AADO results are only shown above $T = 50$ K, which is already too cold for them.

number of states to consider, the molecular rotation is expressed in a "localized rotational basis" weighted for $\theta = 0$, the energetically favored orientation. Capture is defined by setting a reaction probability to 1 for lower J values and to 0 for $J > J_{\mathrm{max}}$, where J_{max} gives the highest angular momentum for which the centrifugal barrier can be crossed. The J-resolved cross sections are evaluated by summing up to J_{max}.

Figure 3.4 shows a comparison of the low temperature ACCSA, PRS, and SACM predictions for H_3^+ + HCN, along with some low temperature classical trajectory calculations [129]. The ACCSA calculation agrees well with the trajectory calculation, but that is of dubious merit. The agreement between ACCSA and SACM is much worse, especially at the lowest temperatures. Although Troe's SACM treatment involves many approximations, they do not affect the $T \rightarrow 0$ limit, which should, then, be accurate. The SACM curve agrees well with the PRS calculation (as well as a more recent AC treatment [143] by Marković and Nordholm). For these reasons, and for the ease of calculation, the SACM treatment is the method of choice for low temperature results in this thesis.

Chapter 4

RESULTS AND KINETIC MODELS

When muons are stopped in helium or neon, no muonium is observed owing to both the high ionization potentials of these gases relative to Mu and the magnitude of the epithermal charge exchange cross sections involved [44,85]. At pressures around 1 atm or higher, essentially all the muon polarization is retained in some diamagnetic species and is manifest as a long-lived large-amplitude precession at the diamagnetic (or bare muon) Larmor frequency. Sample spectra are shown in figure 4.1 (for He) and back in figure 1.4 (Ne). Positive identification of the diamagnetic species involved is part of the rationale for this thesis, but a tentative identification as the muonated molecular ions $HeMu^+$ and $NeMu^+$ can be made following a previous study [44]. For now, suffice it to say that the molecular ion is the only reasonable possibility.

The signal changes dramatically upon the addition of even 10 ppm of easily ionizable gas, as illustrated in figure 4.2 for 6.8×10^{14} molec cm^{-3} of NH_3 added to 2280 torr $(8.06 \times 10^{19}$ molec cm$^{-3})$ of He. The diamagnetic signal clearly shows a two-component relaxation described by $A_D G_x(t) = A_1 \exp(-\lambda_1 t) + A_2 \exp(-\lambda_2 t)$, i.e., equation (1.15). In the case of figure 4.2 $\lambda_2 = 2.3$, $\lambda_1 = 0.04$ μs^{-1}, $A_2 = 0.074$, and $A_1 = 0.243$. Results of this nature are tabulated in Appendix B for a wide variety of reagent gases in helium and neon moderators, with a few results obtained in argon and nitrogen moderators also. All but a few cases exhibit the characteristic diamagnetic relaxation. Also tabulated are the
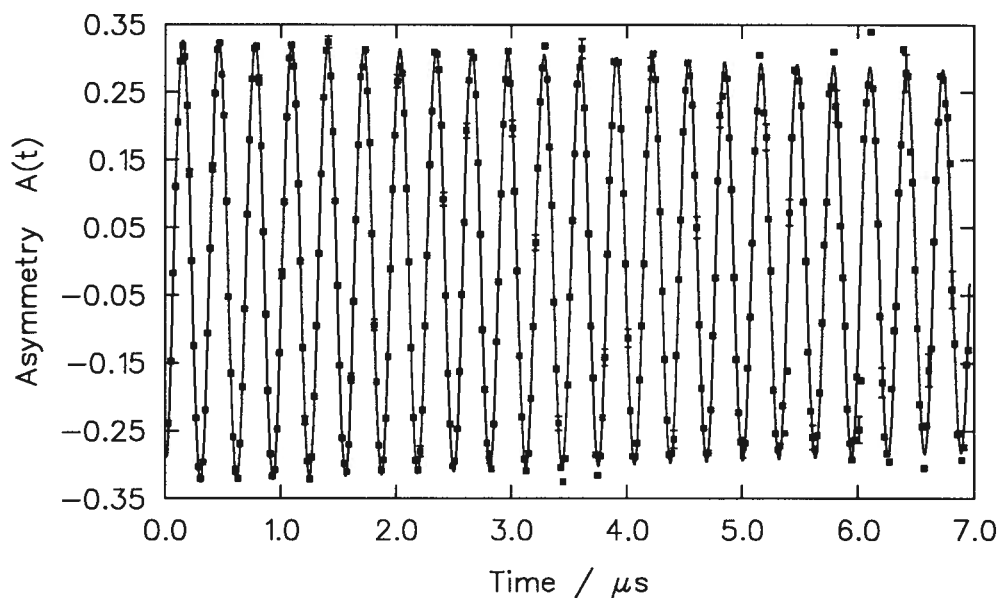
Figure 4.1   The 300 G μSR signal $A(t)$ for 2280 torr helium showing a large, long-lived diamagnetic signal, attributed to the molecular ion HeMu$^+$. The slow relaxation $(\lambda = 0.02\,\mu\text{s}^{-1})$ is consistent with the magnetic field inhomogeneity.
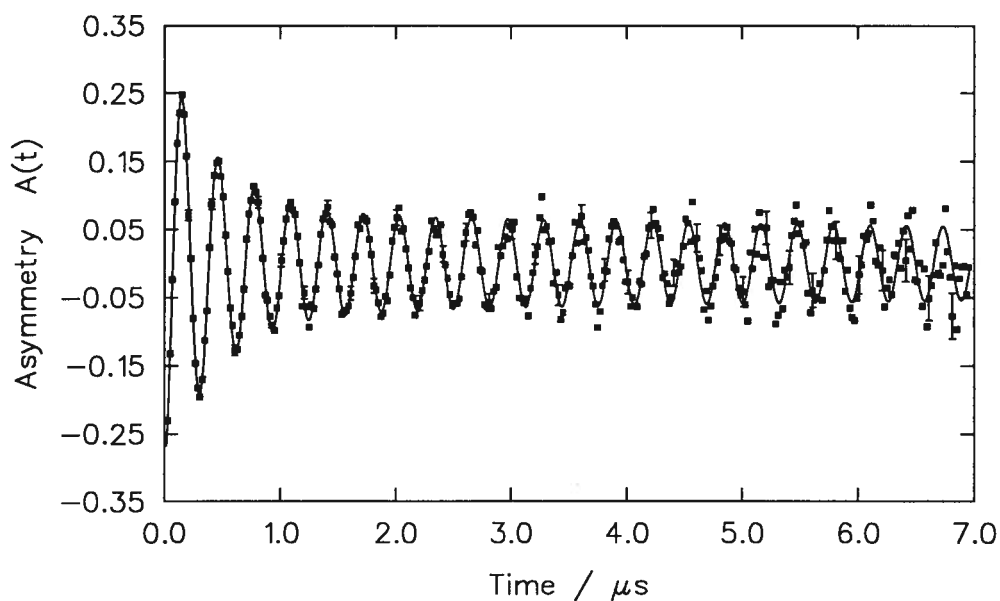
Figure 4.2   The relaxing signal seen in 2280 torr He with 6.8×10^{14} molec cm^{-3} of added NH$_3$ (8 ppm). The curve is a fit of equations (1.10) and (1.15) to the data. The relaxation is attributed to Mu formation by dissociative charge exchange between HeMu$^+$ and NH$_3$.

results from investigations of temperature and pressure dependences, and of mixtures of reagent gases.

This chapter progresses through three stages. In the first, relaxation data are presented and the minimal reaction mechanism to account for that data is found, and used for the data analysis. In the second stage (§4.5–4.8) a complete reaction model is presented, and the effects of its various reaction channels and limiting cases are considered. Finally, other data are presented whose analysis and interpretation are independent of the main reaction mechanism.

4.1 Measured Relaxations and Amplitudes

As indicated by figure 4.2, or by a more laborious inspection of appendix B, the two components have very different[1] relaxation rates, which may be called the "fast" and "slow" components. The parameters of interest are then A_f, A_s, λ_f, and λ_s. In general, λ_s did not vary much; its interpretation is deferred and the slow-relaxing component is treated as non-relaxing. Conversely, λ_f varied with reagent and moderator gas, and is the most important parameter measured.

The amplitudes of the components varied as well, and this variation can provide useful information. In order to get a meaningful amplitude for the slow component though, the contribution made by muons that stopped in the metal walls of the target vessel had to be subtracted. This correction was determined for each run period (or beam tune) and moderator density by adding O_2, air, or Xe to the moderator. It is known that O_2 depolarizes Mu by spin exchange with a rate of 4×10^{-10} cm^3 molec^{-1} s^{-1} at room temperature [44,106], and no signal at all is seen in inert gas containing more than a

---

[1] One could claim that they are "very" different due to numerical considerations alone — if the rates were similar, they could not be separated by a fit, and would probably never have been noticed; however, the rates can always be made very different by adding more reagent gas.

few torr of O_2. Xe produces 100% Mu and no diamagnetic fraction at pressures below 25 atm [91]. Thus, the amplitudes measured in these mixtures directly give the contribution from muons in the target walls. The amplitudes of these 'wall signals' were generally small (sometimes vanishingly small) thanks mainly to the very large target vessel and variable-momentum beamlines. The amplitudes listed in appendix B have already had the wall contributions subtracted.

4.2 Relaxation Mechanism

The relaxation of the diamagnetic signal is interpreted as due to muonium formation by charge transfer between the reagent gas 'X' and the muonated rare gas ion MMu^+ (M = He, Ne, ...). The prototype for charge transfer is

$$W^+ + X \longrightarrow W + X^+ \tag{4.1}$$
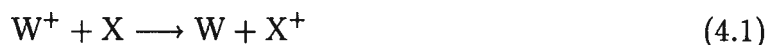
but since W = MMu is not bound (figure 1.1), the ion undergoes dissociative charge transfer according to

$$MMu^+ + X \xrightarrow{k_e} Mu + M + X^+. \tag{4.2}$$
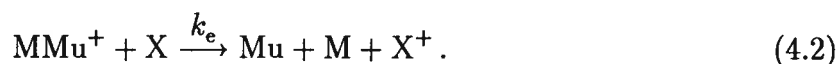
The fast-precessing Mu rapidly (in effect, instantaneously) loses phase coherence with the rest of the muons, giving relaxation of the signal at the chemical reaction rate as previewed in section 1.7.

A slight modification to this process is the switching reaction

$$MMu^+ + X \longrightarrow Mu + MX^+ \tag{4.3}$$

which is energetically more favorable, though entropically less so. It could be important when reaction (4.2) is endothermic and there is not quite enough excitation energy available to make it go. The binding energies of all HeX^+ and NeX^+ are so small (BE of $XeNe^+$ = 4.1 kJ/mol = 0.042 eV [144]) that such switching reactions should be of little consequence in these studies.

The only other possibility for the relaxation is the formation of a different paramagnetic product by muon transfer, say by

$$HeMu^+ + NO \xrightarrow{k_\mu} NOMu^+ + He \; . \tag{4.4}$$

Of the reactants studied, this should only occur for $X = NO$ and O_2 forming the radical ions $NOMu^+$ and O_2Mu^+. At 300 G, the μ^+ spin in these radicals, even with their reduced (from Mu) hyperfine couplings, would still lose phase coherence with the diamagnetic ensemble very rapidly. For these two cases it is possible that the apparent k_e is actually the sum $k_\mu + k_e$. Alternatively, fragmentation of diamagnetic products, e.g.

$$NeMu^+ + CH_3NO_2 \xrightarrow{k_\mu} (CH_3NO_2Mu^+)^* \longrightarrow CH_3Mu^+ + NO_2 \tag{4.5}$$
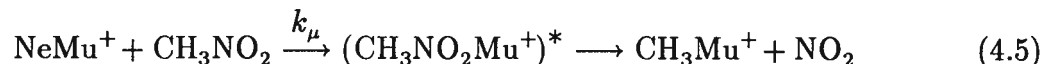
could produce paramagnetic ions, but fragmentation is much more likely to produce other diamagnetic species, e.g.

$$NeMu^+ + CH_3NO_2 \longrightarrow Ne + (CH_3NO_2Mu^+)^* \longrightarrow \begin{cases} CH_3^+ + MuNO_2 \\ CH_3Mu + NO_2^+ \end{cases} \tag{4.6}$$

$$HeMu^+ + C_2H_4 \longrightarrow He + (C_2H_4Mu^+)^* \longrightarrow C_2H_2Mu^+ + H_2 \; . \tag{4.7}$$
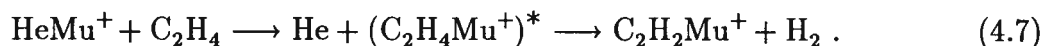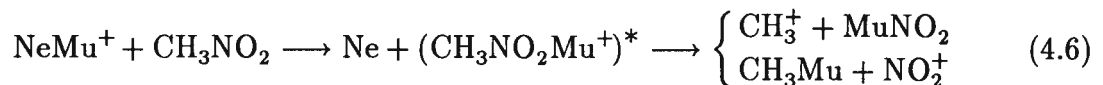
Radical formation, both directly and by fragmentation, is considered further later, but it does not affect the fits to the data presented here.

For all of reactions (4.2)–(4.4) one expects a linear dependence of the relaxation rate λ_f on reagent concentration [X]. Such is indeed the case for the reactions investigated; some results of linear fits to the relaxation data are shown in figures 4.3 and 4.4, and the experimental rate constants (slope, k_{exp}) are listed in table 4.1. These fits use the modified regression method outlined in section 2.3 incorporating both the statistical uncertainties in relaxation rates λ and concentrations [X]. The error bars shown are 1σ, as are the reported uncertainties in k. (For clarity, the plots show the weighted average λ for each run, but individual values of λ from each histogram were used for the fits.) The
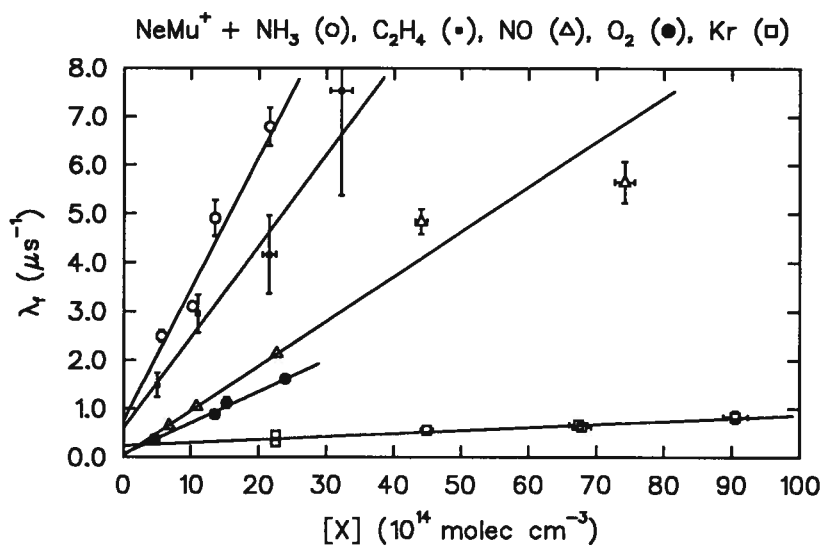
Figure 4.3   Linear fits of λ_f vs. concentration for a number of reactants in neon, where the slopes give the experimental rate constants $k_{exp} = 26$ (NH_3, o), 19 (C_2H_4, •), 9.2 (NO, △), 6.4 (O_2, •), and 0.6 (Kr, □) $\times 10^{-10}\, cm^3\, molec^{-1}\, s^{-1}$ for for the total reaction rate with $NeMu^+$, at neon moderator pressures from 800 to 1300 torr, and at room temperature.
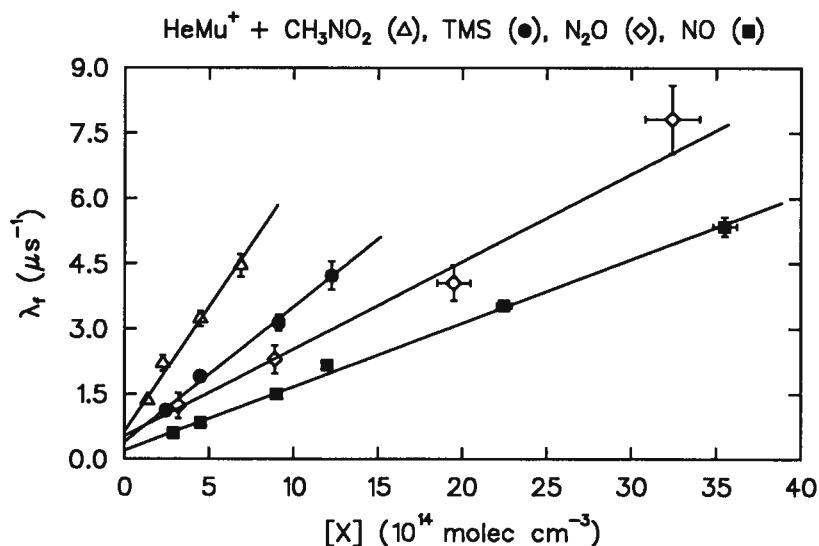
Figure 4.4   Reaction rates of $HeMu^+$ with various neutrals, plotted with linear fits which give $k_{exp} = 58$ (CH_3NO_2, △), 31 (TMS $= (CH_3)_4Si$, •), 20 (N_2O, ◇), and $14.7 \times 10^{-10}\, cm^3\, molec^{-1}\, s^{-1}$ (NO, ■, which has another point off the graph). All points were measured at room temperature and at 2280 torr of He, except for the N_2O runs which were taken at 1500 torr pressure.

random uncertainties in [X] were estimated from the nominal accuracy (0.5%) and the observed variability of the pressure measurements (when filling the standard volume with reagent gas). In some cases, an additional, systematic, uncertainty was added to the rate constant to reflect uncertainty in the 'standard' volume. In almost all cases, the uncertainty in [X] was of much less consequence than the uncertainty in λ. Occasionally, as well, the uncertainty reported for k_{exp} was increased somewhat arbitrarily because of excessive scatter in the points (high χ^2).

The rate constants do vary somewhat in their uncertainties: $3\% \sim 40\%$, with a typical error bar of $\sim 15\%$. These compare favorably with more established ion–molecule kinetics measurements [26]. There are several repetitions in table 4.1 that reveal the level of reproducibility. This is usually good, but two stand out and deserve special mention:

• Methyl fluoride reacts with $NeMu^+$ twice as fast at 800 torr as at 1400 torr. The measurements were done consecutively which suggests this is a real effect involving quenching by the moderator (see later). These runs were done without cold-trapping the neon though, suggesting that the different k_{exp}'s and the high intercepts are due to some impurity in the neon. This scenario is inconsistent, though, because of the reverse dependence on pressure. The high value of 12.26 at 800 torr is closer to the measurements made at different temperatures.

• Nitric oxide in 800 torr argon gave very different rate constants and amplitudes for two separate determinations. Based partly on prejudice, the measurement with the lower rate and higher amplitude seems right. The high relaxation may have been due to an impurity, either from the NO bottle or from leaks; the latter would cast some doubt on measurements taken in the same run period [$(C_2H_5)_3N$ and the 400 torr NO in Ar, and some ternary mixtures, given below]. Alternatively, the inconsistency may be the result of the reduced diamagnetic signal in Ar as compared with He or Ne.

It is worth emphasizing that these cases are exceptional, in that most repeated measurements of k_{exp} agreed within their uncertainties.

Table 4.1 Experimental Rate Constants Determined by Fitting λ_{f}

Reactant	M^a	p^b	T^c	$k_{\mathrm{exp}}{}^d$	Intercept^e	$k_{\mathrm{q}}{}^f$
Kr	Ne	1000		0.50 ± 0.16	0.57 ± 0.18	17.5 ± 5.5
Kr	Ne	800		0.62 ± 0.15	0.243 ± 0.089	9.3 ± 3.4
Xe	Ne	1300		3.0 ± 0.3	0.82 ± 0.15	19.3 ± 3.5
Xe	Ne	1300		3.6 ± 1.3	1.46 ± 0.22	34.3 ± 5.2
Xe	Ne	1000		5.4 ± 2.8	0.51 ± 0.13	15.4 ± 4.0
Xe ^{g}	Ne	800		5.35 ± 0.28^g	0.317 ± 0.034	12.1 ± 1.3
Xe	Ne	1400	445	4.93 ± 0.32	0.55 ± 0.10	18.2 ± 3.2
Xe ^{g}	Ne	565	179	5.30 ± 0.38^g	0.136 ± 0.087	4.5 ± 2.9
Xe	Ne	370	117	5.39 ± 0.24	0.044 ± 0.014	1.44 ± 0.46
Xe ^{g}	Ne	1000	117	4.77 ± 0.40^g	0.009 ± 0.019	0.11 ± 0.23
O_2	Ne	800		6.43 ± 0.37	0.063 ± 0.034	2.4 ± 1.3
NO	Ne	800		7.17 ± 0.64	0.315 ± 0.091	12.0 ± 3.5
NO	Ne	800		9.17 ± 0.39	0.036 ± 0.053	1.4 ± 2.0
N_2O	Ne	1000		11.1 ± 1.3	0.61 ± 0.17	18.6 ± 5.2
N_2O	Ne	1400	445	14.7 ± 1.3	0.16 ± 0.18	5.4 ± 5.9
N_2O	Ne	~700	177	12.30 ± 0.82	0.06 ± 0.15	1.5 ± 3.8
NH_3	Ne	800		27.7 ± 4.8	1.19 ± 0.26	$45. \pm 10.$
NH_3	Ne	1300		26.4 ± 2.0	0.82 ± 0.20	19.2 ± 4.7
NH_3	Ne	various		26.6 ± 4.0		
NH_3	Ne	1400	445	22.60 ± 0.86	0.149 ± 0.053	4.9 ± 1.7
NH_3	Ne	567	179	27.01 ± 0.89	-0.059 ± 0.067	-1.9 ± 2.2
C_2H_4	Ne	1000		18.6 ± 3.5	0.61 ± 0.33	$19. \pm 10.$
$(CH_3)_4Si$	Ne	800		16.2 ± 2.4	0.26 ± 0.19	9.9 ± 7.3
CH_3NO_2	Ne	800		41.6 ± 4.1	-0.04 ± 0.15	-1.5 ± 5.7
CH_3NO_2	Ne	1300	406	27.7 ± 3.0	0.27 ± 0.15	8.7 ± 4.8
CH_3NO_2	Ne	740	223	31.6 ± 6.3	0.12 ± 0.47	$4. \pm 15.$
CF_4	Ne	800		6.59 ± 0.47	0.37 ± 0.12	14.1 ± 4.6
CH_3F	Ne	1400		6.4 ± 1.4	1.98 ± 0.28	43.2 ± 6.1
CH_3F	Ne	800		12.3 ± 3.3	1.47 ± 0.39	$56. \pm 15.$
CH_3F	Ne	1400	445	15.5 ± 1.2	0.51 ± 0.11	16.8 ± 3.8
CH_3F	Ne	700	179	11.9 ± 1.2	0.75 ± 0.19	19.9 ± 5.0

Table 4.1 (continued) Experimental Rate Constants Determined by Fitting λ_f

Reactant	M[a]	p[b]	T[c]	k_{exp}[d]	Intercept[e]	k_q[f]
Xe	He	1500		12.9 ± 2.6	1.60 ± 0.33	32.6 ± 6.7
NO	He	2280		14.68 ± 0.36	0.194 ± 0.039	2.60 ± 0.52
N_2O	He	1500		20.0 ± 2.2	0.53 ± 0.23	10.8 ± 4.7
NH_3	He	1500		76.9 ± 14.2	2.16 ± 0.58	44. ± 12.
NH_3	He	2280		34.7 ± 1.4	0.056 ± 0.067	0.75 ± 0.90
C_2H_4	He	2400	398	25.0 ± 1.8	−0.10 ± 0.15	−1.7 ± 2.6
$(CH_3)_4Si$	He	2280		31.1 ± 2.3	0.39 ± 0.12	5.2 ± 1.6
CH_3NO_2	He	2280		57.5 ± 4.4	0.63 ± 0.14	8.4 ± 1.9
CH_3CHO	He	2400	406	31.5 ± 2.5	0.77 ± 0.11	13.5 ± 1.9
CH_3CHO	He	950	163	65.0 ± 7.8	0.09 ± 0.26	1.7 ± 4.6
CF_4	He	2280		16.2 ± 1.4	0.17 ± 0.13	2.3 ± 1.7
CH_3F	He	1500		33.0 ± 4.9	0.68 ± 0.27	13.8 ± 5.5
CH_3F	He	2400	398	26.5 ± 2.8	0.09 ± 0.18	1.6 ± 3.1
CH_3F	He	800	128	47.7 ± 3.4	−0.11 ± 0.12	−1.8 ± 2.0
$C_2H_4F_2$	He	1700		14.0 ± 4.9	2.06 ± 0.72	37. ± 13.
$C_2H_4F_2$	He	2400	406	9.2 ± 1.0	0.63 ± 0.11	11.0 ± 1.9
$C_2H_4F_2$	He	1330	208	18.7 ± 1.6	1.01 ± 0.12	16.3 ± 1.9
$C_2H_4F_2$	He	830	148	36.7 ± 3.3	0.76 ± 0.13	14.0 ± 2.4
NO	Ar	800		3.21 ± 0.16	0.018 ± 0.012	0.68 ± 0.45
NO	Ar	800		6.1 ± 1.6	−0.13 ± 0.47	−5. ± 18.
NO	Ar	400		6.3 ± 4.2	−0.07 ± 0.87	−5. ± 66.
$(C_2H_5)_3N$	Ar	800		8.6 ± 4.0	0.63 ± 0.44	24. ± 17.
NO	N_2	800		1.46 ± 0.14	0.176 ± 0.075	6.7 ± 2.9

[a] Moderator gas 'M' implies the molecular ion MMu^+, i.e., $HeMu^+$, $NeMu^+$, $ArMu^+$, and N_2Mu^+. Neither H_2 nor C_2H_6 moderators showed any reaction.

[b] Moderator pressure in torr.

[c] Temperature (kelvin); blank entries imply room temperature.

[d] The experimental rate constant (slope) in 10^{-10} cm^3 $molec^{-1}$ s^{-1}; k_{exp} can usually be identified with the capture rate constant k_c.

[e] The intercept of λ_f vs. [X], in μs^{-1}, identified as the moderator quenching rate $k_q[M]$.

[f] The quenching rate constant, in 10^{-15} cm^3 $molec^{-1}$ s^{-1}, as determined from the intercept.

[g] Relaxation rate did not vary linearly with concentration, as shown in figure 6.6. The tabulated values are from fitting the low concentration points.

4.3 A Simplistic Model

Despite the convincing fits to the relaxation rates, reaction (4.2) alone cannot explain the results because it does not provide for a two-component signal relaxation. The amplitudes of each component are tabulated with the relaxation rates in Appendix B. It can be seen there that the relative amplitudes of the two components varied greatly with reagent gas, as made clear by figures 4.5 and 4.6 for the extreme cases of nitromethane and nitric oxide. A proper model for these reactions must account for both the relaxation rates and the amplitudes.

The observation of two-component relaxations indicates that there are two groups of muons in diamagnetic environments. However, rather than being distributed between these groups initially, all the initial diamagnetic signal likely comes from a single muonated molecular ion species, and the separation is caused by competing reactions, according to

$$
\mathrm{MMu^+ + X} \quad
\begin{array}{l}
\overset{k_e}{\nearrow} \quad \mathrm{Mu + X^+ + M} \\[1.5em]
\underset{k_\mu}{\searrow} \quad \mathrm{XMu^+ + M}
\end{array}
\tag{4.8}
$$
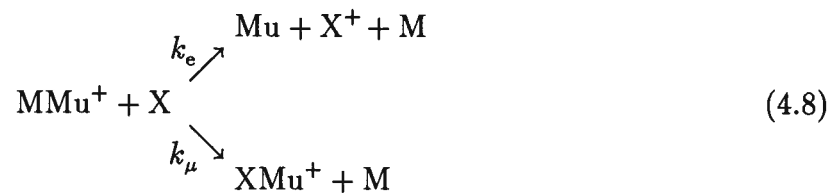
which was proposed in ref. 27. Here the diamagnetic $\mathrm{MMu^+}$ reacts with the dopant, X, by charge (electron) transfer with rate constant k_e to give muonium, or by muon transfer with rate constant k_μ to form diamagnetic $\mathrm{XMu^+}$. Such a muon-transfer reaction is entirely expected, based on the prevalence of the analogous proton-transfer reactions, which have been well studied [16,24,25,79,139,145–149]. Since $\mathrm{XMu^+}$ is (usually) diamagnetic, and as no diamagnetic frequency shift is large enough to give measurable dephasing on the few-microsecond time scale investigated, there is no relaxation associated with the muon-transfer reaction. As mentioned in the previous section, and discussed later, the products of muon transfer may fragment, but other diamagnetic products will be the result. Therefore, the relaxation envelope is given by the total concentration of diamagnetic species over time. As only a few million muons are used per experiment, and only
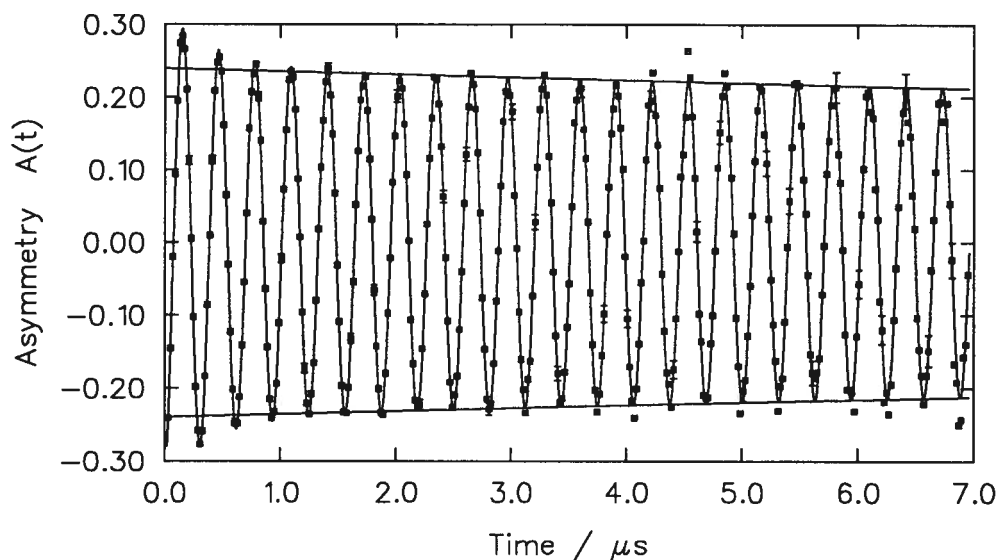
Figure 4.5 The μSR signal $A(t)$ showing the reaction between $HeMu^+$ and 2.3×10^{14} molec cm^{-3} of nitromethane, giving $\lambda_f = 2.4 \, \mu s^{-1}$, $A_f = 0.079$, and $A_s = 0.240$. The slowly relaxing component has been outlined to highlight the small fast-relaxing component. The amplitudes indicate that CH_3NO_2 reacts predominantly by muon transfer in preference to charge transfer.
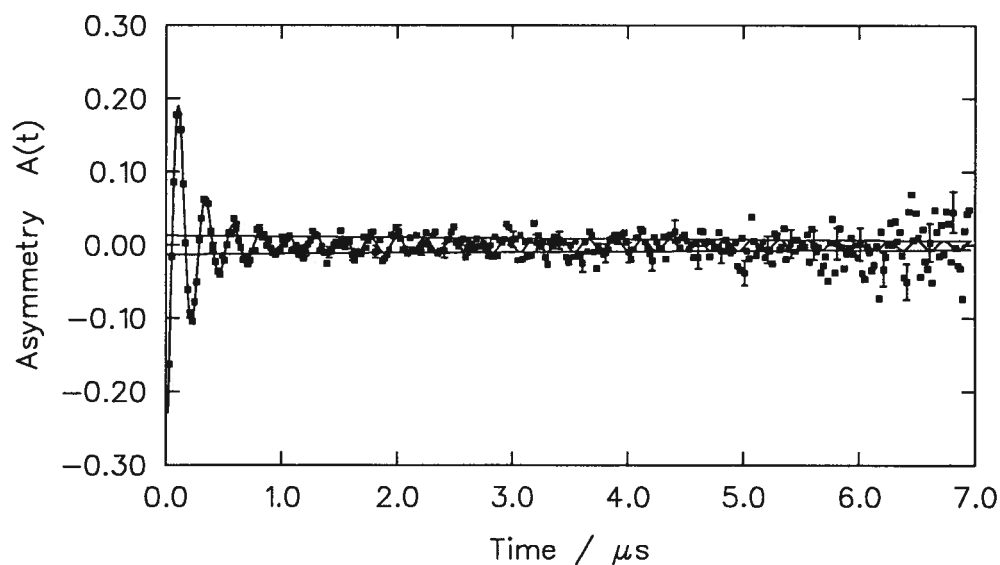
Figure 4.6 The strongly relaxing signal seen for $HeMu^+$ with 35.5×10^{14} molec cm^{-3} of nitric oxide; $\lambda_f = 5.1 \, \mu s^{-1}$, $A_f = 0.307$, and $A_s = 0.012$. The slow relaxation envelope is drawn for clarity. The large relaxing component is attributed to efficient charge transfer coupled with inefficient muon transfer, possibly with depolarization of $NOMu^+$ even after muon transfer.

one muon at a time is permitted in the target, the X and M species are in vast excess, allowing a straightforward analysis from elementary (pseudo-first order) kinetics.

The concentration of the initial ion is

$$[\text{MMu}^+] = [\text{MMu}^+]_0 \, e^{-(k_e + k_\mu)[\text{X}]t} \qquad (4.9)$$

and the concentration of the other diamagnetic species, XMu^+, is

$$[\text{XMu}^+] = \frac{k_\mu [\text{MMu}^+]_0}{k_e + k_\mu} \left\{ 1 - e^{-(k_e + k_\mu)[\text{X}]t} \right\} . \qquad (4.10)$$

The relaxation function is the normalized sum of these:

$$G(t) = [\text{D}]/[\text{D}]_0 = \frac{k_\mu}{k_e + k_\mu} + \frac{k_e}{k_e + k_\mu} \, e^{-(k_e + k_\mu)[\text{X}]t} \qquad (4.11)$$

where MMu^+ is taken to be the only species present at $t = 0$ so that $[\text{D}]_0 = [\text{MMu}^+]_0$. Thus there are two components to the signal: one relaxing at $\lambda = (k_e + k_\mu)[\text{X}]$ and the other not relaxing at all. The relaxing component of this model is identified with the fast-relaxing component of the data, $\lambda = \lambda_f$, and the non-relaxing component corresponds to the observed slowly-relaxing component, and the slow relaxation must be attributed to other processes (e.g., dephasing due to magnetic field inhomogeneity).

This model is a big improvement over simple charge transfer, but it is still incomplete. The first, and most serious, shortfall becomes apparent with a consideration of the energetics for charge transfer. Reaction (4.2) is endothermic by the ionization potential (IP) of reactant X plus the binding energy (D_0) of the initial ion MMu^+, minus the IP of Mu (13.533 eV [81]): $\Delta E = \text{IP(X)} + D_0(\text{MMu}^+) - \text{IP(Mu)}$. Table 4.2 lists the endothermicities for most combinations of X and M measured for this thesis; the cases where a reaction was seen are checked, and combinations where no reaction was evident are indicated by an x. In addition to the combinations tabulated, some investigations of molecular moderators were performed, with no relaxation seen for ammonia, triethylamine or nitric oxide in hydrogen; none for ammonia or nitric oxide in ethane; and none for C_2H_4, CO, or O_2

Table 4.2 Dissociative Charge-Transfer Reaction Endothermicities[a]

Neutral	IP (eV)[b]	Ion					
		HeMu$^+$ 1.53^c		NeMu$^+$ 1.79^c		ArMu$^+$ 3.57^c	
Kr	14.00^d	1.99	x^e	2.25	$\checkmark^e$	4.03	
Xe	12.13	0.12	$\checkmark$	0.38	$\checkmark$	2.16	x
H$_2$	15.43^d	3.42	x	3.67	x	5.46	x
CO	14.01^d	2.01	x	2.26	x	4.04	
O$_2$	12.06	0.05		0.31	$\checkmark$	2.09	x
NO	9.26	−2.75	$\checkmark$	−2.49	$\checkmark$	−0.71	$\checkmark$
N$_2$O	12.89	0.88	$\checkmark$	1.13	$\checkmark$	2.92	
NH$_3$	10.16	−1.85	$\checkmark$	−1.59	$\checkmark$	0.19	x
H$_2$O	12.61	0.60	x	0.86	x	2.64	
CH$_4$	12.51	0.50	x	0.76	x	2.54	
C$_2$H$_6$	11.52	−0.49	x	−0.23	x	1.55	
C$_2$H$_4$	10.51	−1.50	$\checkmark$	−1.24	$\checkmark$	0.54	
(CH$_3$)$_4$Si	9.80	−2.21	$\checkmark$	−1.95	$\checkmark$	−0.17	x
(C$_2$H$_5$)$_3$N	7.1 ^{b}	−4.91		−4.65		−2.87	$\checkmark$
CH$_3$NO$_2$	11.02	−0.99	$\checkmark$	−0.73	$\checkmark$	1.05	
CH$_3$CN	12.19	0.18		0.44	x	2.22	
CH$_3$CHO	10.23	−1.78	$\checkmark$	−1.52		0.26	
CF$_4$	13. ^{b}	0.99	$\checkmark$	1.25	$\checkmark$	3.03	
CH$_3$F	12.47	0.46	$\checkmark$	0.72	$\checkmark$	2.50	
C$_2$H$_4$F$_2$	11.87	−0.14	$\checkmark$	0.12		1.90	

^{a} ΔE for the reaction MMu$^+$ + X → X$^+$ + Mu + M, in eV, where X is the neutral species listed in the first column. For $\Delta E < 0$, the reaction is exothermic from the ground state of the ion.

^{b} First ionization potential of the neutral; taken from ref. 144. The value for CF$_4$ (listed there as "< 14.7") was here estimated from trends in the fluoro- and chloro-methanes. (Tichy et al. [79] bemoan the fact that the literature value is too high, without mentioning which literature or which value!) The IP for (C$_2$H$_5$)$_3$N, is the median of many values reported [144,150].

^{c} The ground state binding energies (D_0) of the ions [75,78].

^{d} Reaction is endothermic even for a bare μ^+.

^{e} Whether or not any ("fast") relaxation was observed is indicated by $\checkmark$ (yes) or x (no); the absence of a mark indicates that the ion/neutral combination was not examined.

in nitrogen, although nitric oxide did give diamagnetic relaxation in N_2. With both the molecular and rare gas moderators, there is no obvious trend with endothermicity, except that no reaction was seen for $X = H_2$ or CO, for which charge transfer is endothermic even for a bare μ^+. (Although reaction with Kr is similarly endothermic, a slow reaction with $NeMu^+$ was observed.) More noteworthy are the cases where the reaction is allowed energetically, but was not observed (C_2H_6 in He & Ne; $(CH_3)_4Si$ in Ar). These cases will be returned to. Note that these negative results come from multiple trials over wide concentration ranges to ensure that no relaxation was missed because it was too fast or too slow. Most at odds with the proposed two-reaction mechanism, eq. (4.8), are the instances where charge transfer is endothermic from the ground state of the molecular ion, but the reaction was seen anyway: O_2, N_2O, CH_3F, CF_4, and Xe in reacting with $HeMu^+$ and $NeMu^+$. These results strongly indicate that the ion is reacting from a rovibrationally excited state. Such a refinement was recognized as necessary even when the too-simple model (4.8) was originally proposed [27]. This excitation will figure prominently in other kinetic models to follow shortly and in later discussion.

Another failing of mechanism (4.8) is its prediction of the amplitudes. Yes, there are two components, but their relative amplitudes are given by $A_s/A_f = k_\mu/k_e$, *independent* of reagent or moderator concentration; this is surely not the situation revealed by the measured data. Figure 4.7 illustrates this for a number of cases; clearly, A_f grows at the expense of A_s as the reagent concentration is increased (note the reciprocal $1/[X]$ scale), and A_f declines as the moderator density is increased. Moreover, figure 4.7 shows that the ratio A_s/A_f varies linearly with $1/[X]$ and with $[M]$.

The third problem lies with the often substantial intercepts of the λ_f vs. $[X]$ fits (see table 4.1 or figures 4.3 and 4.4). These extrapolations to zero concentration are clearly different from the relaxation rate in pure moderator. This problem was noted, with much concern, in ref. 27, but the explanation had not become evident at that early stage of this thesis work.
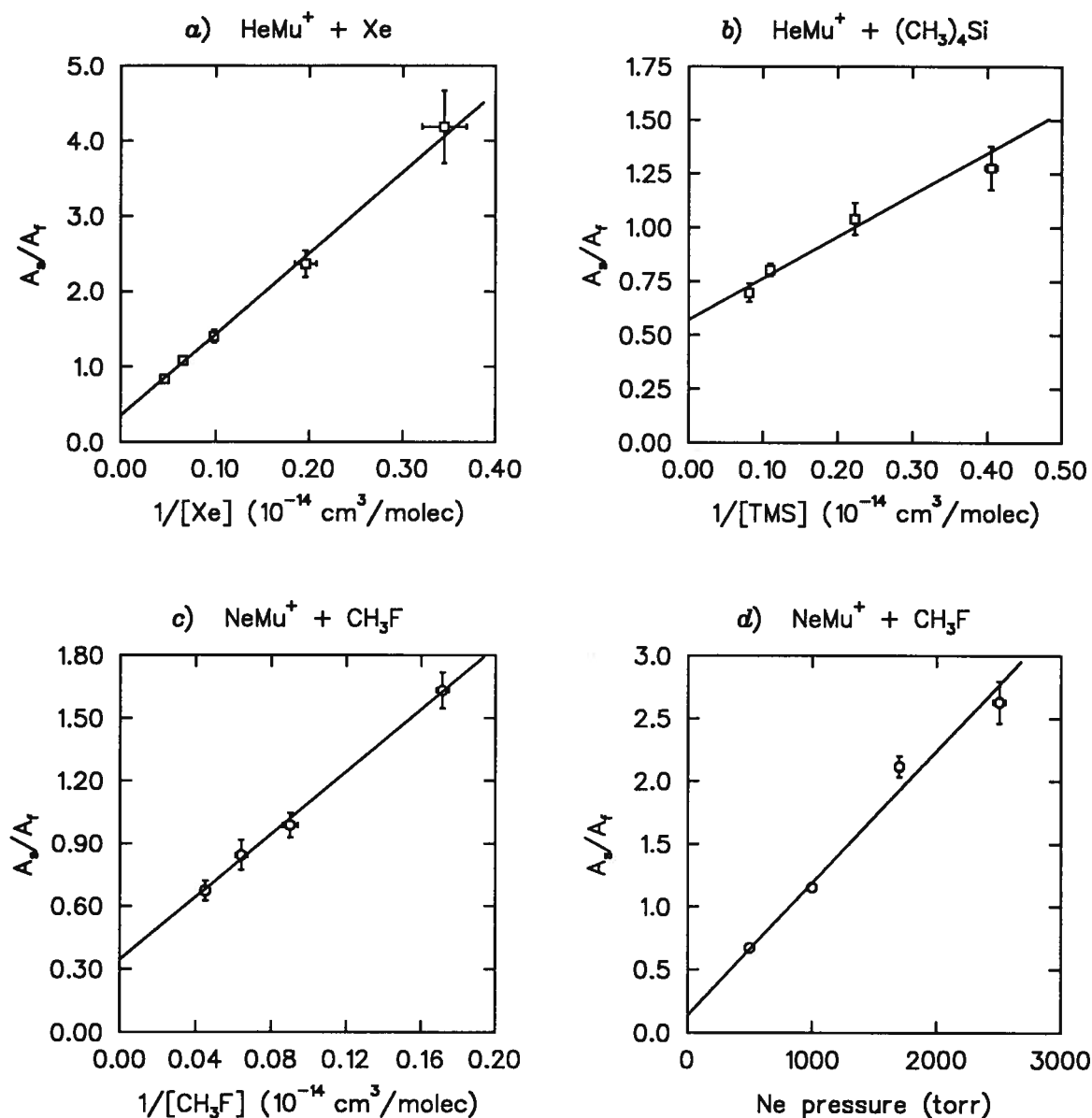
Figure 4.7 Four plots showing the variation of relative amplitudes with reactant concentration and moderator pressure (or density). For both (a) Xe in 1500 torr He and (b) $(CH_3)_4Si$ in 2300 torr He, the linear dependence on reciprocal concentration is clear, although it is much stronger for Xe. Varying the concentration of CH_3F in Ne (c) shows similar behavior, and varying the Ne pressure (d) reveals a strong linear dependence on p. Plots $a, b, \& c$ are fairly typical while plot d shows the strongest pressure dependence measured. Note that plots $c \& d$ give different intercepts—see §4.8.

4.4 A Successful Simple Model

All three shortcomings of the previous two-reaction model can be addressed with addition of a third reaction, between the initial molecular ion and the moderator gas to form a diamagnetic product. Since the ion has to be excited, the obvious reaction is collisional de-excitation or 'quenching.' Thus, the simplest model that consistently accounts for the data is the three-reaction scheme

$$
\begin{array}{c}
\qquad\qquad\qquad \mathrm{Mu} + \mathrm{X}^+ + \mathrm{M} \\
\qquad\qquad k_\mathrm{e} \nearrow \\
(\mathrm{MMu}^+)^* + \mathrm{X} \\
k_\mathrm{q} \downarrow \mathrm{M} \qquad k_\mu \searrow \\
\qquad\qquad\qquad \mathrm{XMu}^+ + \mathrm{M} \\
\mathrm{MMu}^+
\end{array}
\tag{4.12}
$$
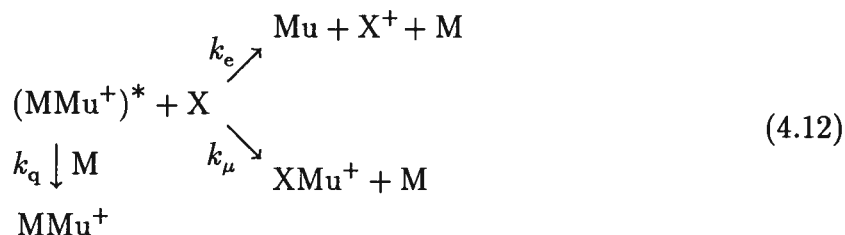
which was proposed in [28,151]. As before, the excited molecular ion $(\mathrm{MMu}^+)^*$ may react with reagent X by charge transfer with rate constant k_e to form Mu and be depolarized, or by muon transfer at k_μ to form the more stable diamagnetic ion XMu^+; or it may be quenched by collisions with the moderator with rate constant k_q, after which the dissociative charge transfer channel is closed. In contrast, based on their proton affinities [22,144], muon transfer is expected to be exothermic for every X studied, even from the molecular ion ground state. While the de-excited MMu^+ may indeed react by muon transfer with X to form XMu^+, that reaction is not shown because, since both ions are diamagnetic, it has no observable effect on the μSR signal. For simplicity, the quenching is assumed to be achieved in a single step.

Treating each channel as an elementary reaction, the depletion rate of $(\mathrm{MMu}^+)^*$ is

$$
\lambda = (k_\mathrm{e} + k_\mu)[\mathrm{X}] + k_\mathrm{q}[\mathrm{M}]
\tag{4.13}
$$

and

$$
\left[(\mathrm{MMu}^+)^*\right] = \left[(\mathrm{MMu}^+)^*\right]_0 e^{-\lambda t}.
\tag{4.14}
$$

Likewise, the concentration of Mu formed over time is

$$
[\mathrm{Mu}] = \frac{k_\mathrm{e}[\mathrm{X}] \left[(\mathrm{MMu}^+)^*\right]_0}{(k_\mathrm{e} + k_\mu)[\mathrm{X}] + k_\mathrm{q}[\mathrm{M}]} \left\{1 - e^{-\lambda t}\right\}.
\tag{4.15}
$$

Since Mu is the only source of depolarization, the relaxation shape is

$$G_x(t) = \frac{[D]}{[D]_0} = \frac{\left[(MMu^+)^*\right]_0 - [Mu]}{\left[(MMu^+)^*\right]_0}$$

$$= \frac{k_\mu[X] + k_q[M]}{(k_e + k_\mu)[X] + k_q[M]} + \frac{k_e[X]}{(k_e + k_\mu)[X] + k_q[M]} e^{-\lambda t} \qquad (4.16)$$

which, like the previous model, predicts a linear dependence of the relaxation rate on concentration ($\lambda_f = \lambda = (k_e + k_\mu)[X] + k_q[M]$) with slope $k_{exp} = k_e + k_\mu$, where the additional term $k_q[M]$ (the intercept) accounts for quenching of the initial excited state. Quenching rate constants determined this way are listed in table 4.1. Furthermore, and in contrast with the previous model, the amplitudes of the two components are related by

$$\frac{A_s}{A_f} = \frac{k_\mu[X] + k_q[M]}{k_e[X]} = \frac{k_\mu}{k_e} + \frac{k_q[M]}{k_e[X]} \qquad (4.17)$$

so that A_s/A_f should vary linearly with [M] and with $1/[X]$. Such is indeed the case, as shown in figure 4.7. Equation (4.17) was used to fit A_s/A_f vs. $1/[X]$ to give the results in table 4.3, which lists the intercepts (k_μ/k_e), slopes ($k_q[M]/k_e$), and values of k_q determined from the slopes. In general, the amplitudes were not as well determined as the relaxation rates, and the reproducibility (especially in the slope) of repeated measurements suffered, notably for Kr, Xe+NeMu$^+$ and NO+ArMu$^+$. The NO in Ar problem has been mentioned in regards to the relaxation rate. (Note that CH$_3$F in Ne is more acceptable here, given the general level of reproducibility). The Xe results show how the amplitudes are less reproducible than the relaxation rates are — compare the slopes in table 4.3 with k_{exp} in table 4.1.

In table 4.3 the slopes are interpreted as $k_q[M]/k_e$ and the intercepts as k_μ/k_e, following eq. (4.17). Thus k_μ and k_e can be determined individually by combining data from the relaxation rates ($k_{exp} = k_\mu + k_e$, from table 4.1) and the amplitudes ($A_s/A_f|_{[X]=0} = k_\mu/k_e$) according to the identities $k_e = (k_\mu + k_e)/(1 + k_\mu/k_e)$ and $k_\mu = (k_\mu + k_e)/(1 + k_e/k_\mu)$. Values for k_μ and k_e are given in table 4.4. A possible exception to this interpretation

Table 4.3 Results of Linear Fits of Relative Amplitudes: A_s/A_f vs. $1/[X]$

Reactant ('X')	Moder.[a] ('M')	p (torr)	T^b (K)	Slope[c] $(k_q[M]/k_e)$	Intercept[c] $(k_\mu/k_e;\ k_D/k_e)$	$k_q{}^d$
Kr	Ne	1000		$14. \pm 23.$	2.15 ± 0.29	0.7 ± 1.1
Kr	Ne	800		-20.9 ± 5.7	1.32 ± 0.14	-2.13 ± 0.79
Xe	Ne	1000		6.37 ± 0.86	-0.12 ± 0.20	11.8 ± 6.9
Xe	Ne	1300		19.77 ± 1.49	-0.0085 ± 0.086	17.0 ± 6.3
Xe	Ne	800		1.98 ± 0.14	-0.022 ± 0.009	4.13 ± 0.37
Xe	Ne	1400	445	4.3 ± 1.1	0.210 ± 0.062	1.1 ± 1.1
Xe	Ne	565	179	-3.80 ± 0.60	0.397 ± 0.027	-4.72 ± 0.82
Xe	Ne	370	117	0.2 ± 1.7	0.016 ± 0.086	0.3 ± 3.0
Xe	Ne	1000	117	0.01 ± 0.44	0.090 ± 0.040	0.00 ± 0.23
O_2	Ne	800		0.93 ± 0.24	0.022 ± 0.016	2.23 ± 0.59
NO	Ne	800		2.47 ± 0.65	-0.081 ± 0.037	7.4 ± 2.1
NO	Ne	800		1.00 ± 0.32	0.0122 ± 0.0090	3.5 ± 1.1
N_2O	Ne	1000		10.8 ± 1.1	0.721 ± 0.068	21.3 ± 3.4
N_2O	Ne	1400	445	8.9 ± 1.6	1.085 ± 0.094	20.7 ± 4.2
N_2O	Ne	~700	177	4.51 ± 0.91	1.103 ± 0.042	6.9 ± 1.5
NH_3	Ne	1300		1.29 ± 0.50	0.377 ± 0.050	5.8 ± 2.3
NH_3	Ne	800		-0.52 ± 1.2	1.36 ± 0.26	-2.3 ± 5.4
NH_3	Ne	1400	445	1.607 ± 0.075	0.343 ± 0.011	8.90 ± 0.54
NH_3	Ne	567	179	0.39 ± 0.21	0.410 ± 0.014	2.4 ± 1.3
C_2H_4	Ne	1000		11.2 ± 1.6	1.28 ± 0.16	27.9 ± 6.9
$(CH_3)_4Si$	Ne	800		2.23 ± 0.61	0.688 ± 0.070	8.2 ± 2.6
CH_3NO_2	Ne	800		3.06 ± 0.45	1.17 ± 0.10	22.4 ± 4.1
CH_3NO_2	Ne	1300	406	1.99 ± 0.66	1.42 ± 0.12	7.3 ± 2.6
CH_3NO_2	Ne	740	223	1.13 ± 0.89	1.34 ± 0.12	4.8 ± 3.9
CF_4	Ne	800		4.12 ± 0.94	0.390 ± 0.031	7.5 ± 1.8
CH_3F	Ne	1400		10.99 ± 1.04	0.765 ± 0.063	8.7 ± 2.1
CH_3F	Ne	800		7.43 ± 0.77	0.348 ± 0.064	25.8 ± 7.5
CH_3F	Ne	1400	445	3.76 ± 0.47	1.77 ± 0.13	6.9 ± 1.1
CH_3F	Ne	700	179	1.54 ± 0.40	1.060 ± 0.035	2.35 ± 0.66

Table 4.3 (continued)   Results of Linear Fits of Relative Amplitudes: A_s/A_f vs. $1/[X]$

Reactant ('X')	Moder.[a] ('M')	p (torr)	T^b (K)	Slope[c] $(k_q[M]/k_e)$	Intercept[c] $(k_\mu/k_e; \ k_D/k_e)$	$k_q{}^d$
Xe	He	1500		10.69 ± 0.98	$0.354 \pm .074$	20.7 ± 4.7
NO	He	2280		1.98 ± 0.12	-0.004 ± 0.005	3.91 ± 0.26
N_2O	He	1500		5.20 ± 0.70	0.936 ± 0.064	10.9 ± 1.9
NH_3	He	1500		2.97 ± 0.46	0.49 ± 0.13	31.2 ± 8.0
NH_3	He	2280		0.91 ± 0.15	0.144 ± 0.022	3.70 ± 0.63
C_2H_4	He	2400	398	0.46 ± 0.33	0.751 ± 0.040	1.13 ± 0.81
$(CH_3)_4Si$	He	2280		1.93 ± 0.22	0.573 ± 0.036	5.11 ± 0.70
CH_3NO_2	He	2280		2.68 ± 0.22	1.28 ± 0.15	9.1 ± 1.2
CH_3CHO	He	2400	406	0.20 ± 0.13	0.905 ± 0.034	0.59 ± 0.37
CH_3CHO	He	950	163	0.57 ± 0.21	1.041 ± 0.059	3.2 ± 1.3
CF_4	He	2280		8.8 ± 1.5	1.28 ± 0.12	8.4 ± 1.7
CH_3F	He	1500		6.86 ± 0.77	1.35 ± 0.17	19.6 ± 3.9
CH_3F	He	2400	398	3.4 ± 1.3	2.29 ± 0.18	4.7 ± 1.9
CH_3F	He	800	128	1.08 ± 0.31	1.436 ± 0.074	3.5 ± 1.0
$C_2H_4F_2$	He	2400	406	-0.95 ± 0.35	0.749 ± 0.034	-0.87 ± 0.34
$C_2H_4F_2$	He	1330	208	2.18 ± 0.23	0.793 ± 0.031	3.68 ± 0.50
$C_2H_4F_2$	He	830	148	1.46 ± 0.17	0.618 ± 0.055	6.11 ± 0.92
NO	Ar	800		-0.115 ± 0.051	0.027 ± 0.011	-0.137 ± 0.061
NO	Ar	800		9.58 ± 3.61	0.21 ± 0.12	18.3 ± 8.7
NO	Ar	400		0.4 ± 9.3	0.71 ± 0.39	$1. \pm 26.$
$(C_2H_5)_3N$	Ar	800		16.5 ± 4.3	0.90 ± 0.36	$28. \pm 16.$

[a] Moderator gas 'M' implies the molecular ion MMu^+, reacting with reagent 'X'.

[b] Temperature (kelvin); blank entries mean room temperature.

[c] Slope is in 10^{14} molec cm^{-3}, intercept is dimensionless. Their interpretation as $k_q[M]/k_e$ and k_μ/k_e follows from equation (4.17), although eq. (4.24) gives a more refined interpretation as $k_D/k_e = (k_\mu + k_d + k_s[M])/k_e$.

[d] k_q, in 10^{-15} cm^3 molec^{-1} s^{-1}, as calculated from $k_q = (slope \times k_{exp}) / \{[M](1 + intercept)\}$.

of the amplitudes occurs when the muon-transfer product XMu^+ is itself paramagnetic, as is the case for $X = O_2$ [152] and NO. Figures 1.6 and 4.6 show that nitric oxide gives little, if any, slow-relaxation component, which may be a result of $NOMu^+$ depolarization. Nevertheless, it is still reasonable to use equation (4.16), as long as it is remembered that "k_e" may really be the total $k_e + k_\mu$. Note that if the muon-transfer reaction causes depolarization, the reaction from the molecular ion ground state should not be ignored; indeed, the quenching channel should have little effect. In that case, the intercepts of the λ_f fits (near zero for both NO and O_2) should not be interpreted as $k_q[M]$. There are difficulties though, notably in explaining the presence of some non-relaxing signal, and these are discussed later.

Another impediment to interpreting the intercepts of the λ_f fits as $k_q[M]$ is their great variability; consistent values should be obtained for the same moderator gas (He or Ne) at the same density (pressure), independent of the X reagent. The tabulated results show not only great variations between different neutrals, but often large differences between the k_q determined from the relaxation rates and the value derived from the amplitudes.

Inflated and varying 'quenching' rates are probably due to reactions of impurities, such as water vapor, in the gas. If the impurity causes no depolarization (as is true for H_2O; table 4.2) its presence is not obvious, but the muon-transfer reaction, e.g.,

$$NeMu^+ + H_2O \longrightarrow Ne + H_2OMu^+ \tag{4.18}$$

would give a non-zero intercept to λ_f. The magnitude of the problem is made clear by the high intercepts typical before routine cold-trapping of the moderator gas was instituted (in recognition of this problem). Even when starting with clean gas, though, water vapor could still be present as it was continuously emitted by the aluminum reaction vessel, even after (ineffective) "baking." Nevertheless, the intercepts of the λ_f fits show reasonable consistency for later runs, and are still interpreted as $k_q[M]$; with discussion in chapter 6.

Table 4.4

Experimental Muon Transfer and Charge Transfer Rate Constants with Total (Capture)
Rate Constants

Reactant	Moder.	p (torr)	T (K)[a]	$k_c{}^b$	k_e	k_μ (k_D)
Kr	Ne	1000[c]		0.56 ± 0.11	0.226 ± 0.050	0.334 ± 0.069
Xe	Ne	800[d]		5.35 ± 0.28	5.47 ± 0.29	−0.120 ± 0.051
Xe	Ne	1400	445	4.93 ± 0.32	3.31 ± 0.34	1.62 ± 0.29
Xe	Ne	565	179	5.30 ± 0.38	3.79 ± 0.28	1.51 ± 0.13
Xe	Ne	[c]	117	5.22 ± 0.24	4.85 ± 0.28	0.37 ± 0.16
O_2	Ne	800		6.43 ± 0.37	6.29 ± 0.38	0.14 ± 0.10
NO	Ne	800[c]		8.63 ± 0.67	8.57 ± 0.68	0.06 ± 0.14
N_2O	Ne	1000		11.1 ± 1.3	6.45 ± 0.80	4.65 ± 0.60
N_2O	Ne	1400	445	14.7 ± 1.3	7.05 ± 0.70	7.65 ± 0.75
N_2O	Ne	∼700	177	12.30 ± 0.82	5.85 ± 0.41	6.45 ± 0.45
NH_3	Ne	1300[c,d]		26.6 ± 1.7[c]	19.3 ± 1.4[d]	7.28 ± 0.84[d]
NH_3	Ne	1400	445	22.60 ± 0.86	16.83 ± 0.65	5.77 ± 0.26
NH_3	Ne	567	179	27.01 ± 0.89	19.16 ± 0.66	7.85 ± 0.32
C_2H_4	Ne	1000		18.6 ± 3.5	8.2 ± 1.6	10.4 ± 2.0
$(CH_3)_4Si$	Ne	800		16.2 ± 2.4	9.6 ± 1.5	6.6 ± 1.1
CH_3NO_2	Ne	800		41.6 ± 4.1	19.2 ± 2.1	22.4 ± 2.4
CH_3NO_2	Ne	1300	406	27.7 ± 3.0	11.4 ± 1.4	16.3 ± 1.8
CH_3NO_2	Ne	740	223	31.6 ± 6.3	13.5 ± 2.8	18.1 ± 3.7
CF_4	Ne	800		6.59 ± 0.47	4.74 ± 0.35	1.85 ± 0.17
CH_3F	Ne	800[d]		12.3 ± 3.3	9.1 ± 2.5	3.2 ± 1.0
CH_3F	Ne	1400	445	15.5 ± 1.2	5.58 ± 0.51	9.88 ± 0.81
CH_3F	Ne	700	179	11.9 ± 1.2	5.78 ± 0.59	6.12 ± 0.63

Table 4.4 (continued)

Experimental Muon Transfer and Charge Transfer Rate Constants with Total (Capture) Rate Constants

Reactant	Moder.	p (torr)	T (K)[a]	$k_c{}^b$	k_e	k_μ (k_D)
Xe	He	1500		12.9 ± 2.5	9.5 ± 2.0	3.37 ± 0.85
NO	He	2280		14.68 ± 0.36	14.74 ± 0.37	-0.059 ± 0.074
N_2O	He	1500		20.0 ± 2.2	10.3 ± 1.2	9.7 ± 1.1
NH_3	He	2280^d		34.7 ± 1.4	30.3 ± 1.4	4.37 ± 0.61
C_2H_4	He	2400	398	25.0 ± 1.8	14.2 ± 1.1	10.70 ± 0.84
$(CH_3)_4Si$	He	2280		31.1 ± 2.3	19.8 ± 1.5	11.3 ± 1.0
CH_3NO_2	He	2280		57.5 ± 4.4	25.2 ± 2.5	32.3 ± 3.0
CH_3CHO	He	2400	406	31.5 ± 2.5	16.5 ± 1.3	15.0 ± 1.2
CH_3CHO	He	950	163	65.0 ± 7.8	31.8 ± 3.9	33.2 ± 4.1
CF_4	He	2280		16.2 ± 1.4	7.11 ± 0.72	9.09 ± 0.87
CH_3F	He	1500		33.0 ± 4.9	14.0 ± 2.3	18.9 ± 3.0
CH_3F	He	2400	398	26.5 ± 2.8	8.0 ± 1.0	18.4 ± 2.0
CH_3F	He	800	128	47.7 ± 3.4	19.6 ± 1.5	28.1 ± 2.1
$C_2H_4F_2$	He	1700		14.0 ± 4.9		
$C_2H_4F_2$	He	2400	406	9.2 ± 1.0	5.25 ± 0.58	3.94 ± 0.44
$C_2H_4F_2$	He	1330	208	18.7 ± 1.6	10.43 ± 0.91	8.27 ± 0.73
$C_2H_4F_2$	He	830	148	36.7 ± 3.3	22.7 ± 2.2	14.0 ± 1.5
$(C_2H_5)_3N$	Ar	800		8.6 ± 4.0	4.5 ± 2.3	4.1 ± 2.1
NO	Ar	800^d		3.21 ± 0.16	3.13 ± 0.16	0.084 ± 0.034
NO	Ar	400		6.3 ± 4.2	3.7 ± 2.6	2.6 ± 1.9

[a] temperature in kelvin; blanks indicate uncontrolled room temperature.

[b] k_{exp} from table 4.1, which equals the capture rate constant if capture is the rate limiting step; k_e and k_μ determined from k_c and k_μ/k_e from table 4.3. All rate constants in units of 10^{-10} cm^3 molec^{-1} s^{-1}.

[c] average of a number of measurements, sometimes at different pressures.

[d] selected from a number of measurements.

The differences between the k_q values determined by the relaxations (table 4.1) and the amplitude-based values (table 4.3) probably do not have a trivial explanation such as impurities, but point to a more complex reaction mechanism involving capture, and stabilization of the excited intermediate complex. In other respects, the simple model (4.12) is sufficient for analyzing, interpreting, and understanding the data.

4.5 A Mechanism with Capture and Breakup

Not made clear in the reaction scheme (4.12) is that both charge transfer and muon transfer should proceed from a single reaction in which the molecule X is captured by the ion; i.e., what is missing from this simple model is any mention of ion–molecule capture. For the case where the capture (collision) rate is the limiting rate, the capture rate constant is just k_{exp} from table 4.1. For such cases, capture is implicit in the simple model, and these capture rates are listed in table 4.4, which also lists the rate constants k_e and k_μ assuming $k_{exp} = k_c = k_e + k_\mu$.

To put this on a more rigorous basis, the capture can be shown explicitly in the reaction scheme:

$$Mu + X^+ + M$$

$$k'_e \uparrow$$

$$(MMu^+)^* \underset{k'_b}{\overset{k_c[X]}{\rightleftharpoons}} (M\ Mu\ X^+)^* \xrightarrow{k'_\mu} XMu^+ + M \qquad (4.19)$$

$$k_q[M] \downarrow \qquad \swarrow k'_d \quad \begin{matrix} k'_s[M] \\ k'_r[X] \end{matrix} \downarrow \qquad \nearrow$$

$$MMu^+ \longrightarrow MMuX^+$$
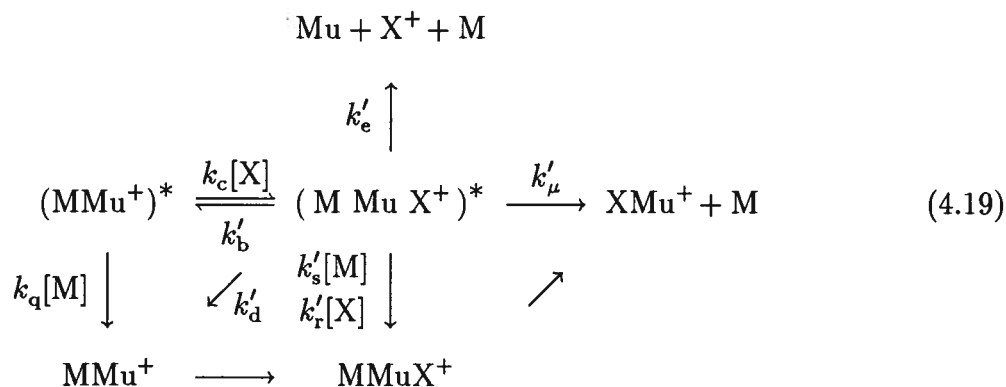
involving an excited ion $(MMu^+)^*$, which may be collisionally de-excited (with rate $k_q[M]$) or may capture a neutral reactant $(k_c[X])$ to form an energetic intermediate complex $(MMuX^+)^*$. This is short-lived, and may undergo back-dissociation with or without energy loss (k'_d, k'_b), breakup into products (k'_e, k'_μ), or collisional stabilization $(k'_s[M], k'_r[X])$.

All of the final products except Mu in reaction scheme (4.19) are diamagnetic and are indistinguishable in the present experiments. Furthermore, many of these may dissociate into smaller fragments which are themselves diamagnetic. Mu formation is the *only* cause of signal relaxation.

It is clear from the outset that there are too many processes in this mechanism to use it directly in analyzing the data. Instead, various limiting cases of the full solution will be examined, and these limits will aid in the interpretation of the fits already presented in this chapter. Before presenting a complete solution to the capture mechanism, let us consider the steady-state behaviour, when the complex is very short-lived and capture is the limiting rate.

The rate of depolarization due to Mu formation is given by the differential equations

$$\frac{d}{dt}[\text{Mu}] = k'_e[(\text{MMuX}^+)^*] \tag{4.20}$$

$$0 = \frac{d}{dt}[(\text{MMuX}^+)^*] = k_c[\text{X}][(\text{MMu}^+)^*] - (k'_b + k'_D + k'_e)[(\text{MMuX}^+)^*] \tag{4.21}$$

$$\frac{d}{dt}[(\text{MMu}^+)^*] = k'_b[(\text{MMuX}^+)^*] - (k_c[\text{X}] + k_q[\text{M}])[(\text{MMu}^+)^*] \tag{4.22}$$

where

$$k'_D = k'_d + k'_s[\text{M}] + k'_r[\text{X}] + k'_\mu \tag{4.23}$$

and the intermediate $(\text{MMuX}^+)^*$ ion is assigned a constant concentration by the steady-state approximation. Since X is very dilute, and the complex is short-lived, k'_r can be ignored. Solving for [Mu] gives the relaxation function

$$G_x(t) = \frac{[(\text{MMu}^+)^*]_0 - [\text{Mu}]}{[(\text{MMu}^+)^*]_0}$$

$$= 1 - \frac{k'_e k_c[\text{X}](1 - e^{-\lambda t})}{k_c[\text{X}](k'_D + k'_e) + k_q[\text{M}](k'_b + k'_D + k'_e)} \tag{4.24}$$

where

$$\lambda = \frac{k_c[\text{X}](k'_D + k'_e)}{k'_b + k'_D + k'_e} + k_q[\text{M}] . \tag{4.25}$$

The primed rate constants are undetermined and are for reactions of the complex; they all have higher order 'overall' counterparts given by $k = k_c k' / \sum k'$ which give the expressions

$$G_x(t) = \frac{k_D[X] + k_q[M] \quad + \quad k_e[X]e^{-\lambda t}}{(k_e + k_D])[X] + k_q[M]} \, , \tag{4.26}$$

$$\lambda = (k_D + k_e)[X] + k_q[M] \, . \tag{4.27}$$

These are the same as the simpler model result, eqs. (4.16)&(4.13), except for k_D replacing k_μ; therefore the k_μ column in table 4.4 should rightly be interpreted as k_D. One might hesitate to make a direct substitution because $k_D = k_\mu + k_d + k_s[M] (+ k_r[X])$ is not really a constant for varying [X] or [M]. However, since $k_r[X]$ is undoubtedly much lower than the other rates, it should be ignored, making k_D constant with respect to [X] and so a viable substitute for k_μ in the results presented thus far. The contribution of stabilization can be (and was) determined separately by varying the moderator density, where k_D/k_e ('k_μ/k_e') should increase with pressure. For most combinations at multiple pressures listed in table 4.3 the opposite trend is seen, indicating that k_s contributes very little. The only case with evidence of substantial stabilization of the complex is CH_3F. Further results from varying [M] (pressure) at fixed [X] are presented in section 4.8.

Another added reaction channel, dissociative de-excitation (k_d), cannot be distinguished from muon transfer (k_μ), and since the ground-state MMu^+ ion will subsequently react by muon transfer anyway, the distinction between the two is almost meaningless.

Finally, back-dissociation *without* de-excitation (k_b) can reduce the observed total rate constant k_{exp} below the actual capture rate k_c, making it more difficult to differentiate between anomalously low collision cross sections and unstable complexes. Dissociation back to the original reactants, including the excited $(MMu^+)^*$ ion, is somewhat hard to believe; production of ground-state MMu^+, with rate constant k_d, seems much more likely. Since all of the neutral reactants studied should be much better quenchers than He or Ne [79,153–157], quenching of $(MMu^+)^*$ by the moderator cannot be important

whenever *cyclic* capture and breakup occurs: if k'_b is significant, k_q should be insignificant, and vice versa. For the neutral reactants that can only undergo charge exchange with an excited ion, and which react below the theoretical capture rate (Xe, the fluoro-alkanes), an explanation with $k_b = 0$ is to be preferred. For more easily ionizable neutrals, however, k_b is expected to be more important than k_d or k_q.

Since an excited state is not required for quite a few of the reactants studied, it is reasonable to consider reversible capture (k_b), disregarding quenching of the initial ion in those cases. If the MMu$^+$ ion is presumed to react from the ground state just as well as from excited states, quenching is ineffective, and k_q and k_d (but not k_s) should be taken as zero. This presumption is not a good one, however. Instead, quenching should still be important, even when charge transfer is exothermic for ground-state reactants, since k_e is bound to be very sensitive to the degree of excitation above threshold.

4.6 Complete Solution of the Capture Mechanism

The exact solution to the complex's concentration in the capture mechanism (4.19) is calculated by solving the coupled differential equations (4.21) and (4.22) (without the "$0=$") to give

$$[(MMuX^+)^*] = \frac{k_c[X][(MMu^+)^*]_0}{\lambda_+ - \lambda_-} \left(e^{-\lambda_- t} - e^{-\lambda_+ t}\right) \tag{4.28}$$

where

$$2\lambda_\pm = k_c[X] + k_q[M] + k'_b + k'_e + k'_D$$
$$\pm \sqrt{\begin{array}{c}(k_c[X] + k_q[M] + k'_b + k'_e + k'_D)^2 - \\ 4\{k_c[X](k'_e + k'_D) + k_q[M](k'_e + k'_D + k'_b)\}\end{array}} \tag{4.29}$$

which leads to the relaxation envelope

$$G_x(t) = 1 - \frac{k'_e k_c[X]}{\lambda_+ \lambda_-} + \frac{k'_e k_c[X]}{\lambda_+ - \lambda_-} \left(\frac{e^{-\lambda_- t}}{\lambda_-} - \frac{e^{-\lambda_+ t}}{\lambda_+}\right). \tag{4.30}$$

This shape is plotted as the solid line in figure 4.8, where the dashed line shows the non-relaxing component and the dot-dashed line shows the simple exponential decay

$\exp(-\lambda_- t)$. The deviation from the dot-dashed line is $\exp(-\lambda_+ t)$. The interpretation of these components depends on the relative values of $\lambda_2 \equiv k_c[X] + k_q[M]$ and $\lambda_3 \equiv k_b' + k_e' + k_D'$ ($\lambda_1 = 0$). This is easiest to see in the limit of $k_b' = 0$ where $\lambda_2 = \lambda_-$ and $\lambda_3 = \lambda_+$.

$\lambda_2 \ll \lambda_3$: The case of the simple model (4.12) & (4.16) or the steady-state approximation to the capture mechanism where a very small constant concentration of complex is rapidly reached, with $k_e = k_c k_e'/(k_e' + k_D')$ and $k_D = k_c k_D'/(k_e' + k_D')$, and the observed relaxation (λ_2) is at $k_c[X] + k_q[M]$.

$\lambda_2 < \lambda_3$: This is the case where capture is the slower step, and the space between the simple decay and the solid line is given by $\exp(-\lambda_3 t)/\lambda_3$, corresponding to the build-up of the intermediate complex. No data was seen to exhibit this relaxation shape, although 'wall signals' at slightly lower magnetic fields occasionally mimicked this dependence.

$\lambda_2 > \lambda_3$: This is the case where the complex break-up is the limiting rate. Even if the deviation from exponential went unnoticed, the late tail does not depend on reactant concentration, contrary to the data. Furthermore, the intermediate complexes are expected
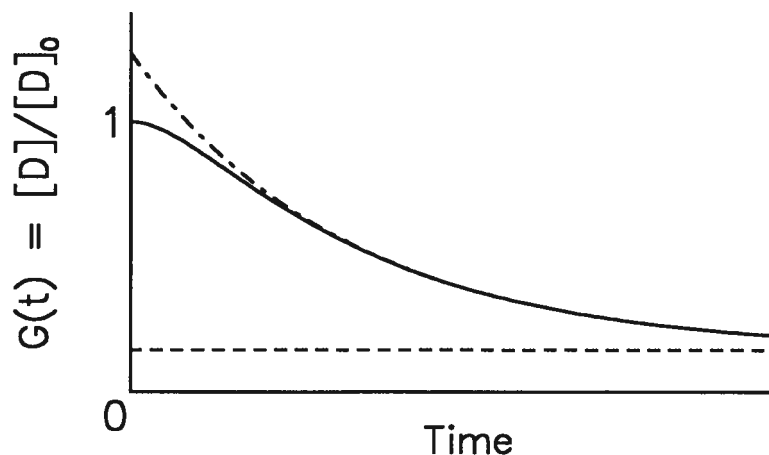
Figure 4.8 Relaxation shape for a capture mechanism with a long-lived complex (——). There are three components: a non-relaxing ($\lambda_1 = 0$) part (- - - - -), an exponential decay (- · - · -) corresponding to the rate in the simple model ($\lambda_2 = k_c[X] + k_q[M]$), and subtracted from that, a faster decay at $\lambda_3 = k_b' + k_e' + k_D'$. The actual relaxations do not appear to have this shape.

to be much too unstable for this situation to occur.

$\lambda_2 \approx \lambda_3$: This is the most uncertain case, with a relaxation shape going as $(1 + \lambda t) \times$ $\exp(-\lambda t)$ which may not be distinguishable from a pure exponential. However the range of relaxation rates usually measured should have been enough to reveal deviations from a simple relaxation, which were not seen.

For the case of no equilibrium step ($k_b' = 0$), the observed rate has no fall-off regime like what is seen for a Lindemann mechanism; λ is given by sums of rates, not by a ratio. Nevertheless, as concentration increases, the observed (late-time) reaction rate does change from $\lambda_2 = k_c[X] + k_q[M]$ to the relatively constant $\lambda_3 = k_D' + k_e'$ when $\lambda_2 = \lambda_3$. Although this is an abrupt transition, if the two exponentials of eq. (4.30) cannot be resolved experimentally, the results might resemble a slow transition from bimolecular to unimolecular kinetics as [X] increases. Such a transition cannot be considered a likely circumstance though, because λ_2 (capture) is expected to be the limiting rate at all X concentrations studied.

Since no three-component relaxations were actually identified in the data, it is sensible to write a single overall relaxation (with a non-relaxing component) based on this model. Using the steady-state approximation has given equation (4.24) but a more general expression, reminiscent of the familiar Lindemann reaction rate, is found by taking the low $k_c[X]$ limit for λ_-:

$$\lambda = \frac{k_c[X](k_e' + k_D') + k_q[M](k_e' + k_D' + k_b')}{k_c[X] + k_q[M] + k_b' + k_e' + k_D'} \qquad (4.31)$$

with $k_D' = k_d' + k_s'[M] + k_r'[X] + k_\mu'$; but $k_r' = 0$ and $k_b' = 0$ must be considered likely, with the complex mostly dissociating into products (k_e', k_μ') or into de-excited reactants (k_d'). The reaction rate (4.31) starts increasing with reagent concentration, but eventually levels off at high [X]. Some such curvature was observed for $Xe + NeMu^+$, but not consistently through the many repeated measurements. This special case is discussed in section 6.5.

4.7 Other Possible Mechanisms

Some additional mechanisms deserve brief consideration, along with variations on the ones that have already been presented.

Multiple excited states: It seems quite unlikely that the ions $NeMu^+$ and $HeMu^+$ are formed in a single excited state, or that they are quenched to the ground state in one step, although that is the approximation used in modeling the reaction. Given a variety of excitation energies, the rate of (ground state) endothermic charge transfer is likely to increase with the degree of excitation. For the case of two excited states contributing to the reaction, and where charge transfer is faster for the higher excited state, there should be a three-component relaxation: slow, fast (*) and very fast (**), as distinct from a two-component relaxation. The states involved in this mechanism might be two different vibrational levels, a vibrationally excited state and ground state (when charge transfer is exothermic), or even an excited state of the molecular ion and a bare μ^+. In contrast to the mechanisms featuring a buildup of an intermediate, the relaxation components would all be decays; i.e., the components are added, not subtracted. The extra component should be present even when capture has the same rate from both states, as long as $k_e/k_D(*) < k_e/k_D(**)$. As noted already, the data do not generally exhibit this, or any other, three-component relaxation shape. This probably indicates that there really is only one 'fast' relaxation rate, or that the very fast component is too fast, in which case it can be completely ignored; but it might also mean that the two fast-relaxing components are similar and cannot be resolved, or that there are many components. Three or more components could not be distinguished; instead, they would appear as some average relaxation rate. In the limit of a continuum of component rates, the result returns to an exact exponential. Note, however, that there are far too few bound vibrational states of $HeMu^+$ and $NeMu^+$ (4 and 5 respectively) [75] to behave as a true continuum of excitation levels, although the rotational excitation could contribute as well. For, say,

two unresolvable relaxing components, the observed average rate would not vary linearly with added neutral reactant. Such an effect was generally not seen.

Note that the simple model (4.12) does not exclude multiple excited states, as long as capture is the limiting step for *all* states from which charge transfer can occur. There might be some deviation from that model's prediction of A_s/A_f in the likely event that k_e/k_μ increases with increasing excitation, causing the amplitudes to vary more than the total rate constant with moderator pressure.

Alternative reactions and fragmentation: Due to the nature of μSR, the identification of the reactions (i.e., the reaction products) is not certain. This is especially true for the 'muon-transfer' reactions which could have contributions from other reactions giving diamagnetic products. Most such reactions would actually involve muon transfer, but with some degree of product fragmentation due to the great exothermicity of the muon-transfer reaction and the resultant high product excitation. Table 4.5 shows some of the many possibilities, with the reaction energetics calculated using the same vibrational zero-point energy corrections when substituting Mu for H in the reactants and the products. Since the rare gas ion reactants are less strongly bound than the products, this treatment is not exact. Using harmonic zero-point corrections where the vibrational frequencies are known (CH_5^+, CH_3^+, NH_4^+, and H_3O^+ [80]) raises the ΔH of reaction by ≈ 0.1 eV.

Since these reactions do not really affect the extraction of rate constants, and since the initial muon transfer is the same, such considerations will usually be ignored in the forthcoming discussion.

In conclusion, despite the plethora of possible processes, *the data are still best described by the simple mechanism* (4.12) of a competition between charge and muon-transfer reactions with X and quenching by M. The minor deviations from this do not affect the fits to the data but can influence their interpretation. Capture is still implicit in this model, but the (unimolecular) rates of product formation, k_e', k_μ' etc., cannot be

Table 4.5 Muon-Transfer and Fragmentation Reactions and Their Energetics

Reaction[a]	ΔH / eV for M = Ne	He
$MH^+ + CH_4 \longrightarrow CH_5^+ + M$	-3.6	-3.9
$\longrightarrow CH_3^+ + H_2 + M$	-1.7	-1.9
$+ C_2H_4 \longrightarrow C_2H_5^+$	-4.8	-5.1
$\longrightarrow C_2H_3^+ + H_2$	-2.8	-3.0
$+ C_2H_6 \longrightarrow C_2H_7^+$	-4.1	-4.4
$\longrightarrow C_2H_5^+ + H_2$	-3.4	-3.7
$\longrightarrow C_2H_3^+ + 2H_2$	-1.4	-1.6
$+ NH_3 \longrightarrow NH_4^+$	-6.8	-7.0
$\longrightarrow NH_2^+ + H_2$	-0.2	-0.4
$+ H_2O \longrightarrow H_3O^+$	-5.1	-5.4
$\xrightarrow{\;\;\not\;\;} OH^+ + H_2$	2.1	1.9
$+ CF_4 \longrightarrow CF_4H^+$	-3.4	-3.6
$\longrightarrow CF_3^+ + HF$	-2.8	-3.0
$+ CH_3F \longrightarrow CH_4F^+$	-4.2	-4.4
$\longrightarrow CH_3^+ + HF$	-2.7	-2.9
$\longrightarrow CH_2F^+ + H_2$	-2.6	-2.8
$+ CH_3CN \longrightarrow CH_3CNH^+$	-6.1	-6.3
$\xrightarrow{\;\;\not\;\;} CH_4 + CN^+$	3.3	3.1
$\longrightarrow CH_3^+ + HCN$	-1.8	-2.0
$+ CH_3NO_2 \longrightarrow CH_3NO_2H^+$	-5.7	-5.9
$\longrightarrow CH_4 + NO_2^+$	-3.7	-3.9
$\longrightarrow CH_3^+ + HNO_2$	-2.5	-2.7

[a] The reactions and reaction enthalpies are shown for NeH^+ and HeH^+ ions rather than $NeMu^+$ and $HeMu^+$ on the assumption that the zero-point energy corrections are the same for reactants and products. In fact, most of the products will have higher zero-point energies, raising ΔH by ≈ 0.1 eV, but most of the corrections are not accurately known.

extracted from the data. Instead, the analysis, and the discussion, must be based on the apparent overall rate constants k_e, k_μ etc. given by $k = k_c k' / \sum k'$. Cyclic capture and breakup, when operative, invalidates the identity $k_{exp} = k_c$, and provides one explanation for the cases where k_{exp} does not match the theoretical k_c. Dissociation with de-excitation is indistinguishable from muon transfer, and in fact will be followed by muon transfer, so k_d will be subsumed in k_μ for the following discussion.

Stabilization of the complex cannot be ignored because it has a moderator dependence ($k_s[M]$). This might cause some confusion because $\sum k' = k'_e + k'_\mu + k'_s[M]$ is not constant when [M] is varied, so k_e and k_μ are not strictly independent of pressure if k_c is pressure independent. The variations are small, however, and can generally be ignored, except that $k_{exp} = k_e + k_\mu + k_s[M]$ should actually be *independent* of total pressure. Thus, equations (4.13), (4.27), and (4.31) for the relaxation rate are best represented as

$$\lambda = k_{exp}[X] + k_q[M] \tag{4.32}$$

with

$$k_{exp} = k_e + k_D = k_e + k_\mu + k_s[M] \tag{4.33}$$

with the relative amplitudes

$$\frac{A_s}{A_f} = \frac{k_\mu}{k_e} + \frac{k_s[M]}{k_e} + \frac{k_q[M]}{k_e[X]} . \tag{4.34}$$

Values for k_e and k_μ in table 4.4 are best interpreted as k_e and $k_\mu + k_s[M]$, respectively. Varying the moderator pressure can serve to elucidate the processes of stabilization and quenching.

4.8 Pressure Dependences

Besides varying the concentration of the dopant gas, studies were made varying the pressure (concentration) of the bath gas. Most of these were performed with neon because low pressure helium offers too little stopping power to the muons, limiting the experimentally

accessible pressure range. Table 4.1 shows a number of instances where the reaction rate constant k_{exp} was measured at two pressures, giving the same value in most cases, as is expected from the simple bimolecular model (4.12). There are only two instances of apparent variations: The $NH_3 + HeMu^+$ rate constant appears to decrease with He pressure, but the 1500 torr measurement was performed long before the 2280 torr measurement, without cold-trapping the helium; the earlier (high, 1500 torr) result is not particularly trustworthy. The other anomaly, CH_3F in 800 and 1400 torr Ne, was questioned in section 4.2. According to the simple model, $k_{exp} = k_c$ should not vary with pressure, and this is the observation in most cases, even for those, such as Xe in Ne, which gave results well below the capture (Langevin or AADO) predictions. It is possible that k_{exp} would decrease due to quenching, but that is not easily accommodated by simple competition kinetics. Results for xenon reported in this section and discussed further in chapter 6 give weight to the CH_3F and NH_3 results.

Other moderator dependences were measured by varying the moderator pressure for a single concentration of reactant. Since the observed relaxations do not have the extra components indicative of the more complex mechanisms, the following results were analyzed according to equations (4.32) and (4.33), where the (fast) relaxation rate, should increase linearly with pressure (i.e., moderator concentration [M]) for a given concentration of dopant, with slope k_q and intercept $k_{exp}[X] \approx k_c[X]$. Moreover, the relative amplitudes A_s/A_f should increase linearly with [M], following eq. (4.34). Table 4.6 lists the parameters determined by linear fits to the relaxation rates and amplitudes for a number of runs varying the moderator pressure with a constant concentration of neutral reactant. Although these values are not as extensive as those determined by varying concentrations of X (table 4.1), they do provide additional insight to the details of the reactions.

As predicted, the relaxation rates generally increase with added moderator, although the variation is small. But there is one obvious disagreement with the mechanism: for

Table 4.6 Results from Varying the Pressure at Fixed [X]

M^a	X	$[X]^b$	relaxations		amplitudes		
			$k_{exp}{}^c$	$k_q{}^d$	$k_\mu/k_e{}^e$	$\dfrac{k_s[X]+k_q}{10^{-5}k_e}{}^f$	$k_s{}^g$
Ne	NH$_3$	various^h	20.7 ± 2.2	14.0 ± 4.3	0.030 ± 0.030	10.0 ± 1.1	
Ne	Xe	44.5	5.91 ± 0.49	-12.3 ± 4.0	-0.482 ± 0.051	65.0 ± 4.6	
					0^i	8.16 ± 0.65	
Ne	Xe	14.4	9.10 ± 0.28	-6.66 ± 0.82	-0.002 ± 0.016	2.68 ± 0.48	6.32 ± 0.65
Ne	Xe	50.5	6.26 ± 0.38	-20.3 ± 2.9	0.066 ± 0.024	6.2 ± 2.3	4.74 ± 0.64
Ne	CH$_3$F	12.8	18.4 ± 1.8	5.5 ± 4.3	0.143 ± 0.054	40.9 ± 2.0	47.1 ± 6.8
He	CH$_3$F	6.06	28.7 ± 10.1	28 ± 13	0.78 ± 0.28	190 ± 40	460 ± 220
Ar	NO	32.5	2.8 ± 2.6	58 ± 34	0.34 ± 0.23	45 ± 29	-15 ± 11
Ar	NO	16.3	2.6 ± 3.0	34 ± 21	0.13 ± 0.38	46 ± 25	-14 ± 15

^{a} The moderator gas whose pressure was varied; also a component in the molecular ion MMu$^+$. All these results were measured at room temperature and fitted using equations (4.32), (4.33), and (4.34).

^{b} Concentration of the neutral reactant, X, in 10^{14} molec cm^{-3}.

^{c} The total rate constant, $k_{exp}\approx k_c$ in units of 10^{-10} cm^3 molec^{-1} s^{-1}, determined from the intercept of λ vs. moderator pressure p. Compare with values in table 4.1.

^{d} Given by the slope of λ vs. p; in units of 10^{-15} cm^3 molec^{-1} s^{-1}.

^{e} The (dimensionless) $p=0$ intercept of A_s/A_f vs. p.

^{f} 10^6 times $(k_s[X]+k_q)/k_e$ determined by the slope of A_s/A_f vs. p.

^{g} k_s in units of 10^{-30} cm^6 molec^{-2} s^{-1}, calculated from other values in this table. Using the values of k_e from table 4.4 gives similar results. $k_s=0$ is expected for NO in Ar because stabilization of ArMuNO$^+$ still leads to depolarization.

^{h} The three NH$_3$ concentrations gave scattered results; reported here is a simultaneous fit to all points.

^{i} Values from fits with the intercept constrained ≥ 0.

Xe in Ne there is a consistently *negative* pressure dependence of the relaxation rate, as shown in figure 4.9. It makes intuitive sense that increased quenching at higher pressures would reduce the rate of an endothermic reaction, but such behavior is hard to reproduce with a simple kinetic model. The first measurement ([Xe] = 44.5) deviates from the trend set by the latter two mainly in being shifted up, closer to the 50.5 values; if the trend in the slopes of the three lines can be believed, k_q becomes more negative with increasing Xe concentration. This particular result will be analyzed further in section 6.4. The inverse pressure dependence does agree with the variation in k_{exp} seen for CH_3F, but not with the constant value measured for Xe.

The value of $k_{exp} = 20.7 \times 10^{-10}$ $cm^3\,molec^{-1}\,s^{-1}$ for NH_3 (from the intercept of the simultaneous fit of λ vs. p) agrees moderately well with the value of 26.4 in table 4.1, but fitting λ vs. $[NH_3]$ for each of the four pressures independently and averaging the results gives the value of 26.6 reported for "various" pressures in table 4.1, in remarkable agreement with 26.4. The k_q for NH_3 in table 4.6 agrees well with the values in table 4.1,
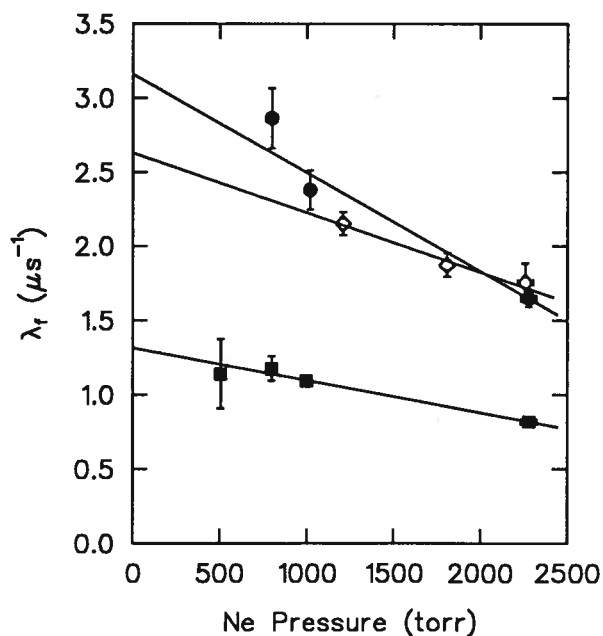
Figure 4.9 Neon pressure dependence of the fast relaxation rate for three concentrations of xenon: 50.5 (•), 14.4 (■), and 44.5 (◇) × 10^{14} $molec\,cm^{-3}$. The 44.5 line was measured in an earlier run period than the other two.

from the intercepts of λ_f vs. concentration, but are much higher than those in table 4.3, derived from the amplitudes vs. [NH$_3$].

The relative amplitudes A_s/A_f vary strongly with pressure — more strongly than would be expected from k_q alone. An example is shown in figure 4.7(c, d) for CH$_3$F + NeMu$^+$. This difference is attributed to stabilization of the complex, which affects the relative amplitudes, but not the overall relaxation rates. Values for k_s were calculated this way and are shown in table 4.6. (Note that these are the overall termolecular k_s, not the bimolecular k'_s.) All the values seem reasonable, although the ones for Xe are probably inflated due to the anomalously negative values for k_q. Even the slightly negative k_s values for NO in Ar are acceptable because stabilized ArMuNO$^+$ is paramagnetic and should still give depolarization; thus, a measured $k_s = 0$ is expected.

The first series of runs for Xe gave a significantly negative value for k_μ/k_e as a zero-pressure intercept of A_s/A_f, but the points are badly scattered; the other Xe measurements had intercepts consistent with zero, while the NH$_3$ results, measured at the same time as the anomalous Xe results, were extremely scattered. The Xe amplitudes gave reasonable results with the intercept (k_μ/k_e) fixed $= 0$, and the NH$_3$ results were all fitted simultaneously to give the quite acceptable results in table 4.6. The values of k_μ/k_e for Xe and NH$_3$ agree well with the low $k_D/k_e = (k_\mu + k_s[M])/k_e$ values listed in table 4.3 determined by the variation of amplitude with [Xe] and [NH$_3$].

The [M] $= 0$ intercepts of the amplitude for CH$_3$F give notably smaller values of k_μ/k_e in table 4.6 than the corresponding k_D/k_e values determined by varying the CH$_3$F concentration (listed in table 4.3 and visible in figure 4.7), indicative of a substantial k_s:

$$k_s = \left(\frac{k_D}{k_e} - \frac{k_\mu}{k_e} \right) \frac{k_e}{[M]} = 12.6 \pm 5.3 \times 10^{-30} \, \mathrm{cm^6 \, molec^{-2} \, s^{-1}} \,. \qquad (4.35)$$

This result is in disagreement with the value (47±7) in table 4.6, but the difference may not be significant given the uncertainties and the general level of variation. It is again noteworthy as well that k_{exp} for CH$_3$F appeared to vary with Ne pressure.

Both the relaxations and amplitudes of the NO/Ar data are too uncertain to say much about. This uncertainty is mainly due to the lower diamagnetic signal amplitude in Ar, resulting from epithermal Mu formation. Nevertheless, the values for k_s were near their expected values of zero.

These results are important in assessing the mechanisms and extents of excitation and quenching in these reaction systems. Most importantly, it was found that stabilization of the capture complex (k_s) could be important (for CH_3F and Xe) but not universally so. Additional measurements of quenching were performed with ternary mixtures of argon plus neon plus 'X' but these will be presented as part of the discussion of quenching in chapter 6. Presentation of other ternary mixture measurements is also deferred until they come up in discussion. The results of pressure dependence measurements have generally agreed with the results presented earlier, but have served to illuminate the importance of quenching the intermediate complex, as distinct from quenching of the initially excited ion.

4.9 Slow Relaxation Rates

Although the kinetics of the slow relaxation rates are unrelated to the mechanisms invoked to interpret the fast relaxations, it seems worthwhile at least to tabulate the slow relaxation results. Table 4.7 lists the slopes (k_{slow}) and intercepts (λ_0) for linear fits of the slow relaxation vs. reactant concentration in helium and neon at room temperature. A number of reactants are listed for which there was no 'fast' relaxation, so their overall relaxation rates were taken as λ_s; and there are some reactants missing from the table because they had slow components of very small amplitude. In about half the systems, the added reactant had a significant effect on the slow relaxation; these are marked by daggers and asterisks in table 4.7. The daggers signify that λ_0 was similar to the relaxation seen in pure moderator, while asterisks indicate that λ_0 shifted to a higher value (with or without a significant k_{slow}).

Table 4.7 Rate Constants for the Slow Relaxation in He and Ne Moderators

Reactant	Moderator	p^a	$k_{slow}{}^b$	$\lambda_0{}^c$	
Kr	Ne	1000	0.0010 ± 0.0027	0.01801 ± 0.00087	
Xe	Ne	1300	0.002 ± 0.022	0.0151 ± 0.0024	
Xe	Ne	1000	0.166 ± 0.092	0.0135 ± 0.0011	
CO	Ne	800	-0.0047 ± 0.0015	0.0301 ± 0.0010	†
O_2	Ne	800	0.038 ± 0.049	0.0330 ± 0.0015	
NO	Ne	800	0.72 ± 0.25	0.033 ± 0.015	†
N_2O	Ne	1000	0.012 ± 0.022	0.0139 ± 0.0011	
NH_3	Ne	800	-0.052 ± 0.038	0.0731 ± 0.0020	
NH_3	Ne	1300	-0.059 ± 0.054	0.0195 ± 0.0072	
CH_4	Ne	1000	0.0137 ± 0.0061	0.01530 ± 0.00080	
C_2H_4	Ne	1000	0.056 ± 0.019	0.0139 ± 0.0011	†
$(CH_3)_4Si$	Ne	800	0.0005 ± 0.036	0.0340 ± 0.0025	
CH_3NO_2	Ne	800	-0.102 ± 0.029	0.0316 ± 0.0014	†
CF_4	Ne	800	0.082 ± 0.046	0.095 ± 0.016	*
CH_3F	Ne	1400	0.000 ± 0.017	0.0323 ± 0.0036	
CH_3F	Ne	800	0.047 ± 0.057	0.0271 ± 0.0069	
Kr	He	2280	0.00095 ± 0.00036	0.01950 ± 0.00070	
Kr	He	1500	0.00024 ± 0.00084	0.0674 ± 0.0015	
Xe	He	1500	0.032 ± 0.031	0.0321 ± 0.0034	
CO	He	2280	0.00006 ± 0.00058	0.0171 ± 0.0015	
NO	He	2280	0.053 ± 0.014	0.080 ± 0.021	*
N_2O	He	1500	0.069 ± 0.023	0.0541 ± 0.0051	†
NH_3	He	1500	0.154 ± 0.052	0.0267 ± 0.0029	†
NH_3	He	2280	-0.23 ± 0.18	0.047 ± 0.017	*
$(CH_3)_4Si$	He	2280	-0.269 ± 0.074	0.0488 ± 0.0068	*
CH_3NO_2	He	2280	-0.189 ± 0.028	0.02050 ± 0.00080	†
CF_4	He	2280	0.111 ± 0.042	0.1145 ± 0.0069	*
CH_3F	He	1500	0.103 ± 0.017	0.0743 ± 0.0025	†

^{a} The moderator pressure in torr, at room temperature.

^{b} The slope of λ_s vs. reactant concentration, in $10^{-10}\,cm^3\,molec^{-1}\,s^{-1}$.

^{c} The zero-concentration intercept of the λ_s line, in μs^{-1}. When this differs substantially from the relaxation rate in pure moderator the number is followed by an asterisk (*); when the intercept is the same, but there is a substantial slope, a dagger (†) is shown.

Most of the rate constants are consistent with zero, but a few are significantly different, both positive and negative. (The negative values indicate k_{slow} is not really a rate constant.) The reproducibility is generally good for repeated pairs of reactant and moderator, with the possible exception of NH_3 in He. Nitromethane is the only reactant that gave a negative dependence in both He and Ne; CO and $(CH_3)_4Si$ each had a negative slope in Ne and He respectively. Although there are three negative values of k_{slow} listed for NH_3, all are consistent with zero. The "significant" slopes, both positive and negative, could be ascribed to the random distribution of values near zero, but there does seem to be a real effect on λ_0 in some cases. Strangely, this effect seems to be much stronger in helium bath gas than in neon; four of the reactants give increased λ_0 in He, with CF_4's being the highest, but only CF_4 has any visible effect in neon. This hints that the process responsible involves collisions with the moderator, e.g., $XMu^+ + He$ collisions.

Given the distributions of both positive and negative values for k_{slow}, and the lack of any real trend in 'significant' λ_0 values, there is no chance of elucidating the slow relaxation mechanism from the present results. If there *is* any contribution from collisional relaxation mechanisms, it is probably well masked by the inevitable relaxation due to magnetic field inhomogeneity. The apparent offsets (λ_0) can easily be attributed to parameter correlations when fitting two-component relaxations as opposed to single-component fits for the pure moderator runs.

4.10 Total Diamagnetic Amplitudes

Analysis of the *total* diamagnetic amplitudes, $A_f + A_s$, relates to processes occurring *during μ^+ thermalization* rather than to thermal kinetics, but the results prove interesting in themselves, and can even shed some light on thermal charge transfer forming Mu.

Since, as discussed in chapter 1, He and Ne have ionization potentials (IP) much higher than Mu (24.587 and 21.564 eV vs. 13.5 eV [81]), and subsequently have very low cross sections for epithermal Mu formation and high cross sections for Mu loss, all the

μ^+ polarization observed in these inert gases is in a diamagnetic environment [44, and this thesis]. As small quantities of more easily ionizable gas are mixed with the noble gas, some Mu is observed; and eventually, *only* Mu is observed. Figure 4.10 shows this effect for a number of gases used in this thesis, and demonstrates the different effect of each gas.

The thermalization of Mu and μ^+ in a mixture of X and M can be loosely represented by

$$P \; + \; \begin{matrix} M \\ \\ X \end{matrix} \quad \begin{matrix} \xrightarrow{\sigma_1[M]} & D \\ \xrightarrow{\sigma_2[M]} & Mu \\ \xrightarrow{\sigma_3[X]} & Mu \\ \xrightarrow{\sigma_4[X]} & D \end{matrix} \tag{4.36}$$
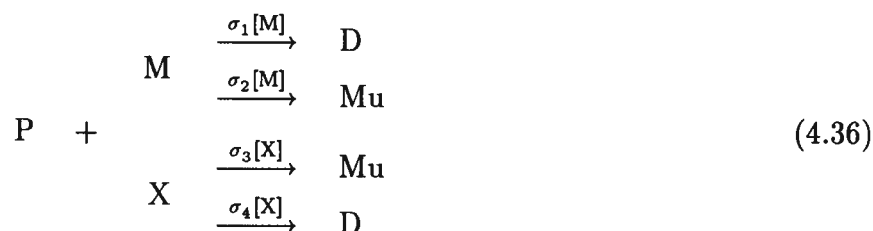
where the muon-bearing precursor P, at some arbitrary initial energy, can eventually
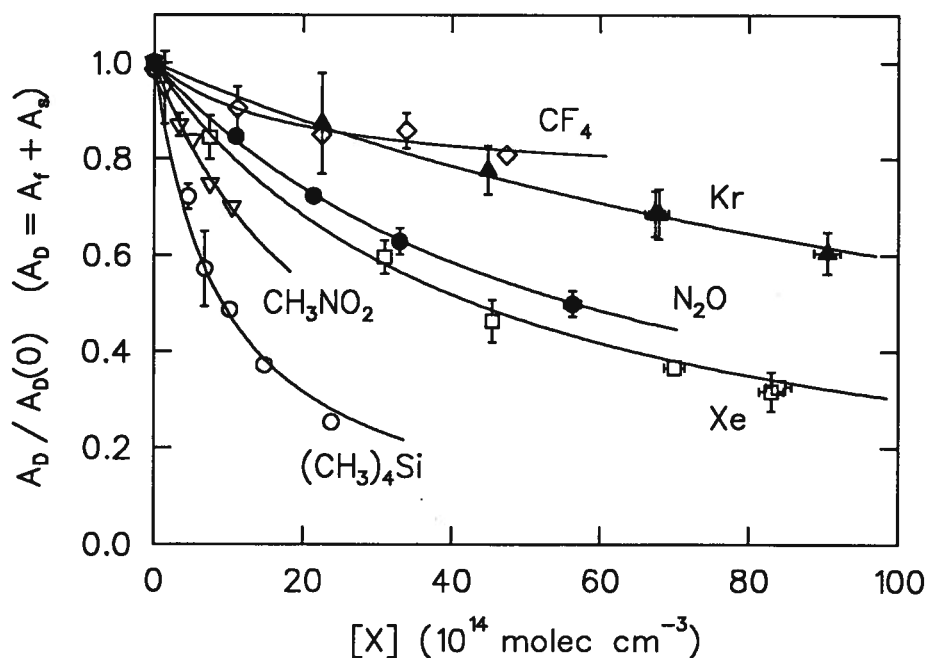
Figure 4.10 The variation of diamagnetic amplitude $A_D = A_f + A_s$ with reactant gas concentration [X] in neon moderator, due to Mu formation by the various reactants. The wide variety of Mu-formation effectiveness is reflected in the values of β varying from 0.35 for $(CH_3)_4Si$ (IP $= 9.8\,eV$) to 5.5 for Kr (IP $= 14.0\,eV$). Most $\beta_X \approx 0$ but for CF_4, $\beta_X = 3$.

thermalize as Mu or in a diamagnetic species D after collisions with the reactant gas X and the moderator gas M (M = He, Ne). For a diamagnetic P, particularly μ^+, the four collisional processes are: thermalization by moderator collisions (σ_1), muonium formation by charge exchange with M (σ_2), muonium formation by charge exchange with X (σ_3), and μ^+ thermalization or production of other diamagnetic species by collisions with X. Actually, σ_1 and σ_4 are cross sections only in the vague sense that σ_1, for example, is a velocity-independent rate constant for the kinetic thermalization 'reaction.' There are three possible processes that contribute to σ_1: for P $= \mu^+$ there are MMu$^+$ formation and simple μ^+ thermalization, and for P $=$ MMu$^+$ there is MMu$^+$ thermalization.

In order to do calculations based on this model of thermalization, the ratios of the rates or cross sections will be assumed constant over the energy range of interest. With this condition, the concentration of diamagnetic species after full thermalization is

$$[D]_\infty = \frac{[P]_0 \left(\sigma_1[M] + \sigma_4[X]\right)}{\sigma_1[M] + \sigma_2[M] + \sigma_3[X] + \sigma_4[X]} \, . \tag{4.37}$$

Since this equation is over-determined, and only the ratios of rates matter, one should define

$$A_D = A_0 \, [D]_\infty / [P]_0, \qquad \beta = \sigma_1/\sigma_3, \qquad \beta_X = \sigma_4/\sigma_3, \qquad \beta_M = \sigma_2/\sigma_1 \tag{4.38}$$

to give

$$A_D = A_0 \frac{\beta[M] + \beta_X[X]}{\beta[M] + \beta_M\beta[M] + [X] + \beta_X[X]} \tag{4.39}$$

where A_D is the experimental total diamagnetic amplitude, and A_0 is the total of all amplitudes: $A_0 = A_D + 2A_{Mu}$.

Equation (4.39) is still over-determined, however, and it can only be used to fit the experimental amplitudes if one or more parameters are known a priori. For pure helium and neon moderators, all the signal is diamagnetic, so $\beta_M = 0$ and $A_0 = A_D$ when [X] $= 0$. A similar assessment can often be made for β_X which should be given

Table 4.8 Fits of Total Diamagnetic Amplitudes at Variable Reactant Concentrations

Reactant	IP (eV)	M	p(torr)	T(K)	A_0	β^a	$\beta_X{}^b$
Kr	14.00	Ne	1000		0.2705 ± 0.0018	3.88 ± 0.55	0.165 ± 0.093
Kr		Ne	800		0.2826 ± 0.0010	5.54 ± 0.61	
Xe	12.13	Ne	1300		0.2537 ± 0.0038	1.85 ± 0.17	
Xe		Ne	1000		0.2664 ± 0.0021	2.7 ± 1.5	
Xe		Ne	800		0.2902 ± 0.0083	1.23 ± 0.10	
Xe		Ne	1400	445	0.3465 ± 0.0021	1.413 ± 0.036	
Xe		Ne	565	179	0.3563 ± 0.0027	2.085 ± 0.066	c
Xe		Ne	370	117	0.3252 ± 0.0032	1.131 ± 0.072	
Xe		Ne	1000	117	0.3353 ± 0.0022	1.07 ± 0.11	
CO	14.01	Ne	800		0.2850 ± 0.0020	6.42 ± 0.31	
O_2	12.06	Ne	800		0.284 ± 0.011	2.14 ± 0.76	d
NO	9.26	Ne	800		0.2844 ± 0.0022	2.90 ± 0.18	c
NO		Ne	800		0.2684 ± 0.0010	2.94 ± 0.26	
N_2O	12.89	Ne	800		0.2684 ± 0.0010	1.69 ± 0.11	
N_2O		Ne	1400	445	0.3460 ± 0.0021	1.854 ± 0.089	
N_2O		Ne	567	177	0.3539 ± 0.0030	1.81 ± 0.34	0.79 ± 0.40
NH_3	10.16	Ne	800		0.2535 ± 0.0029	1.60 ± 0.19	
NH_3		Ne	1300		0.3015 ± 0.0070	2.56 ± 0.71	
NH_3		Ne	1400	445	0.3454 ± 0.0019	1.713 ± 0.089	
NH_3		Ne	567	179	0.3534 ± 0.0028	2.91 ± 0.46	
CH_4	12.51	Ne	1000		0.2716 ± 0.0017	1.134 ± 0.055	c
C_2H_4	10.51	Ne	1000		0.2673 ± 0.0021	1.391 ± 0.092	c
$(CH_3)_4Si$	9.80	Ne	800		0.2853 ± 0.0025	0.353 ± 0.014	c
CH_3NO_2	11.02	Ne	800		0.2865 ± 0.0022	0.772 ± 0.042	c
CH_3NO_2		Ne	1300	406	0.2553 ± 0.0010	0.770 ± 0.042	
CH_3NO_2		Ne	740	223	0.2509 ± 0.0012	1.134 ± 0.081	
CH_3CN	12.19	Ne	1300	406	0.2552 ± 0.0010	0.419 ± 0.018	
CF_4	~13.	Ne	800		0.2847 ± 0.0023	2.7 ± 1.4	3.0 ± 1.1

Table 4.8 (continued)

Fits of Total Diamagnetic Amplitudes at Variable Reactant Concentrations

Reactant	IP (eV)	M	p (torr)	T (K)	A_0	β^{a}	β_X^{b}
CH_3F	12.47	Ne	1400		0.2823 ± 0.0053	1.64 ± 0.16	c
CH_3F		Ne	800		0.2575 ± 0.0360	0.50 ± 0.76	0.51 ± 0.17
CH_3F		Ne	1400	445	0.3469 ± 0.0020	0.959 ± 0.089	0.42 ± 0.11
CH_3F		Ne	700	179	0.3557 ± 0.0028	1.359 ± 0.056	
Kr	14.00	He	1500		0.2838 ± 0.0049	8.6 ± 2.6	0.47 ± 0.24
Kr		He	2280		0.3241 ± 0.0018	11.4 ± 1.6	0.37 ± 0.23
Xe	12.13	He	1500		0.2658 ± 0.0057	4.9 ± 2.9	c
CO	14.01	He	2280		0.3249 ± 0.0021	10.2 ± 4.7	2.9 ± 1.3
N_2O	12.89	He	1500		0.2762 ± 0.0066	7.4 ± 3.9	d
H_2O	12.61	He	2280		0.3256 ± 0.0016	3.02 ± 0.15	e
C_2H_6	11.52	He	2280		0.3246 ± 0.0019	2.63 ± 0.19	
C_2H_4	10.51	He	2400	398	0.2545 ± 0.0067	7.4 ± 7.4	e
$(CH_3)_4Si$	9.80	He	2280		0.3248 ± 0.0020	1.85 ± 0.54	
CH_3CHO	10.23	He	2400	406	0.2657 ± 0.028	0.88 ± 0.26	
CH_3CHO		He	950	163	0.2594 ± 0.0013	3.1 ± 1.1	d
CH_3F	12.47	He	1500		0.2778 ± 0.0038	$16. \pm 17.$	d
CH_3F		He	2400	398	0.2608 ± 0.0060	3.8 ± 1.5	e
CH_3F		He	800	128	0.2672 ± 0.0054	$9. \pm 15.$	e
$C_2H_4F_2$	11.87	He	2400	406	0.2753 ± 0.010	1.67 ± 0.53	
$C_2H_4F_2$		He	1330	208	0.2686 ± 0.0012	4.9 ± 1.3	d
$C_2H_4F_2$		He	830	148	0.2639 ± 0.0071	-2.6 ± 2.0	e

[a] The relative efficiencies of muon thermalization and molecular ion formation by the moderator versus muonium formation by the reactant X; $\beta = \sigma_1/\sigma_3$.

[b] The rate of formation of diamagnetic products by X relative to the rate of Mu formation; $\beta_X = \sigma_4/\sigma_3$. Blank entries are zero; either because the fit gave that result, or for the reason noted.

[c] The fit gave a negative β_X, so it was constrained to be zero.

[d] Poor results could not reasonably determine three parameters; β_X was fixed at its expected value of zero.

[e] Results were nearly constant and were fitted by a linear regression, taking $\beta[M] = $ −intercept/slope.

by the ratio of diamagnetic to muonium fractions in pure X. However, although Mu hot atom reactions generally give rise to $\sim$20% diamagnetic μSR signal in pure molecular gases [38,89,90], such reactions should be greatly suppressed in the present experiments by the vast excess of inert moderator. Thus, the muon fractions observed in pure X are probably not a good indication of β_X; instead, for molecules whose IP is below 13.533 eV, 100% Mu formation is expected at sufficiently high concentrations, so β_X can be set to zero when necessary. Table 4.8 lists the results of fits to equation (4.39), all of which had β_M set to zero, and some also had $\beta_X = 0$ assigned. The reproducibility and precision of the parameters are quite good for Ne moderator, but somewhat worse for He; the reproducibility of β is poor for CH_3F (in He and Ne) and for $C_2H_4F_2$.

The interesting parameter is β, which measures the efficiency of muon thermalization and/or molecular ion formation by M relative to muonium formation by X. For both Ne and He moderators, the values of β for CO and Kr stand out as the highest. This is is the expected result based on those molecules' high ionization potentials, which make Mu formation unfavorable. Is the converse also true? Although there are some low values of β, for $(CH_3)_4Si$, CH_3NO_2, and CH_3CN, there seems to be no correlation with IP. Why should CH_3CN (IP = 12.2 eV) have a low β while NO and C_2H_4 (IP = 9.3, 10.5 eV) do not? An answer may be that all these molecules can form Mu right down to thermal energies, so their IP's are not an issue. Instead, the low-β molecules are those with the highest polarizabilities and dipole moments, indicating that their capture (collision) cross sections for μ^+ determine their epithermal Mu-formation cross sections. This is what one would expect if the final Mu formation occurs at quite low energy, say below 1 eV.

An interesting exercise is to compare β in He and Ne for a given X. The average values of β were taken for each X & M pair, the ratio $\beta(He)/\beta(Ne)$ was taken for every X that had β determined in both He and Ne, and all those ratios were averaged to give $\langle \beta(He)/\beta(Ne) \rangle = 2.40 \pm 0.35$. So what is the meaning of this number? Recall $\beta = \sigma_1/\sigma_3$,

where σ_3 is independent of M, so

$$\frac{\beta(\text{He})}{\beta(\text{Ne})} = \frac{\sigma_1(\text{He})\,\sigma_3(\text{Ne})}{\sigma_1(\text{Ne})\,\sigma_3(\text{He})} = \frac{\sigma_1(\text{He})}{\sigma_1(\text{Ne})} \ . \tag{4.40}$$

Now it is time to define the 'thermalization reaction' and σ_1 better. The pseudo-cross section is best represented as a collision cross section σ multiplied by an energy loss factor ϵ, the average energy loss per collision, so $\sigma_1 = \sigma\epsilon$. This is related to the stopping power of the moderator, $dE/dx = \sigma\epsilon\,n\,v$, (the number density n is generally referred to as concentration [M] in this thesis). The energy range of importance is set by the energy of final Mu formation by X (the competing process), which for the mixtures in question probably extends from thermal up to a few eV kinetic energy [44,85,91, and mentioned above], but well below the energy for Mu formation in pure He (≈ 100 eV) and Ne (≈ 60 eV) [85], where no Mu reaches thermal energies. The characteristic energy is thus independent of whether the moderator is He or Ne, depending only on X. Since collisions with Ne and He should be elastic in the thermal-to-few-eV range, and assuming isotropic scattering, the energy loss is a purely kinematic factor,

$$\epsilon = E\left(1 - \frac{M^2 + m^2}{(M + m)^2}\right) \tag{4.41}$$

where M and m are the masses of the colliding species. For the case of molecular ion thermalization, $M \approx m$, and $\epsilon = E/2$. This is much too high to have a viable competition between Mu formation by X and thermalization by M — once the molecular ion is formed, it is thermalized in just a few collisions. For the case of μ^+ thermalization in neon, $\epsilon = 0.011\,E$, and in helium, $\epsilon = 0.052\,E$, so

$$\frac{\beta(\text{He})}{\beta(\text{Ne})} = \frac{\sigma_1(\text{He})}{\sigma_1(\text{Ne})} = \frac{\sigma(\text{He})\,\epsilon(\text{He})}{\sigma(\text{Ne})\,\epsilon(\text{Ne})} = 4.8\,\frac{\sigma(\text{He})}{\sigma(\text{Ne})} \ . \tag{4.42}$$

The elastic cross sections σ for protons in He and Ne have been measured [94] at low energies, and their ratio is likely indicative of the ratio for muons [85,86]. The cross sections level off and converge somewhat below 10 eV, and their ratios are $\sigma(\text{Ne})/\sigma(\text{He}) = 1.9$ at

1 eV and 2.8 at 10 eV, giving values for $\beta(\text{He})/\beta(\text{Ne}) = 2.4$ and 1.7 respectively. These are both in excellent agreement with the average value of 2.4 arrived at above, with the 1 eV value agreeing exactly! Given the approximations involved, though, it is not really possible to pin down the exact energy range, but it does indicate that the thermalizing species is a bare μ^+, reinforcing the picture of some Mu formation during μ^+ thermalization, followed at low kinetic energy by the remaining μ^+ attaching to a moderator gas atom to form a muonated molecular ion. The muon kinetic energy at the point of molecular ion formation is probably less than 0.5 eV, based on the discussion above and on studies of H^+–He scattering [158].

As an alternative to μ^+ thermalization in this scheme, there is the process of epithermal molecular ion formation, which might compete with Mu formation in a similar way. The cross sections for this association are not known, but the Langevin value is $\sigma_\text{L} = \pi q \sqrt{2/\alpha E}$ which would give $\beta(\text{He})/\beta(\text{Ne}) = 0.72$ — somewhat lower than measured. As just mentioned, the association reaction would not happen above 0.5 eV [158], whereas most Mu formation is already finished at this energy — the Mu that forms does so at higher energies than molecular ion formation. Although ion formation does not directly compete with the bulk of Mu formation, the Mu-formation regime will be terminated by creation of a molecular ion which is then thermalized very rapidly.

In an earlier paper [27], two ways of forming NeMu^+ were suggested:

$$\mu^+ + \text{Ne} \xrightarrow{\text{Ne}} \text{NeMu}^+ \tag{4.43}$$

$$\text{Mu}^* + \text{Ne} \longrightarrow \text{NeMu}^+ + e^-. \tag{4.44}$$

The latter process need not have a third-body collision because two separate products are formed, while the former requires collisions by the moderator to stabilize the NeMu^+ ion. However, since the Mu must be ionized in the second reaction, it must involve quite a high (kinetic) energy Mu, ~ 10 eV. The measurements presented in this section have shown that the first process, eq. (4.43), is clearly the correct one.

Chapter 5

KINETICS DISCUSSION

In the previous chapter, kinetics results for the reaction of $HeMu^+$, $NeMu^+$, $ArMu^+$, and N_2Mu^+ with a wide range of neutral species were presented. Various reaction models were suggested to interpret the results, with the simplest viable model being the mechanism (4.12) of competing collisional de-excitation, Mu formation, and μ^+ transfer from a rovibrationally excited MMu^+. More detailed models were considered, but they could not be used for data analysis without simplification. One supplement to the simple model was found necessary: stabilization of the capture complex, with the overall rate $k_s[X][M]$. With this addition, the mechanism agreed very well with the data, and this situation will be reaffirmed in the following discussion. Nevertheless there are some features of the measured data that require consideration of modified mechanisms, although the rates will still be parameterized in terms of the simplified model, equations (4.32)–(4.34).

Another topic to be covered is the role played by the initial excitation and subsequent quenching — processes which must be present but are not clearly defined by the data. Before dealing with the excitation of the reacting ions, though, it is necessary to show that the ions are indeed the muonated rare gases $HeMu^+$, $NeMu^+$, and $ArMu^+$.

5.1 Identification of the Reacting Ions

A restriction of the basic μSR method employed for this research is its inability to identify different closed-shell or diamagnetic species. In the more common study of Mu kinetics, the reacting species is definitely known to be the Mu atom based on its distinct spin precession frequency [97,99,103], although the reaction products must often be identified with reference to theory or the analogous H-atom experiments [30,82,102]. Identification of paramagnetic products has been achieved by observing level-crossing resonances [159–161], or by the characteristic precession frequencies if the reaction is faster than the precession period [159,162]. Diamagnetic products can be identified as such by RF resonance techniques [163], although this does not distinguish between different diamagnetic species since chemical shifts are usually far too small. None of these specialized techniques is amenable to the experiments at hand, and no product analysis was performed.

In the present measurements, the experimental signal is at a diamagnetic frequency so the initial species is not strictly determined. As described in chapter 1, there are four situations that give rise to such a precession signal: a bare μ^+, a (diamagnetic) μ^+ molecular ion, a muonium-substituted (diamagnetic) molecule, or a paramagnetic species such as Mu or a Mu-substituted radical undergoing very rapid spin exchange [164]. The results presented were already attributed to molecular ions, but the other possibilities can be considered now, and eliminated.

The case of fast spin exchange can be rejected immediately because there is no high concentration of paramagnetic molecules to exchange spin with. This is true even in the case of O_2 and NO dopants, which were always used in low concentration.

Muonium-substituted molecules, such as C_2H_5Mu, are commonly formed by reactions of molecular gases with Mu in the few-eV range, but while molecular species might account for the lack of relaxation in H_2 and C_2H_6 moderators, there are no such closed-

shell neutral molecules that could be formed in He, Ne, Ar, or even N_2. Even with the addition of reactive dopants to the inert gases, the preponderance of inert gas moderator would serve to minimize hot atom reactions with 'X' by thermalizing Mu through the energy range where those reactions occur. Furthermore, whatever effect the added reactants have, they could not contribute to the 100% diamagnetic signal in pure He and Ne moderators.

The case of a bare μ^+ could not be dismissed a priori, although it was deemed very unlikely [§1.3, and ref. 44] given muon affinities of 1.5 eV (for helium) and higher [22,144]. The general lack of reaction in Ar, N_2, H_2, and C_2H_6 indicates that, at least for these gases, the muon is not free; rather, it is bound in a molecular ion. This still leaves the possibility of a bare μ^+ in He and Ne, where the low polarizabilities and lower muon affinities might make μ^+ capture inefficient. The measured reaction rates, however, rule against this possibility. As seen in table 4.1, the reactions are consistently faster in He than in Ne, consistent with the higher collision frequency of lighter (and faster) $HeMu^+$. The expected ratio is given by the square roots of the reduced masses of each $X + MMu^+$ system; for a heavy neutral, the ratio is $k_{HeMu^+}/k_{NeMu^+} = \sqrt{20.1/4.1} = 2.2$ [see equations (3.7) and (3.13)], which agrees well with the values measured. A bare μ^+ would react at the same rate in both moderators, but much faster than actually seen: 6 times faster than $HeMu^+$ and a stupendous 13 times faster than $NeMu^+$. Since (as described in section 5.2) the present results agree with established capture theories, the reactive diamagnetic species in the rare gases and N_2 is clearly the muonated rare gas molecular ion, rather than a neutral molecule or bare muon.

5.2 Comparison With Theory

A comparison of the experimental (room temperature) rate constants is presented in tables 5.1 through 5.3. Table 5.1 compares the rates for non-polar neutral reactants with the Langevin predictions for both $HeMu^+$ and $NeMu^+$ ions. Cases where no reaction

was evident are noted. $ArMu^+$ showed no relaxation with Xe, H_2, O_2, or $(CH_3)_4Si$, and N_2Mu^+ showed none with C_2H_4 or O_2. Experimental results for dipolar molecules are compared with theoretical dipole capture rate constants, as calculated by various methods, in table 5.3. Table 5.2 lists the parameters used for calculating the theoretical rates; some of the parameters chosen should be commented on.

The polarizabilities are average-orientation (isotropic) values taken mostly from general references [150,165], which were determined by index of refraction and dielectric constant measurements. Judging by the disagreements among sources, there is substantial uncertainty in these values. The polarizability of $(CH_3)_4Si$ was not listed and so was calculated from the index of refraction [166] using the Lorentz and Lorenz (Clausius–Mosotti) equation [166]. A value of 7.37 $Å^3$ reported [150,165] for nitromethane is from the dielectric constant measured at too low a frequency [165], so a value of 4.94 was calculated from the index of refraction. Neither the polarizability nor the index of refraction were available for difluoroethane, so α was estimated from the trends in similar molecules. Note that the high-frequency polarizability calculated from the index of refraction is the more appropriate measure for ion–molecule capture because low-frequency measurements have a contribution from the dipole, which is treated separately in the capture theories.

The moments of inertia (I) were mostly derived from rotational spacings of spectra [167], but I for CH_3F, $C_2H_4F_2$, CH_3NO_2 and $(C_2H_5)_3N$ were calculated from bond lengths and angles [168,169]. For $(C_2H_5)_3N$, NH_3, and $C_2H_4F_2$ the axis of rotation chosen for calculating I was not the principal rotation axis, but one perpendicular to the dipole. This is a matter not dealt with in the literature, where a linear molecule is usually assumed, but it seems reasonable, except perhaps for the quantum treatments. In any case, the moment of inertia has only a small effect on the calculated rate constant so it is not critical that it be precisely known.

The comparison between theory and experiment in tables 5.1 and 5.3 reveals agreement over a wide range of polarizability, dipole moment, and exothermicity, with experi-

Table 5.1 Experimental Rate Constants[a] for Non-Polar Neutrals Reacting with HeMu[+] and NeMu[+] Compared with Langevin Capture Rates

Reactant	α (Å^3)[b]	M (amu)	HeMu[+]		NeMu[+]	
			k_{exp}	k_L	k_{exp}	$k_L{}^a$
Kr	2.484	83.80	c	18.65	0.56 ± 0.11	9.13
Xe	4.044	131.3	12.9 ± 2.5	23.59	5.35 ± 0.28	11.23
H$_2$	0.805	2.016	c	18.06	c	15.51
O$_2$	1.581	32.00	—	15.43	6.43 ± 0.37	8.36
CH$_4$	2.593	16.04	c	20.85	c	12.60
C$_2$H$_6$	4.47	30.07	c	26.04	c	14.23
C$_2$H$_4$	4.252	28.05	25.0 ± 1.8^d	25.51	18.6 ± 3.5	14.07
(CH$_3$)$_4$Si	12.0	88.23	31.1 ± 2.3	40.92	16.2 ± 2.4	19.97
CF$_4$	3.838	88.00	16.2 ± 1.4	23.15	6.59 ± 0.47	11.30

[a] All rate constants in 10^{-10} cm^3 molec^{-1} s^{-1}.

[b] Isotropic polarizability in Å^3, from [150,165], except for (CH$_3$)$_4$Si where the value of 12.0 was calculated from the index of refraction and density of the liquid [166].

[c] No relaxation observed. Other non-polar combinations that showed no relaxation are ArMu[+] plus Xe, H$_2$, O$_2$, and (CH$_3$)$_4$Si; and N$_2$Mu[+] plus C$_2$H$_4$ and O$_2$.

[d] Measured at a temperature of 398 K; all others were measured at room temperature, $\approx$ 295 K.

Table 5.2

Parameters for Dipole Capture Calculations

Neutral	α^a	$\mu_D{}^b$	M^c	I^c	$T_R(300)^d$
NO	1.70	0.153	30.01	0.01641	6.025
N_2O	3.03	0.167	44.01	0.06675	9.002
NH_3	2.26	1.47	17.03	0.00282	0.08666
H_2O	1.45	1.85	18.02	0.00301	0.03511
CH_3F	2.97	1.85	34.03	0.03274	0.07190
$C_2H_4F_2$	4.5	2.27	66.05	0.15930	0.07236
$(C_2H_5)_3N$	13.1	0.66	101.19	0.48600	2.492
CH_3CN	4.48	3.92	41.05	0.09115	0.02416
CH_3CHO	4.49	2.69	44.05	0.08250	0.05141
CH_3NO_2	4.94	3.46	61.04	0.13840	0.03419

[a] The isotropic polarizability of the molecule in $Å^3$, from [150,165], except for $C_2H_4F_2$ whose value was estimated from similar molecules, and CH_3NO_2 for which the value of 7.37 was rejected as too high (see text) and the value of 4.94 was calculated from the index of refraction and density of the liquid [166].

[b] The electric dipole moments [150,166], in Debye (10^{-18} esu cm).

[c] The masses (in amu) and moments of inertia (10^{-37} g cm^2). Values for I were taken from tabulated spectroscopic parameters [167] or calculated from molecular geometries [168,169]. In calculating I, an axis perpendicular the dipole was chosen rather than the axis of greatest I.

[d] The reduced temperature, $T_R = 2\alpha kT/\mu_D^2$, for $T = 300$ K.

Table 5.3

Comparison of Experimental Rate Constants with Various Capture Theory Predictions

Reactants	k_{exp}	k_{theory} [a]						
		LGS	LD	ADO	AADO	CT	VTST	SACM
$HeMu^+ + NO$	14.68 ± 0.36	16.07	23.46	16.75	17.30	16.95	19.06	10.93
N_2O	20.0 ± 2.2	21.02	28.93	21.65	22.62	21.92	24.72	14.01
NH_3	34.7 ± 1.4	19.34	93.52	37.37	39.60	43.32	47.89	39.88
CH_3NO_2	57.5 ± 4.4	26.52	188.40	68.65	92.54	84.83	96.81	82.96
CH_3F	33.0 ± 4.9	21.07	109.77	43.02	51.04	50.53	56.13	47.16
$C_2H_4F_2$	14.0 ± 4.9	25.25	131.20	51.45	68.28	60.41	67.10	56.75
H_2O	b	15.41	108.26	39.53	42.74	48.78	55.61	47.89
CH_3CHO	c	25.60	152.97	57.97	73.58	69.68	78.24	66.16
$NeMu^+ + NO$	8.63 ± 0.67	8.78	12.81	9.15	9.45	9.26	10.41	5.97
N_2O	11.1 ± 1.3	10.93	15.05	11.26	11.76	11.40	12.86	7.28
NH_3	26.6 ± 1.7	11.57	55.92	22.35	23.68	25.91	28.64	23.84
CH_3NO_2	41.6 ± 4.1	13.33	94.73	34.52	46.53	42.65	48.68	41.72
CH_3F	12.3 ± 3.3	11.32	58.95	23.10	27.41	27.14	30.15	25.33
H_2O	b	9.13	64.11	23.41	25.31	28.88	32.93	28.36
CH_3CN	b	13.45	111.12	39.29	51.76	49.60	57.43	49.28
$ArMu^+ + NO$	3.21 ± 0.16	7.38	10.76	7.68	7.94	7.78	8.75	5.01
NH_3	b	10.18	49.22	19.67	20.84	22.80	25.21	20.99
$(C_2H_5)_3N$	8.6 ± 4.0	15.82	27.13	17.21	19.43	17.39	19.43	12.79
$N_2Mu^+ + NO$	1.46 ± 0.14	8.02	11.70	8.35	8.63	8.46	9.51	5.45

[a] Capture rate constants, in 10^{-10} cm^3 molec^{-1} s^{-1}, calculated by the Langevin-Gioumousis–Stevenson method [110] (ignoring the dipole moment); by the equation of Moran and Hamill for a locked dipole [115]; by Su and Bowers' ADO and AADO methods [116,117]; from the parameterized classical trajectory calculations of Chesnavich et al. [120]; by variational TST [120]; and by the quantum SACM method of Troe [133].

[b] No relaxation was observed.

[c] Was not measured at room temperature.

mental rates at or below the capture limits. Figure 5.1 illustrates the agreement between the results for dipolar molecules and the dipole capture theories, plotting k/k_L vs. reduced temperature. The solid symbols show the results for $NeMu^+$ and the empty symbols are for $HeMu^+$. The results for high-dipole molecules are fairly widespread, extending from near the AADO line to below the Langevin line, while the low-dipole points (for N_2O and NO) are clustered near the common intersection at $k = k_L$. Figure 5.1 and table 5.3 show that the ADO predictions are closer, on average, to the experimental rates but this assessment is unduly influenced by results that are clearly lower than their capture limits. The AADO and CT calculations give the best upper limits to the measured rates, with CT slightly better than AADO.

Referring to tables 5.1 and 5.3, most of the results for both dipoles and non-dipoles are in fair to excellent agreement with the AADO or Langevin calculations respectively. Only the $C_2H_4 + NeMu^+$ reaction is significantly faster than theory, and there are many reactions that match or are marginally slower than the capture rates. However, a number of the reactions are significantly slower than their capture limits: xenon, krypton, tetrafluoromethane, methyl fluoride, and difluoroethane with the $HeMu^+$ and/or $NeMu^+$ ions, triethylamine with $ArMu^+$, and nitric oxide with both $ArMu^+$ and N_2Mu^+; the reaction of krypton with $NeMu^+$ is remarkably slow, and its reaction with $HeMu^+$ was not seen. There is no general relationship between this shortfall and the reaction exothermicity (table 4.2), except for the Kr reaction which is particularly slow and is endothermic even for a bare μ^+. There might be a slight tendency for the endothermic (from the molecular ion ground state) reactions to be slow (Xe, CF_4, CH_3F) but this 'trend' is violated by the endothermic N_2O reactions occurring at the capture limit and by the exothermic $C_2H_4F_2$ reaction which is even slower than the Langevin capture rate! This independence from ground-state exothermicity confirms the presence of sufficient excitation energy to allow these reactions to proceed unhindered by a need for additional activation processes. This conclusion is also mandated by the majority of the studied reactions which proceed at
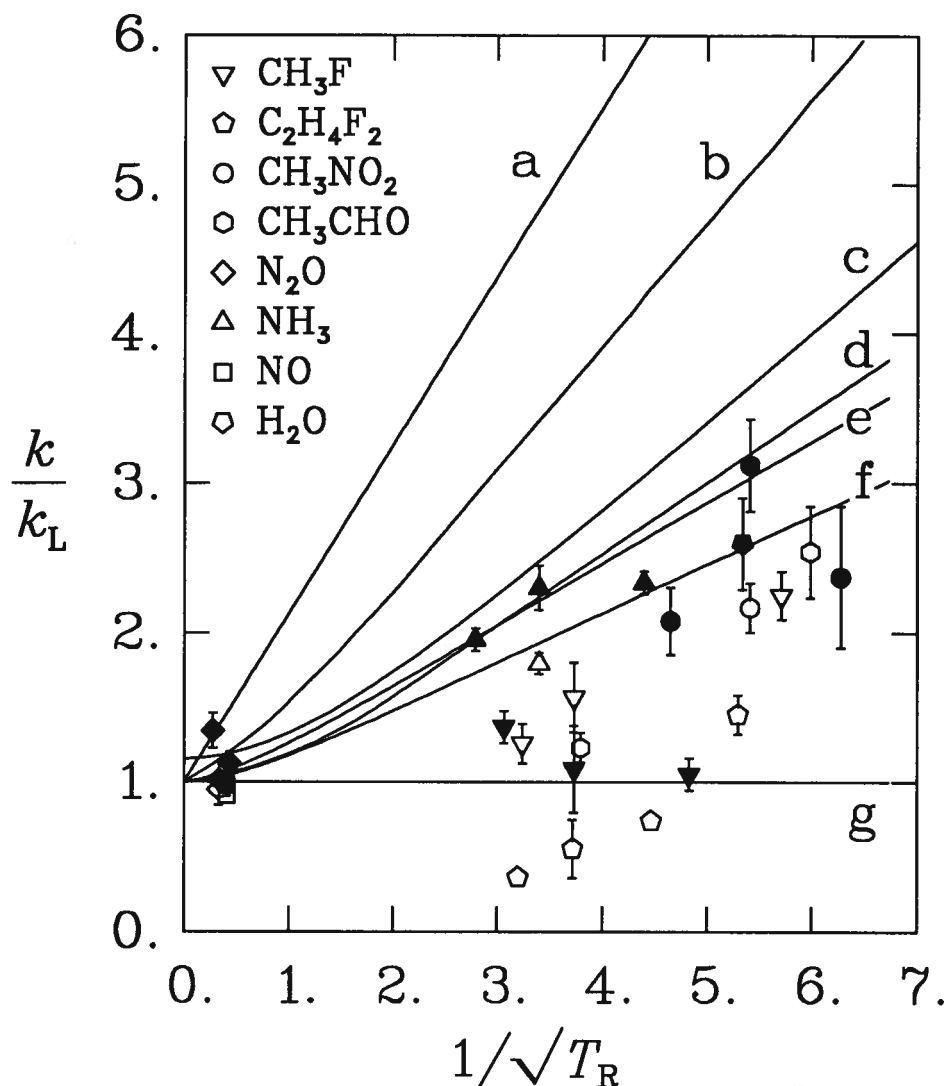
Figure 5.1 Plot of experimental results, expressed as k/k_L vs. $1/\sqrt{T_R} = \mu_D/\sqrt{2\alpha kT}$, for $HeMu^+$ and $NeMu^+$ reacting with various dipoles at various temperatures, superimposed on theoretical curves for various theories of ion–molecule capture. The neutral reactants are identified by the symbol shapes (see legend); empty symbols are shown for $HeMu^+$ and solid symbols for $NeMu^+$. The theoretical curves are: a) locked dipole [115]; b) Barker and Ridge average energy treatment [119]; c) variational transition state theory [120]; d) parameterized trajectory calculations [118]; e) AADO theory [117]; f) ADO theory [116,117]; g) Langevin–Gioumousis–Stevenson [110]. The classical trajectory and AADO lines (d,e) appear to give the best upper limit to the reaction rates. Most neutrals react at near this capture limit, but CH_3F and $C_2H_4F_2$ react considerably more slowly.

their collision (capture) rates.

The fact that all the reactions seen for $ArMu^+$ and N_2Mu^+ are relatively slow raises the possibility that the reacting ions are clustered with additional Ar or N_2, e.g., Ar_2Mu^+ or N_4Mu^+, which give a lower collision rate due to their greater masses. Such clusters are well known for the corresponding H ions [64,149,170,171] as well as for the unprotonated ions [26,145,172–177]. It is clear that clustering was not significant for the $HeMu^+$ and $NeMu^+$ ions because many of the neutrals reacted at the expected capture rate, but clusters might be more prevalent for Ar and N_2 than for unpolarizable He and Ne, as supported by the observation that the termolecular formation rate of Ar_2H^+ is three times the rate of He_2H^+ formation [172] (although it could also be argued that a factor of 3 is not enough to make a major difference). The stability of Ar_2Mu^+ might also provide an explanation of why no reaction was seen for $(CH_3)_4Si$ in argon, where charge transfer is exothermic from the ground state of $ArMu^+$. Such cluster ions cannot totally account for the slow rates in Ar and N_2 though — even with large clusters, the reduced mass of the ion–neutral pair is not increased enough to give rates as low as seen, especially for NO in N_2 where the greatest decrease in capture rate expected from ion clustering is a factor of 1.4 whereas $k_{AADO}/k_{exp} = 5.9$. Thus, the differences cannot be due to heavier ions undergoing capture; instead, when k_{exp} falls below the predicted rate, the reaction is not capture limited.

A remote possibility for the low reaction rates is that the simplifications (point charge, etc.) necessary for the capture predictions are too extensive for those species. The actual capture rate could be reduced due to steric repulsion or other 'chemical' interactions which could extend beyond the capture radius of a large molecule. While this could conceivably apply to the larger molecules like $C_2H_4F_2$ it is untenable for Xe and Kr, and the muonated (protonated) rare gases are excellent approximations to point-charge ions — the combination of small closed-shell ions and neutral atoms (or small molecules) is optimum for having strict separation of capture and 'chemical' interactions. Another

unlikely explanation for reaction rates below the capture limit is that the reactions are activation limited rather than collision limited. The independence of reaction rate from endothermicity noted above discredits this supposition, as do the temperature dependences to be discussed in section 5.7.

A different explanation for the slow-reaction cases may be found in resonant charge transfer and Franck–Condon overlaps [130,178,179]. The dissociative charge-transfer reaction (4.2) can be represented as two half-reactions [180]:

$$X \longrightarrow X^+ + e^- \quad \text{(ionization)} \tag{5.1}$$

$$MMu^+ + e^- \longrightarrow M + Mu \quad \text{(dissoc. recombination)} \tag{5.2}$$
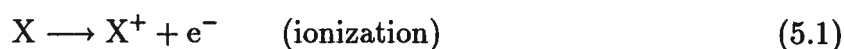
the direct ionization of the neutral X, and the dissociative recombination (neutralization) of the MMu^+ ion. For the overall charge transfer to be resonant, the energetics of the half-reactions must cancel, but resonance is not expected to be important because the dissociating $M + Mu$ provides a continuum of available states. On the other hand, the rates of each half-reaction could be heavily influenced by the Franck–Condon overlap between the initial and final states. Each half will be considered in turn; first the dissociative recombination, then the ionization.

The potentials for $HeMu^+$ and $NeMu^+$ have their minima at a distance well within the repulsive region of the dissociative $He + Mu$ and $Ne + Mu$ potentials (see figure 1.1), so for a (vertical) electron-jump transition, the overall reaction is less exothermic (or more endothermic) than expected. The lost energy goes into translational motion of the He (Ne) and Mu. This effect is less at greater internuclear separations, so the charge-transfer reaction may only be possible at the largest separation in the $HeMu^+$ vibration. The result is a low transition probability, or Franck–Condon factor. FC factors have often been cited to explain charge-transfer reaction rates [178,181–184], although usually for transitions between two bound states. The FC effect is applicable to a ground state

ion or to a rovibrational excited state, whichever needs to be at the far end of its vibrational level for a vertical transition which is part of an overall exothermic reaction. Since vibrational excitation not only increases the available energy but stretches the bond, excitation does double duty in promoting charge-transfer reactions, but since there was no observable relationship between reaction endothermicity and rate, FC factors must have little importance in the dissociative recombination half of the charge-transfer reaction.

Franck–Condon factors also apply to the ionization of the neutral molecule reactants, such as C_2H_4, CF_4, CH_3F, etc., but excluding the atomic reactants Xe and Kr. The slow reactions seen for the fluoro-alkanes might indicate low FC factors, reflecting unfavourable direct ionization. However, there is *no measurable* FC overlap between CF_4 and any rovibrational state of CF_4^+ [144,185] (which is why the ionization potential of CF_4 is not accurately known), yet the charge-transfer reaction occurs for both $HeMu^+$ and $NeMu^+$, albeit more slowly than the Langevin prediction. Since there is no identification of products, it might be argued that the CF_4^+ is produced with energy above its dissociation limit, but the reaction to produce ground-state CF_4^+ is already endothermic (i.e., it requires initial excitation) so there is little chance of producing excited products. (Note that the neutral reactants have the energy distribution of the ambient temperature.) Since the observed reaction rate is within a factor of two of the Langevin rate, the FC overlap (or lack thereof) must not be very important. This is the situation for many other ion reactions [186–190], usually indicative of transient complex formation as opposed to long-range electron jumps, although FC factors are sometimes unimportant even for long-range direct reactions [186].

The Franck–Condon effect operates on the unperturbed reactants, and requires an instantaneous transition to products; but is not applicable when there is a slow (adiabatic) transformation of a capture complex from reactants to products, or if the complex distorts the reactants sufficiently. Since neither the neutralization of the muonated ion nor the ionization of the reactive neutral (especially Xe and CF_4) appear to be controlled

by FC overlaps, the observed charge-transfer reactions must be predominantly mediated by ion–molecule capture. This is obvious for the many cases that proceed with rates at or near the capture limit, but, with the arguments given above, now seems to be the case even for the slow reactions. The explanation for these cases is more likely found within the capture mechanism involving complex formation, stabilization, and/or breakup.

Further support for the capture mechanism is the observation of *both* charge transfer and muon transfer. If charge transfer occurred by long-range electron jumps, it would tend to prohibit muon transfer. Instead, charge exchange seems to occur at the short ranges where muon transfer is also possible.

5.3 Unreactive Neutrals

In the previous chapter, table 4.2 gave a succinct summary of which ion/molecule combinations showed no reactivity. To it may be added the non-reactive combinations of ammonia, triethylamine or nitric oxide in hydrogen; ammonia or nitric oxide in ethane; and ethylene, carbon monoxide, or oxygen in nitrogen. That is not to say that $k_c = 0$, or even that $k_e + k_D = 0$ for these reactants, but rather that $k_e \ll k_D$, possibly with $k_e = 0$; see eqs. (4.12) and (4.34). Although charge exchange (k_e), quenching (k_q), and other (k_D) reactions contribute to the signal's relaxation rate, it is *essential* that charge exchange occurs if any relaxation is to be observed, for it is this process which is responsible for the loss of spin coherence and hence muon depolarization. As revealed in table 4.2 and the accompanying text, the energetics of charge transfer fall into three broad categories, with unreactive combinations in each.

Charge transfer is endothermic for H_2, CO, and Kr even with a bare μ^+, so no depolarization was expected for these, and none was observed except for Kr + NeMu$^+$, and that reaction was very slow.[1] It is tempting to explain this one reaction in terms of Xe

---

[1] Looking at it another way, the NeMu$^+$ + Kr reaction is remarkably *fast* given that the rate of the endothermic Mu formation reaction should be *zero*.

impurity in the Kr, but measurements in both He and Ne were made successively with the same Kr, and no reaction was seen in He, so the relaxation must really be due to the $Kr + NeMu^+$ reaction. Except for this anomaly, the lack of charge-transfer reactions for H_2, CO, and Kr meets expectations. Note that the *muon*-transfer reaction is exothermic in all cases, even the combination of $H_2 + ArMu^+$, so muon transfer likely proceeds even when there is no charge transfer to cause depolarization.

For the more easily ionizable neutral reactants, charge transfer is expected for a bare μ^+, but it is still endothermic for a ground state molecular ion. Yet charge transfer was seen for a number of such neutral species, and this was interpreted in section 4.3 as an indication that the molecular ion reacts from a rovibrationally excited state. However, not all such neutrals gave relaxation; CH_3CN, H_2O, and CH_4 showed no reaction with $HeMu^+$ or $NeMu^+$, and Xe, O_2, and NH_3 gave none with $ArMu^+$. In the latter case, this probably indicates that $ArMu^+$ is in its ground state, as *nothing* reacted with $ArMu^+$ except triethylamine and nitric oxide, for which charge transfer is exothermic from the $ArMu^+$ ground state. This is to be expected because Ar is a much better quencher of ions than either He or Ne [79,153,154]. The non-reactions with the He and Ne ions are less easy to explain because of the many similar reactions that *were* observed. It does not seem reasonable that H_2O and CH_4 would be excellent quenchers of $(NeMu^+)^*$ and $(HeMu^+)^*$ while NH_3 is not. The literature on collisional quenching of molecular ion vibrational excited states indicates that these particular molecules can be expected to exhibit wide variations in quenching rates; e.g., relative to NH_3 and C_2H_4, both H_2O and CH_4 are an order of magnitude less efficient in quenching $(NO^+)^*$ [154,155] but they are both relatively efficient at quenching $(O_2^+)^*$ [156], as is CH_4 in quenching $(ArH^+)^*$ [191]. In the absence of any evidence for superlative quenching by CH_3CN, H_2O, and CH_4, another explanation for their non-reactivity must be sought.

Quenching should not even be considered for the third class of reactants: those for which charge transfer is exothermic even for a ground state molecular ion. Ethane showed

no reaction with HeMu$^+$ or NeMu$^+$ although charge transfer is exothermic, and the same is true for $(CH_3)_4Si$ (not) reacting with ArMu$^+$. For both these exothermic cases and the mildly endothermic cases above, charge transfer has somehow been suppressed relative to muon transfer.

Are the cross sections for charge transfer in the case of X = CH_4, C_2H_6, CH_3CN, and H_2O likely to be appreciably smaller than those of the other reactants investigated? There are no equivalent measurements on NeH$^+$ or HeH$^+$ to compare with, although charge transfer (often accompanied by fragmentation) has been seen with a variety of other ions [57,147,148,192–196] so it is unlikely to be something inherent to those particular molecules. Near thermal energies, one may expect the total cross sections for charge neutralization for a bare muon to be comparable to those for the proton [44,86] The measured proton cross sections [197] give no indication, e.g., that $\sigma(CH_4) \ll \sigma(NH_3)$; indeed, if anything, the reverse may be the case, although the large uncertainties (factors of 10!) in the low energy proton cross sections should be kept in mind.

The present measurements of the total diamagnetic amplitudes give some indication of the epithermal charge exchange cross sections for μ^+ with the neutral molecules. The trends in total amplitudes were presented in section 4.10, with the results listed in table 4.8. The parameter β is an indication of the relative efficiencies of muon thermalization and molecular ion formation by the moderator vs. muonium formation by the reactant, so a high value for β implies relatively inefficient epithermal charge exchange, and vice versa. Particularly high values for β were measured for Kr and CO in both He and Ne, a finding which meets expectations based on the high ionization potentials of those neutrals, and which is also reflected in the lack of thermal charge-transfer reactions (with generally no relaxation seen). On the other hand, the other non-reactive molecules, CH_4, C_2H_6, CH_3CN, and H_2O, reveal no particular trend in β; in fact, CH_3CN gives a particularly *low* value for β, indicating a large epithermal charge exchange cross section.

There seems to be no established trend in the ion–molecule literature that proton

transfer from protonated ions (including the protonated rare gases) to CH_4, C_2H_6, or H_2O is anomalously fast [25,26,147,148,191,198], though there is one measurement of enhanced proton transfer for $H_2^+ + H_2O$ [199]. Proton transfer of ArH^+ with CH_4, for example, is fairly slow [198]. Although proton transfer for these molecules is usually seen without any charge transfer, the same is true for most other molecules, so that does not necessarily imply a predominance of the muon-transfer reaction. If there is any correlation between proton affinity and proton (muon) transfer rate constants [25,195], one might expect NH_3, with a proton affinity of 9 eV [22], the largest for the reactants sampled (except for $(C_2H_5)_3N$), to exhibit the fastest muon transfer ($k_\mu \gg k_e$), contrary to observation.

Although there seems to be no indication of enhanced *proton* transfer to CH_4, C_2H_6, CH_3CN, and H_2O, there is a possibility of enhanced *muon* transfer due to quantum tunnelling. Tunnelling has been shown to be very important in studies of muonium reactivity [29–31], with isotope effects (k_{Mu}/k_H) as high as 40 [30]. If there is a propensity for the μ^+ to tunnel through a barrier to internal rearrangement of the complex, then muon transfer could be greatly enhanced at the expense of charge transfer, and no relaxation would be seen. This type of tunnelling has no precedent in conventional measurements, although hydrogen (H and H_2) tunnelling through the rotational barrier has been implicated in some fragmentation reactions following ion–molecule association [32–35]. This effect probably favours the emission of Mu from the capture complex; i.e., it promotes the dissociative charge-transfer reaction rather than the muon-transfer reaction! Perhaps such Mu tunnelling contributes to the general predominance of charge transfer for the reactions studied, and it is somehow suppressed in the non-reactive cases. The calculated potential [200] for triplet H_3^+ has three minima, and tunnelling between them is an important process. Similar barriers for intra-complex rearrangement leading to muon transfer could be particularly narrow for CH_4, C_2H_6, CH_3CN, and H_2O, in which case muon transfer could be selectively enhanced for these molecules.

Other means of enhancing muon transfer at the expense of charge transfer are energy

dispersal and fragmentation of the muon-transfer product. Since muon transfer is quite exothermic for all the reactants studied, there might be a problem with energy disposal for small molecules, hindering this channel. Large complexes like $NeMuC_2H_6^+$ disperse excitation energy among many vibrational modes, making it less likely to be concentrated for breaking the bond to Mu. Also, proton transfer to C_2H_6 is immediately followed by H_2 elimination from $(C_2H_7^+)^*$, which is not itself observed [25,201] and the same thing undoubtedly happens for Mu. With fragmentation into such diamagnetic products as $C_2H_4Mu^+$ and HMu, muon transfer could proceed without any back-dissociation as might occur for $XeMu^+$. Fragmentation reactions are expected to occur, but if energy disposal is the real limitation on muon transfer, it is not clear why charge transfer was observed for other large molecules like $C_2H_4F_2$, $(CH_3)_4Si$, and CH_3NO_2.

Returning to table 4.3, it shows that the highest measured value for k_D/k_e ('k_μ/k_e') was 2.3 (CH_3F in He, followed closely by Kr in Ne). As long as moderator quenching is relatively slow ($k_q[M]$ is small), ratios as high as $k_D/k_e \approx 5$ should give measurable relaxation; higher than this, the relaxing component might well be undetectable. Thus, the muon-transfer reaction (or quenching by the neutral) would need only moderate enhancement for there to be no reaction seen.

5.4 Ternary Mixtures: Monitor Gas Measurements

In order to see that there was *some* reaction with the apparently non-reactive neutrals, and to determine if their muon-transfer rates were enhanced beyond the capture rate, measurements were made with additional reactive gas (i.e., one that *does* undergo charge exchange). The extra reactant gives a visible relaxation which facilitates measurement of muon-transfer rates. This is the monitor ion method, typically used to measure the quenching rate of excited molecular ions [79,153–157,202–204]; here, though, the appearance of the monitor ion is not measured, but the disappearance of the reactant ion.

Assuming there is no interference between the two neutrals X and Y, the simple model (4.12) is applicable, and the experimental reaction rate is the total of all rates:

$$\lambda = (k_e^X + k_D^X)[X] + (k_e^Y + k_D^Y)[Y] + k_q[M] \tag{5.3}$$

and the relative amplitudes are given by

$$\frac{A_s}{A_f} = \frac{k_D^X[X] + k_D^Y[Y] + k_q[M]}{k_e^X[X] + k_e^Y[Y]} . \tag{5.4}$$

When the monitor gas concentration [Y] is kept constant, the relaxation rate is fitted by a straight line having the slope $k_c^X = k_e^X + k_D^X$, and the intercept $(k_e^Y + k_D^Y)[Y] + k_q[M]$. The relative amplitudes cannot be fitted linearly, as they were for binary mixtures, but there is no difficulty in fitting them to the three parameters $k_e^Y[Y]/k_D^X$, $(k_D^Y[Y] + k_q[M])/k_D^X$, and k_e^X/k_D^X. (The actual rate constants cannot be determined from eq. (5.4) alone, and the ratio k_e/k_D was chosen for fitting because k_D/k_e tends to infinity for reactants such as CH_4.) Plots showing these fits to the relaxations and amplitudes (A_f/A_s) for Y = NH_3 and X = C_2H_6 and H_2O are given in figures 5.2 and 5.3. Measurements were also made for X = CH_4, H_2O, and NH_3 with Y = Xe; as summarized in table 5.4.

Two different monitor gases were chosen: xenon and ammonia. Xe has the advantage of being inert, but might suffer from complications, especially due to quenching, while NH_3 might be susceptible to clustering with H_2O. The measurement of $H_2O + NeMu^+$ was performed with both monitors, during different run periods, to check for interferences, and the two results were quite different (table 5.4), with the rate constant measured for the H_2O/NH_3 mixture agreeing quite well with the AADO prediction, and the H_2O/Xe mixture giving an anomalously low rate. If the interfering side reaction

$$NH_3 + H_2O \longrightarrow NH_3 \cdot H_2O \tag{5.5}$$

was occurring, the observed rate constant would be expected to be reduced for NH_3 due to the reduced concentration of free NH_3 and H_2O. Instead, it is the reaction measured with the Xe spectator that is anomalously slow, and there is no evidence for clustering.
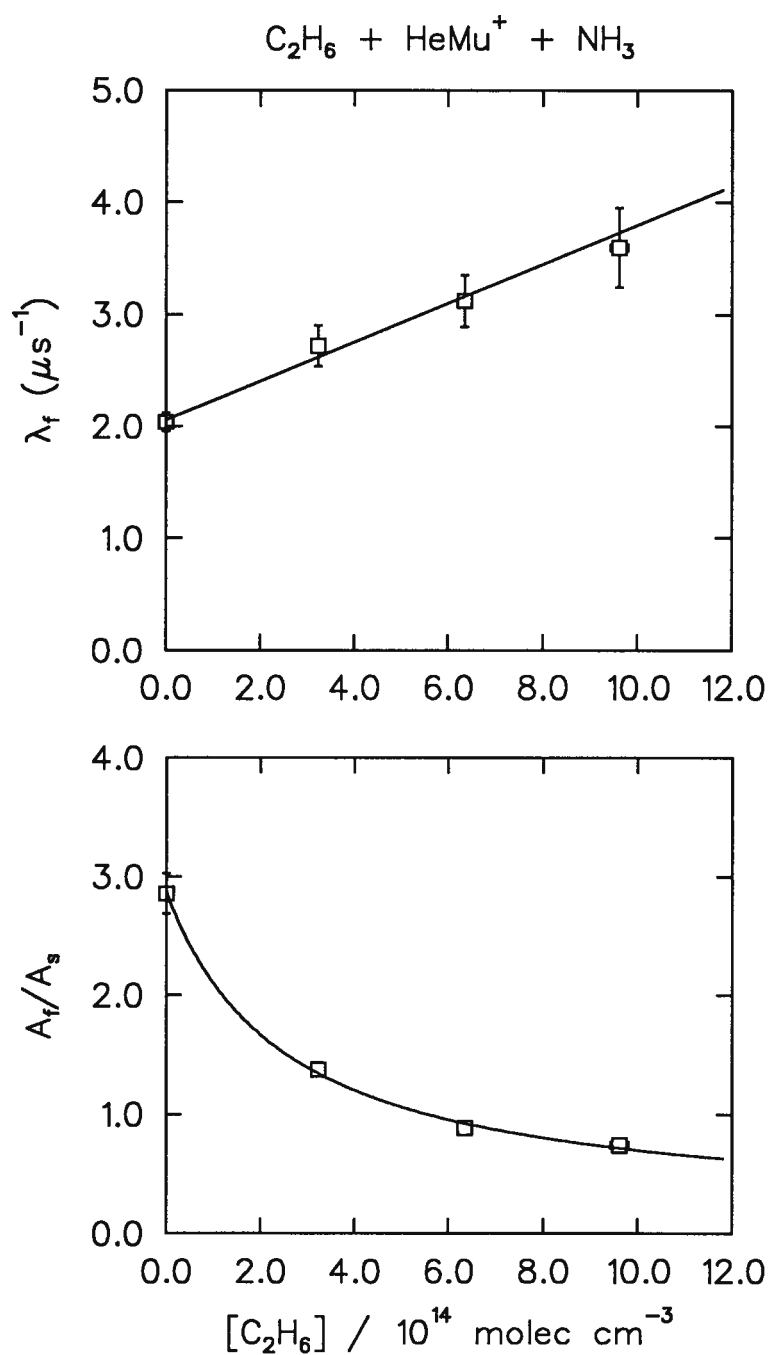
Figure 5.2 Relaxation rates (top) and relative amplitudes (bottom) for the reaction of C_2H_6 with $HeMu^+$ in the presence of 5.08×10^{14} molec cm^{-3} of NH_3. The slope of λ_f gives $k_c = 17.4 \pm 2.6 \times 10^{-10}$ cm^3 molec^{-1} s^{-1}, and the high-concentration asymptote of A_f/A_s is $k_e/k_D = 0.15 \pm 0.11$. Note that A_f/A_s is plotted here, whereas A_s/A_f is shown in figures 4.7 and 6.2.
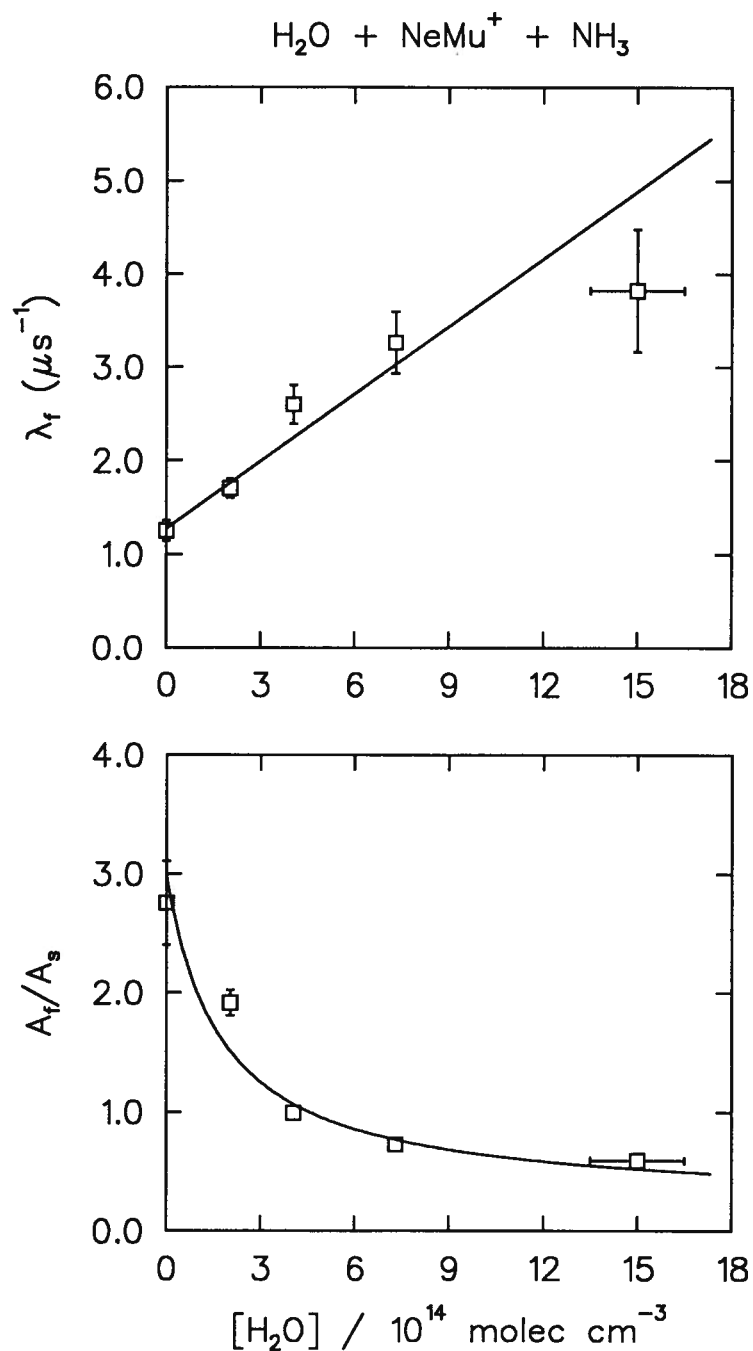
Figure 5.3 Relaxation rates (top) and relative amplitudes (bottom) for the reaction of H_2O + $NeMu^+$, with 6.12×10^{14} molec cm^{-3} of added NH_3 monitor gas. The fits give $k_c = 23.7 \pm 2.8 \times 10^{-10}$ cm^3 molec^{-1} s^{-1}, and $k_e/k_D = 0.23 \pm 0.09$ ($k_D/k_e = 4.4 \pm 1.6$). Note that the plot of the amplitudes shows A_f/A_s, which is the reciprocal of what is plotted in figure 4.7.

Table 5.4 Results for Ternary Mixtures Employing a Reactive Monitor Gas

Reagent (X)	CH_4	C_2H_6	H_2O	H_2O	NH_3
Ion	$HeMu^+$	$HeMu^+$	$NeMu^+$	$NeMu^+$	$NeMu^+$
Moderator	He	He	Ne	Ne	Ne
Pressure / torr	1500	1500	800	800	800
Monitor (Y)	Xe	NH_3	NH_3	Xe	Xe
$[Y]^a$	11.1	5.08	6.12	10.0	10.0
$k_c^{X\,b}$	22.8 ± 8.0	17.4 ± 2.6	23.7 ± 2.8	13.4 ± 1.9	17.7 ± 1.0
k_L, k_{AADO}	20.85	26.04	25.31	25.31	23.68
$k_c^Y[Y]+k_q[M]^c$	2.51 ± 0.19	2.056 ± 0.078	1.275 ± 0.078	0.880 ± 0.023	0.869 ± 0.028
k_e^X/k_D^X	0^d	0.15 ± 0.11	0.23 ± 0.09	0^d	2.7 ± 0.9
k_D^X/k_e^X	∞^d	6.5 ± 4.8	4.4 ± 1.6	∞^d	0.37 ± 0.13
k_D^X/k_e^Y	0.91 ± 0.19	0.70 ± 0.13	1.16 ± 0.17	0.255 ± 0.013	0.51 ± 0.23
$k_D^{X\,e}$	8.6 ± 2.6	21.2 ± 4.1	22.4 ± 3.7	1.39 ± 0.10	2.8 ± 1.3

^{a} The concentration of the monitor gas, in 10^{14} molec cm^{-3}.

^{b} Total rate constant ($k_c = k_e + k_D$) for the reaction of the ion with the reagent gas, in 10^{-10} cm^3 molec^{-1} s^{-1}. For these reagents (except NH_3), $k_e \ll k_D$ so $k_c \approx k_D = k_\mu + k_s[M] \approx k_\mu$.

^{c} The intercept of λ_f vs. [X], in μs^{-1}, representing the reaction rate with the monitor gas at its fixed concentration [Y] plus a small contribution by moderator quenching.

^{d} In two cases the ratio k_e/k_D was fixed to zero: For methane, the parameter was completely undetermined by the data and so $k_e/k_D = 0$ was chosen based on the absence of any relaxation for $CH_4 + HeMu^+$. For water vapor, k_e/k_D went to a slightly negative value in a free fit so it was fixed at zero for a refit.

^{e} k_D^X values calculated from the row above and the values of k_e^Y listed in table 4.4.

All the xenon ternary mixture reactions are slow, including the $NH_3 + NeMu^+$ reaction with a Xe monitor whose k_{exp} came out much lower than the measurement for NH_3 alone (table 4.1). The low rates can be regarded either as a spurious artifact, since the measurements were made consecutively, or as an effect of Xe itself. The anomalously low measurements were also performed consecutively with a measurement of the $Xe + NeMu^+$ rate (5.35) which agreed with earlier determinations, supporting the validity of those low values. It was already apparent (section 5.2) that Xe reacts at only half the expected capture rate (k_{exp} vs. k_L), and, like all the slow reactions, this is likely due to a more complex reaction mechanism than the simple one chosen, eq. (4.12).

Although the total rate constant determined for $NH_3 + NeMu^+$ in the presence of Xe was low, the relative contribution of each reaction channel, k_D/k_e, agrees well with the earlier determinations (table 4.3), lending support to the general validity of the ternary mixture measurements, and indicating that Xe does not interfere with the NH_3 reaction mechanism. Instead, it is likely that NH_3 *does* interfere with xenon's reaction. The measurements H_2O and NH_3 with a Xe monitor are thus valid, but the resulting k_{exp} values are not appropriate for pure H_2O and NH_3.

Determinations of k_D/k_e for H_2O, CH_4, and C_2H_6 meet expectations that $k_D \gg k_e$, although the value of 4.4 seen for $H_2O + NH_3 + NeMu^+$ seems low enough that some small relaxing component should have been seen for the pure H_2O determination. The two measurements that gave $k_e/k_D > 0$ were taken when the high value for $NO + ArMu^+$ was taken (see section 4.2), which might have been due to leaks in the apparatus. If that is true, the rates for water and ethane may be inflated, especially k_e. However, given that k_D/k_e was still high, this effect must have been small, and is unlikely to have affected the total (capture) rates appreciably.

On the whole, the results from ternary mixtures are quite believable, giving rates in good agreement with theoretical capture rates when monitored by NH_3, but giving overall rates lower than the capture limits when measured in the presence of Xe. Methane is the

exception in that its reaction rate agrees with Langevin theory although it was measured in a xenon/helium mixture.

5.5 Comparison with Protonated Inert Gas Results

As noted earlier, charge exchange is rarely seen in studies of the protonated ions; proton transfer is the overwhelmingly dominant reaction channel [16,24,25,79,139,145–149]. The present study of muonated ions indicates that both electron and muon (proton) transfer are ubiquitous, with rate constants k_e and k_μ such that $k_e + k_\mu = k_{exp}$, identified as the capture rate constant k_c in table 4.4. These results are compared with the corresponding protonated ion reactions in table 5.5, though there are few such studies for comparison; the $ArH^+ + H_2$ reaction seems to be the favorite and occupies nearly half of this table. Only the tandem ICR work of Smith and Futrell [191] has shown both charge exchange and proton transfer but, unfortunately, only their results for C_2H_4, reacting with HeH^+ and NeH^+, are comparable with reaction rates measured for this thesis.

The great pressure difference between the present experiments and the ICR [191] measurements of $C_2H_4 + HeH^+$ and NeH^+ (1 atm vs. $\sim 10^{-7}$ torr) would suggest that different results might be seen. Instead, the agreement is exemplary: both the proton/muon-transfer rates and the charge-transfer rates are in agreement, and both experiments measure reactions of vibrationally excited ions. The Smith and Futrell ICR results listed in table 5.5 were determined in both the limits of zero moderator collisions, corresponding to excited ions, and after many collisions, corresponding to ground-state ions; it is the former that best match the reaction rates measured for $(HeMu^+)^*$ and $(NeMu^+)^*$. Interestingly, there is still a contribution from charge transfer for apparently ground-state HeH^+ and NeH^+, whereas all other protonated ion studies detected only proton transfer. Charge transfer was certainly favored by the excitation, but the total reaction rates were essentially unchanged, as is appropriate for capture-limited reactions. The same apparently applies to the muonated ions as well as the protonated ions.

Table 5.5

Comparison of Present Results with Those for Protonated and Deuterated Inert Gases

Neutral Reactants	k_{theory}[a]	Mu results			H, D results			ref
		k_{exp}	k_e	k_μ	k_{exp}	k_e	k_p	
$HeH^+ + H_2$	18.1	b	$\lesssim 0.2$		18.3 ± 0.6	0.	18.3	205
$HeH^+ + Kr$	18.7	b	$\lesssim 0.2$		12. ± 2.	0.	12.	25
$HeH^+ + O_2$	15.4	12 [c]	11.6^d	0.3	11. ± 2.	0.	11.	25
$HeH^+ + C_2H_6$	30.1	17.4 ± 2.6^e	0.	17.	21. ± 4.	0.	21.	25
$HeH^+ + C_2H_4$	25.5	25.0 ± 1.8^f	14.2	10.7	28. ± 5.	15.	13. [g]	191
					28. ± 5.	7.	21. [h]	191
$NeH^+ + H_2$	15.5	b	$\lesssim 0.2$		0.2	0.	0.2	171
$NeH^+ + C_2H_4$	14.1	18.6 ± 3.5	8.2	10.4	18. ± 4.	8.	İ0. [g]	191
					18. ± 4.	4.	14. [h]	191
$ArH^+ + H_2$	15.2	b	$\lesssim 0.2$		8.9	0.	8.9	145
$ArH^+ + H_2$					3.4	0.	3.4	191
$ArH^+ + H_2$					8.0 ± 2.4	0.	8.0	198
$ArD^+ + H_2$					8.8	0.	8.8	145
$ArD^+ + H_2$					4.5	0.	3.4	191
$ArD^+ + NH_3$	20.8	b	$\lesssim 0.2$		21.4 ± 3.2	6.	15. [g]	191
$ArH^+ + O_2$	7.0	b	$\lesssim 0.2$		4.1	0.	4.1	146
$ArH(D)^+ + O_2$					6.0 ± 1.8	0.	6.0	198
$N_2H^+ + NO$	8.6	1.46 ± 0.14	1.4^d	0.	3.4	0.	3.4	203

[a] All rate constants are in units of 10^{-10} cm^3 molec^{-1} s^{-1}; k_{theory} is the Langevin or AADO prediction for the MMu$^+$ ion. Theory values for HeH$^+$ are ~10% lower than HeMu$^+$ due to the mass difference; other theory values independent of H/D/Mu.

[b] No relaxation seen, so the capture and muon-transfer rates are ill-defined and the charge-transfer reaction is very slow ($k_e \lesssim 0.2$).

[c] The HeMu$^+$ + O$_2$ reaction was not measured, but estimated by scaling the NeMu$^+$ result according to the mass dependence of eq. (3.7).

[d] Both charge transfer and depolarization of NOMu$^+$ and O$_2$Mu$^+$ may contribute to the relaxation.

[e] Measured in the presence of NH$_3$ monitor gas, see table 5.4.

[f] Measured at 398 K; all other measurements were made at room temperature.

[g] Results of Smith and Futrell [191], using the product distributions in the limit of zero collisions, giving the (MH$^+$)* reactivity.

[h] The same, but measured after many quenching collisions, corresponding to ground-state reactants.

Smith and Futrell also measured reactions of ArH^+ under similar conditions [191,198] and saw some charge transfer with NH_3 before quenching of $(ArH^+)^*$, whereas no reaction was seen for $ArMu^+$. This is not to say that there is no reaction at all — muon transfer undoubtedly takes place, but in the absence of any depolarization from Mu formation, the reaction remains undetectable. This difference, after the agreement for He and Ne ions, indicates that $ArMu^+$ is quickly quenched to its ground state by the ~ 1 atm argon bath. Note that the only reactions observed for $ArMu^+$ were with nitric oxide and tri-ethylamine, for which charge transfer is exothermic from the ground state. These results agree with the usual finding that N_2 and Ar de-excite molecular ions much better than do He or Ne [16,79,153,154,206–208].

Villinger, Futrell and co-workers [198] had similar results for the reaction of $(ArH^+)^*$ with O_2 — some charge transfer before de-excitation of the ion, and a predominance of proton (deuteron) transfer — while Lindinger et al. [146] saw only proton transfer whose rate increased with vibrational excitation. $ArMu^+$ gave no visible reaction with oxygen, but no charge transfer was expected, based on the energetics for ground-state $ArMu^+$, in seemingly good agreement with the H-ion results. The problem with this is that O_2H^+ has a diradical triplet electronic ground state [152,209] in which the μ^+ spin would be dephased and depolarized in a transverse magnetic field, even in the absence of Mu for-mation. Might the effect of excitation observed by Lindinger be even stronger for $ArMu^+$; so much so that there is *no* muon transfer for ground-state $ArMu^+$? It is a possibility, as the proton transfer is only 0.55 eV exothermic and energetics probably favor proton over muon transfer: A likely zero-point correction for O_2Mu^+ is 0.39 eV, based on the calculated O_2H^+ vibrations [209], whereas the ZPE shift for $ArMu^+$ is 0.27 eV [78], which make the $ArMu^+$ reaction 0.12 eV less exothermic than for ArH^+ (0.43 eV vs. 0.55 eV). This should still be enough for the reaction to proceed.

Rather than positing that μ^+ transfer is non-existent for $ArMu^+$, the result could be attributed to the formation of *electronically* excited O_2Mu^+. The first three electronic

excited states of O_2H^+ are spin-singlet, 0.26, 1.28, and 3.31 eV [152] above the triplet ground state, and muon transfer from ground-state ArH^+ to the lowest of these is still exothermic by $0.43 - 0.26 = 0.17$ eV.[2] The lack of depolarization would require that singlet O_2Mu^+ is formed almost exclusively. Selective population of product states is a common occurrence, but typically only for resonant reactions [187,210]. Resonant μ transfer *is* a possibility because the remaining 0.17 eV exothermicity could easily be used up by forming rotationally excited O_2Mu^+. (Note that 0.17 eV is much less than the expected (~ 1 eV) vibrational spacing.)

An alternative explanation was mentioned in section 5.2: the possibility that the $ArMu^+$ might form clusters Ar_nMu^+. In particular, the Ar_2H^+ ion is 0.51 eV more stable than ArH^+ [64,170], making the reaction

$$Ar_2H^+ + O_2 \longrightarrow O_2H^+ + 2Ar \tag{5.6}$$

exothermic by just 0.04 eV (all species in their ground states) and the Mu analog *endothermic* by 0.08 eV! This is more a case of a near-resonant reaction rather than an endothermic one, so it is not clear that this reaction would prevent the formation of O_2Mu^+ and its subsequent depolarization; it might even *promote* it. The presence of Ar_nMu^+ was also implied by the lack of depolarization for $(CH_3)_4Si + Ar$ mixtures, although the $(CH_3)_4Si + ArMu^+$ charge exchange reaction is more exothermic than $O_2 + ArMu^+$ muon transfer. It is a pity that there are no good comparisons of $ArH^+/ArMu^+$ reaction rates to prove (or disprove) that the ionic reactant is really $ArMu^+$. The comparisons for the He and Ne ions demonstrate that no clustering takes place in those moderators, giving a similar expectation for Ar. Nevertheless, clustering seems a more viable explanation for the lack of depolarization in $ArMu^+ + O_2$ than does the formation of excited O_2Mu^+.

---

[2] ...presuming that the O_2Mu^+ ZPE is the same for each state; this is likely true for the lowest singlet state ($1^1A'$) whose potential energy curve has much the same shape as the ground ($1^3A''$) state [152].

The other entry for O_2 in table 5.5, due to Bohme and co-workers [25], gives the proton-transfer rate constant for $O_2 + HeH^+$. Unfortunately, this combination slipped through the cracks of the present experimental program, which has measured only the reaction of $O_2 + NeMu^+$, so the value of $k_{exp} = 12$ for the $O_2 + HeMu^+$ reaction had to be estimated from the neon result based on the difference in reduced mass. Nevertheless, this estimate agrees very well with the HeH^+ result of $11 \pm 2 \times 10^{-10} \, cm^3 \, molec^{-1} \, s^{-1}$, and both are slightly below the Langevin prediction. Yet there is a striking difference between the measurements: Bohme observed only proton transfer while we saw apparently *no* muon transfer, only charge exchange. This appearance may be caused by spin precession and depolarization of triplet O_2Mu^+ formed by muon transfer, but there is reason to believe that this is not the whole story.

As discussed above, formation of O_2Mu^+ in Ar gave no depolarization, with the possibility of excitation in the muonated oxygen. Muon transfer from $NeMu^+$ is more exothermic than from $ArMu^+$ and so should give *more* excited singlet O_2Mu^+. It is hard to believe that there would be as little singlet product as indicated by the apparent k_μ/k_e. Instead, there is probably little muon transfer taking place, with a predominance of charge exchange. Some part of the difference from Bohme's results may be due to depolarization of O_2Mu^+ after muon transfer, and also to differences between the $HeMu^+$ and $NeMu^+$ ions, but the major difference is probably in the excitation — the muon ion results involve excited $NeMu^+$ while the proton ion results are for ground state ions, for which the charge exchange reaction is endothermic.

Another point of comparison between this work and that of Bohme, Mackay, & Schiff [25] is the $HeH^+ + C_2H_6$ reaction. The two measurements agree quite well in the rate constant and in detecting only proton (muon) transfer, though the $C_2H_7^+$ product was not observed because of its rapid fragmentation into $C_2H_5^+ + H_2$. This is probably a feature of the μ-transfer reaction as well. The Langevin rate over-estimates both measurements significantly.

There are several measurements of protonated and deuterated ions reacting with H_2 by proton (deuteron) transfer, but none of these were visible for the muonated inert gas ions.

The N_2Mu^+ reaction with NO was the only case where there is significant disagreement with literature values for total reaction rate; the Mu rate is only half of the H rate measured by Rakshit [203], which is itself less than half the AADO capture rate. Like the oxygen reactions, both Mu and $NOMu^+$ formation may contribute to the total reaction rate. The N_2H^+ ion reacts purely by proton transfer.

The impressive agreement, insofar as comparisons are possible, between the reaction kinetics of the muonated, protonated, and deuterated ions reveals a total lack of isotopic sensitivity; surprising when viewed in terms of the very large effects seen for reactions of neutral Mu [29–31]. Some isotope effect on the proton/muon-transfer rate had been expected, and even charge transfer could be affected. However, any differences observed are more probably a result of differences in excitation; the muon ion results involve excited $NeMu^+$ while the proton ion results are for ground state ions, for which the charge exchange reaction is endothermic. The excellent agreement between the present work and the proton ion data, considering the vastly different pressure regimes utilized, indicates that total pressure plays a negligible role in ion–molecule reactivity, *even when ion excitation is important*, in sharp contrast to other measurements of excited ion reactivity [201,205,211]. What makes this even *more* remarkable is the fact that the high pressure Mu ion measurements reveal more ion excitation than is evident in the low pressure H ion results.

While these comparisons are illuminating, the relative lack of data for the corresponding reactions of the HeH^+, NeH^+, and ArH^+ ions frustrates the potentially important broad comparisons that could otherwise be made with the present μSR results. It is important to emphasize, in this context, that the μSR measurements have considerably expanded the data base of ion–molecule reactions undergone by these simple point-charge ions.

5.6 Unreactive Ions

In the investigations of molecular moderators, and therefore polyatomic molecular ions, very little (charge transfer) reactivity was seen. No signal relaxation was seen for ammonia, triethylamine or nitric oxide in hydrogen; none for ammonia or nitric oxide in ethane; and none for C_2H_4, CO, or O_2 in nitrogen, although NO did react with N_2Mu^+.

It is not at all surprising that there was no relaxation in ethane moderator, even with nitric oxide reactant. The binding energy of $C_2H_6Mu^+$ is not known exactly, but the proton affinity of $C_2H_6 \approx 6$ eV [22,144]. Assuming a zero-point energy correction for $C_2H_6Mu^+$ of 0.3 eV, the charge-transfer reaction with NO would still be endothermic by 1.4 eV. The ethane moderator is undoubtedly an extremely efficient quencher of $(C_2H_6Mu^+)^*$, it quenches $(NO^+)^*$ very well [155] and would benefit from its similarity with $(C_2H_6Mu^+)^*$, which generally enhances quenching efficiency [153,154,157], so there should be very little excitation of the muonated ethane. The supposed zero-point correction of 0.3 eV is a very generous estimate; the true value is probably considerably less because $C_2H_7^+$ very weakly bound, being prone to fragment into $C_2H_5^+ + H_2$ [212]. In fact, this undoubtedly happens in the present studies, placing the Mu in either the even-more-stable $C_2H_4Mu^+$ ion or the diamagnetic molecule MuH, neither of which would react with even nitric oxide.

These considerations may not come into play because it is likely that no molecular ion is formed! The diamagnetic signal in low pressure C_2H_6 is consistent with the molecular products of muonium hot atom reactions which occur during μ^+ thermalization [38,90]. There are apparent contributions from MuH produced by H-atom abstraction at $\lesssim 10$ eV kinetic energy, and from C_2H_5Mu formed by Mu substitution occurring near 5 eV, followed by collisional stabilization of the $(C_2H_5Mu)^*$ [38]. Such reactions occur too quickly to be observed directly by μSR, but are reflected in the 'initial' (after Mu thermalization) amplitudes of Mu and diamagnetic signals; there has been much study of hot-Mu chem-

istry [38,89,90]. The formation of the molecular ion was not *absolutely* ruled out in those studies, but its existence was deemed improbable. Even *if* the muonated ethane ion is formed initially, *and* it doesn't fragment, it may react by proton transfer with other ethane molecules according to

$$C_2H_6Mu^+ + C_2H_6 \longrightarrow C_2H_5Mu + C_2H_7^+ \ . \tag{5.7}$$
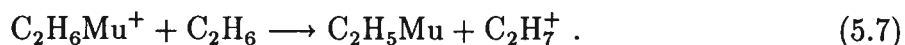
It is not certain that this reaction proceeds, as only a detailed calculation of the energetics could reveal the small differences in stabilities; however, the equivalent reaction for H_2Mu^+ is calculated to be exothermic [81], and the ethane reaction is likely to be as well. With all these processes working against it, it is hardly surprising that no $C_2H_6Mu^+$ was seen.

This brings us to the other molecular moderator that gave no relaxation of the signal: H_2. The binding energy of $H_2 + Mu^+$ has been calculated [81,144] as $D_0 = 4.142\,\text{eV}$, so although charge transfer with NH_3 is endothermic by 0.77 eV, it is exothermic for NO and $(C_2H_6)_3N$ by 0.13 and 2.3 eV respectively. But no reaction was seen for any of these three, not even a muon-transfer reaction with NO.

It is almost certain that the diamagnetic signal in H_2 is due to MuH rather than H_2Mu^+. The molecular ion might be formed initially, but the reaction

$$H_2Mu^+ + H_2 \longrightarrow H_3^+ + MuH \tag{5.8}$$

has been calculated [81] to be exothermic by 0.07 eV (7.0 kJ/mol), even though the H_3^+ has a $J = 1$ ground state while H_2Mu^+ is $J = 0$, and so the Mu would be quickly shuttled into MuH. However, the dominant source of MuH is likely to be the neutral exchange reaction

$$Mu + H_2 \longrightarrow MuH + H \ , \tag{5.9}$$

again due to Mu hot atom chemistry. Thermally, this endothermic reaction is slow, but it has been well studied over the temperature range 470–840 K [82]. At many eV, it

should have a substantial cross section [213]. Furthermore, measurements of the diamagnetic fractions in H_2 and D_2 fit established notions of hot atom reactivity, including the Wolfgang–Estrup formalism [90,213,214]. These considerations point to the absence of H_2Mu^+, and so explain the absence of observable molecular-ion reactions with H_2. Epithermal Mu reactions with the noble gases and N_2 are not really feasible.

5.7 Temperature Dependences

Several reactants were studied over a range of temperatures, from as low as 117 K up to 445 K. The lowest attainable temperature was often limited by the vapor pressure of the reactant gas — when too low, it was impossible to introduce the vapor to the reaction vessel — thus, e.g., the lowest temperature attained for nitromethane was 223 K. In fact, acetonitrile, acetaldehyde, and difluoroethane were chosen as reactants for their high vapor pressures relative to their dipole moments. The thermal homogeneity of the gas was less than ± 1 K, but the variation of T over time was larger, more like ± 5 K at the low
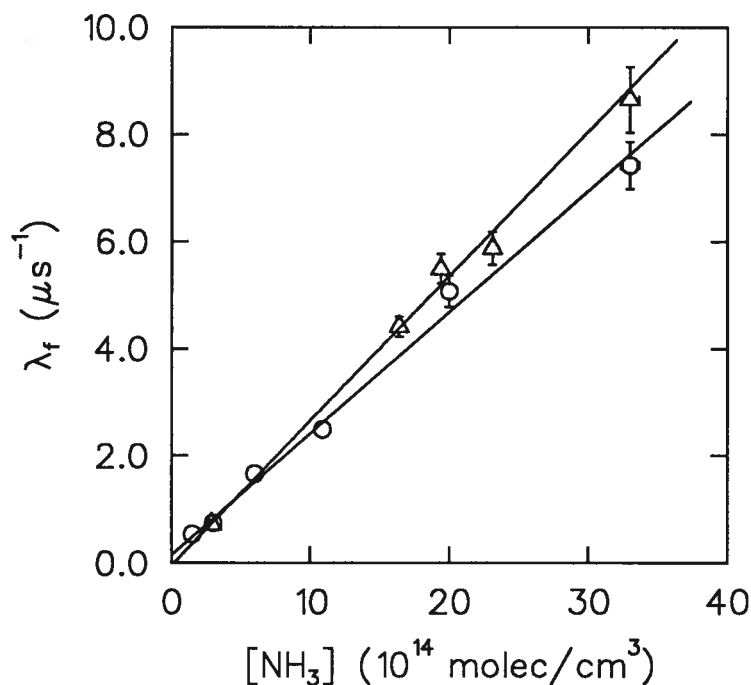
Figure 5.4 The relaxation (reaction) rates for $NH_3 + NeMu^+$ vs. NH_3 concentration at 445 K (o) and 179 K ($\triangle$). The slopes give rate constants of 22.6 and 27.0×10^{-10} cm^3 molec^{-1} s^{-1} respectively.

temperatures. The experimental rate constants measured at the various temperatures were given in tables 4.1 and 4.4. The variation of the rates with T were generally small, as shown by figure 5.4, which plots the relaxation rates measured at 179 K and 445 K for the NH_3 + $NeMu^+$ reaction.

According to the Locked Dipole, AADO, and other theories of ion–dipole capture, the rate constant should vary as $1/\sqrt{T}$, so linear fits of k vs. $1/\sqrt{T}$ to the data were performed with the results listed in table 5.6. Figures 5.5–5.12 show the measured total rate constants vs. $1/\sqrt{T}$, with the linear fits to the data plus the AADO and SACM (or Langevin) predictions. The AADO (and other) calculations deviate from being linear insofar as the locking "constant" C varies[3] with temperature, but the variation is small over the temperature ranges investigated, so the theory lines are linear in the range of the data. Linear extrapolation beyond this range accounts for intercepts visibly different from the Langevin values (figure 5.5 shows $k_{AADO} = 9.5$ at $T^{-1/2} = 0$ whereas $k_L = 11.6$). Because of this difference, table 5.6 also lists the slopes and intercepts of the AADO calculation as determined by values at 200 and 400 K, thus facilitating comparison with the linear fits of the experimental data (and also reducing computation).

Some of the reactions are fitted well by capture theory: $NeMu^+$ plus NH_3, CH_3NO_2, and N_2O. Although the NH_3 measurements show considerably less variation with temperature than the AADO and SACM calculations do, all three lines on figure 5.5 intersect in the midst of the data points, indicating good agreement. The experimental slope for the N_2O temperature dependence also appears to differ from the AADO prediction, but, given the uncertainties in the points, the difference is not really significant; and the AADO line *does* agree well with the points themselves. The corresponding SACM calculation falls far below the points, but one can have no confidence in SACM's predictive ability for such a weak dipole as N_2O: in the derivation of the SACM treatment it was assumed that the

---

[3] Although C is not constant with temperature, the term "locking constant" is as sensible as "rate constant" or "equilibrium constant."

Table 5.6

Fits to Temperature Dependences Compared with Theory

Neutral (X)	M	experiment		AADO	
		slope[a]	$k(300)^b$	slope[a]	$k(300)^b$
Xe	Ne	3.1 ± 8.0	5.19 ± 0.14^c	0	11.2
N_2O	Ne	-56 ± 52	12.99 ± 0.73	19	11.8
NH_3	Ne	158 ± 45	24.54 ± 0.59	245	23.7
CH_3NO_2	Ne	580 ± 400	34.3 ± 2.6	610	46.5
CH_3F	Ne	-130 ± 62	14.02 ± 0.84	314	27.4
CH_3F	He	550 ± 110	31.1 ± 2.1	584	51.0
$C_2H_4F_2$	He	640 ± 76	14.00 ± 0.81	823	68.3
CH_3CHO	He	1170 ± 290	41.0 ± 2.8	903	73.6

[a] The slope of $k(T)$ vs. $\sqrt{1/T}$, in $10^{-10}\,K^{1/2}\,cm^3\,molec^{-1}\,s^{-1}$, from fitting the experimental rate constants and the nearly-linear AADO predictions.

[b] The rate constant at 300 K, in $10^{-10}\,cm^3\,molec^{-1}\,s^{-1}$ determined by the fit to the experimental data or by the linearization of the AADO theory.

[c] The results for Xe are clearly flat, as expected, so the average k is given for $k(300)$ instead of the result from the linear fit. The theoretical $k(300)$ listed is the Langevin rate.
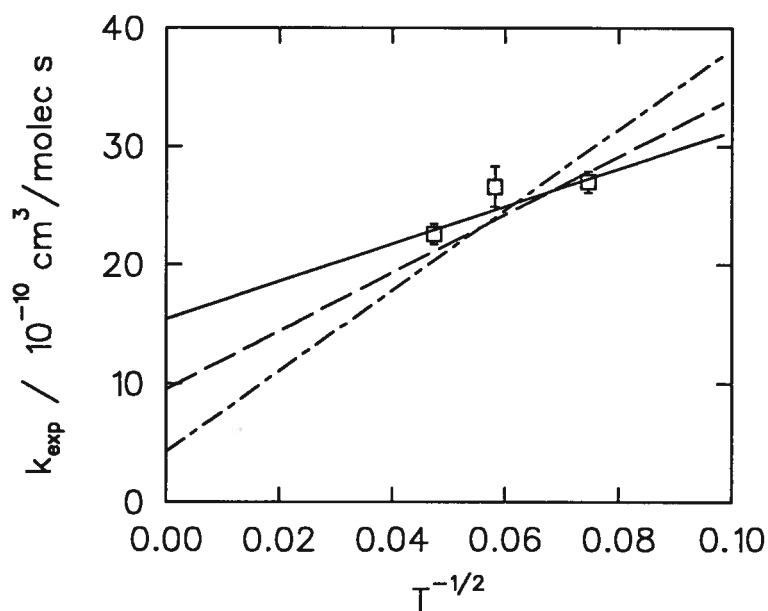
Figure 5.5 The experimental rate constants for $NH_3 + NeMu^+$ over the temperature range 179–445 K, plotted as $1/\sqrt{T}$. The solid line is the fit to the data, the dashed line is the AADO prediction, and the dot-dashed line is the SACM calculation. Although the slopes are somewhat different, all lines agree with the data.
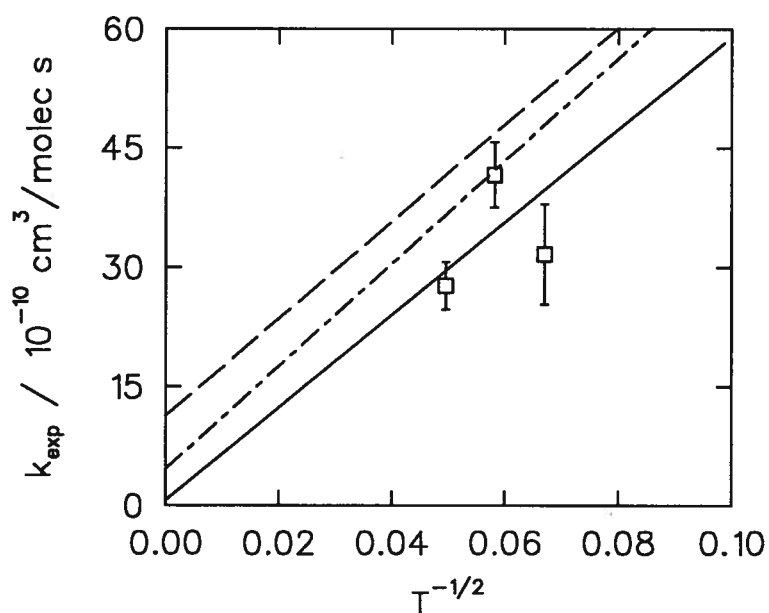
Figure 5.6 k_{exp} for $CH_3NO_2 + NeMu^+$ vs. $1/\sqrt{T}$ for T in the range 223–406 K. The dashed and dot-dashed lines are AADO and SACM predictions, respectively. The points fall only slightly below theory, although, given their scatter, it is somewhat fortuitous that the fit matches the slopes of the theory lines so well.
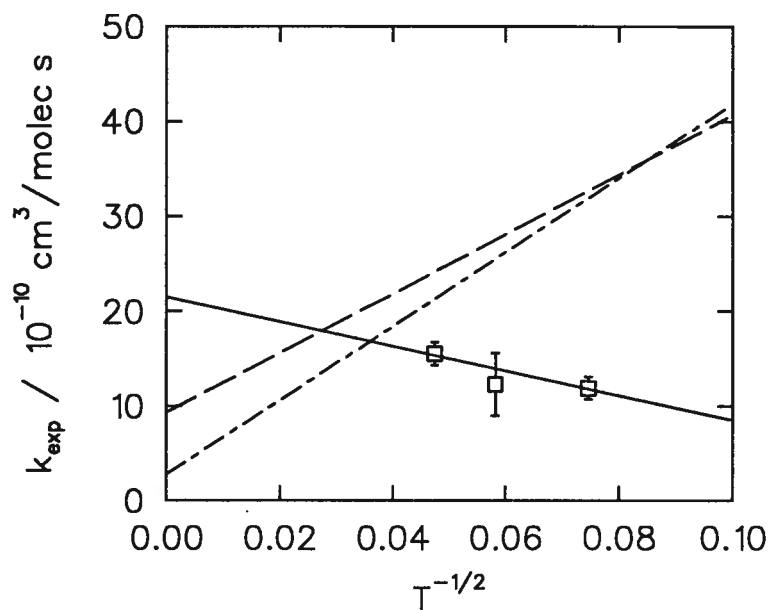
Figure 5.7 k_{exp} at various temperatures for the reaction $CH_3F + NeMu^+$. The solid line is a fit to the data and the dashed and dot-dashed lines are the AADO and SACM predictions, which miss the data entirely.
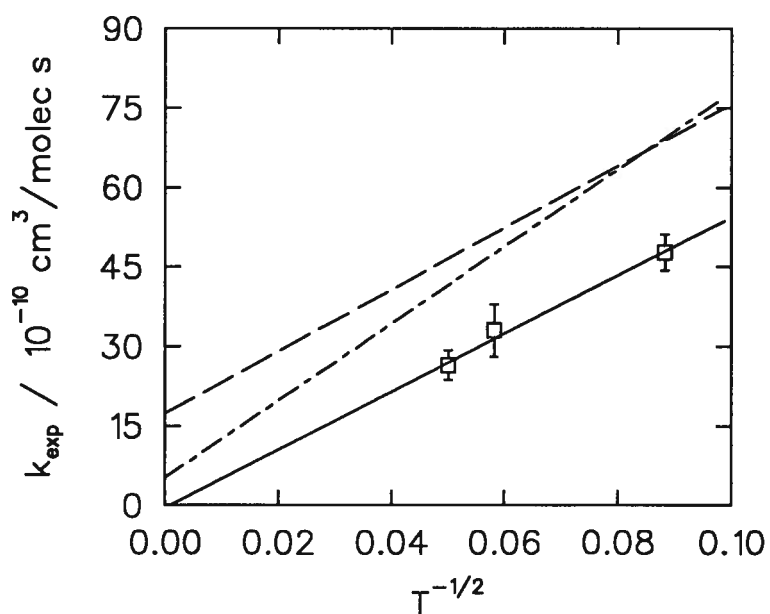
Figure 5.8 k_{exp} vs. $1/\sqrt{T}$, as above, but for the $HeMu^+$ ion. The agreement with capture theory is much better, though the data is significantly below the predictions.
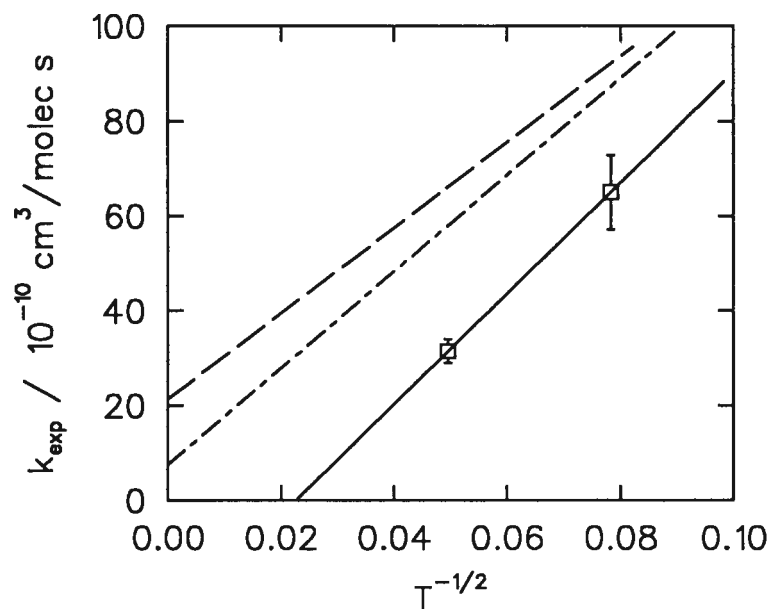
Figure 5.9   The two values of k_{exp} at different temperatures for the $CH_3CHO + HeMu^+$ reaction, compared with capture theory; the line types are the same as for preceding plots. The points fall well below the theory, but with a similar slope, giving an unphysical $k(\infty) < 0$.
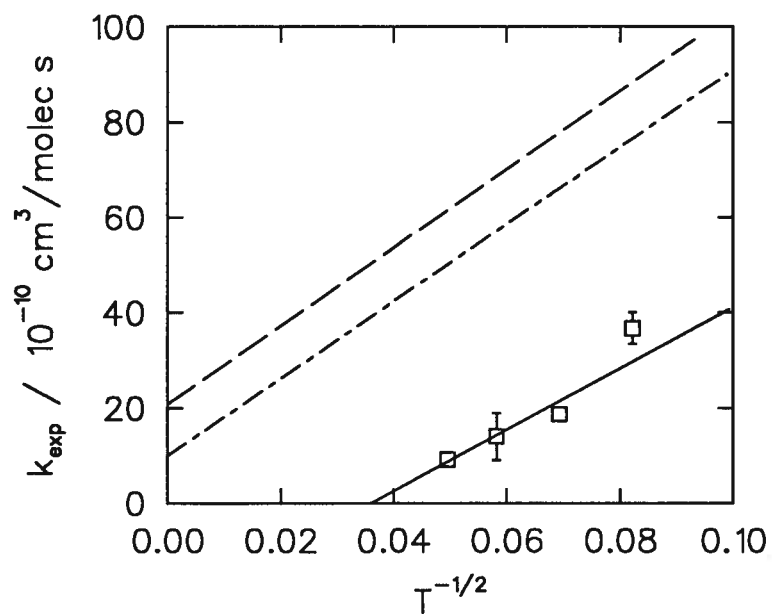
Figure 5.10   As above, for $C_2H_4F_2$ over the temperature range 148–406 K. This data falls far below theory, but, again, with the same slope.
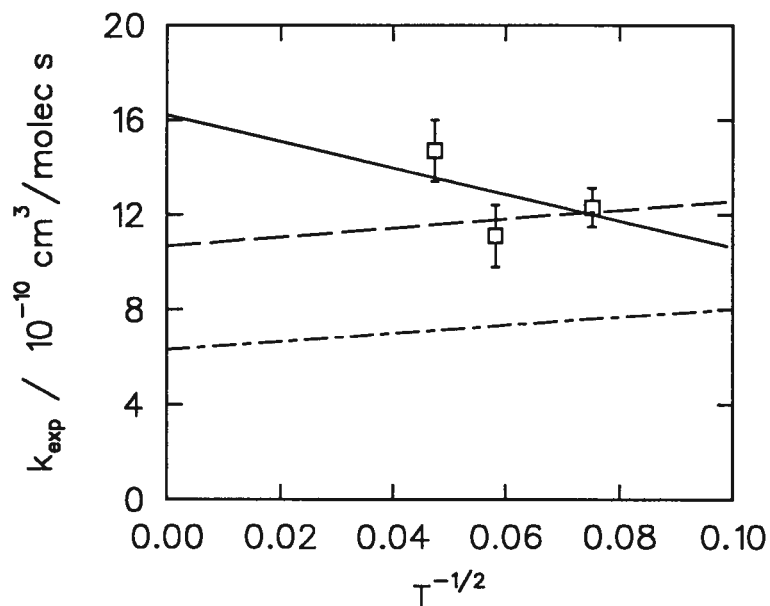
Figure 5.11   Results for N_2O + $NeMu^+$ at various temperatures. Although the experimental points decrease with decreasing temperature (increasing $1/\sqrt{T}$), the trend is probably not significant, and the AADO predictions fit the data well. The SACM values are very low, but the SACM treatment is invalid for such a weak dipole.
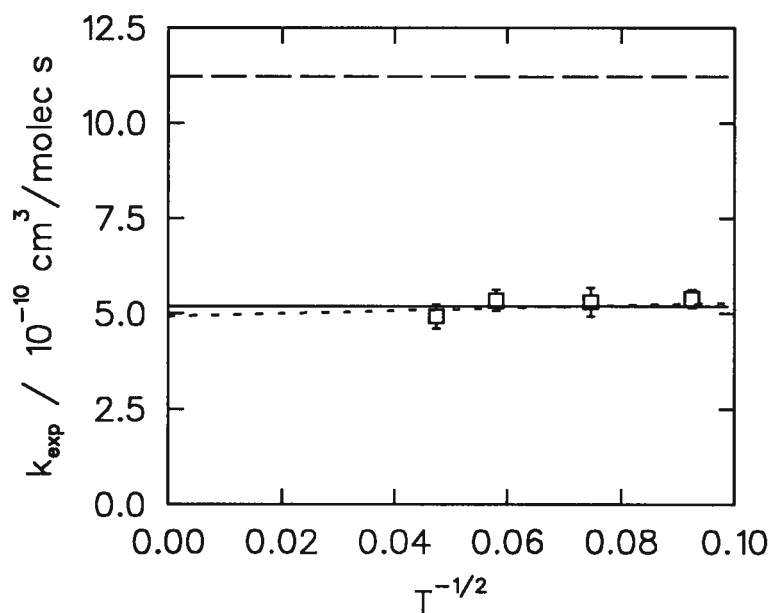
Figure 5.12   Experimental rate constants for $Xe + NeMu^+$ over the temperature range 117–445 K, plotted as $1/\sqrt{T}$. The line of small dashes is the fit to the points, which are obviously independent of T; thus, the horizontal solid line is drawn at the average $k = 5.19 \times 10^{-10}\,\mathrm{cm^3\,molec^{-1}\,s^{-1}}$. The high dashed line is the Langevin prediction, $k_L = 11.2$.

permanent dipole dominated the polarizability. The agreement in the case of CH_3NO_2 is impressive, especially for SACM; however, it should be noted that the parallel lines of figure 5.6 are fortuitous because the slope of the fit is very uncertain (table 5.6).

For several other reactants, the situation with CH_3NO_2 is magnified — the trends with temperature match theory, but the points are displaced to lower values. For the $Xe + NeMu^+$ reaction (figure 5.12), the data are impressively temperature-independent, as expected for non-polar Xe, but with rate constants only half the Langevin value. Both $C_2H_4F_2$ and CH_3CHO reacting with $HeMu^+$ give the predicted variations with temperature (slopes), but have negative intercepts! While a slight displacement to lower k values might be due to polarizabilities being lower than the literature values, this could not give an unphysical negative k at high temperatures. Nor are the low values due to thermally-activated reactions, for if they were, they would have the reverse temperature dependence. Instead, some subtleties in the reaction mechanism are indicated.

The reaction of CH_3F with $NeMu^+$ increases in rate at higher temperatures, unlike a capture process. The charge-transfer reaction *is* endothermic by $0.72\,eV = 69\,kJ/mol$, but that is too high to believe the reaction is thermally activated, especially for such a weak temperature dependence. Although there may be some small barrier to muon transfer within the capture complex, there would be more than enough energy available in $(NeMu^+)^*$ to cross it without needing thermal excitation. Recalling the great effect Ne moderator pressure had on this reaction ($\{k_q + k_s[M]\}/k_e$ in table 4.6), it is likely that the temperature dependence is a result of changes in moderator quenching of the capture complex, or some similar quenching mechanism.

The quantum SACM calculations for the rate constants are included in figures 5.5–5.12 to see if they could fit low-temperature results better than the classical AADO calculations. Although the SACM lines do not overlap the AADO ones, they do run parallel for all reactants except NH_3; and they are truly linear over the range of temperatures studied. It could be argued that the measured points do, on average, lie closer to SACM

predictions than to the AADO, but the SACM calculations underestimate the effect of the polarizability and the difference between SACM and AADO is mainly due to this, rather than to discrete rotational levels. Of the molecules studied, NH_3 has the lowest moment of inertia and the widest rotational quantization and, indeed, is the only molecule for which the SACM calculation exceeds AADO within the temperature range of the data. The difference is slight, however, and both predictions fit the data well. For the reactions studied, capture is still essentially classical, even at the lowest temperatures investigated.

Selecting the best classical treatment is more difficult, as many of the reaction rates fall below all the capture predictions; these reactions are obviously not capture limited, even though the muonated rare gas ions are the molecular ions that most resemble a point charge. The best upper limits on the observed reaction rates are provided by the VTST [120], AADO [117], or the parameterized trajectory [118] calculations.

Chapter 6

EXCITATION AND QUENCHING

The energetics of the ion–molecule reactions studied are central to an understanding of their kinetics, and this topic has been considered in the discussions thus far, but only to a limited extent. The observation of several instances of endothermic charge transfer led to the conclusion that the muonated rare gas ions $HeMu^+$ and $NeMu^+$ must have an excess of energy, probably in the form of rovibrational excitation (see §4.3), while $ArMu^+$ probably reacts from its ground state, or even from an Ar_nMu^+ cluster.

Since the data called for an unseen reaction between the moderator and the ions, quenching of the excited ions through collisions with the moderator gas was implicated. Excitation energy could also be lost to the dilute reagent, which may have quenching efficiencies ranging to thousands of times higher than He or Ne [79,153–157], generally with greater efficiency for complex molecules and those of similar structure to the ion. Quenching by the reagent is hard to distinguish experimentally from the muon-transfer reaction, but not so for quenching by the moderator, which is manifest in many forms: Quenching rates were measured as zero-reagent-intercepts of the signal relaxation rate, as the variation of the relative amplitudes with reagent concentration, and as variations in both amplitudes and relaxation rates with changes in moderator density. The discussion in this chapter will focus on the details of the reaction energetics and on the various measurements of quenching, including some measurements of quenching by argon not presented yet.

6.1 Molecular Ion Formation and Excitation State

As described in chapter 1, muonated (and protonated) rare gas molecular ions are expected to form by the association of a bare muon (proton) with the appropriate gas atom at kinetic energies below 1 eV. This was substantiated by the results presented in section 4.10 indicating that association probably happens at a low enough energy to be affected by the polarizabilities and dipole moments, and also below where most epithermal Mu formation happens. Although some energy must be carried off by the moderator for the association

$$\mu^+ + \begin{Bmatrix} He \\ Ne \end{Bmatrix} \xrightarrow{\ M\ } \begin{Bmatrix} HeMu^+ \\ NeMu^+ \end{Bmatrix} \tag{6.1}$$
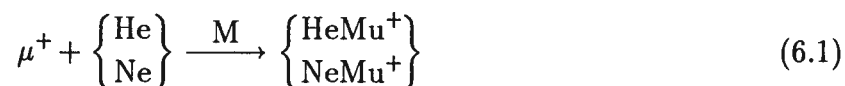
to occur, the low quenching efficiencies of He and Ne [16,79,153–157,206–208] and H_2 as well [153,204] allow substantial rovibrational excitation to remain. HeH^+ and NeH^+ have both been observed in excited states [71,191], although at much lower bath gas densities than employed for these experiments.

What is the minimum excitation needed to allow the Mu formation reactions that were observed? Table 4.2 shows that, except for Kr, which is dealt with in the next section, the most endothermic charge-transfer reactions observed were those of CF_4, in both He and Ne, requiring ~ 0.99 and $\sim 1.25\,eV$ of excitation respectively. These numbers are uncertain, though, as the ionization potential of CF_4 had to be estimated; the next most endothermic reactions, for N_2O, are not much different at 0.88 and 1.13 eV. From the calculations of Fournier, Le Roy, and Lassier-Govers [75] (table 1.2) the necessary excitation corresponds to $(v, J) = (2,0)$, $(1,2)$, or $(0,6)$ for $HeMu^+ + N_2O$; and $(v, J) = (2,0)$, $(1,5)$, or $(0,9)$ for $NeMu^+$. It is unlikely that just one vibrational level is populated, and certainly not just one rotational state.

Although the present experiments have determined the approximate degree of excitation involved, they put no restriction on the distribution of energy between vibration and rotation. Conventional molecular ions are often formed in excited vibrational

states by electron impact or exothermic charge transfer, although when rotational excitation has been measured [153,215,216] it appears to be high. Furthermore, measurements [79,153,204] and calculations [217] show that ions are excited rotationally as they are de-excited vibrationally. Perhaps the same process could populate high J states of $HeMu^+$ and $NeMu^+$ even if these ions are formed with purely vibrational excitation.

It appears, then, that the muonated rare gases could well be present with just about any partitioning between vibrational and rotational energy, and perhaps a wide range. For vibrational levels $v > 0$ the high-J states are longer lived for radiative decay [75]. It should be noted as well that $HeMu^+$ and $NeMu^+$ have rotational energy spacings $\approx 1000\ cm^{-1}$ [75], more typical of vibrational spacings than rotational.

The reactivity of $ArMu^+$ and N_2Mu^+ follows an entirely different pattern. In argon moderator, depolarization was seen only for the neutrals nitric oxide and triethylamine, for which charge transfer is exothermic from the ground state of $ArMu^+$. There was no reaction visible even for tetramethyl silane whose reaction is barely exothermic (table 4.2). This indicates that $ArMu^+$ is in its ground state, achieved, undoubtedly, by rapid collisional quenching by the Ar bath, and it may be in a cluster with additional Ar (§5.2). The story is similar for N_2Mu^+, with only NO giving depolarization. These results agree with the usual finding that N_2 and Ar de-excite molecular ions much better than do He or Ne [16,79,153,154,156,157,206–208].

6.2 The Reactivity of Krypton with $NeMu^+$

As reported in chapter 4 and shown in figure 4.3, krypton reacts with $NeMu^+$ even though Mu formation from ground state $NeMu^+$ and Kr is endothermic by 2.25 eV, and formation from even a bare μ^+ is endothermic [i.e., IP(Kr) > IP(Mu)] by 0.47 eV. How is this possible?

An artifact due to impure Kr has been considered and rejected (§5.3) based on repetitions of the measurement and the absence of any reaction between Kr and $HeMu^+$.

Parallel reactions with any impurity should still give $k_{\text{exp}} \approx k_c$, just as for the deliberate measurements of ternary mixtures (§5.4), not the observed $k_{\text{exp}} \ll k_c$. Note that Mu formation with HeMu$^+$ is *less* endothermic than the NeMu$^+$ reaction yet there was no charge transfer seen in He. To add to the puzzle, CO gave no relaxation, although it has the same ionization potential and reaction endothermicity as Kr.

While it is odd that k_e is not zero, it is equally odd that k_μ is so low. The muon-transfer reaction is exothermic, probably by ≈ 2.3 eV, so it was expected to proceed at or near the capture rate. Instead, k_μ is just a little greater than k_e ($k_\mu \leq k_D = 0.33$ vs. $k_e = 0.23 \times 10^{-10}$ cm^3 molec^{-1} s^{-1} in table 4.4), and the total rate constant is just $1/16$ of k_L.

There are a number of possibilities for increasing the energy available for Mu formation. Both HeMu$^+$ and NeMu$^+$ have one long-lived quasibound state: the HeMu$^+$ $v = 0, J = 8$ state at 0.029 eV above the dissociation limit with a predissociation lifetime of 3.5×10^{-7} s, and the NeMu$^+$ $v = 0, J = 11$ state at 0.060 eV having a lifetime of 4.2×10^{-6} s [75, see table 1.2]. The former is shorter-lived than a μ^+, but the latter is slightly longer-lived than the muon itself at 2.2 μs, and so could contribute to the observed reaction. Even from the quasibound state, however, the charge-transfer reaction of (NeMu$^+$)* with krypton is still 0.40 eV endothermic.

This endothermicity may be reduced further if bound NeKr$^+$ was formed by charge exchange, contributing its binding energy of 0.057 eV [144]. Such "switching reactions"

$$\text{(NeMu}^+)^{*\,(J=11)} + \text{Kr} \longrightarrow \text{Mu} + \text{NeKr}^+ - 0.34\,\text{eV} \tag{6.2}$$

were considered in section 4.2 but, as in this case, the energy difference is not great enough to have much effect: $\exp(-0.34\,\text{eV}/kT) = 10^{-6}$ whereas the reaction occurs at 0.06 of the collision rate. There are much more strongly bound rare gas dimer ions though; Kr$_2^+$ is bound by 1.15 eV [144], which is more than enough to allow the reaction

$$\text{(NeMu}^+)^* + 2\,\text{Kr} \longrightarrow \text{Mu} + \text{Ne} + \text{Kr}_2^+ \tag{6.3}$$
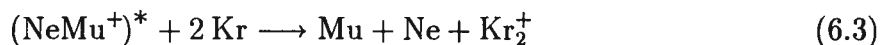
to proceed; in fact the minimum excitation of NeMu$^+$ needed is only 1.10 eV — less than that for charge exchange with N$_2$O! This termolecular reaction could also be compatible with the non-reactivity of CO — not on the basis of energetics, but by claiming a slow (CO)$_2^+$ formation rate. Other observations are not explained though: the reaction rate is clearly first-order in krypton concentration (see the straight line in figure 4.3); the He-equivalent of reaction (6.3) is even less endothermic, needing less excitation, but was not observed; and there is no explanation of why the muon-transfer reaction would be so slow. The simple-model determination of k_μ listed in table 4.4 is quite uncertain, and it would need reinterpretation if the reaction is termolecular, but it would still need to be unusually low to achieve such a low k_{exp}. This is made even clearer by considering a termolecular capture and break-up mechanism explicitly

$$(\text{NeMu}^+)^* + \text{Kr} \xrightleftharpoons[k_b]{k_c} (\text{Ne Mu Kr}^+)^* \xrightarrow[k_e'[\text{Kr}]]{\text{Kr}} \text{Mu} + \text{Kr}_2^+ + \text{Ne} \qquad (6.4)$$

$$k_\mu' + k_s'[\text{Ne}] \downarrow$$

$$\text{Ne} + \text{KrMu}^+$$
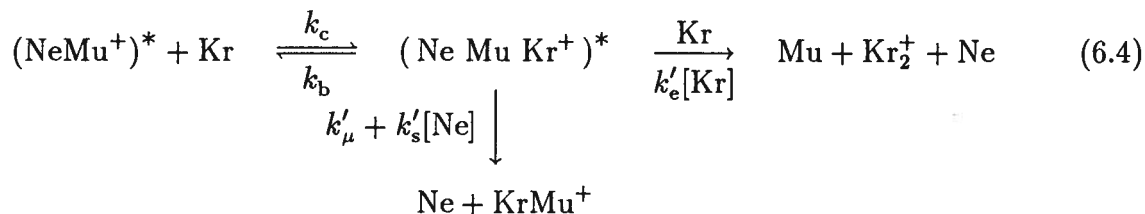
In this mechanism, as opposed to any considered so far, two Kr atoms react sequentially, and both the initial capture and the subsequent Mu formation should have comparable rates ($k_c \approx k_e'$). However, muon transfer (k_μ') should be *much* faster than this. The k_μ' dissociation channel is endothermic (for a ground-state complex) by just ~ 10 kJ/mol, while the k_e' channel is endothermic ≈ 360 kJ/mol, which is the minimum excitation energy of (NeMuKr$^+$)* to account for the observed depolarization. A simple RRK [218] estimate of k_μ' is then

$$k_\mu' \approx \nu \left(\frac{360-10}{360}\right)^{s-1} \approx \nu \qquad (6.5)$$

where s is the number of vibrational modes in the complex (or, more typically, about half that number), and ν can be approximated by a vibrational frequency; in this case, $k_\mu' \approx \nu \gtrsim 10^{12}\,\text{s}^{-1}$. On the other hand, $k_e'[\text{Kr}] \approx k_L[\text{Kr}] \approx 10^7\,\text{s}^{-1}$, so essentially *all* the reacting ions would react by muon transfer, even though Mu formation is energetically feasible.

Another feature of the reaction scheme (6.4), which it shares with the previously-considered capture mechanism (4.19), is cyclic capture and break-up (with the unimolecular dissociation rate constant k_b). Rapid dissociation of such a highly energized complex to re-form the original reactants is to be expected, and can serve to reduce k_{exp} below k_c; in this case $k_c/k_{exp} = (k_b + \sum k')/\sum k' = 16$. A high k_b is to be expected from the lack of available vibrational states in the $NeMuKr^+$ complex. No real calculations have been done for this (or any of the other) complexes, but this one is only triatomic, and it has lighter constituents (thus, wider rovibrational spacings) than the corresponding triatomic xenon complex. Only $HeMuKr^+$ is likely to have fewer available states, in accord with the absence of depolarization there. The problem here is that the excited $(NeMu^+)^*$ ion would likely *not* be restored after a cycle of capture and breakup. Instead, quenched $NeMu^+$ should result, which could not subsequently form Mu, but only $KrMu^+$.

In summary, this model has been considered because there is no other apparent way for charge transfer forming Mu to occur in the $NeMu^+ + Kr$ reaction. It does, however, have several shortcomings:

- The complex would likely not last long enough to encounter a second Kr; its breakup would be rapid, especially through the muon-transfer channel (k'_μ). Thus, no charge transfer should have been seen. Instead, the observed charge-transfer rate was only marginally lower than for muon transfer.

- No charge exchange reaction was seen for the similar systems $HeMu^+ + Kr$ and $NeMu^+ + CO$.

- The mechanism gives a reaction rate that is second-order with respect to [Kr], and third-order overall, but the observed kinetics were clearly first-order with [Kr].

Perhaps the complex is much more long-lived than expected. Perhaps the two Kr atoms are not independent, but are bound as Kr_2 — another extremely unlikely circumstance at the temperatures and pressures employed. Depolarization of $KrMu^+$ due to spin–

rotational interactions could also be considered, thus circumventing the requirement for forming Mu. This effect is expected to be minimal [219], but studies in this direction would be useful. At the moment, there is no clear explanation for the observable reaction between NeMu$^+$ and Kr.

6.3 Analysis of Quenching by the Moderator

Moderator quenching rates are listed in tables 4.1 and 4.3 but these show a lot of scatter influenced by variations in moderator purity. More consistent measurements of k_q, made by varying the moderator pressure with the same reagent gas, were reported in section 4.8. The strongest effect of quenching was on the relative amplitudes of the signals, especially for CH_3F, shown in figure 4.7d. The relaxation rates varied less (table 4.6) and, strangely, the total relaxation rate for xenon *decreased* with increasing pressure.

Although variations in the apparent k_q, have been attributed herein to impurity (most likely water vapor), there are indications that quenching still makes a contribution. First, quenching of the energized complex could affect the amplitudes more than the rates, while a parallel proton (muon) transfer reaction with a dilute impurity is much less likely to. Secondly, there are the cases where quenching should have *no* effect, and the amplitudes *did* agree with the relaxations.

Several of the neutral gases studied are able to form Mu even when the ion is in its ground state, yet excitation might still increase the rate of charge transfer in those cases as muon transfer is the more exothermic reaction. Nitric oxide and oxygen form paramagnetic ions [152,209] after muon transfer, which should themselves be depolarized, so quenching should have *no effect* for them. Comparing the values of 'k_q' derived from the relaxation rates (table 4.1) and the amplitudes (table 4.3) shows relatively low values for these two cases and good agreement between the methods, confirming that quenching is unimportant for NO and O_2, and also suggesting an impurity concentration: $[H_2O] \approx 0.4 \times 10^{-10}$ cm^3 molec^{-1} s^{-1}. This level should be reproducible for exper-

iments performed with cold-trapping, or at least for those performed contiguously with the O_2 and NO runs, but k_q is often much higher, indicating that quenching is indeed important.

Some measurements of quenching were made with argon as a collider, but these differed from the pressure dependences in that small quantities of Ar (0–2 torr) were added to NO/Ne and N_2O/Ne mixtures; the NO and N_2O served as monitor gases for the $NeMu^+$ excitation. The results of these measurements are shown in figures 6.1 and 6.2. The simple-model prediction is for the relaxation rate to increase linearly with [Ar], and for A_s/A_f to do the same since $k_e^{Ar} = 0$:

$$\lambda_f = k_c[X] + k_q^{Ar}[Ar] + k_q^{Ne}[Ne] \tag{6.6}$$

and

$$\frac{A_s}{A_f} = \frac{k_q^{Ar}[Ar] + k_s^{Ar}[Ar][X]}{k_e[X]} + \frac{k_D[X] + k_q^{Ne}[Ne]}{k_e[X]} \; . \tag{6.7}$$

Fits to these equations were used to give the results in table 6.1, using the values of k_e from table 4.4. These fits show again that quenching affects the relaxation rates much less than the amplitudes, just as happened for the pressure dependences, indicative of stabilization of the complex. There is also a much greater quenching effect for N_2O than for NO, with $k_q + k_s[X]$ a factor of 60 larger!

N_2O has a much higher IP than NO (12.89 vs. 9.26 eV) and will undergo charge transfer only if the $NeMu^+$ is excited. NO will undergo charge transfer even with ground-state $NeMu^+$; furthermore, any $NOMu^+$ formed by muon transfer will be depolarized as if it were Mu, so it is to be expected that quenching would have little effect on NO reactivity, and be more important for N_2O. The fact that this expectation is borne out (table 6.1) indicates that the argon reaction in N_2O/Ne *really is collisional quenching* of $NeMu^+$ rather than formation of $ArMu^+$, either initially or through muon transfer. The rate constant determined from the NO relaxation rates is within errors of $k_q + k_s[X]$
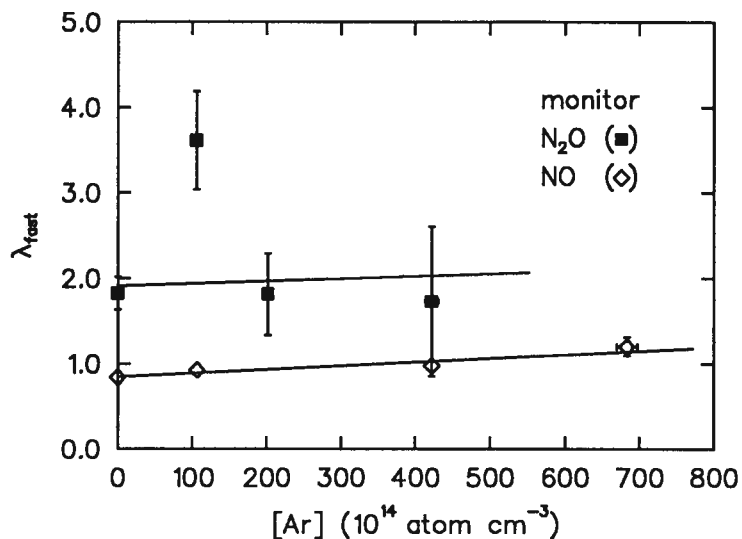
Figure 6.1   The effect of argon on the total reaction rate of NeMu$^+$ with N_2O (■) and NO (◇) monitor gases. The effect is small in both cases although the N_2O results are very scattered.
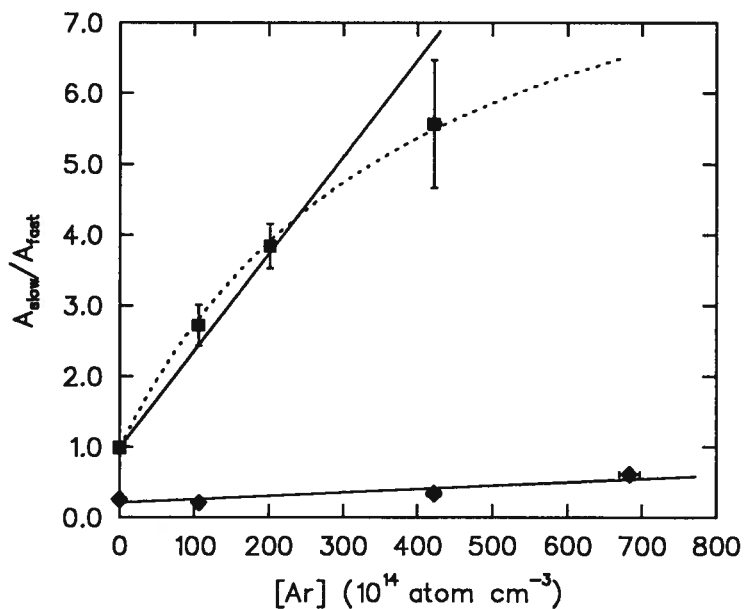
Figure 6.2   The effect of argon quenching on the amplitudes for N_2O (■) and NO (◇) showing how the endothermic N_2O reaction is affected much more by quenching than the exothermic NO reaction. The curves are explained in the text.

Table 6.1 Results from Measurements of Argon Quenching of $(NeMu^+)^*$

X	$[X]^a$	$k_e{}^b$	from λ_f	from A_s/A_f	
			k_{exp}	$k_q^{Ar} + k_s^{Ar}[X]$	k_e^{Ar}
N_2O	20.1	8.57 ± 0.68	0.028 ± 0.124	1.78 ± 0.27	0^c
				3.1 ± 1.1	0.32 ± 0.27
NO	7.33	6.45 ± 0.80	0.043 ± 0.015	0.0302 ± 0.0085	0.00 ± 0.06

^{a} Concentrations of N_2O and NO were held constant while the [Ar] was varied; concentrations given in 10^{14} molec cm^{-3}.

^{b} Values for k_e taken from table 4.4, this thesis. All the rate constants have units of 10^{-10} cm^3 molec^{-1} s^{-1}.

^{c} Although k_e should be zero for Ar, it gave a higher value in one fit. The uncertainties of the points do not support the addition of this parameter; it should be taken as zero.

determined from the amplitudes, but the reaction is not really quenching in the NO case. Instead, it is likely to be the muon-transfer reaction forming ArMu$^+$. Of course, the presence of NO does not *stop* the quenching process, but merely masks it.

The $k_q + k_s[N_2O]$ determined by the amplitudes for N_2O is $1.78 \pm 0.27 \times 10^{-10}$ cm^3 molec^{-1} s^{-1} (the solid line in figure 6.2), which, for $k_c = k_L = 8.18 \times 10^{-10}$ cm^3 molec^{-1} s^{-1}, says that argon quenches NeMu$^+$ with an efficiency of 0.22 — one in five collisions causes de-excitation. This is 11 times higher than the efficiency with which Ar quenches $(ArH^+)^*$ [149, but questioned in 198], it is 150 times the efficiency for $(O_2^+)^*$ [153], and very much higher than for $(NO)^*$ [154], but it is less than the quenching efficiency of Ar on $(HCl^+)^*$ [79]. The quenching rate for Ar seems surprisingly high, given the sparse rovibrational states of NeMu$^+$. Tichy et al. had a similar surprise in their study of $(HCl^+)^*$ quenching [79].

The curved dotted line shown in figure 6.2 is a fit that allowed for some Mu forma-

tion (or at least some depolarization) by Ar. Although the fit is 'better,' it uses three parameters for only four points and charge transfer with Ar is simply not possible. The perfectly reasonable linear fit is chosen instead.

Comparing the $k_q + k_s[X]$ values determined by the amplitudes for CH_3F in table 4.6 with the Langevin collision rate shows quenching efficiencies of 0.0004 for $He + (HeMu^+)^*$, and 0.00014 for $Ne + (NeMu^+)^*$. Both are a factor of ~ 1000 lower than the Ar quenching efficiency, and both are in accord with the usual low efficiencies for He or Ne quenching [16,79,153,154,156,157,206–208]. For the cases of He and Ne quenching, the moderator is also a constituent of the molecular ion, and the quenching mechanism may be more than collisional de-excitation, with some ligand switching

$$(NeMu^+)^* + Ne' \longrightarrow Ne'Mu^+ + Ne \tag{6.8}$$
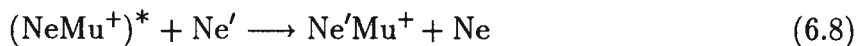
occurring as well. Such an exchange should be more effective than a simple collision for removing vibrational excitation. Exchange is not absolutely necessary for this effectiveness, however. If there is an intimate collision to form a transient Ne_2Mu^+ complex wherein vibrational energy is randomized, it is immaterial which Ne eventually leaves. Since the observed quenching efficiencies were so low, this type of switching appears unimportant.

As stated, the relaxation rates are not much affected by quenching, whether by added Ar or by the Ne bath gas, while the amplitudes are (tables 4.6&6.1). This difference was interpreted as being due to quenching of the association complex, with rate $k_s'[Ar][NeMuN_2O^+]$, or the apparent overall rate $k_s[Ar][NeMu^+]$. The difficulty with this interpretation is similar to that for the termolecular Kr reaction model in section 6.2: the complex should have too short a lifetime for it to collide with Ar at the concentrations utilized. On the other hand, the lifetime of $NeMuN_2O^+$ may be much longer than for $NeMuKr^+$. Note that muon transfer to Ar, which should also be expected to occur, would have the same effect on the relaxation rates as on the amplitudes, just as was observed for the NH_3 monitor ion measurements of the C_2H_6 and H_2O reactions (table 5.4).

An alternative explanation for the pronounced effect of quenching on the amplitudes relative to the relaxations is that quenching of $(NeMu^+)^*$ may not produce ground-state $NeMu^+$; instead, a lower excited state should be populated for which charge transfer (depolarization) is still possible, i.e., a state still above the threshold for charge exchange. This lower state would presumably have a much higher k_μ/k_e branching ratio, but still be capture-limited. Other experiments [79,201,202,220] have seen endothermic reactions 'turn on' when excitation reaches threshold (which is how the simple model treats quenching) but still increase a lot as the excitation is increased further [156,221]. Furthermore, when endo- and exothermic reactions compete, as is the case here, the exothermic reaction rate may also decrease with excitation level [220]. Such behavior would cause k_μ/k_e to increase with decreasing excitation, to give the observed trends in the amplitudes while the continued presence of depolarization would keep the total relaxation rate nearly constant. Two inconsistencies with this description, though, are that there may not be enough states available in $HeMu^+$ or $NeMu^+$, and different reactants (N_2O, CH_3F) with different thresholds behave qualitatively the same. It is too unlikely to have de-excitation to a state just above threshold in each case, especially when there are so few states available.

This "weak quenching" picture makes more sense for stabilization of the loosely associated capture complex, which would affect the branching ratio of the reactions from the complex in the way just described. There could still be some degree of direct quenching of $(NeMu^+)^*$, along with muon transfer producing $ArMu^+$ to give the (small) increase in relaxation rate with quenching and the non-zero intercepts of λ_f vs. [X].

There is wide scope to extend these measurements: by varying the neutral reagent (the monitor, X) to set different reaction thresholds, by varying its concentration looking for evidence of termolecular quenching $Ar + X + NeMu^+$, by varying the quencher, and by studying quenching of $(HeMu^+)^*$.

6.4 Neon Moderator Pressure and the Xe + NeMu$^+$ Reaction

The case of xenon is interesting, albeit confusing, with many anomalies not understandable within a simple competition-kinetics model. Noteworthy are the consistently low experimental "capture" rate constants reported in tables 4.1 and 4.4, for both He and Ne moderators — only half the Langevin predictions. Xe + NeMu$^+$ is such a simple system that the Langevin rate should give the real collision rate. The measured rates also exhibited an unusual reverse pressure dependence (table 4.6, figure 4.9), decreasing with increasing moderator pressure. Less consistently, Xe measurements have given curved kinetic plots, which delayed understanding the processes involved, if indeed they are understood yet.

Is the unusual behavior of xenon mere perversity, or is it made understandable by a more sophisticated kinetic model? What features must such a kinetic scheme have to reproduce the observations? Answering these questions consumed a disproportionate amount of time and effort in comparison with elucidating the simple capture kinetics exhibited by other reactants. Like the krypton conundrum, there is no single satisfactory answer, but an exploration of the possibilities is useful. One option would be to drop the notion of ion–molecule capture entirely, but that would be rash. If the measured rates were much faster than the Langevin capture rate, it might be necessary to invoke long range interactions that supersede capture, but the actual rates are *lower* than the predicted capture rates so it is reasonable to say that the initial capture still operates, but it is not the limiting step because of rapid breakup.

As a start to understanding the pressure dependence of the 'fast' relaxation λ_f for Xe + NeMu$^+$, with reference to table 4.6 note that the simple-model (linear) fits gave negative values for "k_q" that were roughly proportional to Xe concentration. Thus, without defining $k_?$, $\lambda \sim k_c[\text{Xe}] - k_?[\text{Xe}][\text{Ne}]$, where k_c need not be the real capture rate. On the surface, none of the models considered in chapter 4 give this behaviour, but on

closer examination the general mechanism of cyclic capture and breakup (4.19) may well apply if the dissociation of the complex could involve the moderator, with k_b replaced by $k_b[Ne]$. The limiting solution (4.31) can then be expressed as

$$\lambda = \frac{k_c[Xe](k'_e + k'_\mu)}{k_c[Xe] + k_b[Ne] + k'_e + k'_\mu} \tag{6.9}$$

which, for large values of $k'_e + k'_\mu$ is approximated by

$$\lambda = k_c[Xe] - \frac{(k_c[Xe])^2}{k'_e + k'_\mu} - \frac{k_c[Xe]\, k_b[Ne]}{k'_e + k'_\mu} \tag{6.10}$$

[by expanding around $1/(k'_e + k'_\mu) = 0$], which closely matches the desired behaviour.

Based on this promising approximation, the measured rates were fitted using the general expression for λ_-, eq. (4.29), giving the curves displayed in figure 6.3. The agreement with the data is remarkable, including the points at $[Xe] = 44.5 \times 10^{14}\,\text{molec}\,\text{cm}^{-3}$,

$[Xe] = 50.5$ (●), 44.5 (◇), 14.4 (■)
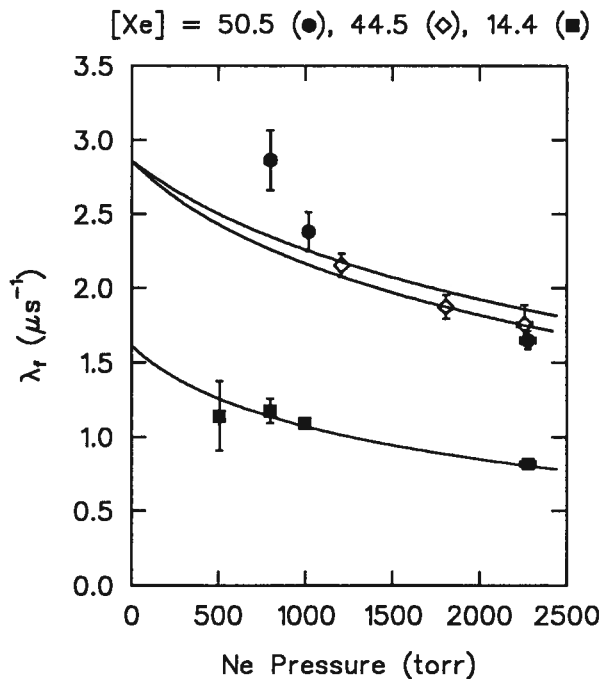
Figure 6.3 Simultaneous fits of equation (4.29) to the neon pressure dependence of the fast relaxation rate for three concentrations of xenon: 50.5 (●), 14.4 (■), and 44.5 (◇) $\times 10^{14}\,\text{molec}\,\text{cm}^{-3}$. The two variable parameters were determined to be $k_b = 2.78 \pm 0.34 \times 10^{-14}\,\text{cm}^3\,\text{atom}^{-1}\,\text{s}^{-1}$ and $k'_e + k'_\mu = 2.86 \pm 0.15\,\mu\text{s}^{-1}$, with k_c fixed at $11.23 \times 10^{-10}\,\text{cm}^3\,\text{molec}^{-1}\,\text{s}^{-1}$, the Langevin value. Releasing k_c gave an almost identical fit.

Table 6.2 Results of Fits to the $Xe + NeMu^+$ Pressure Dependences

Fit what, with what	$k_c{}^a$	$k_b{}^b$	$k'_e + k'^c_\mu$
All points, all variables	13.4 ± 1.4	4.5 ± 1.2	3.06 ± 0.20
44.5 points omitted	13.5 ± 1.5	4.3 ± 1.3	2.93 ± 0.22
All points, k_c fixed	11.23	2.78 ± 0.34	2.86 ± 0.15
No 44.5 points, k_c fixed	11.23	2.60 ± 0.34	2.74 ± 0.17

$^a\ 10^{-10}\,cm^3\,molec^{-1}\,s^{-1}.$ $^b\ 10^{-14}\,cm^3\,atom^{-1}\,s^{-1}.$ $^c\ \mu s^{-1}.$

which were at first thought to be amiss. If the fit is performed omitting these points, the results are almost the same, indicating that both the data and the fits are reasonable. Fits were done with k_c both as a free parameter and fixed at its Langevin value. With the capture rate variable, it became slightly *higher* than the Langevin value, although the difference is barely significant. The results of all these fits are shown in table 6.2. One point of passing interest is that the curves in figure 6.3 have very similar slopes, even though an expectation of varying slopes led to the consideration of this model.

Why should there be a discernable back reaction for xenon, but apparently not for other neutrals? Perhaps it is the lack of vibrational modes among which to distribute the excess energy of $(Xe\,Ne\,Mu^+)^*$, making it susceptible to rapid breakup. This has already been indicated for the Kr case. Or maybe the unimolecular rate constants k'_e and k'_μ are unusually low, as indicated by the fits, giving more time for breakup. These two possibilities are antagonistic in that instability of the complex should promote all forms of breakup, including dissociation into products. A large barrier to Mu^+ transfer within the complex would be necessary for such a low k'_μ. In addition, what role could the moderator play in the back reaction? Thermal collisions should *stabilize* the complex rather than break it apart. The moderator-mediated breakup fits the pressure dependent reaction rates well, but seems physically untenable, and leaves many unanswered questions.

This mechanism partially accounts for curved λ_f vs. [Xe] plots (fig. 6.6) because of the 'fall-off' regime where $\lambda_- \approx \lambda_+$, with the rate leveling off at $k'_e + k'_\mu = 3\,\mu s^{-1}$ at high xenon concentration. Yet this does *not* agree with the *straight* lines that were usually seen for Xe (and for other reactants) including maximum relaxation rates well above $3\,\mu s^{-1}$. Despite its partial success in describing the reaction rates, the cyclic capture mechanism does not agree with other aspects of the Xe results. The amplitudes of the two components would not vary with Xe concentration under such a mechanism, in contrast to the measurements listed in tables 4.3 and 4.6 (see also figure 4.7). And surely, there should be quenching of the $(NeMu^+)^*$ through a cycle of capture and breakup. Additionally, the observed signals did not show the two-fast, one-slow relaxations predicted by this, and the other, explicit capture models. While this last difficulty may really be no problem at all, there are too many contradictions to take the good fits at face value.

6.5 Modeling the Anomalous Xenon Results

Besides having λ_f varying non-linearly, one set of results — Xe in Ne at 177 K — showed the ratio A_s/A_f non-linearly *decreasing* with Xe concentration (illustrated below in figure 6.6) whereas it increased linearly within most sets of Xe (and other) data in accord with the simple model prediction, eq. (4.13). Such a unique anomaly is easy to dismiss, especially since a non-relaxing wall signal, if left unaccounted for, could cause the same result; but other data taken at the same time show no such behavior, indicating that the xenon reagent might be responsible. The following explanation has some major difficulties, and it should not be taken too seriously, but it is presented nonetheless as it has wider implications for the application of the general capture mechanism (4.19) to the μSR results.

As mentioned in the previous section, ion–neutral capture to form a long-lived complex, as in mechanism (4.19) should match the observation of the λ_f vs. [Xe] line curving down at high xenon concentration: the rate of the second (unimolecular) step, which is

independent of reactant concentration, places an upper limit on the overall reaction rate so the line must curve as this limit is approached. In general, downward curving (concave) rate curves are indicative of sequential reactions of different order while upward curving (convex) curves come from parallel reactions. The strange behavior of the amplitudes in the same series of runs may indicate that the depolarizing (charge-transfer) reaction channel loses effectiveness relative to other channels as Xe is added. To achieve this behavior, xenon must be involved in the secondary reactions, either interfering with charge transfer, or contributing to other channels. One candidate for such a process is collisional de-excitation of the capture complex by the *reagent*: Xe is a much better quencher than He or Ne [157,190]. Such a process, with rate constant k_r' [eq. (4.19)] can be regarded both as a competing reaction channel and as a process interfering with charge exchange. The expectation expressed in section 4.5 was that k_r' could be ignored because it would be much lower than the competing rates. The fits in the previous section gave very low breakup rates, so k_r' may be considered anew.

Ignoring the pressure dependence for the moment, there is one other requirement for a successful description of the Xe reaction: the deviation from a simple two-component relaxation envelope must be small. This requirement is demanded by scrutiny of the actual histograms which revealed no extra relaxation components. As mentioned in section 4.6, such components are to be expected of a two-step mechanism when the rates of the two steps are different but comparable.

A mechanism intended to meet these requirements is:

$$\text{Mu} + \text{Xe}^+ + \text{Ne}$$

$$k_e' \uparrow$$

$$(\text{NeMu}^+)^* \xrightarrow[\text{Xe}]{k_c} (\text{NeMuXe}^+)^* \xrightarrow{k_\mu'} \text{XeMu}^+ + \text{Ne} \qquad (6.11)$$

$$k_q \downarrow \text{Ne} \qquad\qquad k_r' \downarrow \text{Xe} \qquad \nearrow$$

$$\text{NeMu}^+ \qquad\qquad \text{NeMuXe}^+ \, .$$
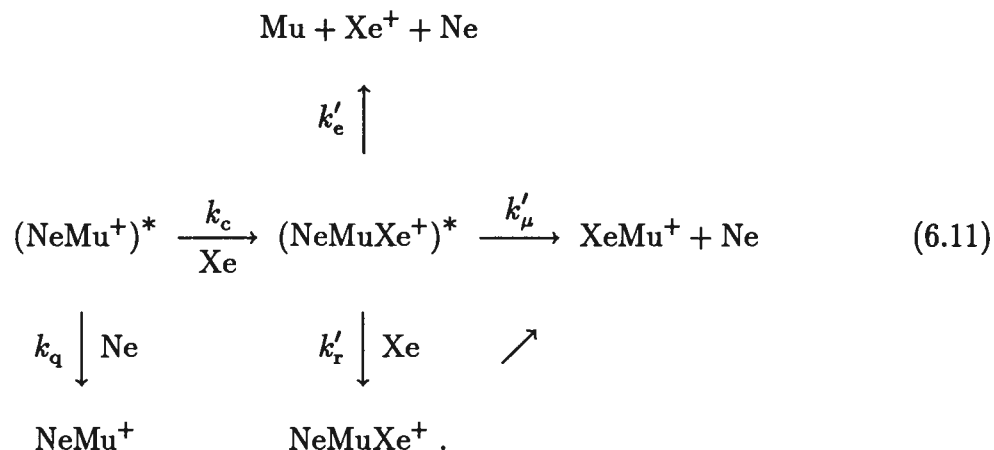
The channel for collisional stabilization of the capture complex by Xe, with a rate of $k_r'[\text{Xe}]$, produces NeMuXe^+, which no longer has sufficient energy to undergo charge transfer, so it is limited to forming diamagnetic XeMu^+. This mechanism clearly meets the requirements of being two-step with a second Xe atom participating in the secondary reactions, although it is not obvious that it could produce spectra with apparently only one relaxing component. The time dependence of the diamagnetic signal (or of the concentration of all diamagnetic species) is

$$\frac{[\text{D}]}{[\text{D}]_0} = \left(1 - \frac{\lambda_3}{\lambda_1 \lambda_2}\right) + \frac{\lambda_3}{\lambda_1 - \lambda_2}\left(\frac{e^{-\lambda_2 t}}{\lambda_2} - \frac{e^{-\lambda_1 t}}{\lambda_1}\right) \qquad (6.12)$$

where

$$\lambda_1 = k_c k_e'[\text{Xe}]$$

$$\lambda_2 = k_e' + k_\mu' + k_r'[\text{Xe}]$$

$$\lambda_3 = k_c[\text{Xe}] + k_q[\text{Ne}]$$

which is a slight simplification of the similar mechanism (4.30), but such a dependence was originally rejected because the form of the observed relaxation didn't support it. The time has come for a second look.
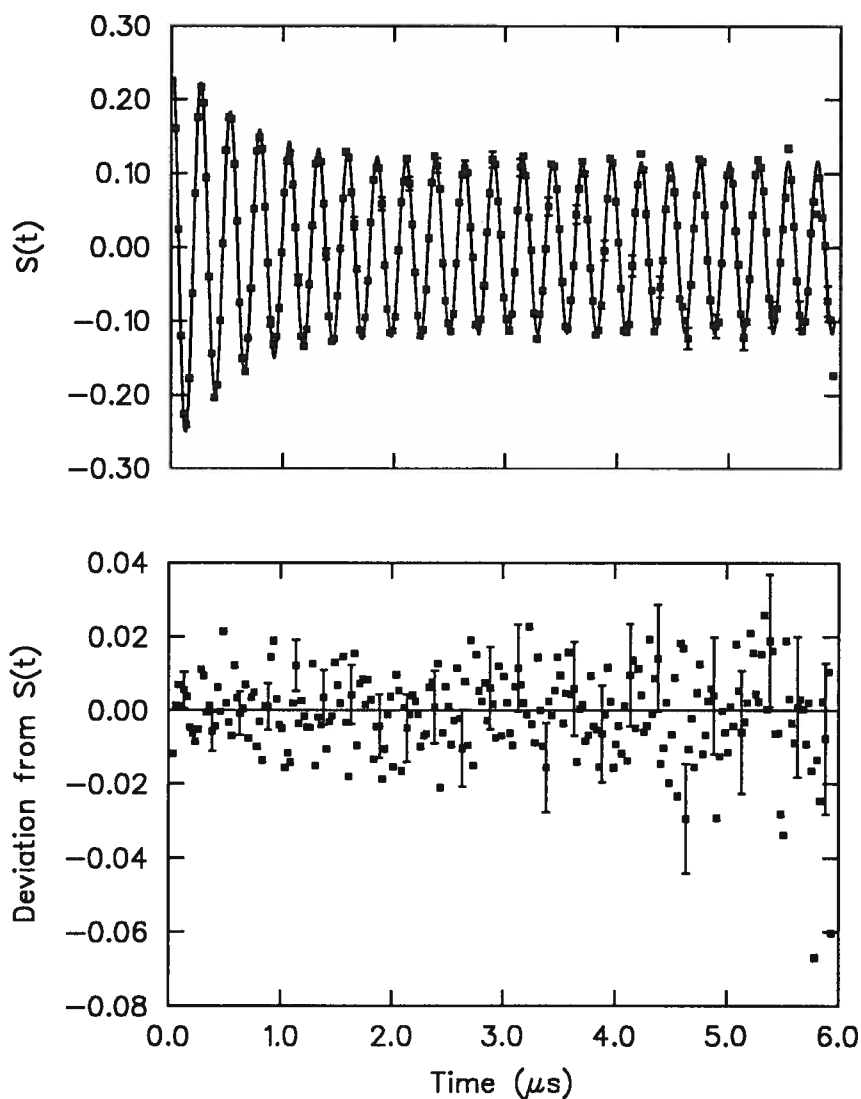
Figure 6.4   The simple model fitted to a representative synthetic data run based on the Xe model showing the asymmetry signal on top and the difference between the points and the fit below. Although the points were generated with three components to the relaxation and fitted with only two, there is hardly any residual signal in the lower plot (note the expanded scale there). This run corresponds to the $[X] = 40 \times 10^{14}$ molec cm^{-3} point of figure 6.5

To investigate whether a three-component relaxation could appear to have only two components in the present experiments, and also to assess the relevance of the specific Xe capture/quenching model, several runs were simulated with 'decay' asymmetries given by equation (6.12) using a wide variety of values for the relevant rate constants but with the capture rate always set to $11 \times 10^{-10}\,\mathrm{cm^3\,molec^{-1}\,s^{-1}}$, the Langevin rate. Random scatter was given to the points using the counting statistics appropriate for a better-than-typical run (4 million events). The runs were then analysed according to the simple model with only two components to the relaxation. For most combinations of parameters the fits were surprisingly good, with the residual signals not visible against the random scatter of the points. One representative run is illustrated in figure 6.4, with the asymmetry plot on top and the difference between the data and the fit shown as difference in asymmetry below. The fit gives a relaxation rate of $\lambda_f = 1.71\,\mu s^{-1}$ which is not closely related to any of the input parameters. Indeed this is the general situation — good fits which do not give back the input parameters. Good fits were expected for limiting cases with one step much faster than the other, but this result was a surprise. Moreover, it was very difficult to find combinations of parameters that did *not* give straight or near-straight λ_f vs. concentration plots, such as figure 6.5.

What, then, of the curved plots of both λ_f and A_s/A_f (figure 6.6) for the Xe reaction? Parameters were found that do mimic this behavior: k'_e, k'_μ, and $k_q[\mathrm{M}] = 2.7$, 0.6, and $0.0\,\mu s^{-1}$ respectively, with $k_c = 11$ and $k'_r = 0.9 \times 10^{-10}\,\mathrm{cm^3\,molec^{-1}\,s^{-1}}$, giving the results shown in figure 6.7. The remarkable similarity of figures 6.6 and 6.7 demonstrates the viability of both the mechanism and the specific parameters used, but it does not amount to a *measurement* of those parameters. Nevertheless, these values can still serve as a guide to the relative importance of each channel. In particular, note that k'_r is only 1/12 the value of k_c, yet it has a great effect on the amplitudes, causing A_s/A_f to decrease instead of increasing with reciprocal concentration, and to curve in just the way that the Xe results do.

The other notable parameter is k_q, which has a value of zero, effectively nullifying that channel and simplifying the mechanism to

$$\text{Mu} + \text{Xe}^+ + \text{Ne}$$

$$k_e' \uparrow$$

$$(\text{NeMu}^+)^* \xrightarrow[\text{Xe}]{k_c} (\text{NeMuXe}^+)^* \xrightarrow{k_\mu'} \text{XeMu}^+ + \text{Ne} \qquad (6.13)$$

$$k_r' \downarrow \text{Xe} \qquad \nearrow$$

$$\text{NeMuXe}^+ .$$
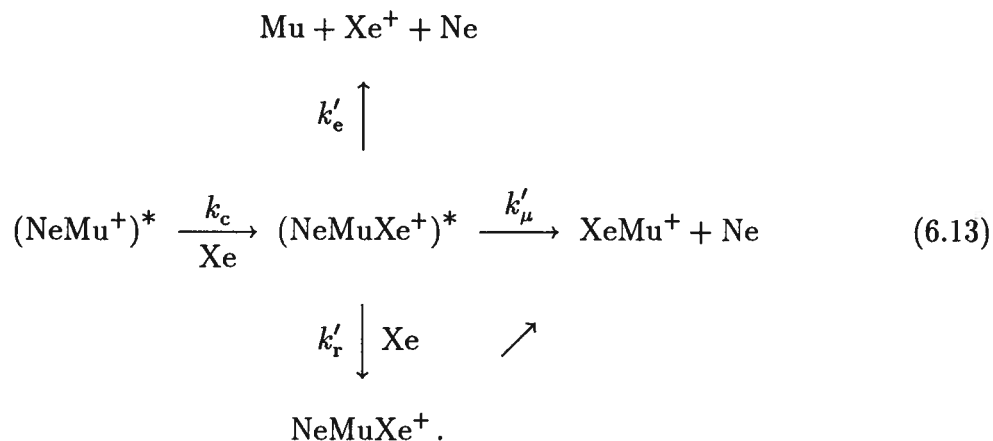
leaving no moderator effect, in disagreement with the data. This is a serious blow, especially after the cyclic capture model fit the pressure dependences so well.
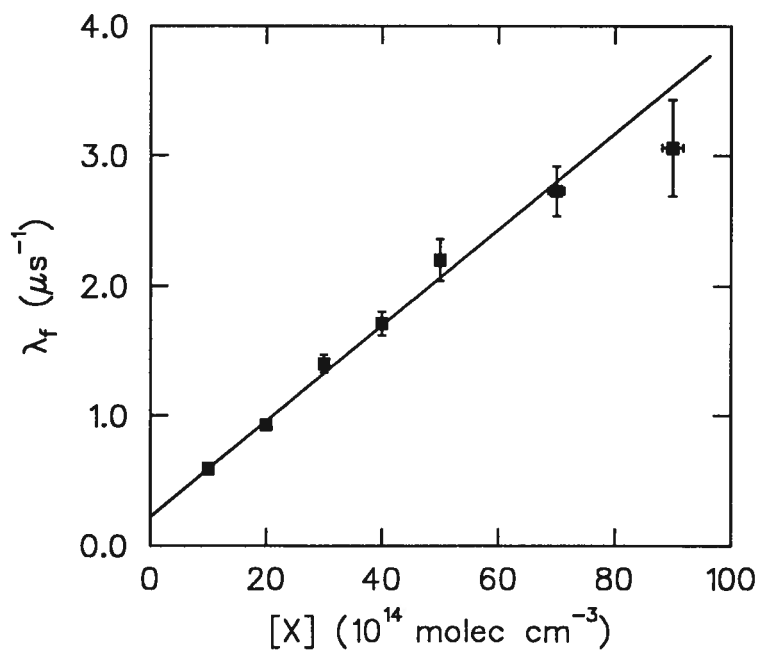
Figure 6.5 The near-linear dependence of λ_f on idealized reactant concentration for a series of synthetic runs showing an apparent $k_c = 3.7 \times 10^{-10}$ cm^{3}molec^{-1}s^{-1} although the value used to generate the data was $k_c = 11.0 \times 10^{-10}$ cm^{3}molec^{-1}s^{-1}. Other parameters were $k_e' = 1.5$ μs^{-1}, $k_\mu' = 0.2$ μs^{-1}, $k_r' = 3 \times 10^{-10}$ cm^{3}molec^{-1}s^{-1}, and $k_q[\text{M}] = 0.1$ μs^{-1}.
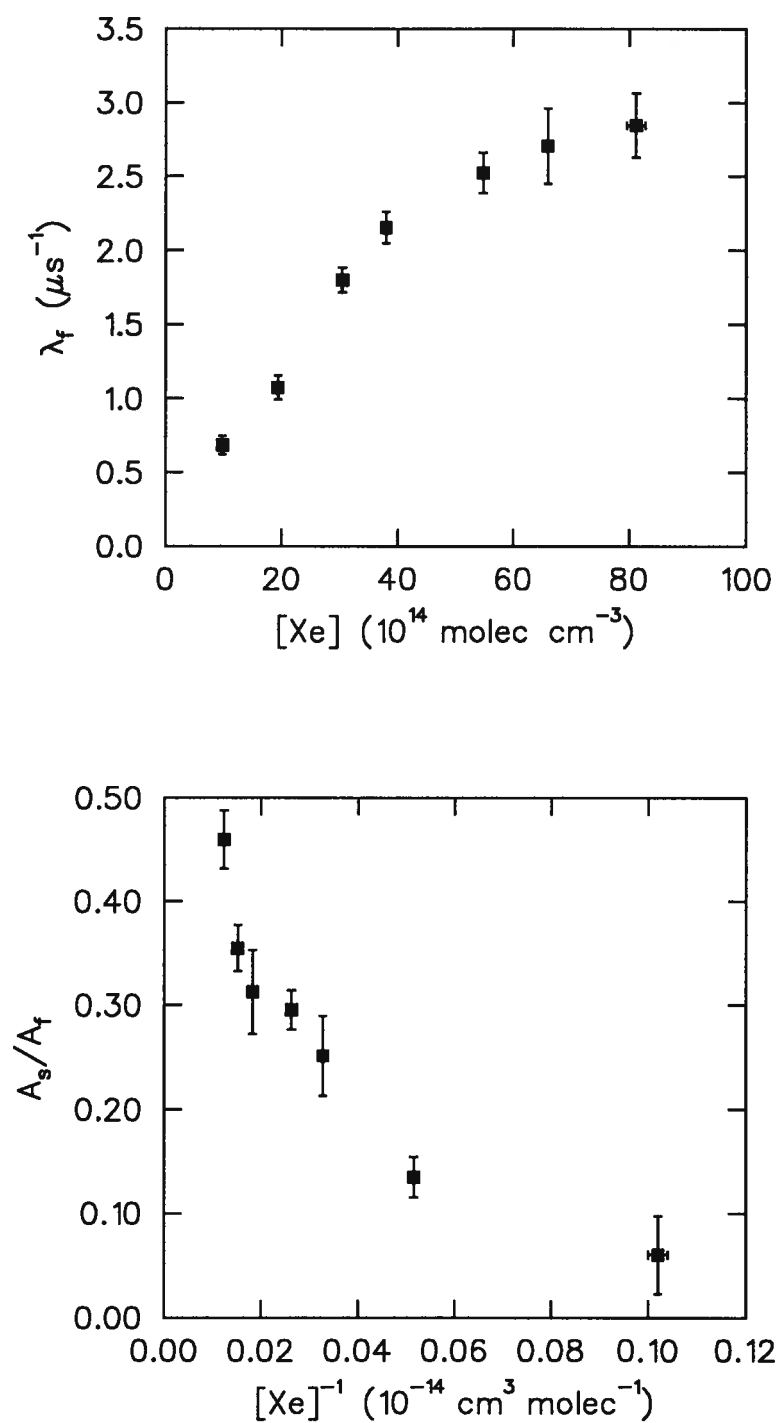
Figure 6.6   Experimental results for Xe + NeMu$^+$ at 177 K showing the non-linear dependence of λ_f on [Xe] (top) and the very unusual decrease in A_s/A_f with [Xe]$^{-1}$ (bottom).
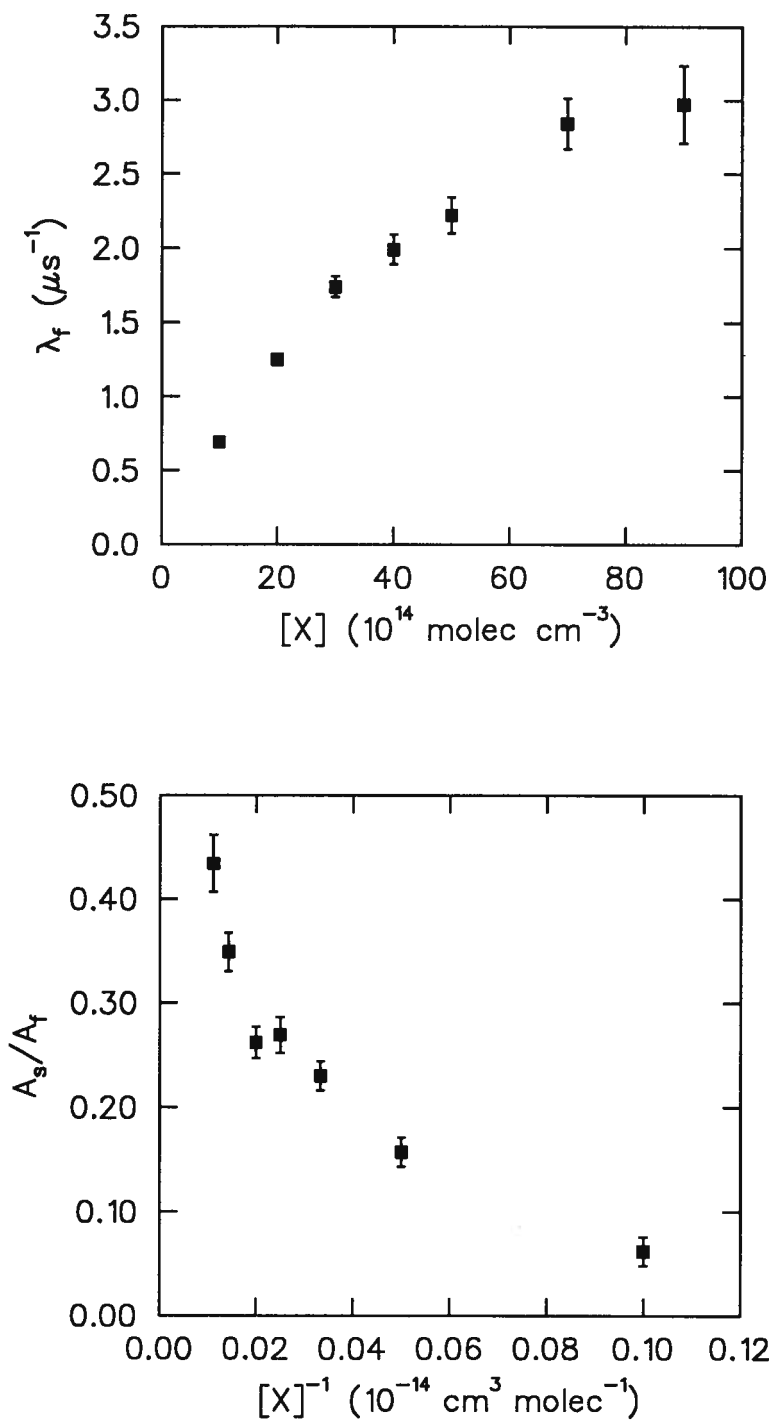
Figure 6.7 Results synthesized to mimic the Xe data shown in the previous figure. Each reactant 'concentration' [X] corresponds to a histogram generated using the parameters given in the text, and analyzed according to the simple model.

Since only one set of data in fact showed the unexpected increase in A_s/A_f with Xe concentration, invoking special mechanisms to explain these results is probably not warranted. The cause is more likely to be an isolated spurious artifact of muons stopping in the target walls; the diamagnetic μSR signals of a molecular ion and of a muon in aluminum are virtually indistinguishable, and it is very difficult to ensure that all muons stop in the gas. Measured values of A_s were always corrected for the wall signal amplitudes, and the corrected amplitudes usually behaved as predicted, but if the wall correction used was too small, the resulting inflated values for A_s could give just the dependence shown in figure 6.6 (top). The results seen at 177 K were not observed in any other Xe data, suggesting that they are such an artifact, even though 'normal' results were obtained for other reagents just before the Xe runs were taken. It is likely that for the one anomalous series of Xe runs, some shift in the beam tune or apparatus position caused an increased wall signal that went unnoticed, so it is best to just ignore the unusual amplitudes.

It is possible for a wall signal to interfere even more insidiously when it has a slightly different frequency, phase, and/or relaxation rate from the molecular ion signal. The obvious solution is to include all the wall signal parameters in the analysis of each histogram, but this does not work. As shown by the synthetic data presented in this section and by experience with actual runs, signals with extra components are fitted well by a simpler function, while the introduction of extra parameters leaves the function over-determined and insensitive to the chemical signal. The magnitude of this problem depends on the natural amplitude of the relaxing component: when the amplitude is small, the wall problem is severe. The amplitudes depend on reagent concentration, and when the influence of the wall signal varies with the concentration, curved kinetic plots may result.

With these considerations, it is reasonable to abandon the special-purpose Xe capture/quenching mechanism (6.11), and attribute the anomalies observed at 177 K to wall signals. But the modeling of those (unreliable) results has shown that an extraordinarily long-lived complex could be accommodated within the present data with only a

two-component relaxation observable. The relaxation function of the xenon model, equation (6.12), is really no different from that of the generalized capture model, given in equation (4.30); in particular, both can be fitted well by the simpler equations (4.26), (4.16), or (4.32) to give values for λ_f that depend linearly on concentration. The implication is that straight lines might not always give the capture rate; subsequent reactions may affect the overall rate with no outward indication. Such cases cannot be identified by their multi-component relaxations. In addition, when deviations from the simple mechanism are evident, it is not practical to fit the data assuming a more complex mechanism because several different models may fit equally well. This was mentioned earlier, but it bears repeating: the capture mechanism places an upper bound on the overall reaction rate, but not all "k_{exp}" rate constants reported in this thesis are capture rate constants — some of the reactions are not capture limited. The difference between k_{exp} and the calculated k_c (k_L, k_{AADO}; see tables 5.1&5.3) indicates the extent of the departure from simple capture kinetics.

In figure 6.7, note that there is an apparent intercept, $\lambda_f(0) > 0$, even though a value of $k_q = 0$ was used to generate the data. This casts doubt on the general interpretation of such intercepts as giving $k_q[M]$. Such an interpretation already had problems though, as the values were not the same for different reagents X, probably because of impurities in the moderator gas.

6.6 Weak Quenching of the Capture Complex

The results of modeling have shown that the Xe and Kr data are insufficient to fully determine the reaction mechanism involved; such attempts lead to unrealistic models — ones with very long-lived complexes and moderator-assisted breakup. Measurements of quenching by Ar and Ne showed that stabilization of the complex is more effective than quenching of the initial excited ion. An acceptable model of this stabilization must be more intuitively satisfying.

Returning to the reverse pressure dependence of the Xe reaction rate, it certainly seems reasonable that the increased quenching at higher pressures would decrease the rate of the endothermic Xe reaction, which relies on reactant excitation. Such a mechanism would necessarily involve 'weak quenching' whereby each collision with the moderator gas decreases the excitation energy slightly. In particular, each collision with Ne may reduce the excitation of $(XeMuNe^+)^*$ slightly, reducing the rate of unimolecular Mu formation, $k'_e(E)$:

$$(MMu^+)^* + X \xrightarrow{k_c} \begin{pmatrix} (M\,Mu\,X^+)^{**} \\ \vdots \quad k_s(E) \\ (M\,Mu\,X^+)^* \end{pmatrix} \begin{array}{l} k'_e(E) \nearrow \quad Mu + X^+ + M \\ \\ k'_\mu(E) \searrow \quad XMu^+ + M \, . \end{array} \tag{6.14}$$
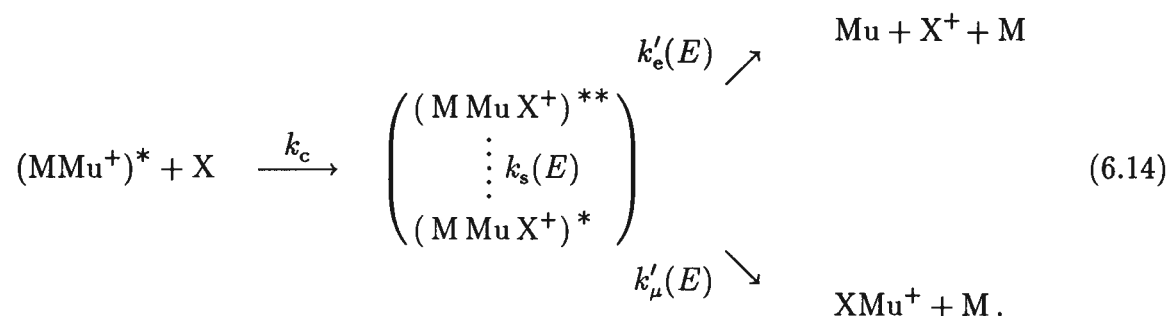
The weak quenching is represented by the vertical dots, indicating that the excitation energy E in the complex declines at a rate of $k_s(E)$.

This is a much more realistic model of quenching than the strong quenching mechanism assumed so far; in a single collision, a small moderator atom like He and Ne cannot carry away enough energy to fully stabilize an excited ion. The (He) pressure-dependent association rate of $CH_3^+ + HCN$ indicates an average energy loss of only 0.015 eV per He collision [37,222], and quenching by Ne should not be much stronger [37,153,156,157].

For reactions of the muonated ions, there is good reason to believe that such quenching operates on the capture complex rather than on the muonated rare gas ion: the expected energy loss of ~ 0.015 eV is less than the *smallest rotational spacing* of NeMu$^+$! (The spacings of HeMu$^+$ are even larger [191].) The low density of rovibrational states in the muonated ions makes weak quenching nigh impossible.[1] On the other hand, poly-atomic capture complexes have smaller vibrational/rotational energy spacings, particu-

---

[1] Although it is certainly more viable for quenching of rotational excitation than

larly for the overall rotations and any vibrations not involving Mu. The measurements of quenching by Ar in the $N_2O + NeMu^+$ reaction, and by Ne for $CH_3F + NeMu^+$, indicated also that the complex itself was quenched because the amplitudes were affected much more than the relaxation rates. Note that, before stabilization, the association complex has the same total energy as the reactants, which amounts to a greater excitation energy because it has a lower ground state. After quenching below the threshold for Mu formation, a complex will dissociate by expelling Ne(He) to form XMu^+.

Once the excess energy in the complex falls below the threshold for ejection of Mu, charge transfer is impossible, so this threshold could give behavior resembling a strong collision model (with some efficiency factor) as was assumed for the previous kinetics models, especially eq. (4.12). However, as the energy declines towards threshold, the microscopic rate constant for Mu formation $k'_e(E)$ will decline [130,223], in accord with the microcanonical TST/RRKM expression

$$k'_e(E) = \frac{W^\ddagger(E - E_0)}{h\,\rho(E)} = \frac{\int_0^{E-E_0} \rho^\ddagger(E^\ddagger)\,dE^\ddagger}{h\,\rho(E)} \tag{6.15}$$

where E_0 is the minimum excitation energy needed for Mu formation, and ρ and $\rho^\ddagger$ are the densities of states in the (already excited) complex and the transition state for Mu formation from the complex, respectively. Stabilization competes with dissociation into reactants, dissociation into diamagnetic products (muon transfer, at k'_μ) and de-excitation by (weak) moderator collisions.

The difficulty is that the calculation of the total rate constant (the expected k_{exp}) must follow a statistical model [222,224–226] rather than simple competition kinetics; it must integrate all rate constants over the time-varying distribution of excitation energies $E(t)$. An exact description of the intermediate complex, including vibrational

---

vibrational; "weak vibrational quenching" is a contradiction in terms for $HeMu^+$ and $NeMu^+$.

frequencies, is needed before the various microscopic rates [$k(E)$'s] can be calculated, and there must be some measure of the energy distribution of the reactants. More work is needed on both fronts.

In the simple kinetic models used to evaluate the data, quenching by X was included with the muon-transfer reaction channel as the two were experimentally indistinguishable for a strong collisional quenching model. For weak quenching, however, collisional stabilization by the neutral reactant would need to be accounted for separately. Since partial de-excitation should decrease the reaction rate, quenching by Xe itself might provide yet another explanation for the curved λ_f vs. [Xe] sometimes obtained.

All the mechanisms considered to explain the unexpected results from xenon (and krypton) have explicitly involved a capture complex existing for some time, but results for the many other systems investigated give no explicit indication of a capture mechanism, beyond having overall rates that agree with the theoretical capture rates. Capture theories place no special reliance on long-lived complexes, only on the overwhelming influence of the long-range attractive potential, so the many experimental rate constants probably indicate a *short-lived* capture complex. It is hard to understand how a simple complex like $NeMuXe^+$ could be long-lived when a much larger conglomeration such as $NeMuCH_3NO_2^+$ is short-lived; surely the many degrees of freedom in the latter could keep it together longer. Could there be a barrier to internal rearrangement that dramatically stabilizes the smaller species?

"Long-lived" in the context of these experiments is of order 1 μs, which is still very short compared to the time-scale in a typical study of ion–molecule reactions (1–100 ms), so an enhanced lifetime could have gone unnoticed in other experiments; but 1 μs is still very long in the time frame of elementary reactions, and is $\sim 10^5$ times longer than the expected lifetime of the transient complex. Yet there is evidence that the intermediate complexes of xenon, krypton, and probably the fluoro-alkanes, are long-lived relative to the ~ 1 μs time frame of these experiments, and relative to the fleeting existence of the

intermediates in the other reactions. It is noteworthy that the majority of reactions studied showed no evidence for intermediate complex formation except for reacting at their predicted capture rates. For whatever time the complex exists, collisional stabilization appears to operate much more efficiently on the short-lived association than on the original ions, which are amazingly resistant to rovibrational de-excitation, a result, no doubt, of the very low density of their vibrational and rotational states.

Chapter 7

SUMMARY AND CONCLUDING REMARKS

The principal goal of these experiments was to use the technique of muon spin rotation to study the ion–molecule reactions of the muonium isotopomers of the protonated inert gases: $HeMu^+$, $NeMu^+$, and, to some extent, $ArMu^+$ and N_2Mu^+, and in so doing, provide an extensive new body of data on the reactivity of these, the simplest closed shell (point charge) molecular ions, which could also be applied to their protonated cousins. This goal has been met, with the measurement of muon-transfer (like proton-transfer) reactions and, particularly, charge-transfer reactions for a wide variety of reactants of differing polarizabilities and dipole moments.

A related goal, to compare with corresponding studies of the protonated rare gases, has been frustrated somewhat by the lack of data on molecules of common interest. By studying the muonated analogs of protonated ions, it was hoped that mass effects would be made evident, especially the influence, if any, of quantum tunnelling in ionic reactions. Also, since μSR facilitates measurements at much higher pressures than possible with conventional techniques, the effect of moderator density could be investigated. Yet the comparisons made with protonated ion studies indicate that neither high pressure nor quantum tunnelling are particularly important for the proton- (muon-) and charge-transfer reactions studied. This is, in itself, an important conclusion.

7.1 Reaction Rates

Ion–molecule reaction rates were measured for the muonated inert gas molecular ions $HeMu^+$, $NeMu^+$, $ArMu^+$, and N_2Mu^+ reacting with a wide variety of polar and non-polar neutral species (tables 4.1–4.4 & 5.4), at various inert gas pressures in the range 400–2400 torr, and at various temperatures from 120 to 450 K, with most experiments performed at room temperature. In almost all cases, both charge transfer (which causes μ^+ depolarization) and muon transfer (which does not) were observed, manifest as a two-component decay of the μSR signal, where the relaxation rate is interpreted as the total reaction rate, and the ratio of the amplitudes is indicative of the product distribution (the 'simple model', §4.4). Since charge transfer is endothermic for ground-state reactants in many cases, the reaction is believed to occur from rovibrationally excited states of $(HeMu^+)^*$ and $(NeMu^+)^*$, with approximately 1 eV of excitation energy.

The experimental rate constants are generally in very good agreement with the theoretical (AADO [117] or Langevin [110]) maximum values, demonstrating anew the viability of simple capture theories. In comparing the various formulations for ion–dipole capture, it appears that the AADO [117] and parameterized trajectory [118] calculations give the best upper limits on the reaction rates. Several temperature dependences (120–450 K) were measured which agreed satisfactorily with classical AADO capture theory, showing no great deviations at 'low' temperatures characteristic of quantum-mechanical capture treatments. Reactions of some neutrals were observed to be significantly slower than the capture predictions: Xe, Kr, CF_4, CH_3F, and $C_2H_4F_2$, typically giving only half the theoretical maxima, but with Kr reacting at only 1/16 of the Langevin rate. These exceptions might be due to formation of very long-lived complexes ($\sim 1\ \mu s$) and/or the back-dissociation of such complexes before charge transfer is accomplished, though neither interpretation is straightforward. The majority of cases that agreed closely with capture theory must similarly react through an intermediate complex, although the complex may

be very transitory and rapidly dissociate into products.

Comparing the results of the present experiments with the few corresponding protonated ion measurements shows a high level of agreement for the total reaction rates, better even than the correspondence between experiment and theory. Reactivity of the protonated rare gases is dominated by proton transfer, with charge exchange being reported in only a few cases with HeH^+ and NeH^+ [191] when these ions are vibrationally excited—an almost identical situation as for the present experiments — and the prevalence of charge transfer for the μ^+ molecular ions is attributed to increased excitation rather than to a kinetic isotope effect. Although the reactant ions were rovibrationally excited, which enhances charge transfer over muon transfer, the total reaction rates were apparently unaffected by the excitation. There is certainly no indication of a significant isotope effect on the *total* reaction rates. The general level of agreement between the ion–molecule reactivity of the protonated rare gases, at pressures often substantially less than 1 torr, and their muon ion counterparts, above 1 atm, demonstrates that there is no significant effect of total pressure on these simple reactions, indicating that long-lived intermediate complexes are not involved. Transient complexes could still be formed, however, based on the agreement with capture theory, but they must be short-lived, compared with the $\sim 1\,\mu s$ reaction times investigated, and they must form products rather than dissociating into reactants. The *expected* lifetimes are in the range $10^{-12} \sim 10^{-10}\,s$, although detailed (ab initio and RRKM) calculations were not performed.

The reaction of Xe with $NeMu^+$ had anomalies that could indicate a much longer-lived intermediate complex. Likewise for $Kr + NeMu^+$, which may actually be second order in Kr concentration, and third order overall, with formation of Kr_2^+ to allow otherwise-endothermic charge transfer to occur, although it appeared bimolecular over the [Kr] range investigated. These exceptions are in contrast to the results for most other neutrals.

There was no observable reaction (no charge transfer) with Kr and $HeMu^+$. Other neutrals which exhibited no charge-transfer reaction were H_2 and CO (none was expected

for these), CH_4, H_2O, and CH_3CN. Muon transfer *does* occur, at near the capture rate, for H_2O and CH_4 as measured by a modified monitor ion method. This is interpreted in terms of enhanced muon transfer (perhaps due to muon tunnelling) though there is no definitive explanation; these molecules are not anomalous with respect to other reactions [25,57,147,148,154–156,191–196,198,199] they undergo.

While muonated molecular ions were observed for (and in) He, Ne, Ar, and N_2 moderators, neither the ions H_2Mu^+ nor $C_2H_6Mu^+$ were seen. It is expected that, if formed, these ions immediately react with the respective moderator gas to place the Mu in a neutral molecule, HMu, C_2H_5Mu, or the stable ion $C_2H_4Mu^+$. It is more likely that no muonated ions are formed in these gases, with the diamagnetic μ^+ signal in H_2 and C_2H_6 gases attributable to epithermal reactions of neutral Mu.

7.2 Ion Formation, Excitation, and Quenching

Since charge transfer was observed in many cases where it is endothermic from the ionic ground state, the reacting molecular ions are believed to be rovibrationally excited: $(HeMu^+)^*$ and $(NeMu^+)^*$. Rather than acquiring this excitation through energetic collisions, it is believed that the energy is left from the initial formation of the ions by association of Mu^+ (i.e., a bare μ^+) with He or Ne. The ions are remarkably resistant to collisional quenching by the bath gas, due both to the very low density of their rovibrational states [191], and to the low quenching efficiencies of He and Ne generally.

At the time of reaction, the $(HeMu^+)^*$ and $(NeMu^+)^*$ ions still have ≈ 1 eV of excitation, as indicated by their charge-transfer reactions with CF_4, N_2O, and other neutrals (see table 4.2). This corresponds to $v = 2$ or to a lower vibrational level with some degree of rotational excitation. Charge transfer was seen with $ArMu^+$ only for triethylamine and nitric oxide, for which the reaction is exothermic from the ground state of $ArMu^+$, indicating that, whatever the initial excitation, it has been effectively removed by the Ar moderator gas.

Measurements of de-excitation of $HeMu^+$ and $NeMu^+$ by collisions with the respective moderator or by argon were also performed. The effect on the product distributions (amplitudes) was much greater than on the total reaction rates, which is taken to indicate a weak quenching mechanism whereby a small portion of the excess energy is lost with each collision. Based on the amplitudes, the quenching efficiency for Ar was found to be $k_q/k_L = 0.22 \pm 0.03$, while He and Ne are much less efficient at 0.0004 and 0.00014 respectively. This is the same trend found in other studies [79,153,154]. Since the $HeMu^+$ and $NeMu^+$ ions have such wide rovibrational spacings, they are not good candidates for weak collisional quenching. From this, and from the lack of effect on the total reaction rates, it is argued that quenching is accomplished mainly by third-body collisions on the transient capture complex (e.g., $Ne + XeMuNe^+$), though this assignment of a mechanism is much less certain than the observation of quenching itself.

7.3 Prospects

The μSR technique used for this thesis allows measurement of ion–molecule reactions in regimes far removed from those accessible to other techniques. By following one muon at a time, all ion–ion interactions are eliminated, and all other reacting species are unseen. Muon spin rotation is useful for observing fast reactions, particularly reactions of unstable species, as all reactions observed must have rates of $\sim 0.1\text{--}10\ \mu s^{-1}$, set by the mean life of the μ^+ radioactive decay (2.2 μs). This can also be a limitation if one wants to study slow reactions, but the vastly different time range is complementary to other techniques. The high pressures accessible to μSR experiments also complements other methods well, allowing measurements from $\sim 10^{-7}$ torr (ICR) to 1000 torr (μSR) and higher.

These advantages apply only to the positive muon analogs of protonated ions of course. Instead of observing reactants and products directly, μSR tracks the magnetic environment of individual muons. This is very useful for observing spin interactions, but makes it difficult to study mechanisms with more than one reaction, as the products

usually cannot be detected individually, though diamagnetic and paramagnetic products can be distinguished. The initial reactants cannot be selected as in a SIFT apparatus, which further limits the ions amenable to study.

The greatest contribution of μSR to the field of chemical kinetics, though, is its detection of large kinetic isotope effects in many systems [29–31,82]. Such effects on the reactivity of muonated ions were found to be much smaller than those observed for neutral reactions.

This thesis has demonstrated the usefulness of μSR in measuring several ion–molecule reaction rates, the majority of which have not been studied for the corresponding protonated ions. Charge transfer was usually seen, although studies of protonated ions are dominated by proton transfer [24–26], but for the total reaction rates, there was a remarkable *lack* of isotope effects to be seen in making comparisons with earlier work [25,191,203]. Since the substitution of Mu^+ for H^+ has little effect, it is likely that these studies will not be immediately pursued due to the difficulty and expense of using a high energy particle accelerator (TRIUMF) to generate muons. Any further measurements will take direction from studies using conventional methods, answering questions particularly suited to the μSR technique. It is hoped that this thesis will help spur others to undertake much more extensive and detailed studies of the reactions of the protonated rare gases, which could answer some of the questions raised by this work, and raise new questions that could be answered, in turn, by μSR studies.

References

1. A.J. Dempster, Phil. Mag. **31** (1916) 438.

2. H.D. Smyth, Phys. Rev. **25** (1925) 452.

3. T.R. Hogness and E.G. Lunn, Phys. Rev. **26** (1925) 44.

4. V.L. Tal'rose and A.K. Lyubimova, Dokl. Akad. Nauk SSSR, **86** (1952) 909.

5. T.D. Mark and A.W. Castleman, Jr., in *Advances in Atomic and Molecular Physics* vol. **20**, D. Bates and B. Bederson, eds. (Academic, Orlando, 1984) 65.

6. D. Smith and N.G. Adams, J. Chem. Soc. Far. Trans. 2 **85** (1989) 1613.

7. G.L. Verschuur, Sky & Telescope, April 1992, 379.

8. W.D. Watson, Astrophys. J. **188** (1974) 35.

9. A.A. Viggiano, F. Howorka, D.L. Albritton, F.C. Fehsenfeld, N.G. Adams, and D. Smith, Astrophys. J. **236** (1980) 492.

10. E.E. Ferguson, F.C. Fehsenfeld, and D.L. Albritton, in *Gas Phase Ion Chemistry* vol. **1**, M.T. Bowers, ed. (Academic, New York, 1979) 45.

11. D.A. Williams, in *Galactic and Extragalactic Infrared Spectroscopy*, M.F. Kessler and J.P. Phillips, eds. (Reidel, New York, 1984), pp. 59–67.

12. T.G. Phillips, G.A. Blake, J. Keene, R.C. Woods, and E. Churchwell, Astrophys. J. **294** (1985) L45.

13. J.-P. Maillard, P. Drossart, J.K.G. Watson, S.J. Kim, and J. Caldwell, Astrophys. J. **363** (1990) L37; P. Drossart, J.-P. Maillard, J. Caldwell, S.J. Kim, J.K.G. Watson, W.A. Majewski, J. Tennyson, S. Miller, S.K. Atreya, J.T. Clarke, J.H. Waite, Jr., and R. Wagener, Nature, **340** (1989) 539.

14. S. Miller, R.D. Joseph, and J. Tennyson, Astrophys. J. **360** (1990) L55.

15. S. Lepp, A. Dalgarno, and A. Sternberg, Astrophys. J. **321** (1987) 383; S. Lepp and A. Dalgarno Astrophys. J. **358** (1990) 262.

16. W. Wagner-Redeker, P.R. Kemper, M.T. Bowers, and K.R. Jennings, J. Chem. Phys. **80** (1984) 3606.

17. I. Dabrowski and G. Herzberg, Ann. N. Y. Acad. Sci. **38** (1977) 14; I. Dabrowski, G. Herzberg, and R. H. Lipson, Mol. Phys. **63** (1988) 289; I. Dabrowski, G. Herzberg, B. P. Hurley, R. H. Lipson, M. Vervloet, and D.-C. Wang, ibid. 269.

18. J. M. Moorhead, R. P. Lowe, J.-P. Maillard, W. H. Wehlau, and F. P. Bernath, Astrophys. J. **326** (1988) 899.

19. K.-P. Cheng and F. C. Bruhweiler, Astrophys. J. **364** (1990) 573.

20. W. Roberge and A. Dalgarno, Astrophys. J. **255** (1982) 489.

21. B. Zygelman and A. Dalgarno, Astrophys. J. **365** (1990) 239; B. Zygelman, A. Dalgarno, M. Kimura, and N. F. Lane, Phys. Rev. **A 40** (1989) 2340.

22. R. Walder and J. L. Franklin, Int. J. Mass Spec. & Ion Phys. **36** (1980) 85.

23. N. G. Adams, ,D. Smith, M. Tichy, G. Javahery, N. D. Twiddy, and E. E. Ferguson, J. Chem. Phys. **91** (1989) 4037.

24. D. K. Bohme, R. S. Hemsworth, H. W. Rundle, and H. I. Schiff, J. Chem. Phys. **58** (1973) 3054; R.S. Hemsworth, H. W. Rundle, D. K. Bohme, H. I. Schiff, B. D. Dunkin, and F. C. Fehsenfeld, J. Chem. Phys. **59** (1973) 61; P. F. Fennelly, R. S. Hemsworth, H. I. Schiff, and D. K. Bohme, J. Chem. Phys. **58** (1973) 6405; J. D. Payzant, H. I. Schiff, and D. K. Bohme, J. Chem. Phys. **63** (1975) 149; F. C. Fehsenfeld, J. Chem. Phys. **64** (1976) 4887; G. I. Mackay and D.K. Bohme, Int. J. Mass Spec. & Ion Phys. **26** (1978) 327; S. D. Tanner, G. I. Mackay, A. C. Hopkinson, and D. K. Bohme, Int. J. Mass Spec. & Ion Phys. **29** (1979) 153.

25. G. I. Mackay, H. I. Schiff, and D. K. Bohme, Can. J. Chem. **59** (1981) 1771; D.K Bohme, G. I. Mackay, and H. I. Schiff, J. Chem. Phys. **73** (1980) 4976.

26. Y. Ikezoe, S. Matsuoka, M. Takebe, and A.Viggiano, *Gas Phase Ion–Molecule Reaction Rate Constants Through 1986* (The Mass Spectroscopy Society of Japan, Tokyo, 1987).

27. D. G. Fleming, R. J. Mikula, M. Senba, D. M. Garner, and D. J. Arseneau, Chem. Phys. **82** (1983) 75.

28. D.J. Arseneau, D.G. Fleming, M. Senba, I.D. Reid, and D.M. Garner, Can. J. Chem. **66** (1988) 2018.

29. D.M. Garner, D.G. Fleming, D.J. Arseneau, M. Senba, I.D. Reid, and R.J. Mikula, J. Chem. Phys. **93** (1990) 1732.

30. A. C. Gonzalez, I. D. Reid, D. M. Garner, M. Senba, D. G. Fleming, D. J. Arseneau,

and J. R. Kempton, J. Chem. Phys. **91** (1989) 6164.

31. E. Roduner, P. W. F. Louwrier, G. A. Brinkman, D. M. Garner, I. D. Reid, D. J. Arseneau, M. Senba, and D. G. Fleming, Ber. Bunsenges. Phys. Chem. **94** (1990) 1224.

32. J. Barassin, C. Reynaud, and A. Barassin, Chem. Phys. Lett. **123** (1986) 191.

33. M. F. Jarrold, A. J. Illies, and M. T. Bowers, Chem. Phys. Lett. **92** (1982) 653.

34. J. E. Moryl and J. M. Farrar, J. Phys. Chem. **86** (1982) 2020; R. M. Bilotta and J. M. Farrar, J. Phys. Chem. **85** (1981) 1515.

35. N. J. Kirchner and M. T. Bowers, J. Phys. Chem. **91** (1987) 2573.

36. N. G. Adams and D. Smith, Chem. Phys. Lett. **79** (1981) 563.

37. P. R. Kemper, L. M. Bass, and M. T. Bowers, J. Phys. Chem. **89** (1985) 1105; L. M. Bass, P. R. Kemper, and V. G. Anicich, J. Am. Chem. Soc. **103** (1981) 5283.

38. J. R. Kempton, D. J. Arseneau, D. G. Fleming, M. Senba, A. C. Gonzalez, J. J. Pan, A. Tempelmann, and D. M. Garner, J. Phys. Chem. **95** (1991) 7338; J. R. Kempton, M. Senba, D. J. Arseneau, A. C. Gonzalez, D. M. Garner, J. J. Pan, D. G. Fleming, P. W. Percival, J.-C. Brodovitch, and S.-K. Leung, J. Chem. Phys. **94** (1991) 1046.

39. P. W. Percival, E. Roduner, and H. Fischer, Chem. Phys. **32** (1978) 353; P. W. Percival, Radiochimica Acta **26** (1979) 1; P. W. Percival, K. M. Adamson-Sharpe, J.-C. Brodovitch, S.-K. Leung, and K. E. Newman, Chem. Phys. **95** (1985) 321.

40. B. F. Kirillov, B. A. Nikol'sky, A. V. Pirogov, V. G. Storchak, V. N. Duginov, V. G. Grebennik, S. Kapusta, A. B. Lazarev, S. N. Shilov, and V. A. Zhukov, Hyper. Int. **65** (1990) 819; V. N. Duginov, V. G. Grebennik, B. F. Kirillov, B. A. Nikol'sky, V. G. Ol'shevsky, A. V. Pirogov, V. Yu. Pomyakushkin, V. G. Storchak, and V. A. Zhukov, I. V. Kurchatov Institute of Atomic Energy Preprint IAE-4980/9 (1989).

41. V. G. Storchak, V. N. Duginov, V. G. Grebennik, B. F. Kirillov, V. G. Ol'shevsky, A. V. Pirogov, V. Yu. Pomyakushkin, A. N. Ponomarev, A. B. Lazarev, S. N. Shilov, and V. A. Zhukov, I. V. Kurchatov Institute of Atomic Energy Preprint IAE-5333/9 (1991).

42. V. G. Storchak, V. N. Duginov, B. F. Kirillov, A. V. Pirogov, V. G. Grebennik, A. N. Ponomarev, V. A. Zhukov, A. B. Lazarev, and S. N. Shilov, I. V. Kurchatov Institute of Atomic Energy Preprint IAE-5214/10 (1991).

43. Yu. M. Belousov, A. L. Getalov, S. P. Kruglov, L. A. Kuz'min, V. P. Smilga, and V. G. Storchak, Sov. Phys. JETP **64** (Sept. 1986) 423.

44. D. G. Fleming, R. J. Mikula, and D. M. Garner, Phys. Rev. **A 26** (1982) 2527; R. J. Mikula, D. G. Fleming, and D. M. Garner, Hyper. Int. **6** (1979) 379; R. J. Mikula, Ph. D. Thesis, University of British Columbia (1981).

45. C. C. Anderson and S. H. Neddermeyer, Phys. Rev. **51** (1937) 88.

46. N. G. Adams and D. Smith; W. Lindinger and D. Smith, in *Reactions of Small Transient Species: kinetics and energetics*, A. Fontijn and M. A. A. Clyne, eds. (Academic, New York, 1983) chap. 6, 7.

47. K. P. Wanczek, Int. J. Mass Spec. & Ion Proc. **95** (1989) 1.

48. J. H. Futrell, in *Gaseous Ion Chemistry and Mass Spectrometry*, J. H. Futrell, ed. (Wiley, New York, 1986) 127.

49. W. Lindinger, in *Gaseous Ion Chemistry and Mass Spectrometry*, J. H. Futrell, ed. (Wiley, New York, 1986) 141.

50. D. Smith and N. G. Adams, in *Gas Phase Ion Chemistry* vol. **1**, M. T. Bowers, ed. (Academic, New York, 1979) 2.

51. J. H. Futrell, in *Gaseous Ion Chemistry and Mass Spectrometry*, J. H. Futrell, ed. (Wiley, New York, 1986) 155.

52. C. F. Giese and W. B. Maier II, J. Chem. Phys. **39** (1963) 739.

53. D. L. Smith and J. H. Futrell, Int. J. Mass Spec. & Ion Phys. **14** (1974) 171.

54. M. B. Comisarow and A. G. Marshall, CPL **25** (1974) 282; **26** (1974) 489.

55. N. G. Adams and D. Smith, Int. J. Mass Spec. & Ion Phys. **21** (1976) 349.

56. B. R. Rowe, G. Dupeyrat, J. B. Marquette, D. Smith, N. G. Adams, and E. E. Ferguson, J. Chem. Phys. **80** (1984) 241; B. R. Rowe, J.-B. Marquette, and C. Rebrion, J. Chem. Soc. Far. Trans. 2 **85** (1989) 1631.

57. B. R. Rowe, J. B. Marquette, G. Dupeyrat, and E. E. Ferguson, Chem. Phys. Lett. **113** (1985) 403.

58. O. E. Mögensen, J. Chem. Phys. **60** (1974) 998; O. E. Mögensen and P. W. Percival Radiat. Phys. Chem. **28** (1986) 85.

59. D. E. Tolliver, G. A. Kyrola, and W. H. Wing, Phys. Lev. Lett. **43** (1979) 1719.

60. S. Peyerimhoff, J. Chem. Phys. **43** (1965) 998.

61. W. Kolos, Int. J. Quant. Chem. **X** (1976) 217; W. Kolos and J. M. Peek, Chem. Phys. **12** (1976) 217.

62. D. M. Bishop and L. M. Cheung, J. Mol. Spec. **75** (1979) 462.

63. K. Vasudevan, Mol. Phys. **30** (1975) 437.

64. R. L. Matcha and M. B. Milleur, J. Chem. Phys. **69** (1978) 3016; R. L. Matcha, M. B. Milleur, and P. F. Meier, J. Chem. Phys. **68** (1978) 4748.

65. P. Rosmus and E.-A. Reinsh, Z. Naturforsch. **35A** (1980) 1066; P. Rosmus, Theor. Chim. Acta **51** (1979) 359.

66. G. A. Gallup, Phys. Rev. **A 35** (1987) 1.

67. W. P. Kraemer, A. Komornicki, and D. A. Dixon, Chem. Phys. **105** (1986) 87.

68. W. G. Rich, S. M. Bobbio, R. L. Champion, and L. D. Doverspike, Phys. Rev. **A 4** (1971) 2253.

69. F. A. Gianturco, G. Niedner, M. Noll, E. Semprini, and J. P. Toennies, Z. Phys. D **7** (1987) 281; F.A Gianturco and F. Gallese, Chem. Phys. Lett. **148** (1988) 365.

70. J. W. C. Johns, J. Mol. Spec. **106** (1984) 124.

71. A. Carrington, J. Battenshaw, R. A. Kennedy, and T. P. Softley, Mol. Phys. **44** (1981) 1233.

72. M. Wong, P. Bernath, and T. Amano, J. Chem. Phys. **72** (1982) 693.

73. J. W. Brault and S. P. Davis, Physica Scripta **25** (1982) 268; R. S. Ram, P. F. Bernath, and J. W. Brault, J. Mol. Spec. **113** (1985) 451.

74. D. J. Liu, W.-C. Ho, and T. Oka, J. Chem. Phys. **87** (1987) 2442.

75. P. G. Fournier and B. Lassier-Govers, J. Physique Lettres **43** (1983) L483; P. G. Fournier and R. J. Le Roy, Chem. Phys. Lett. **110** (1984) 487.

76. G. Theodorakopoulos, I. D. Petsalakis, and R. J. Buenker, J. Phys. B: At. Mol. Phys. **20** (1987) 5335.

77. E. A. Gislason and G. Parlant, J. Chem. Phys. **94** (1991) 6598.

78. R. Wedlich, M. W. Karl, N. Nakanishi, and D. M. Schrader, in *Positron Annihilation: Proceedings of the Seventh International Conference, New Delhi* (World Scientific, Singapore, 1985) p. 408.

79. M. Tichy, G. Javahery, N. D. Twiddy, and E. E. Ferguson, Int. J. Mass Spec. & Ion Proc. **97** (1990) 211; Chem. Phys. Lett. **144** (1988) 131.

80. D. J. DeFrees and A. D. McLean, J. Chem. Phys. **82** (1985) 333.

81. J. Tennyson and S. Miller, J. Chem. Phys. **90** (1989) 2524.

82. I.D. Reid, D.M. Garner, L.Y. Lee, M. Senba, D.J. Arseneau, and D.G. Fleming, J. Chem. Phys. **86** (1987) 5578; I.D. Reid, L.Y. Lee, D.M. Garner, D.J. Arseneau, M. Senba, and D.G. Fleming, Hyp. Inter. **32** (1986) 801; D.M. Garner, D.G. Fleming, and R.J. Mikula, Chem. Phys. Lett. **121** (1985) 80.

83. T. Bowen, Physics Today, July (1985) 22; A.E. Pifer, T. Bowen, and K.R. Kendall, Nucl. Instrum. Methods **135** (1976) 39.

84. J.L. Beveridge, J. Doornbos, D.M. Garner, D.J. Arseneau, I.D. Reid, and M. Senba, Nucl. Instrum. Methods in Phys. Research **A 240** (1985) 316.

85. M. Senba, Hyper. Int. **65** (1990) 779; J. Phys. B: At. Mol. Opt. Phys. **21** (1988) 3093; **22** (1989) 2027; **23** (1990) 1545.

86. D.G. Fleming and M. Senba, in *Atomic Physics with Positrons*, J.W. Humberston and E.A.G. Armour, eds. (Plenum, New York, 1987) p. 343.

87. E. Segrè, *Experimental Nuclear Physics* vol. II (Wiley, New York, 1953) 166 ff.

88. M. Senba, D.J. Arseneau, A.C. Gonzalez, J.R. Kempton, J.J. Pan, A. Tempelmann, and D.G. Fleming, Hyper. Int. **63–65** (1990) 793; and paper in preparation.

89. D.J. Arseneau, D.M. Garner, M. Senba, and D.G. Fleming, J. Phys. Chem. **88** (1984) 3688; D.G. Fleming, D.J. Arseneau, D.M. Garner, M. Senba, and R.J. Mikula, Hyper. Int. **17–19** (1984) 655; D.J. Arseneau, M.Sc. Thesis, University of British Columbia (1984).

90. D.G. Fleming, M. Senba, D.J. Arseneau, I.D. Reid, and D.M. Garner, Can. J. Chem. **64** (1986) 57; D.G. Fleming, L.Y. Lee, M. Senba, D.J. Arseneau, I.D. Reid, and D.M. Garner, Radiochimica Acta **43** (1988) 98; D.G. Fleming, Radiat. Phys. Chem. **28** (1986) 115.

91. J.R. Kempton, M. Senba, D.J. Arseneau, A.C. Gonzalez, J.J. Pan, A. Tempelmann, and D.G. Fleming, Hyper. Int. **63–65** (1990) 801; M. Senba, R.E. Turner, D.J. Arseneau, D.M. Garner, L.Y. Lee, I.D. Reid, and D.G. Fleming, Hyper. Int. **32** (1986) 795.

92. M. Senba, A.C. Gonzalez, J.R. Kempton, D.J. Arseneau, J.J. Pan, A. Tempelmann, and D.G. Fleming, Hyper. Int. **63–65** (1990) 979.

93. M. Senba, D.J. Arseneau, and D.G. Fleming, "Muonium Hot Atom Chemistry: theory and experiment," in *Recent Trends and Prospects in Hot Atom Chemistry*, T. Matsuura, ed. (Elsevir, Kodansha, submitted 1991).

94. M. H. Yam, Ph. D. Thesis, Yale University (1979).

95. A. M. Sachs and A. Sirlin, in *Muon Physics* vol. **II**, C. S. Wu and V. W. Hughes, ed. (Academic, New York, 1975).

96. G. G. Myasishcheva, Yu. V. Obukhor, V. S. Roganov, and V. G. Firsov, Sov. Phys. JETP (Engl. Trans.) **26** (1968) 298.

97. B. D. Patterson, Rev. Mod. Phys. **60** (1988) 69.

98. M. Camani, E. Klempt, W. Ruegg, A. Schenck, R. Schulze, and H. Wolf, Phys. Lett. **77B** (1978) 326.

99. D. G. Fleming, D. M. Garner, L. C. Vaz, D. C. Walker, J. H. Brewer, and K. M. Crowe, *Positronium and Muonium Chemistry*, H. J. Ache, ed. A. C. S. Adv. Chem. Series 175 (1979) 279.

100. E. Holzschuh, W. Kündig, and B. D. Patterson, Helvetica Physica Acta **54** (1981) 552; Hyper. Int. **8** (1981) 819.

101. R. H. Heffner and D. G. Fleming, Physics Today, Dec. (1984) 30.

102. D. M. Garner, Ph. D. Thesis, University of British Columbia (1979).

103. D. C. Walker, Acc. Chem. Res. **18** (1985) 167; D. C. Walker, J. Phys. Chem. **85** (1981) 3960; D. C. Walker, *Muon and Muonium Chemistry* (Cambridge University, Cambridge, 1983).

104. F. James and M. Roos, MINUIT, CERN Computer 7600 Interim Programme Library, (1971).

105. W. H. Press, B. P. Flannery, S. A. Teukolski, and W. T. Vetterling, *Numerical Recipies: The Art of Scientific Computing*, (Cambridge University, New York, 1986).

106. M. Senba, D. G. Fleming, D. J. Arseneau, D. M. Garner, and I. D. Reid, Phys. Rev. A **39** (1989) 3871; M. Senba, D. M. Garner, D. J. Arseneau, and D. G. Fleming, Hyper. Int. **17–19** (1984) 703; D. G. Fleming, R. J. Mikula, and D. M. Garner, J. Chem. Phys. **73** (1980) 2751.

107. W. J. Chesnavich, T. Su, and M. T. Bowers, "Ion–Dipole Collisions: Recent Theoretical Advances," in *Kinetics of Ion–Molecule Reactions*, P. Ausloos, ed. (Plenum, New York, 1979) 31.

108. T. Su and M. T. Bowers, in *Gas Phase Ion Chemistry* vol. **1**, M. T. Bowers, ed. (Academic, New York, 1979).

109. D. C. Clary, Ref. 131, p. 1613.

110. G. Gioumousis and D. P. Stevenson, J. Chem. Phys. **29** (1958) 294.

111. H. Eyring, J. O. Hirschfelder, and H. S. Taylor, J. Chem. Phys. **4** (1936) 479.

112. E. Vogt and G. H. Wannier, Phys. Rev. **95** (1954) 1190.

113. P. M. Langevin, Ann. Chim. Phys. **5** (1905) 245.

114. R. C. C. Lao, R. W. Rozett, and W. S. Koski, J. Chem. Phys. **49** (1968) 4202;.

115. T. F. Moran and W. H. Hamill, J. Chem. Phys. **39** (1963) 1413.

116. T. Su and M. T. Bowers, J. Chem. Phys. **58** (1973) 3027; T. Su and M. T. Bowers, Int. J. Mass Spectrom. & Ion Phys. **17** (1975) 211.

117. T. Su, E. C. F. Su, and M. T. Bowers, J. Chem. Phys. **69** (1978) 2243.

118. T. Su and W. J. Chesnavich, J. Chem. Phys. **76** (1982) 5183.

119. R. A. Barker and D. P. Ridge, J. Chem. Phys. **64** (1976) 4411.

120. W. J. Chesnavich, T. Su, and M. T. Bowers, J. Chem. Phys. **72** (1980) 2641.

121. D. R. Bates, Proc. Roy. Soc. A, **384** (1982) 289; D. R. Bates, Chem. Phys. Lett. **97** (1983) 19; **111** (1984) 428.

122. P. P. Dymerski and R. C. Dunbar, J. Chem. Phys. **57** (1972) 4049.

123. T. Su and M. T. Bowers, J. Chem. Phys. **60** (1974) 4897.

124. K. Sakimoto, Chem. Phys. **63** (1981) 419.

125. D. P. Ridge, "Comments on Intermolecular Potentials for Polyatomic Ions and Molecules," in *Kinetics of Ion–Molecule Reactions,* P. Ausloos, ed. (Plenum, New York, 1979).

126. F. Celli, G. Weddle, and D. P. Ridge, J. Chem. Phys. **73** (1980) 801.

127. J. Turulski and J. Niedzielski, J. Chem. Soc. Faraday Trans. 2, **84** (1988) 347.

128. J. V. Dugan and J. L. Magee, J. Chem. Phys. **47** (1967) 3103; J. V. Dugan, R. W. Palmer, and J. L. Magee, Chem. Phys. Lett. **6** (1970) 158.

129. T. Su, J. Chem. Phys. **88** (1988) 4102.

130. W. Forst, *Theory of Unimolecular Reactions,* (Academic, New York, 1973).

131. J. Chem. Soc. Faraday Trans. 2, **85** (1989), entire issue.

132. J. Troe, Chem. Phys. Lett. **122** (1985) 425.

133. J. Troe, J. Chem. Phys. **87** (1987) 2773.

134. K. Sakimoto and K. Takayanagi, J. Phys. Soc. Jpn. **48** (1980) 2076; K. Takayanagi, J. Phys. Soc. Jpn. **45** (1978) 976; K. Sakimoto, J. Phys. Soc. Jpn. **48** (1980) 1683.

135. K. Sakimoto, Chem. Phys. **68** (1982) 155; K. Sakimoto, Chem. Phys. Lett. **116** (1985) 86.

136. K. Sakimoto, Chem. Phys. **85** (1984) 273.

137. D. C. Clary, Mol. Phys. **53** (1984) 3; **54** (1985) 605.

138. D. C. Clary, J. Chem. Soc. Faraday Trans. **83** (1987) 139.

139. D. C. Clary, D. Smith, and N. G. Adams, Chem. Phys. Lett. **119** (1985) 320; C. Rebrion, J. B. Marquette, B. R. Rowe, and D. C. Clary, Chem. Phys. Lett. **143** (1988) 130.

140. M. Quack and J. Troe, Ber. Bunsenges. Phys. Chem. **78** (1974) 240; **79** (1975) 170, 469.

141. Wm. L. Morgan and D. R. Bates, Astrophys. J. **314** (1987) 817.

142. L. D. Landau and E. M. Lifshitz, *Mechanics* (Pergamon, Oxford, 1969) 154–158.

143. N. Marković and S. Nordholm, J. Chem. Phys. **91** (1989) 6813.

144. S. G. Lias, J. E. Bartmess, J. F. Liebman, J. L. Holmes, R. D. Levin, and W. G. Mallard, J. Phys. & Chem. Ref. Data **17** (1988) Supplement 1.

145. D. K. Bedford and D. Smith, Int. J. Mass Spec. & Ion Proc. **98** (1990) 179.

146. W. Lindinger, M. McFarland, F. C. Fehsenfeld, D. L. Albritton, A. L. Schmelttekopf, and E. E. Ferguson, J. Chem. Phys. **63** (1975) 2175; W. Lindinger, Phys. Rev. **A 7** (1973) 328.

147. N. G. Adams and D. Smith, J. Phys. B: At. Mol. Phys. **9** (1976) 1439; N. G. Adams, D. Smith, and J. F. Paulson J. Chem. Phys. **72** (1980) 288.

148. Z. Karpas, V. G. Anicich, and W. T. Huntress Jr., Chem. Phys. Lett. **59** (1978) 84.

149. A. B. Rakshit and P. Warneck, J. Chem. Phys. **74** (1981) 2853.

150. *CRC Handbook of Chemistry and Physics, 71st ed.*, D. R. Lide, ed. (CRC Press, Boca Raton, 1990).

151. R. E. Turner, M. Senba, and D. J. Arseneau, Int. J. Quant. Chem. **29** (1986) 1493.

152. G. J. Vazquez, R. J. Buenker, and S. D. Beyeremhoff, Mol. Phys. **59** (1986) 291.

153. E. E. Ferguson, J. Phys. Chem. **90** (1986) 731.

154. W. Federer, W. Dobler, F. Howorka, W. Lindinger, M. Durop-Ferguson, and E. E. Ferguson, J. Chem. Phys. **83** (1985) 1032.

155. R. A. Morris, A. A. Viggiano, F. Dale, J. F. Paulson, J. Chem. Phys. **88** (1988) 4772.

156. M. Durup-Ferguson, H. Böhringer, D. W. Fahey, F. C. Fehsenfeld, and E. E. Ferguson, J. Chem. Phys. **81** (1984) 2657.

157. P. R. Kemper and M. T. Bowers, J. Chem. Phys. **81** (1984) 2634.

158. M. Konrad and F. Linder, J. Phys. B: At. Mol. Phys. **15** (1982) L405.

159. D. G. Fleming, R. F. Kiefl, D. M. Garner, M. Senba, A. C. Gonzalez, J. R. Kempton, D. J. Arseneau, K. Venkateswaran, P. W. Percival, J.-C. Brodovitch, S.-K. Leung, D. Yu, and S. F. J. Cox, Hyper. Int. **63–65** (1990) 767; P. W. Percival, J.-C. Brodovitch, S.-K. Leung, D. Yu, R. F. Kiefl, D. M. Garner, D. J. Arseneau, D. G. Fleming, A. C. Gonzalez, J. R. Kempton, M. Senba, K. Venkateswaran, and S. F. J. Cox, Chem. Phys. Lett. **163** (1989) 241.

160. R. F. Kiefl, S. R. Kreitzman, M. Celio, R. Keitel, G. M. Luke, J. H. Brewer, D. R. Noakes, P. W. Percival, T. Matsuzaki, and K. Nishiyama, Phys. Rev. **A 34** (1986) 681; P. W. Percival, R. F. Kiefl, S. R. Kreitzman, D. M. Garner, S. F. J. Cox, G. M. Luke, J. H. Brewer, K. Nishiyama, and K. Venkateswaran, Chem. Phys. Lett. **133** (1987) 465.

161. M. Heming, E. Roduner, B. D. Patterson, W. Odermatt, J. Schneider, H. Baumeler, H. Keller, and I. M. Slavić, Chem. Phys. Lett. **128** (1986) 100; M. Heming, E. Roduner, and B. D. Patterson, Hyper. Int. **32** (1986) 727.

162. E. Roduner, Prog. React. Kinet. **14** (1986) 1; *The positive Muon as a Probe of Free Radical Chemistry* (Springer, Berlin, 1988).

163. T. Sugai, T. Kondow, A. Matsushita, K. Nishiyama, and K. Nagamine, Chem. Phys. Lett. **188** (1992) 100.

164. M. Senba, J. Phys. B: At. Mol. Opt. Phys. **24** (1991) 3531; **23** (1990) 4051.

165. A. A. Maryott and F. Buckley, NBS circular 537 (1953).

166. *Lange's Handbook of Chemistry*, J. A. Dean, ed. (Mc Graw–Hill, New York, 1985).

167. G. Herzberg, *Molecular Spectra and Molecular Structure* **III** (Van Nostrand, New

York, 1966); K. P. Huber and G. Herzberg, *Molecular Spectra and Molecular Structure* **IV** (Van Nostrand, New York, 1979).

168. P. Jesson and E. L. Muetterties, *Basic Chemical and Physical Data* (Marcel Dekker, New York, 1969).

169. *Tables of Interatomic Distances and Configuration in Molecules and Ions*, L. E. Sutton, ed. (The Chemical Society, London, 1958); *Supplement 1956–1959*, (1965).

170. G. Hvistendahl, O. W. Saastad, and E. Uggerud, Int. J. Mass Spec. & Ion Proc. **98** (1990) 167.

171. N. G. Adams, D. K. Bohme, and E. E. Ferguson, J. Chem. Phys. **52** (1970) 5101.

172. J. D. C. Jones, D. G. Lister, D. P. Wareing, and N. D. Twiddy, J. Phys. B: At. Mol. Phys. **13** (1980) 3247.

173. H. H. Michels, R. H. Hobbs, and L. A. Wright, J. Chem. Phys. **69** (1978) 5151.

174. Y. Morioka, M. Ogawa, T. Matsumoto, K. Ito, K. Tanaka, and T. Hayaishi, J. Phys. B: At. Mol. Opt. Phys. **24** (1991) 791.

175. L. K. Randeniya, X. K. Zeng, R. S. Smith, and M. A. Smith, J. Phys. Chem. **93** (1989) 8031.

176. P. A. M. van Koppen, M. F. Jarrold, M. T. Bowers, L. M. Bass, and K. R. Jennings, J. Chem. Phys. **81** (1984) 288.

177. K. Giles, N. G. Adams, and D. Smith, J. Phys. B: At. Mol. Opt. Phys. **22** (1989) 873; D. Smith and N. G. Adams, Chem. Phys. Lett. **161** (1989) 30.

178. J. B. Laudenslager, W. T. Huntress, Jr., and M. T. Bowers, J. Chem. Phys. **61** (1974) 4600.

179. R. Marx, "Charge Transfers at Thermal Energies: Energy disposal and reaction mechanisms," in *Kinetics of Ion–Molecule Reactions*, P. Ausloos, ed. (Plenum, New York, 1979) 103.

180. M. F. Jarrold, L. Misev, and M. T. Bowers, J. Chem. Phys. **81** (1984) 4369.

181. M. T. Bowers and D. D. Elleman, Chem. Phys. Lett. **16** (1972) 486.

182. C. E. Hamilton, V. M. Bierbaum, and S. R. Leone, J. Chem. Phys. **83** (1985) 601.

183. Z. Herman, V. Pacák, A. J. Yencha, and J. Futrell, Chem. Phys. Lett. **37** (1976) 329.

184. T. Kato, J. Chem. Phys. **80** (1984) 6105.

185. B. Brehm, R. Frey, A. Küstler, and J. H. D. Eland, Int. J. Mass Spec. & Ion Phys. **13** (1974) 251.

186. F. A. Houle, S. L. Anderson, D. Gerlich, T. Turner, and Y. T. Lee, J. Chem. Phys. **77** (1982) 748.

187. L. Hüwel, D. R. Guyer, G.-H. Lin, and S. R. Leone, J. Chem. Phys. **81** (1984) 3520.

188. R. J. Shul, R. Passarella, L. T. DiFazio, Jr., R. G. Keesee, and A. W. Castleman, Jr., J. Phys. Chem. **92** (1988) 4947.

189. N. G. Adams, D. Smith, and E. Alge, J. Phys. B: Atom. Molec. Phys. **13** (1980) 3235.

190. P. R. Kemper, M. T. Bowers, D. C. Parent, G. Mauclaire, R. Derai, and R. Marx, J. Chem. Phys. **79** (1983) 160.

191. R. D. Smith and J. H. Futrell, Int. J. Mass Spec. & Ion Phys. **20** (1976) 33, 43, 59, 71.

192. H. Chatham, D. Hils, R. Robertson, and A. C. Gallagaher, J. Chem. Phys. **79** (1983) 1301.

193. W. T. Huntress Jr., J. B. Laudenslager, and R. F. Pinizzotto Jr., Int. J. Mass Spec. & Ion Phys. **13** (1974) 331.

194. J. B. Marquette, B. R. Rowe, G. Dupeyrat, G. Poissant, and C. Rebrion, Chem. Phys. Lett. **122** (1985) 431.

195. I. Dotan, W. Lindinger, B. Rowe, D. W. Fahey, F. C. Fehsenfeld, and D. L. Albritton, Chem. Phys. Lett. **72** (1980) 67.

196. G. Mauclaire, R. Derai, and R. Marx, Int. J. Mass Spec. & Ion Phys. **26** (1978) 289.

197. S. L. Varghese, G. Bissinger, J. M. Joyce, and R. Laubert, Phys. Rev. **A31** (1984) 2202; H. Tawara, At. Data and Nucl. Data Tables **22**, (1978) 491; H. Tawara and A. Russek, Rev. Mod. Phys. **45**, (1973) 178.

198. H. Villinger, J. H. Futrell, F. Howorka, N. Duric, and W. Lindinger, J. Chem. Phys. **76** (1982) 3529.

199. J. K. Kim and W. T. Huntress, Jr., J. Chem. Phys. **62** (1975) 2820.

200. P. E. S. Wormer and F. de Groot, J. Chem. Phys. **90** (1989) 2344.

201. W. T. Huntress and M. T. Bowers, Int. J. Mass Spec. & Ion Phys. **12** (1973) 1.

202. E. E. Ferguson, N. G. Adams, D. Smith, and E. Alge, J. Chem. Phys. **80** (1984) 6095.

203. A. B. Rakshit, Int. J. Mass Spec. & Ion Phys. **41** (1982) 185; **36** (1980) 31.

204. A. A. Viggiano, R. A. Morris, F. Dale, J. F. Paulson, and E. E. Ferguson, J. Chem. Phys. **90** (1989) 1648.

205. L. P. Theard and W. T. Huntress, J. Chem. Phys. **60** (1974) 2840.

206. W. Lindinger, F. Howorka, P. Lukac, S. Kuhn, H. Villinger, E. Alge, and H. Ramler, Phys. Rev. **A 23** (1981) 2319.

207. D. Smith and N. G. Adams, Phys. Rev **A 23** (1981) 2327.

208. H. Böhringer, M. Durup-Ferguson, D. W. Fahey, F. C. Fehsenfeld, and E. E. Ferguson, J. Chem. Phys. **79** (1983) 4201.

209. G. E. Quelch, Y. Xie, B. F. Yates, Y. Yamaguchi, and H. F. Schaefer III, Mol. Phys. **68** (1989) 1095.

210. I. Kusunoki and T. Ishikawa, J. Chem. Phys. **82** (1985) 4991.

211. H. Böhringer, Chem. Phys. Lett. **122** (1985) 185.

212. K. Hiraoka and P. Kebarle, J. Am. Chem. Soc. **98** (1976) 6119; Adv. Mass Spec. **7B** (1978) 1408.

213. H. Mayne, D. G. Fleming, M. Senba, and D. J. Arseneau, work in progress.

214. P. J. Estrup and R. Wolfgang, J. Am. Chem. Soc. **82** (1960) 2661; R. Wolfgang, Ann. Rev. Phys. Chem. **16** (1965) 15.

215. S. Scherbarth and D. Gerlich, J. Chem. Phys. **90** (1989) 1610.

216. D. M. Sonnenfroh and S. R. Leone, J. Chem. Phys. **90** (1989) 1677; D. C. Clary and D. M. Sonnenfroh, J. Chem. Phys. **90** (1989) 1686.

217. P. Tosi, M. Ronchetti, and A. Laganá, J. Chem. Phys. **88** (1988) 4814.

218. For example, H. S. Johnston, *Gas Phase Reaction Rate Theory* (Ronald, New York, 1966).

219. Yu. M. Belousov, V. N. Gorbunov, and V. P. Smilga, Hyper. Int. **65** (1990) 829.

220. D. van Pijkeren, E. Boltjes, J. van Eck, and A. Niehaus, Chem. Phys. **91** (1984) 293; D. van Pijkeren, J. van Eck, and A. Niehaus, Chem. Phys. **95** (1985) 449.

221. M. Durup-Ferguson, H. Böhringer, D. W. Fahey, and E. E. Ferguson, J. Chem. Phys. **79** (1983) 265.

222. S. C. Smith, M. J. McEwan, and R. G. Gilbert, J. Chem. Phys. **90** (1989) 1630; J. Phys. Chem. **93** (1989) 8142.

223. R. G. Gilbert and S. C. Smith, *Theory of Unimolecular and Recombination Reactions* (Blackwell Scientific, Oxford, 1990).

224. R. Patrick and D. M. Golden, J. Chem. Phys. **82** (1985) 75.

225. J. Troe, Ber. Bunsenges. Phys. Chem. **87** (1983) 161; R. G. Gilbert, K. Luther, and J. Troe, Ber. Bunsenges. Phys. Chem. **87** (1983) 169.

226. L. Bass, W. J. Chesnavich, and M. T. Bowers, J. Am. Chem. Soc. **101** (1979) 5493.

Appendix A

INTEGRATION OF THE NUMBER OF

TRANSITION STATES

For the transition state theory derivation of the Langevin rate constant, the number of transition states was given as

$$W^{\ddagger}(E - V) = \frac{1}{h^2} \int_0^{2\pi} \int_0^{\pi} \iint_{E_{\text{orb}}=0}^{E-V} dp_\phi \, dp_\psi \, d\phi \, d\psi \qquad (3.31)$$

evaluated at $r = r^{\ddagger}$, where ϕ and ψ are the spherical-polar angles for the orbital motion. The integration proceeds as follows.

To apply the E_{orb} limits, the momentum variables should be changed to energy according to

$$E_{\text{orb}} = \frac{p_\phi^2}{2mr^2} + \frac{p_\psi^2}{2mr^2(\sin\phi)^2} \qquad (A.1)$$

which describes a circle in the cartesian coordinates p_ϕ vs. $p_\psi / \sin\phi$. Introducing ζ as the angle around that circle allows a change to polar coordinates according to

$$p_\phi = r\sqrt{2mE_{\text{orb}}} \cos\zeta \qquad (A.2)$$

$$p_\psi = r\sqrt{2mE_{\text{orb}}} \sin\phi \sin\zeta . \qquad (A.3)$$

The Jacobian for this change of variables is $mr^2 \sin\phi$, so rewriting (3.31) in terms of E_{orb} and ζ gives

$$W^{\ddagger}(E - V) = \frac{1}{h^2} \int_0^{2\pi} d\psi \int_0^{\pi} \sin\phi \, d\phi \int_0^{E-V} mr^2 \, dE_{\text{orb}} \int_0^{2\pi} d\zeta \qquad (A.4)$$

$$= \frac{8\pi^2 mr^2}{h^2}(E - V) \qquad (A.5)$$

$$= \frac{8\pi^2 mr^2}{h^2}(E + \alpha q^2 / 2r^{\ddagger 4}) \qquad$$

which is the result quoted as equation (3.32).

The approach used by Chesnavich and Bowers [107] was to calculate the flux through the surface in phase space dividing reactants from products according to

$$k(E) = \iiiint\!\!\iiint \delta(r^{\ddagger} - r)\,\delta(E - H)\frac{p_r}{m}\,dr\,dp_r\,d\phi\,dp_\phi\,d\psi\,dp_\psi / h^3 \rho_t(E) \qquad (A.6)$$

which is not obviously the same as equation (3.29). The two can be reconciled though. First, the equation

$$W^{\ddagger} = \frac{1}{h^2} \int_0^{2\pi} \int_0^{\pi} \iint_{E_{\text{orb}}=0}^{E-V} dp_\phi \, dp_\psi \, d\phi \, d\psi \qquad (3.31)$$

is multiplied by $1 = \int \delta(r^{\ddagger} - r)\,dr$; and the Heavyside or step function $h(E - V - E_{\text{orb}})$ is used to replace the integration limit $E_{\text{orb}} = E - V$, giving

$$W^{\ddagger} = \frac{1}{h^2} \int_0^{2\pi} \int_0^{\pi} \iint_{E_{\text{orb}}=0}^{\infty} \int_{-\infty}^{\infty} h(E - V - E_{\text{orb}})\,\delta(r^{\ddagger} - r)\,dr\,dp_\phi\,dp_\psi\,d\phi\,d\psi\,. \qquad (A.7)$$

The argument $E - V - E_{\text{orb}}$ can be written $E - V_{\text{eff}}$, and the Heavyside function itself can be written as an integral,

$$h(E - V_{\text{eff}}) = \int_{-\infty}^{E-V_{\text{eff}}} \delta(z)\,dz \qquad (A.8)$$

where z can be anything with (in this case) units of energy; let

$$z = E - H = E - p_r^2/2m - V_{\text{eff}}\,, \qquad (A.9)$$

where H is the classical Hamiltonian at the transition state. Then $dz = -p_r/m\,dp_r$ because both E and V_{eff} are constant over the integration (they are in the limit). Thus

$$W^{\ddagger} = \frac{1}{h^2} \int_0^{2\pi} \int_0^{\pi} \iint_{E_{\text{orb}}=0}^{\infty} \int_{-\infty}^{\infty} \int_{E-H=-\infty}^{E-V_{\text{eff}}} -\delta(E-H)\frac{p_r}{m}\,\delta(r^{\ddagger}-r)\,dp_r\,dr\,dp_{\phi}\,dp_{\psi}\,d\phi\,d\psi\,.$$

$$(\text{A.10})$$

Finally, the limits of the integral over dp_r can be clarified by noting that the lower limit $E-H = -\infty$ implies $H = \infty$ (E is finite) or $p_r = \infty$, and the upper limit $E-H = E-V_{\text{eff}}$ implies $H = V_{\text{eff}}$ or $p_r = 0$; so, reversing the limits to change the sign,

$$W^{\ddagger} = \frac{1}{h^2} \int_0^{2\pi} \int_0^{\pi} \iint_{E_{\text{orb}}=0}^{\infty} \int_{-\infty}^{\infty} \int_0^{\infty} \delta(E-H)\frac{p_r}{m}\,\delta(r^{\ddagger}-r)\,dp_r\,dr\,dp_{\phi}\,dp_{\psi}\,d\phi\,d\psi\,, \quad (\text{A.11})$$

which, when combined with equation (3.29), gives equation (A.6), the starting equation of Chesnavich and Bowers [107].

Appendix B

TABULATED RESULTS

In this appendix are tabulated the useful parameters from the fits of all the data (table B.1, beginning on the next page). Results are grouped into many series of runs sharing the same reactant(s), moderator, and temperature. Each series begins with an identification of the gases and temperature; when there is no mention of T, room temperature is implied. Results usually occur in pairs, giving the parameters determined for each of two independent histograms of data. The data are listed in approximate chronological order.

The columns are: the reactant X and its concentration in 10^{14} molec cm^{-3}; the moderator gas M, which also identifies the reacting muonated ion, and its pressure in torr; the amplitude and relaxation rate (A_1, λ_1) of one signal, usually the slow relaxation; and then the other signal (A_2, λ_2), with the relaxations in μs^{-1}. Missing (blank) entries indicate that the corresponding signal was absent from the data, meaning the amplitude was near zero and λ was undefined, so the data was fit without those parameters. There are the results with only a single-component relaxation. Parameters reported without associated uncertainties had to be fixed at their expected values in order to get a reasonable fit. This happened whenever the "fast" relaxation became slow enough to be excessively coupled with the "slow" relaxation.

Table B.1.   Tabulated Results

X	M	A_1	λ_1	A_2	λ_2
Xe	Ne				
4.52 ± 0.23	1300	0.1992 ± 0.0056	0.0082 ± 0.0065	0.0437 ± 0.0054	1.55 ± 0.40
4.52 ± 0.23	1300	0.1993 ± 0.0064	0.0242 ± 0.0073	0.0425 ± 0.0057	1.49 ± 0.48
11.50 ± 0.60	1300	0.1454 ± 0.0036	0.0107 ± 0.0065	0.0809 ± 0.0042	2.05 ± 0.24
11.50 ± 0.60	1300	0.1422 ± 0.0047	0.0230 ± 0.0077	0.0960 ± 0.0084	2.03 ± 0.33
2.51 ± 0.13	1300	0.2161 ± 0.0043	0.0058 ± 0.0047	0.0236 ± 0.0045	1.55 ± 0.56
2.51 ± 0.13	1300	0.2223 ± 0.0045	0.0312 ± 0.0049	0.0228 ± 0.0054	2.1 ± 1.1
7.31 ± 0.37	1300	0.1719 ± 0.0048	0.0071 ± 0.0024	0.0448 ± 0.0035	1.71 ± 0.33
7.31 ± 0.37	1300	0.1838 ± 0.0032	0.0399 ± 0.0049	0.0584 ± 0.0093	4.0 ± 1.0
30.8 ± 1.5	1300	0.0873 ± 0.0029	-0.0044 ± 0.0088	0.0783 ± 0.0054	3.24 ± 0.44
30.8 ± 1.5	1300	0.0961 ± 0.0033	0.049 ± 0.010	0.067 ± 0.010	4.06 ± 0.87
20.1 ± 1.0	1300	0.0891 ± 0.0040	0.000 ± 0.011	0.1212 ± 0.0045	1.88 ± 0.15
20.1 ± 1.0	1300	0.0910 ± 0.0041	0.016 ± 0.011	0.1318 ± 0.0057	2.18 ± 0.20
20.1 ± 1.0	1300	0.1091 ± 0.0040	0.018 ± 0.010	0.0893 ± 0.0056	2.28 ± 0.28
20.1 ± 1.0	1300	0.1122 ± 0.0057	0.055 ± 0.014	0.0943 ± 0.0070	2.31 ± 0.40
Xe	He				
21.6 ± 1.1	1500	0.1146 ± 0.0028	0.0168 ± 0.0064	0.130 ± 0.010	4.74 ± 0.56
21.6 ± 1.1	1500	0.1085 ± 0.0040	0.057 ± 0.010	0.1350 ± 0.0093	3.71 ± 0.45
10.20 ± 0.51	1500	0.1547 ± 0.0032	0.0300 ± 0.0039	0.1085 ± 0.0091	4.12 ± 0.68
10.20 ± 0.51	1500	0.1506 ± 0.0054	0.0666 ± 0.0095	0.1088 ± 0.0078	2.75 ± 0.46
5.10 ± 0.30	1500	0.1936 ± 0.0035	0.0308 ± 0.0049	0.0746 ± 0.0082	3.85 ± 0.91
5.10 ± 0.30	1500	0.1731 ± 0.0071	0.0404 ± 0.0086	0.0775 ± 0.0069	1.57 ± 0.30
2.90 ± 0.20	1500	0.2135 ± 0.0033	0.0202 ± 0.0042	0.0442 ± 0.0067	3.19 ± 0.87
2.90 ± 0.20	1500	0.2105 ± 0.0047	0.0536 ± 0.0059	0.0557 ± 0.0085	3.2 ± 1.0
15.20 ± 0.80	1500	0.1280 ± 0.0031	0.0372 ± 0.0065	0.1180 ± 0.0077	3.97 ± 0.47
15.20 ± 0.80	1500	0.1280 ± 0.0044	0.087 ± 0.010	0.119 ± 0.011	3.99 ± 0.65
NH_3	He				
11.50 ± 0.60	1500	0.1179 ± 0.0022	0.0247 ± 0.0055	0.130 ± 0.024	9.9 ± 1.7
11.50 ± 0.60	1500	0.1193 ± 0.0028	0.0696 ± 0.0068	0.222 ± 0.065	16.0 ± 3.5
2.80 ± 0.20	1500	0.1383 ± 0.0023	0.0213 ± 0.0046	0.135 ± 0.018	8.1 ± 1.2
2.80 ± 0.20	1500	0.1396 ± 0.0035	0.0682 ± 0.0073	0.106 ± 0.015	5.5 ± 1.2
1.04 ± 0.10	1500	0.2108 ± 0.0030	0.0198 ± 0.0036	0.0398 ± 0.0064	3.6 ± 1.3
1.04 ± 0.10	1500	0.2002 ± 0.0051	0.0440 ± 0.0057	0.0452 ± 0.0053	2.11 ± 0.61
5.20 ± 0.30	1500	0.1585 ± 0.0025	0.0280 ± 0.0042	0.094 ± 0.014	7.0 ± 1.4
5.20 ± 0.30	1500	0.1496 ± 0.0037	0.0510 ± 0.0062	0.083 ± 0.010	4.43 ± 0.91

Table B.1.   Tabulated Results

X	M	A_1	λ_1	A_2	λ_2
NH$_3$	Ne				
5.60 ± 0.25	1300	0.1136 ± 0.0039	0.022 ± 0.010	0.1910 ± 0.0069	2.67 ± 0.20
5.60 ± 0.25	1300	0.1109 ± 0.0033	0.0181 ± 0.0083	0.1715 ± 0.0043	2.41 ± 0.14
10.20 ± 0.30	1300	0.0896 ± 0.0027	0.0194 ± 0.0092	0.1893 ± 0.0064	3.27 ± 0.20
10.20 ± 0.30	1300	0.0849 ± 0.0021	0.0050 ± 0.0074	0.1839 ± 0.0037	3.03 ± 0.13
13.50 ± 0.30	1300	0.0964 ± 0.0021	0.0122 ± 0.0074	0.196 ± 0.010	5.65 ± 0.41
13.50 ± 0.30	1300	0.0958 ± 0.0018	0.0115 ± 0.0062	0.1700 ± 0.0048	4.61 ± 0.26
21.60 ± 0.50	1300	0.0765 ± 0.0020	0.0087 ± 0.0087	0.198 ± 0.013	7.37 ± 0.55
21.60 ± 0.50	1300	0.0754 ± 0.0016	0.0089 ± 0.0072	0.1722 ± 0.0063	6.45 ± 0.42
NH$_3$	Ne				
3.40 ± 0.15	800	0.1340 ± 0.0046	0.0641 ± 0.0093	0.1115 ± 0.0072	2.72 ± 0.38
3.40 ± 0.15	800	0.1269 ± 0.0042	0.0391 ± 0.0072	0.0906 ± 0.0051	2.17 ± 0.27
3.40 ± 0.15	800	0.1164 ± 0.0048	0.040 ± 0.010	0.0910 ± 0.0055	2.05 ± 0.31
3.40 ± 0.15	800	0.1041 ± 0.0044	0.0201 ± 0.0082	0.0909 ± 0.0051	1.92 ± 0.26
6.10 ± 0.20	800	0.1131 ± 0.0035	0.0602 ± 0.0088	0.1171 ± 0.0070	3.15 ± 0.37
6.10 ± 0.20	800	0.1145 ± 0.0034	0.0492 ± 0.0067	0.0920 ± 0.0047	2.51 ± 0.27
8.20 ± 0.20	800	0.1545 ± 0.0031	0.1343 ± 0.0074	0.0823 ± 0.0086	4.62 ± 0.78
8.20 ± 0.20	800	0.1470 ± 0.0027	0.0574 ± 0.0051	0.0763 ± 0.0055	3.65 ± 0.48
13.20 ± 0.26	800	0.1226 ± 0.0028	0.1154 ± 0.0085	0.102 ± 0.011	5.88 ± 0.86
13.20 ± 0.26	800	0.1271 ± 0.0028	0.0535 ± 0.0059	0.0710 ± 0.0064	4.00 ± 0.66
CH$_3$F	Ne				
19.8 ± 1.0	1400	0.1217 ± 0.0035	0.0210 ± 0.0078	0.0991 ± 0.0052	2.99 ± 0.33
19.8 ± 1.0	1400	0.1319 ± 0.0031	0.0411 ± 0.0070	0.1010 ± 0.0068	3.44 ± 0.45
39.5 ± 2.0	1400	0.0954 ± 0.0023	0.0265 ± 0.0077	0.0840 ± 0.0072	5.40 ± 0.84
39.5 ± 2.0	1400	0.0988 ± 0.0028	0.0369 ± 0.0084	0.0752 ± 0.0067	3.61 ± 0.58
4.96 ± 0.25	1400	0.1942 ± 0.0042	0.0166 ± 0.0058	0.0607 ± 0.0050	2.34 ± 0.50
4.96 ± 0.25	1400	0.2081 ± 0.0032	0.0390 ± 0.0046	0.0554 ± 0.0053	2.48 ± 0.46
10.35 ± 0.21	1400	0.1578 ± 0.0046	0.0300 ± 0.0079	0.0859 ± 0.0051	2.26 ± 0.34
10.35 ± 0.21	1400	0.1645 ± 0.0034	0.0411 ± 0.0063	0.0979 ± 0.0056	2.83 ± 0.35
27.2 ± 1.4	1400	0.1128 ± 0.0024	0.0332 ± 0.0067	0.0957 ± 0.0057	4.48 ± 0.52
27.2 ± 1.4	1400	0.1136 ± 0.0024	0.0329 ± 0.0065	0.1007 ± 0.0064	3.83 ± 0.42
CH$_3$F	Ne				
11.10 ± 0.50	800	0.0793 ± 0.0036	0.025 ± 0.011	0.0812 ± 0.0053	2.72 ± 0.42
11.10 ± 0.50	800	0.0792 ± 0.0042	0.023 ± 0.012	0.0791 ± 0.0059	2.27 ± 0.36
22.3 ± 1.1	800	0.0526 ± 0.0027	0.038 ± 0.013	0.0797 ± 0.0068	4.57 ± 0.85
22.3 ± 1.1	800	0.0550 ± 0.0028	0.050 ± 0.014	0.0799 ± 0.0066	4.27 ± 0.74
5.83 ± 0.12	800	0.1173 ± 0.0034	0.0348 ± 0.0056	0.0747 ± 0.0047	2.84 ± 0.43

Table B.1. Tabulated Results

X	M	A_1	λ_1	A_2	λ_2
5.83 ± 0.12	800	0.1172 ± 0.0039	0.0265 ± 0.0080	0.0676 ± 0.0050	2.09 ± 0.34
15.60 ± 0.80	800	0.0671 ± 0.0023	0.0242 ± 0.0088	0.0854 ± 0.0054	4.12 ± 0.52
15.60 ± 0.80	800	0.0724 ± 0.0032	0.046 ± 0.012	0.0740 ± 0.0056	3.15 ± 0.48
N_2O	Ne				
21.5 ± 1.0	1000	0.0987 ± 0.0030	0.0084 ± 0.0078	0.0933 ± 0.0053	3.17 ± 0.39
21.5 ± 1.0	1000	0.1058 ± 0.0042	0.019 ± 0.010	0.0827 ± 0.0054	2.06 ± 0.30
31.9 ± 1.5	1225	0.1073 ± 0.0024	0.0111 ± 0.0066	0.1009 ± 0.0068	5.26 ± 0.70
31.9 ± 1.5	1225	0.1107 ± 0.0025	0.0270 ± 0.0069	0.0950 ± 0.0071	4.06 ± 0.52
13.30 ± 0.66	1000	0.1345 ± 0.0028	0.0154 ± 0.0056	0.0814 ± 0.0052	3.43 ± 0.46
13.30 ± 0.66	1000	0.1379 ± 0.0033	0.0176 ± 0.0059	0.0813 ± 0.0062	2.81 ± 0.42
5.70 ± 0.11	1000	0.171 ± 0.010	0.015 ± 0.010	0.0743 ± 0.0087	1.05 ± 0.20
5.70 ± 0.11	1000	0.1858 ± 0.0077	0.0320 ± 0.0086	0.0721 ± 0.0072	1.22 ± 0.23
3.420 ± 0.068	1000	0.195 ± 0.013	0.011 ± 0.011	0.047 ± 0.012	0.85 ± 0.31
3.420 ± 0.068	1000	0.2050 ± 0.0074	0.0183 ± 0.0075	0.0501 ± 0.0065	1.29 ± 0.36
C_2H_4	Ne				
11.00 ± 0.22	1000	0.1498 ± 0.0030	0.0156 ± 0.0056	0.0686 ± 0.0049	3.21 ± 0.55
11.00 ± 0.22	1000	0.1594 ± 0.0034	0.0343 ± 0.0060	0.0572 ± 0.0054	2.69 ± 0.55
21.5 ± 1.0	1000	0.1272 ± 0.0025	0.0241 ± 0.0060	0.0671 ± 0.0068	5.5 ± 1.1
21.5 ± 1.0	1000	0.1296 ± 0.0029	0.0210 ± 0.0065	0.0610 ± 0.0067	3.51 ± 0.77
5.00 ± 0.10	1000	0.1877 ± 0.0043	0.0194 ± 0.0056	0.0540 ± 0.0047	1.79 ± 0.33
5.00 ± 0.10	1000	0.1875 ± 0.0064	0.0197 ± 0.0069	0.0556 ± 0.0056	1.23 ± 0.30
32.2 ± 1.6	870	0.0682 ± 0.0020	0.0105 ± 0.0077	0.057 ± 0.010	7.7 ± 2.7
32.2 ± 1.6	870	0.0764 ± 0.0025	0.0368 ± 0.0090	0.049 ± 0.013	7.2 ± 3.6
Kr	Ne				
1.500 ± 0.030	1000	0.2691 ± 0.0014	0.0206 ± 0.0020		
1.500 ± 0.030	1000	0.2804 ± 0.0013	0.0281 ± 0.0019		
79.3 ± 4.0	1000	0.1275 ± 0.0092	0.013 ± 0.012	0.0536 ± 0.0087	0.90 ± 0.21
79.3 ± 4.0	1000	0.1334 ± 0.0082	0.018 ± 0.011	0.0641 ± 0.0076	0.98 ± 0.19
39.7 ± 2.0	1000	0.1741 ± 0.0077	0.0199 ± 0.0051	0.0448 ± 0.0068	1.20 ± 0.40
39.7 ± 2.0	1000	0.152 ± 0.018	0.004 ± 0.018	0.074 ± 0.018	0.66 ± 0.20
$252. \pm 12.$	1000	0.0799 ± 0.0049	0.005 ± 0.012	0.0255 ± 0.0042	1.62 ± 0.38
$252. \pm 12.$	1000	0.0870 ± 0.0033	0.0260 ± 0.0092	0.0333 ± 0.0047	2.18 ± 0.58
119.0 ± 6.0	1000	0.0763 ± 0.0071	0.005 ± 0.017	0.0445 ± 0.0060	1.20 ± 0.36
119.0 ± 6.0	1000	0.0935 ± 0.0061	0.042 ± 0.014	0.0350 ± 0.0056	1.65 ± 0.63
Xe	Ne				
2.52 ± 0.15	1000	0.180 ± 0.026	0.028 ± 0.021	0.083 ± 0.026	0.57 ± 0.18
2.52 ± 0.15	1000	0.175 ± 0.050	0.033 ± 0.037	0.097 ± 0.047	0.48 ± 0.18

Table B.1. Tabulated Results

X	M	A_1	λ_1	A_2	λ_2
1.230 ± 0.070	1000	0.215 ± 0.040	0.013 ± 0.025	0.030 ± 0.040	0.58 ± 0.30
1.230 ± 0.070	1000	0.228 ± 0.030	0.023 ± 0.019	0.034 ± 0.030	0.74 ± 0.51
6.07 ± 0.36	1000	0.122 ± 0.012	0.045 ± 0.016	0.131 ± 0.012	0.86 ± 0.10
6.07 ± 0.36	1000	0.116 ± 0.014	0.039 ± 0.020	0.144 ± 0.014	0.78 ± 0.10
3.00 ± 0.15	1000	0.1876 ± 0.0080	0.0129 ± 0.0077	0.0569 ± 0.0072	1.04 ± 0.21
3.00 ± 0.15	1000	0.186 ± 0.012	0.0159 ± 0.0031	0.068 ± 0.011	0.82 ± 0.20
1.600 ± 0.080	1000	0.2223 ± 0.0095	0.0241 ± 0.0076	0.0393 ± 0.0089	0.89 ± 0.32
1.600 ± 0.080	1000	0.200 ± 0.010	0.02	0.0676 ± 0.0090	0.34 ± 0.20
CH_4	Ne				
79.3 ± 4.0	1000	0.0748 ± 0.0014	0.0184 ± 0.0066		
79.3 ± 4.0	1000	0.0755 ± 0.0015	0.0300 ± 0.0070		
9.54 ± 0.19	1000	0.2212 ± 0.0013	0.0134 ± 0.0022		
9.54 ± 0.19	1000	0.2300 ± 0.0013	0.0229 ± 0.0021		
0.862 ± 0.017	1000	0.2614 ± 0.0013	0.0119 ± 0.0020		
0.862 ± 0.017	1000	0.2792 ± 0.0013	0.0216 ± 0.0020		
N_2O	He				
32.4 ± 1.6	1500	0.1276 ± 0.0023	0.0813 ± 0.0053	0.152 ± 0.014	8.6 ± 1.1
32.4 ± 1.6	1500	0.1407 ± 0.0026	0.0747 ± 0.0070	0.119 ± 0.011	7.1 ± 1.1
19.5 ± 1.0	1500	0.1424 ± 0.0034	0.0678 ± 0.0088	0.1028 ± 0.0063	4.02 ± 0.51
19.5 ± 1.0	1500	0.1528 ± 0.0036	0.0520 ± 0.0071	0.1086 ± 0.0090	4.11 ± 0.66
8.90 ± 0.18	1500	0.1725 ± 0.0034	0.0811 ± 0.0057	0.0932 ± 0.0046	2.92 ± 0.34
8.90 ± 0.18	1500	0.1626 ± 0.0050	0.0304 ± 0.0076	0.1210 ± 0.0056	2.01 ± 0.23
3.200 ± 0.064	1500	0.2005 ± 0.0075	0.0664 ± 0.0088	0.0754 ± 0.0072	1.62 ± 0.33
3.200 ± 0.064	1500	0.184 ± 0.020	0.021 ± 0.019	0.099 ± 0.018	0.90 ± 0.30
CH_3F	He				
10.90 ± 0.54	1500	0.1870 ± 0.0023	0.0958 ± 0.0043	0.0835 ± 0.0076	5.17 ± 0.85
10.90 ± 0.54	1500	0.1904 ± 0.0038	0.0735 ± 0.0062	0.0905 ± 0.0074	3.87 ± 0.77
43.0 ± 2.1	1500	0.1448 ± 0.0022	0.1029 ± 0.0078	0.148 ± 0.029	13.3 ± 2.5
43.0 ± 2.1	1500	0.1647 ± 0.0026	0.1336 ± 0.0090	0.076 ± 0.022	15.7 ± 6.4
5.64 ± 0.11	1500	0.2010 ± 0.0034	0.0878 ± 0.0049	0.0679 ± 0.0046	3.05 ± 0.48
5.64 ± 0.11	1500	0.2124 ± 0.0040	0.0727 ± 0.0054	0.0748 ± 0.0047	2.78 ± 0.49
3.000 ± 0.060	1500	0.2192 ± 0.0032	0.0865 ± 0.0042	0.0581 ± 0.0044	3.00 ± 0.57
3.000 ± 0.060	1500	0.2171 ± 0.0073	0.0523 ± 0.0073	0.0629 ± 0.0067	1.41 ± 0.32
3.870 ± 0.077	1495	0.2003 ± 0.0053	0.0851 ± 0.0065	0.0658 ± 0.0050	1.91 ± 0.35
3.870 ± 0.077	1495	0.1977 ± 0.0075	0.0445 ± 0.0085	0.0812 ± 0.0070	1.52 ± 0.30

Table B.1. Tabulated Results

X	M	A_1	λ_1	A_2	λ_2
Kr	**He**				
45.1 ± 2.2	1500	0.2503 ± 0.0014	0.0747 ± 0.0025		
45.1 ± 2.2	1500	0.2657 ± 0.0018	0.0519 ± 0.0029		
$482. \pm 24.$	1500	0.1595 ± 0.0018	0.0789 ± 0.0046		
$482. \pm 24.$	1500	0.1674 ± 0.0022	0.0557 ± 0.0054		
10.74 ± 0.50	1500	0.2667 ± 0.0017	0.0776 ± 0.0028		
10.74 ± 0.50	1500	0.2880 ± 0.0022	0.0607 ± 0.0032		
NH_3	**Ar**				
21.5 ± 1.0	600	0.0429 ± 0.0011	0.0234 ± 0.0075		
21.5 ± 1.0	600	0.0481 ± 0.0011	0.0173 ± 0.0079		
161.0 ± 8.0	600	0.0075 ± 0.0008	0.014 ± 0.012		
161.0 ± 8.0	600	0.0128 ± 0.0009	0.025 ± 0.014		
80.8 ± 4.0	600	0.0217 ± 0.0013	0.026 ± 0.015		
80.8 ± 4.0	600	0.0288 ± 0.0015	0.035 ± 0.016		
5.50 ± 0.11	600	0.0538 ± 0.0013	0.0089 ± 0.0076		
5.50 ± 0.11	600	0.0611 ± 0.0014	0.0062 ± 0.0077		
CH_4	**He**				
164.0 ± 8.0	1500	0.1356 ± 0.0019	0.0907 ± 0.0057		
164.0 ± 8.0	1500	0.1426 ± 0.0024	0.0732 ± 0.0070		
16.40 ± 0.80	1500	0.2492 ± 0.0018	0.0701 ± 0.0030		
16.40 ± 0.80	1500	0.2655 ± 0.0022	0.0496 ± 0.0035		
CH_4	**He**	(plus 11.1×10^{14} molec/cm^3 Xe)			
19.8 ± 1.0	1500	0.1857 ± 0.0029	0.0868 ± 0.0055	0.087 ± 0.016	7.3 ± 2.0
19.8 ± 1.0	1500	0.1947 ± 0.0036	0.0560 ± 0.0063	0.072 ± 0.017	6.6 ± 2.5
Xe	**Ne**	(at 172° C)			
7.50 ± 0.15	1400	0.073 ± 0.040	0.0	0.204 ± 0.060	0.63 ± 0.21
7.50 ± 0.15	1400	0.124 ± 0.040	0.0	0.180 ± 0.040	0.64 ± 0.13
7.50 ± 0.15	1400	0.137 ± 0.016	0.0	0.140 ± 0.015	1.03 ± 0.17
7.50 ± 0.15	1400	0.194 ± 0.018	0.0	0.117 ± 0.016	1.12 ± 0.27
45.50 ± 0.91	1400	0.0403 ± 0.0025	0.0	0.1058 ± 0.0047	2.91 ± 0.26
45.50 ± 0.91	1400	0.1066 ± 0.0041	0.0	0.0845 ± 0.0067	2.58 ± 0.36
31.00 ± 0.62	1400	0.0489 ± 0.0030	0.0	0.1447 ± 0.0033	2.10 ± 0.11
31.00 ± 0.62	1400	0.1063 ± 0.0038	0.0	0.1383 ± 0.0044	2.18 ± 0.15
31.00 ± 0.62	1400	0.0573 ± 0.0029	0.0	0.1283 ± 0.0039	2.38 ± 0.17
31.00 ± 0.62	1400	0.1092 ± 0.0043	0.0	0.1245 ± 0.0055	2.66 ± 0.26
83.0 ± 1.7	1400	0.0338 ± 0.0028	0.0	0.0671 ± 0.0059	3.23 ± 0.60
83.0 ± 1.7	1400	0.0897 ± 0.0029	0.0	0.062 ± 0.014	6.3 ± 2.4

Table B.1.   Tabulated Results

X	M	A_1	λ_1	A_2	λ_2
70.0 ± 1.4	1400	0.0458 ± 0.0033	0.0	0.0853 ± 0.0064	4.29 ± 0.68
70.0 ± 1.4	1400	0.0491 ± 0.0023	0.0	0.0746 ± 0.0053	4.09 ± 0.53
84.0 ± 1.7	1400	0.0465 ± 0.0036	0.0	0.0657 ± 0.0079	4.6 ± 1.0
84.0 ± 1.7	1400	0.0439 ± 0.0032	0.0	0.0693 ± 0.0057	3.18 ± 0.60
119.0 ± 2.4	1400	0.0405 ± 0.0020	0.0	0.0499 ± 0.0060	5.9 ± 1.3
119.0 ± 2.4	1400	0.0457 ± 0.0016	0.0	0.0517 ± 0.0078	6.7 ± 1.5
NH_3	Ne	(at 172° C)			
6.00 ± 0.50	1400	0.1266 ± 0.0077	0.0	0.1722 ± 0.0070	1.51 ± 0.13
6.00 ± 0.50	1400	0.1332 ± 0.0046	0.0	0.1730 ± 0.0048	1.79 ± 0.12
3.000 ± 0.060	1400	0.140 ± 0.022	0.0	0.186 ± 0.022	0.75 ± 0.10
3.000 ± 0.060	1400	0.146 ± 0.019	0.0	0.181 ± 0.018	0.733 ± 0.090
10.90 ± 0.22	1400	0.0913 ± 0.0050	0.0	0.1949 ± 0.0058	2.50 ± 0.17
10.90 ± 0.22	1400	0.0877 ± 0.0035	0.0	0.2020 ± 0.0049	2.48 ± 0.14
20.00 ± 0.40	1400	0.0749 ± 0.0027	0.0	0.1756 ± 0.0071	5.43 ± 0.40
20.00 ± 0.40	1400	0.0720 ± 0.0021	0.0	0.1679 ± 0.0071	4.79 ± 0.35
1.500 ± 0.030	1400	0.1992 ± 0.0057	0.0	0.1360 ± 0.0051	0.540 ± 0.090
1.500 ± 0.030	1400	0.1946 ± 0.0041	0.0	0.1424 ± 0.0037	0.531 ± 0.080
33.00 ± 0.66	1400	0.0614 ± 0.0019	0.0	0.1586 ± 0.0079	7.81 ± 0.60
33.00 ± 0.66	1400	0.0620 ± 0.0015	0.0	0.1490 ± 0.0090	6.98 ± 0.63
N_2O	Ne	(at 172° C)			
33.00 ± 0.66	1400	0.1308 ± 0.0023	0.0	0.104 ± 0.011	7.4 ± 1.2
33.00 ± 0.66	1400	0.1296 ± 0.0022	0.0	0.0797 ± 0.0073	5.01 ± 0.80
11.00 ± 0.22	1400	0.1906 ± 0.0062	0.0	0.0974 ± 0.0058	1.78 ± 0.26
11.00 ± 0.22	1400	0.1914 ± 0.0042	0.0	0.1036 ± 0.0046	1.84 ± 0.19
1.500 ± 0.030	1400	0.30 ± 0.12	0.0	0.043 ± 0.050	0.32 ± 0.25
1.500 ± 0.030	1400	0.303 ± 0.038	0.0	0.036 ± 0.050	0.34 ± 0.40
21.40 ± 0.43	1400	0.1489 ± 0.0036	0.0	0.1017 ± 0.0061	3.09 ± 0.42
21.40 ± 0.43	1400	0.1516 ± 0.0027	0.0	0.0972 ± 0.0056	3.39 ± 0.40
56.3 ± 1.1	1400	0.0943 ± 0.0024	0.0	0.096 ± 0.016	8.7 ± 2.0
56.3 ± 1.1	1400	0.0950 ± 0.0019	0.0	0.0714 ± 0.0090	6.6 ± 1.4
CH_3F	Ne	(at 172° C)			
16.50 ± 0.33	1400	0.1438 ± 0.0034	0.0	0.0771 ± 0.0044	2.42 ± 0.30
16.50 ± 0.33	1400	0.1888 ± 0.0039	0.0	0.0723 ± 0.0075	3.77 ± 0.76
5.60 ± 0.11	1400	0.1826 ± 0.0087	0.0	0.0983 ± 0.0080	1.17 ± 0.16
5.60 ± 0.11	1400	0.2421 ± 0.0065	0.0	0.0707 ± 0.0066	2.03 ± 0.40
11.10 ± 0.22	1400	0.1665 ± 0.0042	0.0	0.0774 ± 0.0047	2.43 ± 0.38
11.10 ± 0.22	1400	0.1977 ± 0.0056	0.0	0.0824 ± 0.0067	2.71 ± 0.57

Table B.1. Tabulated Results

X	M	A_1	λ_1	A_2	λ_2
11.10 ± 0.22	1400	0.1825 ± 0.0039	0.0	0.0859 ± 0.0066	3.48 ± 0.58
11.10 ± 0.22	1400	0.1722 ± 0.0040	0.0	0.0894 ± 0.0051	2.35 ± 0.29
33.00 ± 0.66	1400	0.1299 ± 0.0029	0.0	0.0638 ± 0.0082	5.2 ± 1.2
33.00 ± 0.66	1400	0.1360 ± 0.0022	0.0	0.0629 ± 0.0082	6.5 ± 1.3
1.530 ± 0.031	1400	0.2708 ± 0.0046	0.05	0.0643 ± 0.0043	0.72 ± 0.13
1.530 ± 0.031	1400	0.3074 ± 0.0027	0.05	0.0254 ± 0.0034	1.11 ± 0.37
26.40 ± 0.53	1400	0.1446 ± 0.0026	0.0	0.0555 ± 0.0066	4.6 ± 1.0
26.40 ± 0.53	1400	0.1409 ± 0.0021	0.0	0.0700 ± 0.0056	4.28 ± 0.61
30.20 ± 0.60	1400	0.1406 ± 0.0021	0.0	0.091 ± 0.012	8.7 ± 1.7
30.20 ± 0.60	1400	0.1412 ± 0.0023	0.0	0.0630 ± 0.0070	5.3 ± 1.1
Xe	Ne	(at $-96°$ C)			
30.50 ± 0.61	560	0.0421 ± 0.0064	0.098 ± 0.043	0.2047 ± 0.0073	1.74 ± 0.13
30.50 ± 0.61	560	0.0539 ± 0.0049	0.047 ± 0.025	0.1902 ± 0.0054	1.84 ± 0.11
19.40 ± 0.39	560	0.0376 ± 0.0088	0.077 ± 0.054	0.261 ± 0.012	1.10 ± 0.14
19.40 ± 0.39	560	0.0338 ± 0.0061	-0.040 ± 0.038	0.2592 ± 0.0062	1.06 ± 0.10
9.80 ± 0.20	570	0.010 ± 0.010	0.0	0.318 ± 0.010	0.670 ± 0.076
9.80 ± 0.20	570	0.032 ± 0.012	0.0	0.295 ± 0.012	0.71 ± 0.10
81.2 ± 1.6	565	0.0459 ± 0.0036	0.104 ± 0.028	0.1056 ± 0.0055	2.83 ± 0.30
81.2 ± 1.6	565	0.0469 ± 0.0029	0.037 ± 0.020	0.0973 ± 0.0051	2.86 ± 0.32
54.8 ± 1.1	565	0.0428 ± 0.0037	0.072 ± 0.028	0.1552 ± 0.0055	2.58 ± 0.19
54.8 ± 1.1	565	0.0499 ± 0.0035	0.050 ± 0.022	0.1398 ± 0.0051	2.47 ± 0.19
66.0 ± 1.3	565	0.0421 ± 0.0041	0.112 ± 0.034	0.1278 ± 0.0058	2.46 ± 0.23
66.0 ± 1.3	565	0.0484 ± 0.0031	0.059 ± 0.021	0.1305 ± 0.0054	2.97 ± 0.24
38.00 ± 0.76	550	0.0505 ± 0.0048	0.116 ± 0.030	0.1657 ± 0.0063	2.12 ± 0.16
38.00 ± 0.76	550	0.0495 ± 0.0038	0.019 ± 0.022	0.1710 ± 0.0052	2.18 ± 0.14
NH_3	Ne	(at $-96°$ C)			
33.00 ± 0.66	565	0.0756 ± 0.0022	0.068 ± 0.012	0.193 ± 0.012	8.84 ± 0.83
33.00 ± 0.66	565	0.0770 ± 0.0019	0.0069 ± 0.0088	0.175 ± 0.013	8.42 ± 0.89
2.900 ± 0.058	570	0.086 ± 0.021	-0.002 ± 0.044	0.256 ± 0.022	0.620 ± 0.070
2.900 ± 0.058	570	0.147 ± 0.015	0.042 ± 0.019	0.194 ± 0.014	0.850 ± 0.080
23.10 ± 0.46	565	0.0831 ± 0.0026	0.064 ± 0.012	0.2037 ± 0.0091	5.98 ± 0.45
23.10 ± 0.46	565	0.0846 ± 0.0022	0.0214 ± 0.0093	0.1871 ± 0.0083	5.78 ± 0.42
19.40 ± 0.39	565	0.0847 ± 0.0027	0.073 ± 0.012	0.2096 ± 0.0081	5.29 ± 0.36
19.40 ± 0.39	565	0.0939 ± 0.0024	0.0338 ± 0.0091	0.2012 ± 0.0087	5.77 ± 0.43
16.40 ± 0.33	560	0.0865 ± 0.0027	0.055 ± 0.011	0.2052 ± 0.0066	4.31 ± 0.25
16.40 ± 0.33	560	0.0936 ± 0.0024	0.0186 ± 0.0085	0.2083 ± 0.0064	4.53 ± 0.27

Table B.1. Tabulated Results

X	M	A_1	λ_1	A_2	λ_2
N_2O	Ne	(at $-96°$ C)			
22.12 ± 0.44	560	0.1568 ± 0.0031	0.0	0.1184 ± 0.0055	3.26 ± 0.32
22.12 ± 0.44	560	0.1525 ± 0.0030	0.0	0.1143 ± 0.0045	2.53 ± 0.23
11.80 ± 0.24	560	0.1715 ± 0.0069	0.0	0.1301 ± 0.0067	1.41 ± 0.14
11.80 ± 0.24	560	0.1828 ± 0.0048	0.0	0.1198 ± 0.0052	1.74 ± 0.16
11.80 ± 0.24	850	0.1978 ± 0.0073	0.0296 ± 0.0089	0.1437 ± 0.0068	1.48 ± 0.16
11.80 ± 0.24	850	0.1919 ± 0.0054	0.0071 ± 0.0068	0.1445 ± 0.0053	1.46 ± 0.12
33.10 ± 0.66	880	0.1635 ± 0.0023	0.0292 ± 0.0047	0.1423 ± 0.0067	4.18 ± 0.33
33.10 ± 0.66	880	0.1572 ± 0.0018	-0.0007 ± 0.0038	0.1422 ± 0.0046	4.17 ± 0.26
33.10 ± 0.66	880	0.1633 ± 0.0033	0.0	0.1286 ± 0.0074	3.57 ± 0.38
33.10 ± 0.66	880	0.1612 ± 0.0023	0.0	0.1427 ± 0.0060	4.50 ± 0.37
CH_3F	Ne	(at $-96°$ C)			
33.00 ± 0.66	565	0.1131 ± 0.0023	0.0899 ± 0.0082	0.0855 ± 0.0070	5.73 ± 0.83
33.00 ± 0.66	565	0.1173 ± 0.0022	0.0416 ± 0.0068	0.0816 ± 0.0069	5.05 ± 0.81
33.00 ± 0.66	835	0.1413 ± 0.0030	0.0500 ± 0.0073	0.1337 ± 0.0073	4.02 ± 0.41
33.00 ± 0.66	835	0.1386 ± 0.0025	0.0225 ± 0.0058	0.1303 ± 0.0050	3.59 ± 0.30
3.800 ± 0.076	565	0.186 ± 0.014	0.047 ± 0.015	0.144 ± 0.013	0.93 ± 0.13
3.800 ± 0.076	565	0.2057 ± 0.0093	0.032 ± 0.010	0.1272 ± 0.0087	1.07 ± 0.12
11.00 ± 0.22	565	0.1661 ± 0.0040	0.0665 ± 0.0076	0.1300 ± 0.0058	2.58 ± 0.23
11.00 ± 0.22	565	0.1613 ± 0.0041	0.0174 ± 0.0070	0.1381 ± 0.0050	2.22 ± 0.19
22.00 ± 0.44	565	0.1343 ± 0.0028	0.0895 ± 0.0077	0.1118 ± 0.0058	4.09 ± 0.43
22.00 ± 0.44	565	0.1359 ± 0.0023	0.0339 ± 0.0058	0.1151 ± 0.0053	3.89 ± 0.35
27.10 ± 0.54	565	0.1256 ± 0.0027	0.0800 ± 0.0079	0.1181 ± 0.0062	4.42 ± 0.47
27.10 ± 0.54	565	0.1268 ± 0.0024	0.0260 ± 0.0063	0.1077 ± 0.0052	3.69 ± 0.36
27.10 ± 0.54	850	0.1511 ± 0.0033	0.0436 ± 0.0071	0.1367 ± 0.0061	3.22 ± 0.30
27.10 ± 0.54	850	0.1551 ± 0.0022	0.0274 ± 0.0048	0.1406 ± 0.0052	4.12 ± 0.29
16.40 ± 0.33	565	0.1437 ± 0.0035	0.0664 ± 0.0082	0.1328 ± 0.0063	3.49 ± 0.36
16.40 ± 0.33	565	0.1539 ± 0.0027	0.0426 ± 0.0060	0.1243 ± 0.0064	4.17 ± 0.43
16.40 ± 0.33	860	0.1732 ± 0.0037	0.0406 ± 0.0064	0.1514 ± 0.0056	2.60 ± 0.21
16.40 ± 0.33	860	0.1753 ± 0.0026	0.0263 ± 0.0047	0.1563 ± 0.0044	3.32 ± 0.22
NH_3	Ne				
14.70 ± 0.29	1510	0.0535 ± 0.0027	0.015 ± 0.014	0.1974 ± 0.0066	3.46 ± 0.22
14.70 ± 0.29	1510	0.0670 ± 0.0027	0.016 ± 0.011	0.2178 ± 0.0051	3.36 ± 0.17
7.40 ± 0.15	1885	0.073 ± 0.010	0.002 ± 0.014	0.201 ± 0.011	1.79 ± 0.21
7.40 ± 0.15	1885	0.090 ± 0.010	0.012 ± 0.011	0.228 ± 0.010	1.78 ± 0.18
7.40 ± 0.15	910	0.0712 ± 0.0058	0.150 ± 0.023	0.1322 ± 0.0070	2.40 ± 0.26
7.40 ± 0.15	910	0.0735 ± 0.0038	0.065 ± 0.013	0.1708 ± 0.0048	2.31 ± 0.14
7.40 ± 0.15	1210	0.0962 ± 0.0080	0.115 ± 0.013	0.125 ± 0.010	3.43 ± 0.62

Table B.1. Tabulated Results

X	M	A_1	λ_1	A_2	λ_2
7.40 ± 0.15	1210	0.1162 ± 0.0077	0.0645 ± 0.0089	0.1344 ± 0.0089	2.48 ± 0.50
7.40 ± 0.15	610	0.041 ± 0.016	0.182 ± 0.036	0.105 ± 0.017	2.43 ± 0.94
7.40 ± 0.15	610	0.039 ± 0.011	0.106 ± 0.021	0.131 ± 0.015	2.73 ± 0.73
7.40 ± 0.15	1135	0.1133 ± 0.0018	0.0041 ± 0.0046	0.0882 ± 0.0048	3.82 ± 0.39
7.40 ± 0.15	1135	0.1447 ± 0.0017	0.0133 ± 0.0036	0.0940 ± 0.0048	4.49 ± 0.42
7.40 ± 0.15	1210	0.0602 ± 0.0039	-0.006 ± 0.015	0.1874 ± 0.0047	1.86 ± 0.11
7.40 ± 0.15	1210	0.0823 ± 0.0037	0.007 ± 0.011	0.2040 ± 0.0045	1.96 ± 0.10
7.40 ± 0.15	1210	0.0614 ± 0.0041	0.000 ± 0.016	0.1868 ± 0.0052	1.91 ± 0.12
7.40 ± 0.15	1210	0.0824 ± 0.0040	0.018 ± 0.012	0.2137 ± 0.0050	2.11 ± 0.11
7.40 ± 0.15	1810	0.1083 ± 0.0034	0.0133 ± 0.0080	0.1565 ± 0.0053	2.37 ± 0.17
7.40 ± 0.15	1810	0.1316 ± 0.0027	0.0148 ± 0.0057	0.1798 ± 0.0043	2.70 ± 0.14
7.50 ± 0.15	1810	0.0942 ± 0.0033	-0.0006 ± 0.0087	0.1726 ± 0.0051	2.15 ± 0.13
7.50 ± 0.15	1810	0.1208 ± 0.0031	0.0210 ± 0.0069	0.1996 ± 0.0043	2.46 ± 0.12
10.90 ± 0.22	1210	0.0537 ± 0.0036	0.016 ± 0.017	0.1749 ± 0.0057	2.54 ± 0.19
10.90 ± 0.22	1210	0.0734 ± 0.0031	0.025 ± 0.012	0.2105 ± 0.0056	3.11 ± 0.18
10.90 ± 0.22	1810	0.1021 ± 0.0027	0.0080 ± 0.0074	0.1613 ± 0.0067	3.32 ± 0.25
10.90 ± 0.22	1810	0.1241 ± 0.0025	0.0134 ± 0.0058	0.1761 ± 0.0049	3.40 ± 0.20
Xe	Ne				
44.50 ± 0.89	1210	0.0148 ± 0.0031	0.000 ± 0.042	0.1507 ± 0.0043	2.14 ± 0.13
44.50 ± 0.89	1210	0.0202 ± 0.0026	-0.014 ± 0.028	0.1765 ± 0.0040	2.16 ± 0.10
44.50 ± 0.89	1810	0.0511 ± 0.0038	-0.011 ± 0.017	0.1661 ± 0.0054	1.94 ± 0.14
44.50 ± 0.89	1810	0.0640 ± 0.0035	-0.009 ± 0.013	0.1806 ± 0.0045	1.84 ± 0.10
44.50 ± 0.89	2260	0.0919 ± 0.0063	0.020 ± 0.017	0.1416 ± 0.0077	1.94 ± 0.25
44.50 ± 0.89	2260	0.1079 ± 0.0055	0.003 ± 0.012	0.1488 ± 0.0064	1.69 ± 0.15
CO	He				
23.80 ± 0.48	2280	0.3172 ± 0.0010	0.0145 ± 0.0013		
23.80 ± 0.48	2280	0.3144 ± 0.0010	0.0114 ± 0.0013		
279.0 ± 5.6	2280	0.2765 ± 0.0014	0.0199 ± 0.0020		
279.0 ± 5.6	2280	0.2754 ± 0.0014	0.0162 ± 0.0020		
Kr	He				
12.80 ± 0.26	2280	0.3190 ± 0.0015	0.0189 ± 0.0019		
12.80 ± 0.26	2280	0.3157 ± 0.0015	0.0154 ± 0.0019		
113.0 ± 2.3	2280	0.2889 ± 0.0016	0.0209 ± 0.0022		
113.0 ± 2.3	2280	0.2869 ± 0.0015	0.0211 ± 0.0022		
$555. \pm 11.$	2280	0.2121 ± 0.0014	0.0260 ± 0.0028		
$555. \pm 11.$	2280	0.2122 ± 0.0014	0.0239 ± 0.0026		

Table B.1. Tabulated Results

X	M	A_1	λ_1	A_2	λ_2
C_2H_6	He				
11.24 ± 0.22	2280	0.3120 ± 0.0096	0.0241 ± 0.0018		
11.24 ± 0.22	2280	0.3042 ± 0.0048	0.0237 ± 0.0019		
115.3 ± 2.3	2280	0.2039 ± 0.0064	0.0261 ± 0.0038		
115.3 ± 2.3	2280	0.2055 ± 0.0054	0.0198 ± 0.0038		
H_2O	He				
1.120 ± 0.022	2280	0.3253 ± 0.0015	0.0136 ± 0.0019		
1.120 ± 0.022	2280	0.3225 ± 0.0015	0.0116 ± 0.0019		
10.8 ± 1.0	2280	0.3133 ± 0.0012	0.0138 ± 0.0016		
10.8 ± 1.0	2280	0.3105 ± 0.0012	0.0118 ± 0.0016		
79.4 ± 4.0	2280	0.2095 ± 0.0013	0.0317 ± 0.0027		
79.4 ± 4.0	2280	0.2100 ± 0.0013	0.0351 ± 0.0026		
CH_3NO_2	He				
2.290 ± 0.046	2280	0.2377 ± 0.0030	0.0163 ± 0.0034	0.0804 ± 0.0040	2.07 ± 0.24
2.290 ± 0.046	2280	0.2395 ± 0.0025	0.0170 ± 0.0030	0.0791 ± 0.0044	2.36 ± 0.26
4.490 ± 0.090	2280	0.2118 ± 0.0022	0.0104 ± 0.0031	0.1280 ± 0.0059	3.36 ± 0.26
4.490 ± 0.090	2280	0.2109 ± 0.0022	0.0101 ± 0.0031	0.1156 ± 0.0057	3.12 ± 0.25
1.370 ± 0.027	2280	0.2459 ± 0.0047	0.0177 ± 0.0043	0.0846 ± 0.0043	1.33 ± 0.15
1.370 ± 0.027	2280	0.2463 ± 0.0042	0.0169 ± 0.0040	0.0778 ± 0.0041	1.35 ± 0.14
6.87 ± 0.14	2280	0.2132 ± 0.0017	0.0090 ± 0.0027	0.1255 ± 0.0080	4.66 ± 0.40
6.87 ± 0.14	2280	0.2114 ± 0.0017	0.0075 ± 0.0026	0.1155 ± 0.0070	4.31 ± 0.34
NO	He				
9.00 ± 0.18	2280	0.0488 ± 0.0090	0.152 ± 0.050	0.2760 ± 0.0075	1.540 ± 0.080
9.00 ± 0.18	2280	0.0417 ± 0.0069	0.100 ± 0.042	0.2810 ± 0.0060	1.460 ± 0.066
22.50 ± 0.45	2280	0.0304 ± 0.0039	0.197 ± 0.051	0.3070 ± 0.0070	3.66 ± 0.16
22.50 ± 0.45	2280	0.0212 ± 0.0027	0.064 ± 0.042	0.2990 ± 0.0067	3.45 ± 0.13
12.00 ± 0.24	2280	0.0709 ± 0.0049	0.074 ± 0.020	0.2502 ± 0.0055	2.14 ± 0.11
12.00 ± 0.24	2280	0.0704 ± 0.0045	0.071 ± 0.018	0.2501 ± 0.0057	2.18 ± 0.11
35.50 ± 0.71	2340	0.0150 ± 0.0024	0.105 ± 0.060	0.335 ± 0.010	5.61 ± 0.25
35.50 ± 0.71	2340	0.0122 ± 0.0024	0.089 ± 0.080	0.307 ± 0.011	5.11 ± 0.24
4.490 ± 0.090	2280	0.078 ± 0.025	0.121 ± 0.060	0.244 ± 0.023	0.828 ± 0.090
4.490 ± 0.090	2280	0.072 ± 0.019	0.100 ± 0.050	0.251 ± 0.018	0.853 ± 0.073
67.4 ± 1.3	2280	0.0083 ± 0.0019	0.1	0.270 ± 0.018	8.69 ± 0.53
67.4 ± 1.3	2280	0.0070 ± 0.0018	0.1	0.320 ± 0.023	10.30 ± 0.60
2.250 ± 0.045	2280	0.199 ± 0.012	0.034 ± 0.011	0.114 ± 0.011	0.89 ± 0.14
2.250 ± 0.045	2280	0.199 ± 0.011	0.030 ± 0.010	0.1180 ± 0.0090	0.97 ± 0.14
2.920 ± 0.058	2280	0.079 ± 0.020	0.03	0.242 ± 0.020	0.545 ± 0.057
2.920 ± 0.058	2280	0.121 ± 0.024	0.084 ± 0.031	0.197 ± 0.023	0.654 ± 0.070

Table B.1. Tabulated Results

X	M	A_1	λ_1	A_2	λ_2
$(CH_3)_4Si$	He				
12.27 ± 0.25	2280	0.1237 ± 0.0026	0.0058 ± 0.0065	0.1652 ± 0.0090	3.90 ± 0.35
12.27 ± 0.25	2280	0.1273 ± 0.0024	0.0203 ± 0.0060	0.198 ± 0.013	4.65 ± 0.40
4.490 ± 0.090	2280	0.1665 ± 0.0054	0.0390 ± 0.0080	0.1430 ± 0.0060	1.88 ± 0.18
4.490 ± 0.090	2280	0.1563 ± 0.0051	0.0200 ± 0.0080	0.1620 ± 0.0060	1.92 ± 0.17
2.470 ± 0.049	2280	0.173 ± 0.011	0.038 ± 0.013	0.150 ± 0.010	1.03 ± 0.12
2.470 ± 0.049	2280	0.1864 ± 0.0090	0.055 ± 0.010	0.1335 ± 0.0078	1.25 ± 0.15
9.12 ± 0.18	2280	0.1355 ± 0.0032	0.0320 ± 0.0073	0.1691 ± 0.0077	3.21 ± 0.26
9.12 ± 0.18	2280	0.1339 ± 0.0033	0.0290 ± 0.0074	0.1668 ± 0.0078	3.08 ± 0.26
NH_3	He				
2.030 ± 0.041	2280	0.128 ± 0.017	0.053 ± 0.024	0.199 ± 0.015	0.790 ± 0.080
2.030 ± 0.041	2280	0.114 ± 0.015	0.031 ± 0.022	0.213 ± 0.014	0.750 ± 0.060
11.10 ± 0.22	2280	0.284 ± 0.010	0.013 ± 0.010	0.0617 ± 0.0040	4.11 ± 0.19
11.10 ± 0.22	2280	0.2571 ± 0.0060	0.032 ± 0.012	0.064 ± 0.012	3.81 ± 0.16
6.79 ± 0.14	2280	0.2635 ± 0.0068	0.021 ± 0.016	0.0703 ± 0.0038	2.49 ± 0.14
6.79 ± 0.14	2280	0.2431 ± 0.0058	0.046 ± 0.016	0.0740 ± 0.0042	2.31 ± 0.12
CF_4	He				
13.70 ± 0.27	2280	0.2209 ± 0.0044	0.1339 ± 0.0065	0.1073 ± 0.0052	2.47 ± 0.27
13.70 ± 0.27	2280	0.2218 ± 0.0041	0.1411 ± 0.0062	0.1083 ± 0.0056	2.63 ± 0.28
22.45 ± 0.45	2280	0.2057 ± 0.0035	0.1300 ± 0.0062	0.1331 ± 0.0063	3.37 ± 0.32
22.45 ± 0.45	2280	0.2135 ± 0.0031	0.1413 ± 0.0057	0.1184 ± 0.0082	4.02 ± 0.45
4.490 ± 0.090	2280	0.248 ± 0.013	0.105 ± 0.010	0.076 ± 0.012	0.96 ± 0.18
4.490 ± 0.090	2280	0.240 ± 0.045	0.1	0.079 ± 0.044	0.82 ± 0.11
8.97 ± 0.18	2280	0.2274 ± 0.0060	0.1219 ± 0.0073	0.1089 ± 0.0055	1.74 ± 0.19
8.97 ± 0.18	2280	0.2278 ± 0.0063	0.1240 ± 0.0075	0.0978 ± 0.0057	1.62 ± 0.19
Xe	Ne				
14.42 ± 0.29	507	0.0145 ± 0.0026	0.05	0.144 ± 0.023	1.16 ± 0.33
14.42 ± 0.29	507	0.1013 ± 0.0025	0.05	0.132 ± 0.023	1.12 ± 0.33
14.42 ± 0.29	1000	0.0107 ± 0.0028	0.000 ± 0.064	0.2518 ± 0.0034	1.114 ± 0.034
14.42 ± 0.29	1000	0.0065 ± 0.0036	0.02 ± 0.12	0.2467 ± 0.0042	1.065 ± 0.036
14.42 ± 0.29	2280	0.043 ± 0.014	0.05	0.281 ± 0.011	0.808 ± 0.046
14.42 ± 0.29	2280	0.0405 ± 0.0036	0.05	0.2701 ± 0.0040	0.822 ± 0.030
14.52 ± 0.29	800	0.019 ± 0.010	0.13 ± 0.12	0.1868 ± 0.0092	1.110 ± 0.081
14.52 ± 0.29	800	0.032 ± 0.012	0.180 ± 0.090	0.180 ± 0.011	1.32 ± 0.12
50.6 ± 1.0	800	0.0200 ± 0.0040	0.127 ± 0.067	0.0973 ± 0.0061	2.63 ± 0.31
50.6 ± 1.0	800	0.0173 ± 0.0028	0.068 ± 0.054	0.1188 ± 0.0063	3.04 ± 0.27
50.6 ± 1.0	1020	0.0095 ± 0.0024	0.12	0.1275 ± 0.0050	2.27 ± 0.16

Table B.1. Tabulated Results

X	M	A_1	λ_1	A_2	λ_2
50.6 ± 1.0	1020	0.0087 ± 0.0038	0.12	0.1474 ± 0.0057	2.55 ± 0.20
50.6 ± 1.0	2280	0.0377 ± 0.0050	0.12	0.2115 ± 0.0056	1.640 ± 0.085
50.6 ± 1.0	2280	0.0334 ± 0.0049	0.12	0.2227 ± 0.0056	1.660 ± 0.085
O_2	Ne				
15.26 ± 0.31	800	0.1662 ± 0.0088	0.038 ± 0.011	0.1013 ± 0.0077	1.13 ± 0.16
15.26 ± 0.31	800	0.1652 ± 0.0081	0.039 ± 0.010	0.0913 ± 0.0074	1.11 ± 0.16
23.90 ± 0.48	800	0.0112 ± 0.0021	0.04	0.1935 ± 0.0050	1.620 ± 0.085
23.90 ± 0.48	800	0.017 ± 0.012	0.16 ± 0.18	0.183 ± 0.011	1.58 ± 0.17
4.630 ± 0.093	800	0.030 ± 0.014	0.04	0.235 ± 0.013	0.324 ± 0.031
4.630 ± 0.093	800	0.061 ± 0.011	0.05	0.210 ± 0.010	0.411 ± 0.035
13.50 ± 0.27	800	0.0173 ± 0.0045	0.05	0.1725 ± 0.0051	0.848 ± 0.067
13.50 ± 0.27	800	0.030 ± 0.017	0.13 ± 0.15	0.174 ± 0.017	1.08 ± 0.15
$(CH_3)_4Si$	Ne				
4.630 ± 0.093	800	0.1192 ± 0.0085	0.0590 ± 0.0060	0.0871 ± 0.0060	1.16 ± 0.20
4.630 ± 0.093	800	0.1040 ± 0.0077	0.027 ± 0.016	0.1006 ± 0.0072	1.01 ± 0.13
10.22 ± 0.20	800	0.0609 ± 0.0042	0.001 ± 0.016	0.0741 ± 0.0043	1.54 ± 0.22
10.22 ± 0.20	800	0.0700 ± 0.0035	0.032 ± 0.014	0.0717 ± 0.0042	2.07 ± 0.30
23.84 ± 0.48	800	0.0341 ± 0.0016	0.040 ± 0.017	0.0380 ± 0.0080	5.3 ± 1.5
23.84 ± 0.48	800	0.0298 ± 0.0018	0.014 ± 0.019	0.0423 ± 0.0050	3.85 ± 0.83
14.87 ± 0.30	800	0.0552 ± 0.0024	0.040 ± 0.015	0.0492 ± 0.0070	3.75 ± 0.90
14.87 ± 0.30	800	0.0527 ± 0.0027	0.033 ± 0.016	0.0545 ± 0.0063	3.11 ± 0.70
6.88 ± 0.14	800	0.032 ± 0.030	0.03	0.135 ± 0.017	0.79 ± 0.60
6.88 ± 0.14	800	0.043 ± 0.025	0.03	0.117 ± 0.015	0.90 ± 0.60
NO	Ne				
74.2 ± 1.5	800	0.0026 ± 0.0009	0.07	0.121 ± 0.010	5.80 ± 0.58
74.2 ± 1.5	800	0.0020 ± 0.0018	0.05 ± 0.49	0.1003 ± 0.0095	5.49 ± 0.60
22.65 ± 0.45	800	0.0103 ± 0.0050	0.13 ± 0.15	0.2202 ± 0.0055	2.06 ± 0.11
22.65 ± 0.45	800	0.0176 ± 0.0080	0.24 ± 0.16	0.2024 ± 0.0080	2.28 ± 0.17
44.04 ± 0.88	800	0.0168 ± 0.0090	0.63 ± 0.33	0.1836 ± 0.0080	4.91 ± 0.55
44.04 ± 0.88	800	0.0125 ± 0.0040	0.39 ± 0.16	0.1891 ± 0.0058	4.82 ± 0.29
10.81 ± 0.22	800	0.024 ± 0.013	0.1	0.229 ± 0.013	0.97 ± 0.12
10.81 ± 0.22	800	0.043 ± 0.020	0.176 ± 0.095	0.207 ± 0.017	1.11 ± 0.12
6.74 ± 0.13	800	0.039 ± 0.025	0.07 ± 0.10	0.228 ± 0.023	0.658 ± 0.070
6.74 ± 0.13	800	0.025 ± 0.015	0.01 ± 0.10	0.239 ± 0.020	0.633 ± 0.050
CH_3NO_2	Ne				
4.520 ± 0.090	800	0.1754 ± 0.0040	0.0505 ± 0.0060	0.0808 ± 0.0050	2.48 ± 0.42
4.520 ± 0.090	800	0.1645 ± 0.0047	0.0360 ± 0.0070	0.0793 ± 0.0047	1.67 ± 0.23

Table B.1.   Tabulated Results

X	M	A_1	λ_1	A_2	λ_2
2.250 ± 0.045	800	0.2108 ± 0.0033	0.06	0.0520 ± 0.0041	0.89 ± 0.16
2.250 ± 0.045	800	0.154 ± 0.032	0.0098 ± 0.0040	0.104 ± 0.029	0.55 ± 0.20
6.76 ± 0.14	800	0.1351 ± 0.0024	0.0175 ± 0.0054	0.0684 ± 0.0052	3.02 ± 0.45
6.76 ± 0.14	800	0.1349 ± 0.0023	0.0245 ± 0.0053	0.0686 ± 0.0053	2.97 ± 0.43
2.250 ± 0.045	800	0.1905 ± 0.0070	0.0400 ± 0.0080	0.0736 ± 0.0063	1.21 ± 0.21
2.250 ± 0.045	800	0.1710 ± 0.0090	0.017 ± 0.010	0.0859 ± 0.0085	0.91 ± 0.15
4.490 ± 0.090	800	0.1448 ± 0.0045	0.0185 ± 0.0075	0.0934 ± 0.0048	1.70 ± 0.21
4.490 ± 0.090	800	0.1500 ± 0.0037	0.0268 ± 0.0067	0.0846 ± 0.0051	2.12 ± 0.31
10.90 ± 0.22	800	0.1078 ± 0.0023	0.0204 ± 0.0068	0.0763 ± 0.0080	4.14 ± 0.73
10.90 ± 0.22	800	0.1045 ± 0.0021	0.0185 ± 0.0065	0.0778 ± 0.0075	4.22 ± 0.64
CF_4	Ne				
11.20 ± 0.22	800	0.100 ± 0.014	0.088 ± 0.028	0.159 ± 0.012	0.98 ± 0.11
11.20 ± 0.22	800	0.126 ± 0.014	0.134 ± 0.024	0.131 ± 0.012	1.16 ± 0.17
22.50 ± 0.45	800	0.0868 ± 0.0043	0.099 ± 0.014	0.1597 ± 0.0041	1.94 ± 0.13
22.50 ± 0.45	800	0.0924 ± 0.0051	0.119 ± 0.017	0.1426 ± 0.0047	1.89 ± 0.14
47.40 ± 0.95	800	0.0760 ± 0.0031	0.134 ± 0.014	0.1535 ± 0.0050	3.18 ± 0.22
47.40 ± 0.95	800	0.0730 ± 0.0027	0.134 ± 0.013	0.1574 ± 0.0056	3.37 ± 0.22
33.90 ± 0.68	800	0.0874 ± 0.0036	0.145 ± 0.015	0.1722 ± 0.0058	3.29 ± 0.24
33.90 ± 0.68	800	0.0779 ± 0.0036	0.108 ± 0.015	0.1533 ± 0.0051	2.56 ± 0.18
Kr	Ne				
22.50 ± 0.45	800	0.056 ± 0.040	0.02	0.206 ± 0.040	0.30 ± 0.13
22.50 ± 0.45	800	0.078 ± 0.040	0.02	0.177 ± 0.040	0.32 ± 0.13
22.50 ± 0.45	800	0.130 ± 0.045	0.02	0.103 ± 0.045	0.43 ± 0.14
22.50 ± 0.45	800	0.134 ± 0.042	0.02	0.096 ± 0.046	0.47 ± 0.15
44.90 ± 0.90	800	0.101 ± 0.017	0.014 ± 0.025	0.120 ± 0.016	0.573 ± 0.090
44.90 ± 0.90	800	0.099 ± 0.013	0.02	0.119 ± 0.013	0.531 ± 0.085
67.4 ± 1.3	800	0.092 ± 0.016	0.02	0.104 ± 0.015	0.649 ± 0.090
67.4 ± 1.3	800	0.097 ± 0.012	0.02	0.096 ± 0.011	0.70 ± 0.10
90.5 ± 1.8	800	0.097 ± 0.012	0.02	0.078 ± 0.011	0.84 ± 0.14
90.5 ± 1.8	800	0.103 ± 0.014	0.044 ± 0.024	0.062 ± 0.013	0.81 ± 0.21
67.9 ± 1.4	800	0.096 ± 0.015	0.02	0.098 ± 0.012	0.64 ± 0.10
67.9 ± 1.4	800	0.094 ± 0.016	0.02	0.100 ± 0.015	0.614 ± 0.090
CO	Ne				
22.50 ± 0.45	801	0.2529 ± 0.0011	0.0266 ± 0.0019		
22.50 ± 0.45	801	0.2510 ± 0.0011	0.0264 ± 0.0018		
275.0 ± 5.5	800	0.1094 ± 0.0015	0.0254 ± 0.0055		
275.0 ± 5.5	800	0.1058 ± 0.0014	0.0126 ± 0.0053		

Table B.1. Tabulated Results

X	M	A_1	λ_1	A_2	λ_2
NO	Ar				
22.50 ± 0.45	800	0.0002 ± 0.0032	0.05	0.0743 ± 0.0030	0.662 ± 0.072
22.50 ± 0.45	800	0.0007 ± 0.0031	0.05	0.0720 ± 0.0029	0.669 ± 0.074
4.520 ± 0.090	800	0.0000 ± 0.0030	0.001	0.0819 ± 0.0016	0.157 ± 0.011
4.520 ± 0.090	800	0.0000 ± 0.0030	0.001	0.0795 ± 0.0015	0.166 ± 0.011
50.5 ± 1.0	800	0.0052 ± 0.0017	0.05	0.0674 ± 0.0043	1.82 ± 0.24
50.5 ± 1.0	800	0.0010 ± 0.0019	0.05	0.0712 ± 0.0033	1.54 ± 0.17
36.18 ± 0.72	800	0.0005 ± 0.0018	0.05	0.0751 ± 0.0031	1.31 ± 0.13
36.18 ± 0.72	800	0.0018 ± 0.0020	0.05	0.0703 ± 0.0029	1.11 ± 0.12
13.50 ± 0.27	800	0.0098 ± 0.0035	0.05	0.0760 ± 0.0032	0.633 ± 0.070
13.50 ± 0.27	800	0.0051 ± 0.0048	0.05	0.0750 ± 0.0042	0.492 ± 0.064
CH_3F	Ne				
12.80 ± 0.26	500	0.0569 ± 0.0024	0.096 ± 0.015	0.0791 ± 0.0055	3.89 ± 0.56
12.80 ± 0.26	500	0.0478 ± 0.0029	0.056 ± 0.018	0.0750 ± 0.0042	2.42 ± 0.29
12.80 ± 0.26	1000	0.1216 ± 0.0033	0.0883 ± 0.0082	0.1050 ± 0.0041	2.34 ± 0.21
12.80 ± 0.26	1000	0.1227 ± 0.0035	0.0892 ± 0.0086	0.1066 ± 0.0046	2.39 ± 0.23
12.80 ± 0.26	1700	0.1893 ± 0.0030	0.1347 ± 0.0056	0.0884 ± 0.0047	3.01 ± 0.32
12.80 ± 0.26	1700	0.1871 ± 0.0036	0.1323 ± 0.0064	0.0895 ± 0.0049	2.64 ± 0.30
12.80 ± 0.26	2500	0.2142 ± 0.0022	0.0312 ± 0.0031	0.0858 ± 0.0041	2.83 ± 0.26
12.80 ± 0.26	2500	0.2201 ± 0.0025	0.0325 ± 0.0034	0.0741 ± 0.0048	2.77 ± 0.33
CH_3F	He				
6.06 ± 0.12	1000	0.1499 ± 0.0035	0.0464 ± 0.0060	0.0777 ± 0.0058	2.48 ± 0.29
6.06 ± 0.12	1000	0.1522 ± 0.0033	0.0661 ± 0.0061	0.0857 ± 0.0063	3.03 ± 0.38
6.06 ± 0.12	1500	0.1950 ± 0.0031	0.0432 ± 0.0047	0.0945 ± 0.0093	3.53 ± 0.54
6.06 ± 0.12	1500	0.1911 ± 0.0039	0.0431 ± 0.0052	0.0843 ± 0.0078	2.63 ± 0.40
6.06 ± 0.12	2000	0.2253 ± 0.0028	0.0413 ± 0.0036	0.0790 ± 0.0084	3.70 ± 0.57
6.06 ± 0.12	2000	0.2219 ± 0.0021	0.0385 ± 0.0029	0.0724 ± 0.0059	3.64 ± 0.57
H_2O	Ne	(plus 6.12×10^{14} molec/cm^3 NH_3)			
2.030 ± 0.041	800	0.0799 ± 0.0056	0.058 ± 0.018	0.1452 ± 0.0054	1.69 ± 0.15
2.030 ± 0.041	800	0.0778 ± 0.0054	0.040 ± 0.018	0.1582 ± 0.0056	1.71 ± 0.14
15.0 ± 1.5	800	0.1009 ± 0.0024	0.0522 ± 0.0078	0.0569 ± 0.0052	3.35 ± 0.61
15.0 ± 1.5	800	0.1060 ± 0.0021	0.0591 ± 0.0069	0.0686 ± 0.0087	5.1 ± 1.0
4.040 ± 0.081	800	0.1003 ± 0.0032	0.0407 ± 0.0094	0.1025 ± 0.0047	2.52 ± 0.26
4.040 ± 0.081	800	0.1058 ± 0.0035	0.053 ± 0.010	0.1017 ± 0.0059	2.75 ± 0.35
7.30 ± 0.15	800	0.1071 ± 0.0025	0.0518 ± 0.0077	0.0728 ± 0.0058	3.47 ± 0.50
7.30 ± 0.15	800	0.1046 ± 0.0029	0.0466 ± 0.0089	0.0822 ± 0.0062	3.10 ± 0.45
0.00	800	0.0728 ± 0.0096	0.0836 ± 0.031	0.1746 ± 0.0080	1.37 ± 0.13
0.00	800	0.0565 ± 0.0067	0.05	0.1844 ± 0.0060	1.13 ± 0.13

Table B.1. Tabulated Results

X	M	A_1	λ_1	A_2	λ_2
C_2H_6	He	(plus 5.08×10^{14} molec/cm^3 NH$_3$)			
6.35 ± 0.13	1500	0.1332 ± 0.0036	0.0265 ± 0.0067	0.1225 ± 0.0062	3.27 ± 0.33
6.35 ± 0.13	1500	0.1344 ± 0.0036	0.0462 ± 0.0073	0.1141 ± 0.0068	2.97 ± 0.33
3.230 ± 0.065	1500	0.1091 ± 0.0035	0.0469 ± 0.0086	0.1542 ± 0.0070	2.98 ± 0.23
3.230 ± 0.065	1500	0.1075 ± 0.0038	0.053 ± 0.010	0.1443 ± 0.0065	2.54 ± 0.19
9.62 ± 0.19	1500	0.1400 ± 0.0031	0.0435 ± 0.0064	0.1042 ± 0.0070	3.57 ± 0.48
9.62 ± 0.19	1500	0.1389 ± 0.0033	0.0505 ± 0.0069	0.1025 ± 0.0076	3.63 ± 0.52
0.00	1500	0.0755 ± 0.0048	0.057 ± 0.016	0.0257 ± 0.0061	2.11 ± 0.11
0.00	1500	0.0648 ± 0.0053	0.027 ± 0.019	0.2021 ± 0.0058	1.95 ± 0.12
NO	Ar				
32.50 ± 0.65	400	0.0225 ± 0.0061	0.167 ± 0.075	0.0190 ± 0.0056	1.6 ± 1.0
32.50 ± 0.65	400	0.0191 ± 0.0035	0.115 ± 0.055	0.0286 ± 0.0044	2.18 ± 0.75
16.30 ± 0.33	400	0.0226 ± 0.0082	0.1	0.0259 ± 0.0060	0.84 ± 0.39
16.30 ± 0.33	400	0.0205 ± 0.0091	0.09 ± 0.11	0.0324 ± 0.0076	1.18 ± 0.52
23.20 ± 0.46	800	0.0264 ± 0.0048	0.02	0.0448 ± 0.0049	1.23 ± 0.24
23.20 ± 0.46	800	0.0258 ± 0.0060	0.02	0.0466 ± 0.0056	1.12 ± 0.24
40.60 ± 0.81	800	0.0206 ± 0.0022	0.017 ± 0.031	0.0464 ± 0.0043	2.47 ± 0.40
40.60 ± 0.81	800	0.0173 ± 0.0034	0.018 ± 0.050	0.0519 ± 0.0044	1.92 ± 0.37
32.50 ± 0.65	800	0.0320 ± 0.0031	0.064 ± 0.031	0.0475 ± 0.0058	2.96 ± 0.73
32.50 ± 0.65	800	0.0292 ± 0.0036	0.05	0.0465 ± 0.0045	2.17 ± 0.37
16.30 ± 0.33	800	0.0327 ± 0.0060	0.02	0.0448 ± 0.0060	1.05 ± 0.50
16.30 ± 0.33	800	0.034 ± 0.011	0.016 ± 0.067	0.0413 ± 0.0093	1.0 ± 1.1
$(C_2H_5)_3N$	Ar				
4.060 ± 0.081	800	0.0632 ± 0.0040	0.02	0.0101 ± 0.0040	0.54 ± 0.45
4.060 ± 0.081	800	0.0640 ± 0.0014	0.02	0.0135 ± 0.0026	1.21 ± 0.53
13.90 ± 0.28	800	0.0404 ± 0.0018	0.053 ± 0.015	0.0141 ± 0.0042	3.0 ± 1.2
13.90 ± 0.28	800	0.0366 ± 0.0027	0.02	0.0253 ± 0.0069	3.0 ± 1.5
8.23 ± 0.16	800	0.0512 ± 0.0040	0.053 ± 0.019	0.0118 ± 0.0036	1.9 ± 1.6
8.23 ± 0.16	800	0.0477 ± 0.0024	0.010 ± 0.014	0.0153 ± 0.0037	2.05 ± 0.92
21.2 ± 2.0	800	0.0364 ± 0.0020	0.022 ± 0.016	0.0162 ± 0.0034	2.2 ± 1.0
21.2 ± 2.0	800	0.0344 ± 0.0026	0.006 ± 0.019	0.0211 ± 0.0035	1.97 ± 0.76
N_2O	Ne				
42.20 ± 0.94	800	0.0710 ± 0.0023	0.069 ± 0.011	0.070 ± 0.010	4.9 ± 1.1
42.20 ± 0.94	800	0.0746 ± 0.0021	0.095 ± 0.011	0.0659 ± 0.0090	4.93 ± 0.84
20.12 ± 0.50	800	0.0917 ± 0.0037	0.062 ± 0.011	0.0940 ± 0.0045	2.06 ± 0.24
20.12 ± 0.50	800	0.0895 ± 0.0052	0.073 ± 0.015	0.0887 ± 0.0052	1.63 ± 0.22

Table B.1. Tabulated Results

X	M	A_1	λ_1	A_2	λ_2
Xe	Ne				
19.00 ± 0.48	700	0.0233 ± 0.0032	0.010 ± 0.034	0.1574 ± 0.0038	1.74 ± 0.10
19.00 ± 0.48	700	0.0266 ± 0.0046	0.076 ± 0.045	0.1444 ± 0.0047	1.69 ± 0.12
19.00 ± 0.48	700	0.0335 ± 0.0055	0.049 ± 0.044	0.1286 ± 0.0064	1.85 ± 0.20
19.00 ± 0.48	700	0.0354 ± 0.0063	0.086 ± 0.050	0.1208 ± 0.0075	1.91 ± 0.24
40.10 ± 0.90	700	0.0056 ± 0.0010	0.05	0.1409 ± 0.0045	2.77 ± 0.14
40.10 ± 0.90	700	0.0012 ± 0.0012	0.05	0.1269 ± 0.0042	2.17 ± 0.13
10.02 ± 0.30	800	0.023 ± 0.023	0.05 ± 0.13	0.252 ± 0.015	0.835 ± 0.055
10.02 ± 0.30	800	0.0135 ± 0.0068	0.05	0.2240 ± 0.0044	0.891 ± 0.034
3.91 ± 0.18	800	0.0890 ± 0.0061	0.04	0.1692 ± 0.0042	0.531 ± 0.059
3.91 ± 0.18	800	0.0943 ± 0.0053	0.04	0.170 ± 0.013	0.488 ± 0.049
2.01 ± 0.14	800	0.205 ± 0.018	0.100 ± 0.018	0.071 ± 0.021	0.37 ± 0.10
105.5 ± 2.2	800	0.0020 ± 0.0015	0.05	0.047 ± 0.014	4.3 ± 1.6
105.5 ± 2.2	800	0.0008 ± 0.0015	0.05	0.051 ± 0.015	5.0 ± 1.7
NO	Ne				
7.33 ± 0.25	800	0.056 ± 0.014	0.092 ± 0.045	0.198 ± 0.013	0.869 ± 0.069
7.33 ± 0.25	800	0.045 ± 0.018	0.081 ± 0.068	0.205 ± 0.016	0.802 ± 0.078
20.24 ± 0.50	800	0.0082 ± 0.0036	0.04 ± 0.12	0.2086 ± 0.0041	1.793 ± 0.082
20.24 ± 0.50	800	0.0086 ± 0.0033	0.05	0.1994 ± 0.0041	1.741 ± 0.081
NH_3	Ne	(plus 10.02×10^{14} molec/cm^3 Xe)			
6.01 ± 0.30	800	0.0338 ± 0.0041	0.028 ± 0.031	0.1742 ± 0.0049	1.86 ± 0.12
6.01 ± 0.30	800	0.0400 ± 0.0049	0.074 ± 0.034	0.1698 ± 0.0058	2.02 ± 0.16
12.02 ± 0.30	800	0.0360 ± 0.0024	0.062 ± 0.021	0.1537 ± 0.0056	3.22 ± 0.21
12.02 ± 0.30	800	0.0383 ± 0.0030	0.089 ± 0.025	0.1432 ± 0.0057	2.91 ± 0.21
3.01 ± 0.30	800	0.0237 ± 0.0073	0.052 ± 0.069	0.1996 ± 0.0066	1.342 ± 0.093
3.01 ± 0.30	800	0.0234 ± 0.0049	0.05	0.1983 ± 0.0049	1.361 ± 0.075
0.00	800	0.023 ± 0.023	0.05 ± 0.13	0.252 ± 0.015	0.835 ± 0.055
0.00	800	0.0135 ± 0.0068	0.05	0.2240 ± 0.0044	0.891 ± 0.034
H_2O	Ne	(plus 10.02×10^{14} molec/cm^3 Xe)			
3.71 ± 0.30	800	0.0924 ± 0.0049	0.058 ± 0.014	0.0864 ± 0.0052	1.65 ± 0.21
3.71 ± 0.30	800	0.1027 ± 0.0054	0.095 ± 0.015	0.0736 ± 0.0058	1.93 ± 0.34
2.00 ± 0.30	800	0.0657 ± 0.0072	0.013 ± 0.023	0.1458 ± 0.0064	1.08 ± 0.10
2.00 ± 0.30	800	0.0784 ± 0.0075	0.062 ± 0.022	0.1399 ± 0.0068	1.27 ± 0.12
6.21 ± 0.30	800	0.1028 ± 0.0045	0.040 ± 0.011	0.0726 ± 0.0048	1.69 ± 0.25
6.21 ± 0.30	800	0.0992 ± 0.0053	0.043 ± 0.013	0.0698 ± 0.0054	1.51 ± 0.25
7.81 ± 0.30	800	0.0914 ± 0.0031	0.0605 ± 0.0091	0.0363 ± 0.0038	1.82 ± 0.43
7.81 ± 0.30	800	0.0876 ± 0.0036	0.061 ± 0.010	0.0389 ± 0.0038	1.67 ± 0.36

Table B.1. Tabulated Results

X	M	A_1	λ_1	A_2	λ_2
0.00	800	0.023 ± 0.023	0.05 ± 0.13	0.252 ± 0.015	0.835 ± 0.055
0.00	800	0.0135 ± 0.0068	0.05	0.2240 ± 0.0044	0.891 ± 0.034
Ar	Ne	(plus 20.12×10^{14} molec/cm^3 N$_2$O)			
201.8 ± 4.0	800	0.1280 ± 0.0036	0.0770 ± 0.0080	0.0320 ± 0.0030	2.20 ± 0.80
201.8 ± 4.0	800	0.1240 ± 0.0060	0.084 ± 0.011	0.0350 ± 0.0050	1.60 ± 0.60
422.0 ± 8.4	800	0.1406 ± 0.0016	0.0500 ± 0.0036	0.0250 ± 0.0045	3.6 ± 1.1
422.0 ± 8.4	800	0.129 ± 0.010	0.045 ± 0.015	0.0243 ± 0.0090	1.08 ± 0.65
105.5 ± 2.1	800	0.1352 ± 0.0020	0.0302 ± 0.0046	0.0430 ± 0.0059	3.64 ± 0.82
105.5 ± 2.1	800	0.1336 ± 0.0022	0.0349 ± 0.0051	0.0538 ± 0.0069	3.59 ± 0.80
0.00	800	0.0917 ± 0.0037	0.062 ± 0.011	0.0940 ± 0.0045	2.06 ± 0.24
0.00	800	0.0895 ± 0.0052	0.073 ± 0.015	0.0887 ± 0.0052	1.63 ± 0.22
Ar	Ne	(plus 7.33×10^{14} molec/cm^3 NO)			
106.4 ± 2.1	800	0.057 ± 0.026	0.219 ± 0.094	0.201 ± 0.025	0.95 ± 0.11
106.4 ± 2.1	800	0.040 ± 0.017	0.132 ± 0.082	0.216 ± 0.016	0.913 ± 0.080
422.0 ± 8.4	800	0.058 ± 0.016	0.155 ± 0.054	0.182 ± 0.014	0.963 ± 0.087
422.0 ± 8.4	800	0.066 ± 0.021	0.181 ± 0.063	0.171 ± 0.019	0.99 ± 0.12
$683. \pm 14.$	800	0.080 ± 0.014	0.162 ± 0.039	0.147 ± 0.013	1.14 ± 0.13
$683. \pm 14.$	800	0.096 ± 0.015	0.196 ± 0.039	0.135 ± 0.013	1.33 ± 0.19
0.00	800	0.056 ± 0.014	0.092 ± 0.045	0.198 ± 0.013	0.869 ± 0.069
0.00	800	0.045 ± 0.018	0.081 ± 0.068	0.205 ± 0.016	0.802 ± 0.078
CH$_3$NO$_2$	Ne	(at $133°$ C)			
10.48 ± 0.31	1300	0.1096 ± 0.0027	-0.0002 ± 0.0056	0.0680 ± 0.0048	2.52 ± 0.38
10.48 ± 0.31	1300	0.1139 ± 0.0027	0.0142 ± 0.0056	0.0658 ± 0.0067	3.00 ± 0.55
5.23 ± 0.20	1300	0.1383 ± 0.0030	0.0201 ± 0.0050	0.0749 ± 0.0041	2.16 ± 0.27
5.23 ± 0.20	1300	0.1394 ± 0.0031	0.0243 ± 0.0052	0.0764 ± 0.0051	2.31 ± 0.32
3.38 ± 0.17	1300	0.1492 ± 0.0057	0.0124 ± 0.0071	0.0712 ± 0.0052	1.18 ± 0.18
3.38 ± 0.17	1300	0.1455 ± 0.0076	0.0133 ± 0.0090	0.0796 ± 0.0066	1.07 ± 0.18
1.44 ± 0.13	1300	0.189 ± 0.016	0.025 ± 0.012	0.052 ± 0.015	0.66 ± 0.22
1.44 ± 0.13	1300	0.179 ± 0.027	0.023 ± 0.019	0.066 ± 0.026	0.52 ± 0.19
7.55 ± 0.25	1300	0.1178 ± 0.0022	0.0057 ± 0.0041	0.0711 ± 0.0035	2.33 ± 0.24
7.55 ± 0.25	1300	0.1208 ± 0.0024	0.0154 ± 0.0044	0.0723 ± 0.0045	2.53 ± 0.31
CH$_3$CN	Ne	(at $133°$ C)			
5.50 ± 0.21	1300	0.1773 ± 0.0022	0.0158 ± 0.0044		
5.50 ± 0.21	1300	0.1812 ± 0.0024	0.0175 ± 0.0047		
0.82 ± 0.12	1350	0.2382 ± 0.0023	0.0090 ± 0.0035		
0.82 ± 0.12	1350	0.2418 ± 0.0025	0.0184 ± 0.0038		

Table B.1. Tabulated Results

X	M	A_1	λ_1	A_2	λ_2
$C_2H_4F_2$	He	(at 133° C)			
10.22 ± 0.30	2400	0.0926 ± 0.0065	0.067 ± 0.012	0.1546 ± 0.0059	1.51 ± 0.13
10.22 ± 0.30	2400	0.0990 ± 0.0070	0.076 ± 0.012	0.1514 ± 0.0064	1.58 ± 0.16
5.14 ± 0.20	2400	0.085 ± 0.010	0.041 ± 0.016	0.1683 ± 0.0091	1.007 ± 0.090
5.14 ± 0.20	2400	0.1074 ± 0.0091	0.065 ± 0.014	0.1624 ± 0.0076	1.31 ± 0.13
16.54 ± 0.43	2400	0.0915 ± 0.0044	0.0724 ± 0.0092	0.1414 ± 0.0051	2.19 ± 0.19
16.54 ± 0.43	2400	0.1025 ± 0.0047	0.0895 ± 0.0095	0.1295 ± 0.0062	2.35 ± 0.26
24.40 ± 0.59	2400	0.0930 ± 0.0038	0.0899 ± 0.0089	0.1253 ± 0.0056	2.82 ± 0.29
24.40 ± 0.59	2400	0.0917 ± 0.0042	0.0839 ± 0.0094	0.1307 ± 0.0067	2.76 ± 0.31
CH_3CHO	He	(at 133° C)			
14.03 ± 0.38	2400	0.1018 ± 0.0015	0.0644 ± 0.0038	0.0968 ± 0.0091	5.88 ± 0.76
14.03 ± 0.38	2400	0.0989 ± 0.0016	0.0581 ± 0.0041	0.119 ± 0.011	5.61 ± 0.65
9.41 ± 0.29	2400	0.1080 ± 0.0022	0.0683 ± 0.0049	0.0971 ± 0.0053	3.64 ± 0.37
9.41 ± 0.29	2400	0.1049 ± 0.0022	0.0673 ± 0.0048	0.1256 ± 0.0079	4.10 ± 0.42
7.16 ± 0.24	2400	0.1056 ± 0.0029	0.0639 ± 0.0060	0.1143 ± 0.0046	2.79 ± 0.26
7.16 ± 0.24	2400	0.1084 ± 0.0029	0.0753 ± 0.0060	0.1189 ± 0.0056	2.82 ± 0.28
1.92 ± 0.14	2400	0.1232 ± 0.0054	0.0758 ± 0.0080	0.1185 ± 0.0061	1.34 ± 0.10
1.92 ± 0.14	2400	0.1270 ± 0.0053	0.0919 ± 0.0080	0.1278 ± 0.0057	1.54 ± 0.13
3.60 ± 0.17	2300	0.1259 ± 0.0031	0.0260 ± 0.0047	0.1174 ± 0.0034	1.79 ± 0.13
3.60 ± 0.17	2300	0.1296 ± 0.0031	0.0296 ± 0.0047	0.1223 ± 0.0042	1.97 ± 0.15
C_2H_4	He	(at 125° C)			
12.84 ± 0.36	2400	0.1151 ± 0.0024	0.0388 ± 0.0047	0.1311 ± 0.0053	3.26 ± 0.25
12.84 ± 0.36	2400	0.1117 ± 0.0026	0.0283 ± 0.0050	0.1383 ± 0.0065	3.09 ± 0.25
7.71 ± 0.25	2400	0.1075 ± 0.0045	0.0284 ± 0.0073	0.1296 ± 0.0046	1.59 ± 0.13
7.71 ± 0.25	2400	0.1120 ± 0.0039	0.0306 ± 0.0066	0.1459 ± 0.0052	2.02 ± 0.16
5.29 ± 0.21	2400	0.1190 ± 0.0049	0.0323 ± 0.0068	0.1337 ± 0.0045	1.306 ± 0.093
5.29 ± 0.21	2400	0.1121 ± 0.0060	0.0210 ± 0.0081	0.1425 ± 0.0053	1.167 ± 0.092
16.34 ± 0.43	2400	0.1015 ± 0.0023	0.0348 ± 0.0051	0.1400 ± 0.0062	3.69 ± 0.28
16.34 ± 0.43	2400	0.1089 ± 0.0023	0.0487 ± 0.0051	0.143 ± 0.010	4.48 ± 0.41
CH_3F	He	(at 125° C)			
20.18 ± 0.50	2400	0.1651 ± 0.0017	0.0352 ± 0.0027	0.0654 ± 0.0059	4.41 ± 0.64
20.18 ± 0.50	2400	0.1732 ± 0.0015	0.0455 ± 0.0026	0.083 ± 0.012	6.8 ± 1.0
11.61 ± 0.33	2400	0.1814 ± 0.0026	0.0393 ± 0.0036	0.0649 ± 0.0058	3.33 ± 0.59
11.61 ± 0.33	2400	0.1820 ± 0.0025	0.0401 ± 0.0035	0.0741 ± 0.0075	3.50 ± 0.55
5.15 ± 0.20	2400	0.1872 ± 0.0050	0.0351 ± 0.0052	0.0651 ± 0.0046	1.53 ± 0.27
5.15 ± 0.20	2400	0.1941 ± 0.0055	0.0453 ± 0.0056	0.0570 ± 0.0051	1.64 ± 0.37
2.70 ± 0.15	2400	0.212 ± 0.013	0.049 ± 0.010	0.054 ± 0.013	0.68 ± 0.18
2.70 ± 0.15	2400	0.197 ± 0.011	0.0357 ± 0.0086	0.064 ± 0.010	0.86 ± 0.23

Table B.1.   Tabulated Results

X	M	A_1	λ_1	A_2	λ_2
CH_3F	He	(at $-145°$ C)			
10.53 ± 0.31	800	0.1588 ± 0.0020	0.0528 ± 0.0035	0.0958 ± 0.0067	4.36 ± 0.47
10.53 ± 0.31	800	0.1612 ± 0.0020	0.0574 ± 0.0036	0.122 ± 0.011	5.46 ± 0.59
4.17 ± 0.18	800	0.1685 ± 0.0033	0.0533 ± 0.0044	0.0916 ± 0.0041	2.15 ± 0.22
4.17 ± 0.18	800	0.1724 ± 0.0031	0.0572 ± 0.0043	0.0994 ± 0.0061	2.34 ± 0.26
7.81 ± 0.26	800	0.1602 ± 0.0019	0.0678 ± 0.0033	0.1042 ± 0.0050	3.72 ± 0.32
7.81 ± 0.26	800	0.1597 ± 0.0022	0.0654 ± 0.0036	0.1019 ± 0.0058	3.11 ± 0.34
2.20 ± 0.14	800	0.164 ± 0.012	0.058 ± 0.010	0.106 ± 0.010	0.784 ± 0.079
2.20 ± 0.14	800	0.1799 ± 0.0084	0.0762 ± 0.0080	0.0849 ± 0.0080	1.10 ± 0.20
2.66 ± 0.15	800	0.1722 ± 0.0059	0.0673 ± 0.0061	0.0945 ± 0.0056	1.14 ± 0.12
2.66 ± 0.15	800	0.1727 ± 0.0059	0.0670 ± 0.0062	0.0943 ± 0.0054	1.27 ± 0.15
Xe	Ne	(at $-156°$ C)			
11.97 ± 0.34	370	0.003 ± 0.016	0.047 ± 0.063	0.213 ± 0.015	0.764 ± 0.070
11.97 ± 0.34	370	-0.014 ± 0.020	-0.04 ± 0.10	0.226 ± 0.019	0.655 ± 0.089
11.97 ± 0.34	370	-0.010 ± 0.011	0.008 ± 0.053	0.225 ± 0.010	0.708 ± 0.044
11.97 ± 0.34	370	0.006 ± 0.014	0.066 ± 0.047	0.209 ± 0.013	0.795 ± 0.065
26.05 ± 0.62	370	-0.0009 ± 0.0064	0.073 ± 0.036	0.1981 ± 0.0063	1.48 ± 0.10
26.05 ± 0.62	370	0.0041 ± 0.0064	0.099 ± 0.031	0.1839 ± 0.0069	1.54 ± 0.12
52.0 ± 1.1	370	-0.0145 ± 0.0030	0.008 ± 0.025	0.1326 ± 0.0057	1.97 ± 0.16
52.0 ± 1.1	370	-0.0018 ± 0.0030	0.087 ± 0.020	0.145 ± 0.010	2.61 ± 0.25
6.94 ± 0.24	370	0.0	0.0	0.2691 ± 0.0020	0.3965 ± 0.0061
6.94 ± 0.24	370	0.0	0.0	0.2771 ± 0.0021	0.4039 ± 0.0063
3.94 ± 0.18	370	0.0	0.0	0.2894 ± 0.0019	0.2652 ± 0.0038
3.94 ± 0.18	370	0.0	0.0	0.2920 ± 0.0018	0.2622 ± 0.0038
3.94 ± 0.18	1000	0.0	0.0	0.3167 ± 0.0016	0.1903 ± 0.0027
3.94 ± 0.18	1000	0.0	0.0	0.3293 ± 0.0019	0.1998 ± 0.0031
6.94 ± 0.24	1000	0.0227 ± 0.0079	0.04	0.2465 ± 0.0068	0.355 ± 0.020
6.94 ± 0.24	1000	0.0263 ± 0.0079	0.04	0.2479 ± 0.0064	0.382 ± 0.024
52.0 ± 1.1	1000	0.0396 ± 0.0072	0.088 ± 0.019	0.1767 ± 0.0063	1.263 ± 0.092
52.0 ± 1.1	1000	0.0376 ± 0.0077	0.083 ± 0.019	0.1794 ± 0.0072	1.218 ± 0.093
26.05 ± 0.62	1000	0.0003 ± 0.0039	0.03	0.279 ± 0.021	0.615 ± 0.057
26.05 ± 0.62	1000	0.0102 ± 0.0044	0.05	0.263 ± 0.017	0.666 ± 0.064
11.97 ± 0.34	1000	0.045 ± 0.017	-0.007 ± 0.028	0.213 ± 0.016	0.566 ± 0.051
11.97 ± 0.34	1000	0.029 ± 0.023	-0.016 ± 0.038	0.221 ± 0.022	0.488 ± 0.056
$C_2H_4F_2$	He	(at $-125°$ C)			
7.24 ± 0.24	830	0.1240 ± 0.0035	0.1569 ± 0.0080	0.1592 ± 0.0064	3.64 ± 0.29
7.24 ± 0.24	830	0.1282 ± 0.0040	0.1572 ± 0.0086	0.1472 ± 0.0080	3.49 ± 0.36
2.54 ± 0.15	830	0.1504 ± 0.0058	0.1327 ± 0.0084	0.1197 ± 0.0055	1.85 ± 0.19

Table B.1.   Tabulated Results

X	M	A_1	λ_1	A_2	λ_2
2.54 ± 0.15	830	0.1500 ± 0.0063	0.1337 ± 0.0092	0.1243 ± 0.0061	1.83 ± 0.19
1.04 ± 0.12	830	0.170 ± 0.011	0.136 ± 0.012	0.098 ± 0.010	1.19 ± 0.17
1.04 ± 0.12	830	0.163 ± 0.012	0.123 ± 0.013	0.102 ± 0.011	1.10 ± 0.17
4.15 ± 0.18	830	0.1363 ± 0.0049	0.1334 ± 0.0081	0.1269 ± 0.0048	1.94 ± 0.16
4.15 ± 0.18	830	0.1455 ± 0.0049	0.1432 ± 0.0081	0.1281 ± 0.0053	2.18 ± 0.20
5.89 ± 0.22	830	0.1232 ± 0.0033	0.1393 ± 0.0071	0.1482 ± 0.0049	3.01 ± 0.21
5.89 ± 0.22	830	0.1231 ± 0.0038	0.1408 ± 0.0078	0.1538 ± 0.0061	2.96 ± 0.24
$C_2H_4F_2$	He	(at $-65°$ C)			
3.11 ± 0.16	1330	0.1727 ± 0.0056	0.1436 ± 0.0075	0.0955 ± 0.0053	1.79 ± 0.20
3.11 ± 0.16	1330	0.1555 ± 0.0077	0.127 ± 0.010	0.1103 ± 0.0068	1.49 ± 0.18
7.22 ± 0.24	1330	0.1439 ± 0.0042	0.1533 ± 0.0077	0.1189 ± 0.0049	2.54 ± 0.24
7.22 ± 0.24	1330	0.1454 ± 0.0046	0.1538 ± 0.0081	0.1256 ± 0.0061	2.73 ± 0.30
10.99 ± 0.32	1330	0.1232 ± 0.0041	0.1510 ± 0.0082	0.1236 ± 0.0045	2.53 ± 0.22
10.99 ± 0.32	1330	0.1285 ± 0.0040	0.1592 ± 0.0082	0.1297 ± 0.0062	3.12 ± 0.34
2.10 ± 0.14	1330	0.1629 ± 0.0086	0.126 ± 0.010	0.1079 ± 0.0076	1.31 ± 0.16
2.10 ± 0.14	1330	0.1701 ± 0.0093	0.135 ± 0.010	0.0947 ± 0.0079	1.38 ± 0.21
9.61 ± 0.29	1330	0.1328 ± 0.0033	0.1486 ± 0.0068	0.1298 ± 0.0046	2.97 ± 0.24
9.61 ± 0.29	1330	0.1394 ± 0.0035	0.1659 ± 0.0071	0.1411 ± 0.0076	3.79 ± 0.39
12.69 ± 0.35	1330	0.1261 ± 0.0035	0.1560 ± 0.0076	0.1251 ± 0.0050	2.99 ± 0.26
12.69 ± 0.35	1330	0.1304 ± 0.0034	0.1608 ± 0.0074	0.1275 ± 0.0071	3.51 ± 0.36
15.98 ± 0.42	1330	0.1100 ± 0.0038	0.1525 ± 0.0084	0.1163 ± 0.0044	2.74 ± 0.26
15.98 ± 0.42	1330	0.1128 ± 0.0038	0.1553 ± 0.0084	0.1259 ± 0.0059	3.12 ± 0.32
5.39 ± 0.21	1330	0.1460 ± 0.0082	0.144 ± 0.012	0.1096 ± 0.0069	1.79 ± 0.26
5.39 ± 0.21	1330	0.1423 ± 0.0079	0.140 ± 0.012	0.1178 ± 0.0072	1.87 ± 0.27
10.48 ± 0.31	1330	0.1267 ± 0.0032	0.1589 ± 0.0068	0.1339 ± 0.0042	3.06 ± 0.23
10.48 ± 0.31	1330	0.1261 ± 0.0030	0.1542 ± 0.0065	0.1379 ± 0.0055	3.17 ± 0.24
CH_3CHO	He	(at $-110°$ C)			
5.70 ± 0.21	960	0.1358 ± 0.0028	0.0584 ± 0.0050	0.1045 ± 0.0052	3.01 ± 0.30
5.70 ± 0.21	960	0.1359 ± 0.0027	0.0656 ± 0.0050	0.1200 ± 0.0073	3.47 ± 0.33
2.70 ± 0.15	960	0.1376 ± 0.0029	0.0673 ± 0.0053	0.1199 ± 0.0053	2.98 ± 0.27
2.70 ± 0.15	960	0.1276 ± 0.0043	0.0615 ± 0.0069	0.0973 ± 0.0052	1.87 ± 0.21
9.35 ± 0.29	960	0.1301 ± 0.0015	0.0525 ± 0.0033	0.132 ± 0.011	7.23 ± 0.73
9.35 ± 0.29	960	0.1291 ± 0.0017	0.0592 ± 0.0036	0.127 ± 0.014	6.93 ± 0.81
1.56 ± 0.13	960	0.151 ± 0.010	0.056 ± 0.010	0.1070 ± 0.0091	0.97 ± 0.13
1.56 ± 0.13	960	0.160 ± 0.012	0.067 ± 0.012	0.095 ± 0.010	1.02 ± 0.19
4.44 ± 0.19	960	0.1421 ± 0.0031	0.0524 ± 0.0054	0.1230 ± 0.0060	3.01 ± 0.28
4.44 ± 0.19	960	0.1461 ± 0.0036	0.0579 ± 0.0059	0.1109 ± 0.0079	3.00 ± 0.40

Table B.1.   Tabulated Results

X	M	A_1	λ_1	A_2	λ_2
CH_3F	Ne	(at $-157°$ C)			
15.26 ± 0.41	370	0.0800 ± 0.0025	0.0543 ± 0.0064	0.1030 ± 0.0055	3.35 ± 0.34
15.26 ± 0.41	370	0.0789 ± 0.0029	0.0583 ± 0.0072	0.0993 ± 0.0069	3.25 ± 0.41
10.27 ± 0.31	370	0.0908 ± 0.0027	0.0511 ± 0.0060	0.1133 ± 0.0040	2.48 ± 0.20
10.27 ± 0.31	370	0.0954 ± 0.0026	0.0641 ± 0.0058	0.1158 ± 0.0056	3.02 ± 0.27
6.94 ± 0.24	370	0.1035 ± 0.0052	0.0550 ± 0.0088	0.1077 ± 0.0053	1.46 ± 0.15
6.94 ± 0.24	370	0.1072 ± 0.0046	0.0625 ± 0.0081	0.1142 ± 0.0058	1.74 ± 0.18
4.23 ± 0.18	370	0.1236 ± 0.0068	0.0648 ± 0.0093	0.1041 ± 0.0061	1.25 ± 0.14
4.23 ± 0.18	370	0.1129 ± 0.0088	0.054 ± 0.011	0.1107 ± 0.0077	1.07 ± 0.13
17.47 ± 0.45	370	0.0929 ± 0.0022	0.0845 ± 0.0060	0.1054 ± 0.0083	4.92 ± 0.59
17.47 ± 0.45	370	0.0888 ± 0.0024	0.0844 ± 0.0065	0.1031 ± 0.0083	4.15 ± 0.47
CH_3NO_2	Ne	(at $-50°$ C)			
2.31 ± 0.50	740	0.188 ± 0.053	0.054 ± 0.029	0.051 ± 0.052	0.50 ± 0.31
2.31 ± 0.50	740	0.134 ± 0.070	0.020 ± 0.037	0.107 ± 0.046	0.31 ± 0.25
11.05 ± 0.64	740	0.1100 ± 0.0020	0.0242 ± 0.0040	0.0726 ± 0.0047	3.39 ± 0.44
11.05 ± 0.64	740	0.1137 ± 0.0017	0.0283 ± 0.0037	0.0938 ± 0.0069	4.21 ± 0.44
5.34 ± 0.42	740	0.1278 ± 0.0034	0.0192 ± 0.0052	0.0898 ± 0.0039	1.90 ± 0.20
5.34 ± 0.42	740	0.1372 ± 0.0039	0.0304 ± 0.0057	0.0751 ± 0.0047	1.80 ± 0.25
8.27 ± 0.54	740	0.1255 ± 0.0020	0.0241 ± 0.0036	0.0808 ± 0.0036	2.58 ± 0.22
8.27 ± 0.54	740	0.1288 ± 0.0023	0.0268 ± 0.0040	0.0793 ± 0.0046	2.60 ± 0.28
$C_2H_4F_2$	He				
5.0 ± 0.1	1700				2.88 ± 0.75
5.0 ± 0.1	1700				2.84 ± 0.84
13.2 ± 0.2	1700				4.3 ± 1.4
13.2 ± 0.2	1700				3.4 ± 0.7
22.8 ± 0.3	1700				4.95 ± 0.86
22.8 ± 0.3	1700				6.72 ± 1.7
17.3 ± 0.3	1700				6.68 ± 1.3
17.3 ± 0.3	1700				4.12 ± 0.65
NO	N_2				
22.57 ± 0.54	800	0.0059 ± 0.0027	0.05	0.0554 ± 0.0028	0.77 ± 0.11
22.57 ± 0.54	800	0.0015 ± 0.0032	0.05	0.0520 ± 0.0031	0.64 ± 0.10
45.1 ± 1.0	800	0.0	0.0	0.0560 ± 0.0026	0.878 ± 0.064
45.1 ± 1.0	800	0.0	0.0	0.0412 ± 0.0023	0.633 ± 0.057
69.1 ± 1.5	800	0.0	0.0	0.0427 ± 0.0065	0.91 ± 0.21
69.1 ± 1.5	800	0.0	0.0	0.0591 ± 0.0079	1.35 ± 0.23
91.6 ± 1.9	800	-0.0042 ± 0.0024	0.05	0.0543 ± 0.0037	1.64 ± 0.24

Table B.1. Tabulated Results

X	M	A_1	λ_1	A_2	λ_2
91.6 ± 1.9	800	-0.0031 ± 0.0012	0.05	0.0479 ± 0.0032	1.77 ± 0.22
129.1 ± 2.7	800	0.0	0.0	0.0653 ± 0.0043	2.52 ± 0.23
129.1 ± 2.7	800	0.0	0.0	0.0415 ± 0.0035	1.98 ± 0.21